Carla Marina Pereira Gomes

PhD Thesis

Functionalized nanoparticles for targeted gene delivery to the nervous system

Dissertação submetida à Faculdade de Engenharia da Universidade do Porto para obtenção de grau de Doutor em Engenharia Biomédica

Faculdade de Engenharia
Universidade do Porto
2017

This thesis was supervised by:

Ana Paula Pêgo, PhD

INEB, Instituto de Engenharia Biomédica, Universidade do Porto, Portugal
i3S, Instituto de Investigação e Inovação em Saúde, Universidade do Porto, Portugal
FEUP, Faculdade de Engenharia da Universidade do Porto, Portugal
ICBAS, Instituto de Ciências Biomédicas Abel Salazar, Universidade do Porto, Portugal

The work described in this thesis was performed in:

INEB, Instituto de Engenharia Biomédica, Universidade do Porto, Portugal

i3S, Instituto de Investigação e Inovação em Saúde, Universidade do Porto, Portugal

and

Institute for Biophysics, Johannes Kepler Universität, Linz, Austria

The research described in this thesis was financially supported by:

- FEDER funds through the Programa Operacional Factores de Competitividade (COMPETE)

- Portuguese funds through FCT (Fundação para a Ciência e Tecnologia) in the framework of the project TARGETS (PTDC/CTM-NAN/115124/2009), BAITS (PTDC/CTM-NAN/3547/2014) and a PhD Grant (SFRH/BD/79930/2011).

Acknowledgements

O finalizar de uma tese de doutoramento é um momento de "*mixed feelings"*. Por um lado, o orgulho de completar esta etapa, que foi longa e, por vezes, extenuante. Por outro lado, desperta um sentimento de nostalgia. Ao longo dos últimos anos conheci pessoas que me marcaram e que vou levar para sempre comigo. Apesar dos obstáculos, vivi momentos muito felizes. A saudade será eterna.

A primeira pessoa a quem gostava de agradecer é a minha orientadora. Obrigada Ana Paula por ter acreditado em mim, mesmo sem me conhecer, e ter aceite concorrer a uma bolsa de doutoramento comigo. Obrigada pela orientação, por tudo o que me ensinou e principalmente pela sua visão optimista, sempre com uma palavra de incentivo, mesmo quando as coisas não corriam assim tão bem. Um doutoramento é como uma montanha russa, repleto de altos e baixos, e se consegui manter o equilíbrio, em parte devo-o a si.

I also would like to thank professor Hinterdorfer, Andreas, Mike and the rest of the group in Linz, who welcomed me so well! Although brief, I had a very good stay and learned a lot with all of you. Thank you for the helpful discussions that we shared and for the ideas that you gave me for my work.

Não poderia deixar de fazer um especial agradecimento a todos os que fizeram parte do projecto *TARGETS* e que, por isso mesmo, me acompanharam na bancada. Um grande obrigado à Aida, que mais do que uma colega de laboratório se tornou uma boa amiga. As horas passadas a trabalhar a teu lado foram sempre as mais divertidas e animadas! À Cátia, minha parceira nesta jornada, obrigada por todas as discussões, pelos desabafos, por toda a ajuda e acima de tudo, pela amizade. Iniciamos esta caminhada juntas e, foste sem dúvida um elemento crucial para me ajudar a terminá-la. Foi um prazer estar a teu lado e aprender contigo.

Aos meus "*Doutores*" que, não fazendo parte do mesmo projecto, estiveram intimamente relacionados com o meu trabalho e, por isso mesmo, são meus co-autores: Pedro, Vicky e Maria. Aprendi imenso com vocês e levo muitos dos vossos ensinamentos para sempre comigo. Obrigada Pedro pelas discussões científicas que partilhámos e pela tua visão crítica. Vicky, tu ensinaste-me um novo mundo de

reacções e compostos químicos! Sem ti para tirar todas as minhas dúvidas teria sido muito mais complicado. E, por último, mas não menos importante, a Maria: obrigada pela tua disponibilidade, pelo teu entusiasmo e pelas 1001 ideias que me foste dando. Acima de tudo, obrigada a todos pela vossa amizade, companheirismo e pelas histórias e sorrisos que partilhamos fora do horário de expediente!

Quero também agradecer a todos os elementos da minha equipa, a "*Neuro Team"*. Ao longo destes anos foram muitos os que foram entrando e saindo, mas levo um bocadinho de todos vocês comigo. À Pires, a primeira pessoa da equipa que conheci, que me foi mostrando os cantos à casa e a quem enchi de perguntas no início, Daniela Rocha, Ritinha, Daniela Salvador, Joana Silva, Diana, Miguel, Rita Bento, Patrick, Marisa, Joyce, João Garcia, Isabel Amaral, Daniela Barros, entre outros. Um especial agradecimento à Ana Sadio, a minha primeira companheira de trabalho e com quem comecei nesta aventura do quitosano! Obrigada por todas as discussões (científicas ou não) e por todas as gargalhadas que me proporcionaste.

Desde que comecei o doutoramento que ouço dizer que o INEB é uma grande família. E eu não podia concordar mais! O sentimento de união e interajuda que existe entre nós não se encontra em nenhum outro lugar. Levo comigo recordações de todos vocês. Desde os técnicos que tanto nos apoiam, aos administrativos, passando pelos colegas de corredor, obrigada a todos por me fazerem sentir parte desta família, e por toda a ajuda e generosidade que sempre senti da vossa parte. O que dizer dos "*Animais da Quinta*": Estrela, Pipa, Luísa, Bianca, Catarina Pereira, Luís, Tiago Santos, Tiago Laundos, João Martins, Vasco, Rúben, Francisca Silva, Rui Ribeiro, Bernardo, Patrícia... e todos os outros. Obrigada pelos momentos não-científicos tão prazerosos que me proporcionaram! Obrigada também à Inês Gonçalves por me ter convencido a fazer parte, ainda que por poucos meses, da equipa de basquetebol do INEB. Apesar de todos os arranhões e empurrões que recebia às quarta-feiras, foi muito divertido dividir o campo convosco!

Por fim, e porque os últimos são os primeiros, não podia deixar de referir aqueles que estiveram lá desde o início e que tornaram a minha jornada tão especial. Sempre que me lembrar do INEB, lembrar-me-ei primeiro de vocês! Aos meus queridos "*Polvinhos"*, incluindo os que já partiram: Ana Silva, Daniel Vasconcelos, Francisca Araújo, Sara Neves, Paula Lima, Mariana Valente, Mariana Fernandes, Ana Freire e o "*invasor*"

António Ribeiro – foi um prazer partilhar o gabinete (e muito mais!) com todos vocês! Obrigada pelo vosso carinho e amizade, pelas brincadeiras, pelos sorrisos, pelos desabafos e coscuvilhices, pelo bolo de chocolate, pelos almoços, jantaradas e, principalmente, obrigada pelo sushi!
Como diria uma conhecida "personagem" televisiva: vocês estão cá dentro! ☺

Não posso também deixar de agradecer a todos os meus amigos "*não-Inebianos*" que, apesar de desconhecerem as vicissitudes da vida de um investigador e nem sempre perceberem o porquê de eu ter de trabalhar a um fim-de-semana, sempre me apoiaram e encorajaram. Além disso, as nossas saídas, jantares e convívios foram fundamentais para conseguir manter a mente sã. Obrigada por estarem sempre lá!

Resta-me agradecer o apoio da minha família, o meu pilar.
Não existem palavras que descrevam a minha gratidão para com os meus pais, que tanto se sacrificaram para me proporcionarem tudo o que alcancei hoje. Obrigada pelo apoio, pelo carinho e pelo orgulho que demonstram por mim. Obrigada também por nunca questionarem as minhas decisões e por acreditarem nelas. Muito do que sou hoje, devo-o a vocês!

Aos meus irmãos (e respectivas "irmãs"), por me mimarem sempre e serem tão meus amigos e companheiros. Sei que poderei sempre contar convosco e que terei sempre o vosso apoio. Um obrigada ternurento também aos meus sobrinhos, que apesar de ainda tão pequeninos, me enchem de alegria e têm a capacidade de me animar mesmo nos piores momentos.

Last but not the least...
Agradeço-te a ti, a minha pedra basilar, pelo apoio incondicional, pelas palavras de conforto e encorajamento e por teres sempre acreditado em mim – às vezes mais do que eu própria. Obrigada por teres estado lado a lado comigo durante este percurso, por me teres "aturado" nas minhas piores crises, e principalmente por tudo o que me ensinaste com o teu exemplo de ética e profissionalismo. Uma parte do meu sucesso devo-o a ti, Sérgio.

Abstract

Peripheral neuropathies comprise a range of degenerative disorders that affect the peripheral nervous system, with no current effective treatment. The ability of neurotrophic factors to promote neuronal survival after injury or protect neurons in toxin-mediated disease models has spurred the idea that such proteins could be engaged for the treatment of peripheral neuropathies. However, in the long term, the administration of these short-lived factors to patients results in unwanted systemic toxicity.

The lack of effective therapies has brought new interest in the gene therapy approach, using DNA as a pro-drug to lead to the production of these therapeutic proteins in a specific fashion. In the last years, many efforts have been made in order to optimize and accomplish successful gene transfer to mammalian cells. Non-viral and viral strategies have been attempted, but an effective and safe system to mediate delivery to neurons is yet to be achieved.

Chitosan (CH), a natural polymer, has been described as a promising gene carrier, having as the main advantages the fact that is non-cytotoxic and biodegradable. However, CH low transfection efficiency under physiological conditions has hampered its widespread application. Here we proposed the use of trimethyl chitosan (TMC), a partially quaternized CH, for the development of a multi-component gene vector targeted to neurons of the peripheral nervous system.

Initial work was conducted in order to prepare nanoparticles (NPs) with improved stability at physiological conditions and optimal biodegradation rate. For this, we altered the biodegradation rate of TMC NPs by varying the degree of acetylation of the starting material, giving rise to NPs with different enzymatic degradation profiles, without compromising the NPs physicochemical properties or physiological stability. To address the influence of NP degradation rate on transfection efficiency we took advantage of imaging flow cytometry, a powerful statistical high-throughput bioimaging technique, to unravel some critical aspects about NP formulation such as the distinction between internalized *versus* cell-associated/adsorbed NP, and even explore NP intracellular localization. With this work, we were able to optimize the NP core in order to obtain an optimal biodegradation rate, which allowed us to correctly balance plasmid DNA protection from premature degradation and its efficient release. Overall, this work

provided novel information about the importance of vector degradation rate for gene delivery into cells, as a way to tune gene expression as a function of the desired application, and advanced imaging flow cytometry as a valuable tool for the initial steps of nucleic acid vector design.

Subsequently, the optimized TMC-based NPs were functionalized via thiol chemistry with neurotropic moieties to attain neuron-targeted NPs. The 50 kDa non-toxic carboxylic C-terminal fragment of the tetanus toxin heavy chain (HC) was grafted to the binary complex via a bi-functional poly(ethylene glycol) (PEG) linker, reactive for the thiol groups in the polymer. As one of the main hurdles in nanomedicine resides in the design of NPs that match the specificities of the target cell, in this work we took advantage of atomic force microscopy (AFM) to evaluate the specificity of neuron-targeted TMC NPs to neuronal cell populations in biological samples of different complexity. By using AFM tips functionalized with targeted or non-targeted NPs we were able to assess the specific interaction of each formulation with determined cell surface receptors in a precise fashion. Moreover, the combination of AFM with fluorescent microscopy allowed to correlate the individual interactions of the ligand-receptor pair in specific cells of heterogeneous primary cultures or subcellular regions of histological tissue sections. Overall, this study confirmed that we had developed a formulation with selective binding towards the neuronal population of cells, independently of the biological model being tested, and proved the feasibility of the proposed method for the development and characterization of targeted nanomedicines.

Finally, to achieve maximum cell-nanoparticle specific interaction, we investigated the impact of both PEG density and length on the vectoring capacity of the previously developed neuron-targeted TMC-based NPs. For this, the HC fragment was coupled to the 5 kDa bi-functional PEG (HC-PEG_{5k}) and grafted at different densities onto the NPs. Internalization and transfection studies on neuronal *versus* non-neuronal cells allowed to determine the intermediate grafting density as the one that yielded superior biological performance. Afterwards, to enhance HC exposition, NPs containing different mixtures of HC-PEG_{5k} and a 2 kDa PEG (PEG_{2k}) at the same grafting density were produced. By intercalating HC-PEG_{5k} with PEG_{2k} we attained a higher performance in terms of internalization (higher payload delivery into cells) and transfection efficiency, using

lower amounts of HC, which highlights the need to fine-tuning PEG-modified NPs for optimal targeting.

Overall, the work described in this thesis demonstrates the development of a non-toxic, stable, targeted and efficient NP based on TMC that can successfully cargo nucleic acids to neurons in a precise fashion, with improved stability and efficiency over the previous described vectors.

Resumo

As neuropatias periféricas incluem uma série de doenças degenerativas que afetam o sistema nervoso periférico, e atualmente não apresentam nenhum tratamento eficaz. A capacidade dos fatores neurotróficos de promoverem a sobrevivência e/ou proteção de neurónios, quer após lesão quer em modelos de doenças mediadas por neurotoxinas, estimulou a ideia de que estas proteínas podem ser utilizadas no tratamento destas patologias. No entanto, a longo prazo, a administração destes fatores que apresentam um curto tempo de semi-vida a pacientes resulta em toxicidade sistémica.

A falta de terapias eficazes despertou um particular interesse na possibilidade da terapia génica, que usa a molécula de ADN como um pró-fármaco para conduzir à produção destas proteínas terapêuticas num alvo específico. Nos últimos anos, têm sido feitos vários esforços para otimizar a transferência de genes para células de mamíferos de forma bem-sucedida. As principais estratégias baseiam-se no uso de vetores virais ou não-virais, mas até hoje ainda não foi desenvolvido nenhum sistema suficientemente eficaz e seguro para mediar a entrega de ácido nucleicos a neurónios.

O quitosano é um polímero natural que tem sido descrito como um vetor de genes bastante promissor, tendo como principais vantagens o fato de não ser citotóxico e ser biodegradável. No entanto, o quitosano apresenta uma baixa eficiência de transfeção em condições fisiológicas, o que tem dificultado a sua aplicação de forma generalizada. Assim, neste trabalho propusemos o uso de trimetil quitosano (TMC), um quitosano parcialmente quaternizado, para o desenvolvimento de um vetor direcionado para neurónios do sistema nervoso periférico.

Para alcançar o nosso objetivo, o nosso trabalho inicial focou-se na preparação de nanopartículas (NPs) com uma melhor estabilidade em condições fisiológicas e ótima cinética de biodegradação. Para tal, alteramos a velocidade de biodegradação de NPs de TMC variando o grau de acetilação do polímero, dando origem a NPs com diferentes perfis de degradação enzimática sem comprometer as propriedades físico-químicas ou estabilidade fisiológica das mesmas. Para determinar a influência da cinética de degradação das NPs na eficiência de transfeção, fizemos uso da técnica de citrometria de fluxo com imagem, uma ferramenta poderosa de alto rendimento estatístico, para desvendar alguns aspetos críticos na formulação de NPs. Nomeadamente, a distinção

entre NPs internalizadas em detrimento de NPs associadas/adsorvidas à membrana celular, e até mesmo explorar a localização intracelular das mesmas. Com este trabalho conseguimos otimizar a estrutura base das NPs de forma a obter uma taxa de biodegradação ideal, o que nos permitiu equilibrar o efeito de proteção do ADN contra a sua degradação prematura e a sua libertação eficiente. Em geral, o nosso trabalho permitiu reconhecer a importância da cinética de degradação dos vetores para a libertação das moléculas de ADN nas células, como forma de ajustar a expressão génica em função da aplicação desejada, e apresenta a citometria de fluxo acoplada a microscopia de fluorescência como uma ferramenta valiosa nos passos iniciais do desenho de vetores para entrega de ácidos nucleicos.

Posteriormente, as NPs de TMC foram funcionalizadas com moléculas neurotrópicas através da introdução de grupos tiol no polímero. O fragmento não tóxico da toxina do tétano de 50 kDa (HC) foi acoplado às NPs através de um polímero bifuncional, o poli(etileno glicol) (PEG), reativo para os grupos tiol no polímero. Como um dos principais obstáculos à nanomedicina reside no desenho de NPs que se ajustam às especificidades da célula alvo, neste trabalho usamos a técnica de microscopia de força atómica (AFM) para avaliar a especificidade das NPs de TMC funcionalizadas em amostras biológicas de diferente complexidade. Ao usar pontas de AFM ligadas a NPs específicas *versus* NPs não específicas, fomos capazes de avaliar de forma precisa a interação de cada formulação com determinados recetores da superfície celular. Além disso, a combinação da AFM com microscopia fluorescente permitiu-nos correlacionar as interações individuais do par ligando-recetor em células alvo de culturas primárias heterogéneas ou regiões sub-celulares de secções histológicas de amostras de tecidos. De forma geral, este estudo confirmou o desenvolvimento de uma formulação capaz de se ligar seletivamente à população neuronal de células, independentemente do modelo biológico testado, e provou a viabilidade do método proposto para o desenvolvimento e caracterização de NPs formuladas para terapias dirigidas.

Por fim, de forma a alcançar a máxima interação entre neurónios e NPs de forma específica, investigamos o impacto da densidade e do tamanho da molécula de PEG na capacidade de vectorização das NPs de TMC previamente desenvolvidas. Para isso, o HC foi associado a um PEG bi-funcional de 5 kDa (HC-PEG_{5k}) que foi posteriormente acoplado às NPs em diferentes densidades. Estudos de internalização e transfeção, tanto

em células neuronais como não-neuronais, permitiram-nos determinar que a densidade intermediária de HC-PEG testada foi aquela que demostrou um desempenho biológico superior. De seguida, de forma a melhorar a exposição da molécula de HC, produziram-se NPs contendo diferentes misturas de HC-PEG_{5k} e um PEG de 2 kDa (PEG_{2k}), mantendo a densidade total de PEGs inalterada à superfície das NPs. Ao intercalar HC-PEG_{5k} com o PEG_{2k}, obtivemos um melhor desempenho em termos de internalização (maior transferência de carga das NPs para as células) e eficiência de transfeção, usando menores quantidades de HC, o que evidência a necessidade de ajustar as modificações com PEG à superfície das NPs de forma a obter o seu rendimento máximo.

Em resumo, o trabalho descrito nesta tese demonstra o desenvolvimento de NPs não tóxicas, estáveis, direcionadas e eficientes com base no uso de TMC, que são capazes de entregar, de forma bem-sucedida e precisa, ácidos nucleicos a neurónios, apresentando maior estabilidade e eficiência em relação aos vetores anteriormente descritos.

Table of Contents

Acknowledgements ix

Abstract xiii

Resumo xvii

Table of Contents xxi

List of Abbreviations xxv

PART 1

CHAPTER I – General Introduction 3

CHAPTER II – Aims and Structure of the Thesis 13

1. Aim of the Thesis 15
2. Structure of the Thesis 17

CHAPTER III – Translating Chitosan into Clinical Delivery of Nucleic Acid-based Drugs 23

1. Chitosan: Sources and Properties 27
2. Chitosan as a Vector for Nucleic Acid Delivery 29
   - *2.1. Plasmid DNA* *29*
   - *2.2. Small interferences RNA* 31
   - *2.3. Single-stranded oligonucleotides* 33
3. *In vivo* Application of Chitosan as a Vector for Nucleic Acid Delivery 36
4. Translating Chitosan into the Clinic for Nucleic Acid Delivery: Progress and Challenges 41
5. Conclusions 44

References 45

CHAPTER IV – Overcoming the Barriers Towards Successful Gene Delivery to the Peripheral Nervous System **51**

1. Biological Barriers for Gene Delivery into Neurons 53
1.1. Extracellular barriers 55
1.2. Intracellular barriers 56
1.2.1. Cellular uptake 57
1.2.2. Intracellular trafficking and endosomal escape 58
1.2.3. Plasmid DNA nuclear entry 59
2. Targeting neuronal cells 60
2.1. Atomic force microscopy as a tool to tailor targeted nanoparticles 62
3. Conclusions 66
References 67

PART 2

CHAPTER V – A High-Throughput Bioimaging Study to Assess the Impact of Nanoparticle Degradation on DNA Delivery Performance **73**

Abstract 77
1. Introduction 78
2. Materials and Methods 80
3. Results 88
4. Discussion 101
5. Conclusions 103
Supplementary Information 104
References 110

CHAPTER VI – Atomic Force Microscopy as a Tool to Assess the Specificity of Targeted Nanoparticles in Biological Models of High Complexity **113**

Abstract 117
1. Introduction 118
2. Materials and Methods 120
3. Results 126
4. Discussion 141
5. Conclusions 144
Supplementary Materials and Methods 145
References 149

CHAPTER VII – Fine Tuning Neuronal Targeting of Nanoparticles by Adjusting the Ligand Grafting Density and Combining PEG Spacers of Different Length **153**

Abstract 157
1. Introduction 158
2. Materials and Methods 161
3. Results 167
4. Discussion 178
5. Conclusions 183
Supplementary Information 184
References 186

CHAPTER VIII – Concluding Remarks and Future Perspectives **189**

APPENDICES

APPENDIX I – Molecular recognition force spectroscopy for probing cell targeted nanoparticles *in vitro* **199**

Abstract 203
1. Introduction 204
2. Materials 206
3. Methods 209
4. Notes 217
References 221

APPENDIX II – BDNF gene delivery mediated by neuron-targeted nanoparticles is neuroprotective in peripheral nerve injury **223**

Abstract 227
1. Introduction 228
2. Materials and Methods 231
3. Results 240
4. Discussion 252
5. Conclusions 257
Supplementary Information 258
References 260

APPENDIX III – Short Biography **263**

List of Abbreviations

A

AFM – Atomic force microscopy

AON – Antisense oligonucleotides

APTES – (3-aminopropyl)triethoxysilane

ASTM – American Society for Testing and Materials

B

BDNF – Brain-derived neurotrophic factor

BNB – Blood-nerve barrier

BP – Binding probability

BSA – Bovine serum albumin

C

CH – Chitosan

CQ - Chloroquine

CTL – Cytotoxic T lymphocyte

CVB3 – Coxsackievirus B3

D

DA – Degree of acetylation

DAPI – 4',6-diamidino-2-phenylindole

Der p 1 – Dermatophagoides pteronyssinus 1

Der p 2 – Dermatophagoides pteronyssinus 2

DLS – Dynamic light scattering

DMEM – Dulbecco's modified Eagle medium

DQ – Degree of quaternization

DRG – Dorsal root ganglia

DTNB – 5,5-dithio-bis-(2-nitrobenzoic acid) (Ellman's reagent)

E

EDC – (3-dimethylaminopropyl) carbodiimide

EDF – Extended depth of field filter

EDTA - Ethylenediaminetetraacetic acid

eGFP – Enhanced green fluorescent protein

F

FACS – Fluorescence-activated cell sorting (applied in flow cytometry)

FBS – Fetal bovine serum

FDA – Food and Drug Administration (US regulatory entity)

FDC – Force-distance curves

G

GADPH - Glyceraldehyde-3´ phosphate dehydrogenase

GAP-43 – Growth-associated protein 43

GLP-1 – Glucagon-like peptide-1

GM-SCF – Granulocyte-macrophage colony-stimulating factor

GPC – Gel permeation chromatography

GRA1 – Dense granule protein 1

GT1b – Trisialoganglioside GT_{1b} receptors

H

HBS – HEPES buffered saline solution

HC – Non-toxic and neurotropic carboxylic C-terminal fragment of the tetanus toxin heavy chain

HEPES - 4-(2-hydroxyethyl)-1-piperazineethanesulfonic acid

HIV – Human immunodeficiency virus

HLA-A2 – Human leukocyte antigen serotype-A2

I

IFN-ɣ – Interferon-ɣ

IL – Interleukin

IR – Infrared spectroscopy

IS – Internalization score

K

k_{eff} – Effective spring constant

k_{off} – Kinetic off-rate constant

M

MAL – Maleimide group

MeO – Methoxy group

miRNA – MicroRNA

Mn – Number molecular weight

MNCV – Motor nerve conduction velocity

MRFS – Molecular recognition force spectroscopy

mRNA – Messenger RNA

Mw – Weight molecular weight

N

NF – Neurotrophic factor

NF-H – Neurofilament H

NF200 – Neurofilament 200

NHS – N-Hydroxysuccinimide

NLV – Nanoparticle-loaded vesicles

NMJ – Neuromuscular junction

NMR – Nuclear magnetic resonance

NP – Nanoparticle

nT NPs – Non-targeted nanoparticles

P

PBS – Phosphate-buffered saline

PDF – Probability density functions

PdI – Polydispersity index

PDL – poly-*d*-lysine

pDNA – Plasmid DNA

PEDF –Pigment epithelium-derived factor

PEG – Poly(ethylene glycol)

PEI – Poly(ethylene imine)

PEISH – Thiolated poly(ethylene imine)

PFA – Paraformaldehyde

PN – Peripheral neuropathies

PNS – Peripheral nervous system

Q

QDs – Quantum dots

R

RALLS – Right angle laser light scattering

RFU – Relative fluorescence units

Rho A – anti-Ras homologous A

RNase H – Endoribonuclease H

RSV – Respiratory syncytial vírus

RT – Room temperature

RT-qPCR – Reverse transcription and quantitative real-time PCR

RXFP1 – Relaxin family peptide receptor

S

S100 – Schwann cell marker

SARS-CoV – Severe acute respiratory syndrome coronavirus

SD – Standard deviation

SDS - Sodium dodecyl sulfate

SFI – Sciatic functional index

shRNA – small hairpin RNA

siRNA – Small interference RNA

ssON – Single-stranded oligonucleotides

STAT4 –Signal transducer and activator of transcription protein 4

T

TCEP - Tris(carboxyethyl)phosphine hydrochloride

TEA - Triethylamine

TEM – Transmission electron microscopy

Tg NPs – Targeted nanoparticles

TG2 – Tissue transglutaminase

TGF-β1 – Transforming growth factor-β1

Th1 – T helper 1 cells

TMC – Trimethyl chitosan

TMC_{SH} – Thiolated trimethyl chitosan

TNF-α – Tumor necrosis factor α

TPP – Tripolyphosphate

trkB – Tyrosine kinase receptor B

V

VEGF – Vascular endothelial growth factor

X

$x_ß$ – Energetic barrier length scale

PART 1

CHAPTER I

GENERAL INTRODUCTION

Peripheral neuropathies (PN) comprise a range of conditions – disease or trauma - that affect the peripheral nervous system (PNS). Patients may present motor insufficiency (weakness, movement impairment), sensory abnormalities (numbness, paresthesia, hyperalgesia/allodynia, pain), autonomic symptoms, or a combination of all, often depending on the disease [1]. The etiologies of PN are diverse, ranging from the most common diabetes mellitus, to traumatic injuries, chronic diseases, autoimmune disorders, genetic neuropathies, tumors, nutritional deficiencies, side effects of certain medications and iatrogenic lesions [2-4]. Other endocrinological abnormalities that can result in neuropathy include hypothyroidism and acromegaly. The neuropathy associated with hypothyroidism commonly manifests as carpal tunnel syndrome. PN of acromegaly (excess growth hormone) include carpal tunnel syndrome and sensorimotor polyneuropathy. Human immunodeficiency virus (HIV) also results in PN, usually involving distal, non-painful paresthesias, decreased ankle reflexes, and abnormal pain and temperature perception, and it affects as many as one-third of the total individuals with the syndrome [4]. Medications that commonly result in PN include the chemotherapy of drugs cisplatin, suramin, paclitaxel, and docetaxel [5, 6], as well as cholesterol-lowering statin drugs [7], HIV antiretroviral drugs, and thalidomide [5].

The nerve fibers in the PNS retain, also in adulthood, a high post-traumatic regeneration potential (**Figure 1**). However, in most cases, the clinical outcome after peripheral nerve lesions is far from being satisfactory and almost never functional recovery is attained [8]. Additionally, the conventional therapies for PN focus on pain management, being palliative rather than curative. These include medications that can be classified into several groups, mainly opioids, antidepressants, anticonvulsants, and local therapies [9]. Consequently, approaches that can promote nerve regeneration are eagerly awaited.

Neuronal survival after axotomy is a prerequisite for regeneration and is facilitated by an array of trophic factors from multiple sources [10]. Recent advances in the understanding of molecular pathways and their physiological role demonstrate that neurotrophic factors (NF) play an important part in the development, maintenance, and regeneration of the nervous system [11, 12].

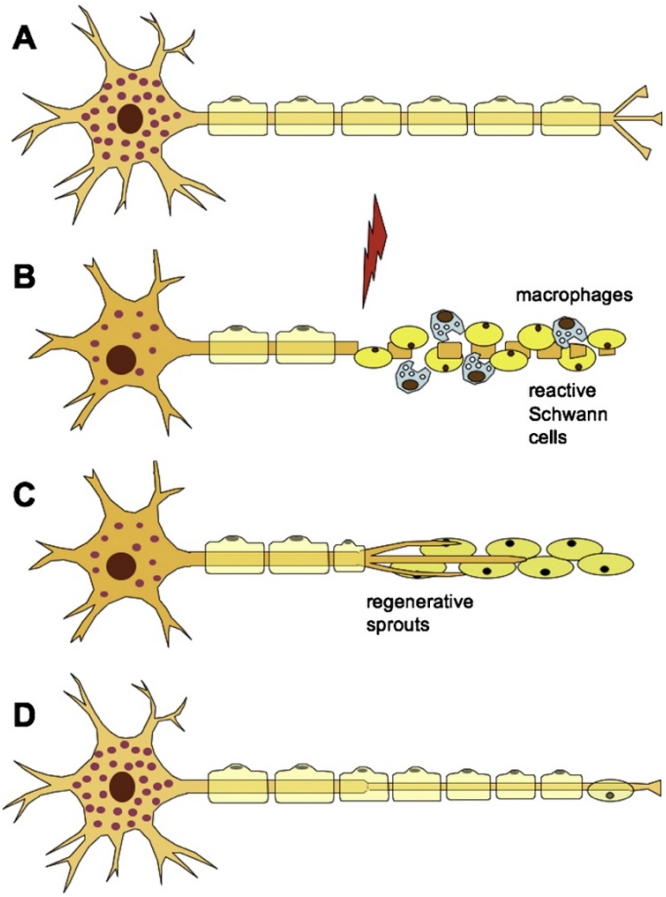

Figure 1. Degeneration and regeneration after peripheral nerve injury. (A) Normal neuron and nerve fiber; (B) Neuron undergoing through Wallerian degeneration: the axotomy results in fragmentation of the distal axon and myelin sheaths. Schwann cells proliferate and macrophages invade the distal nerve segment and phagocytize degrading materials; (C) Schwann cells in the distal segment lined up in bands of Bungner. Axonal sprouts advance embedded in the Schwann cells and are attracted by gradients of neurotrophic factors; (D) Axonal reconnection with end organs and maturation and re-myelination of the nerve fiber. Reprinted from [13], Copyright © 2012 with permission from Elsevier Ltd. All rights reserved.

NFs are a family of typically small proteins (< 30 kDa) that bind to receptor kinases on the cell membrane. Based on animal models of neurological disease, administered NFs can prevent or slow down disease progression by enhancing metabolism, growth and function of neurons. The delivery of NFs has been postulated as a therapy for diseases in which neuronal function is disturbed, such as spinal cord injury, epilepsy, neurodegenerative disorders (Parkinson's disease, Alzheimer's disease, amyotrophic lateral sclerosis, Huntington's disease), neuropathic pain and stroke [11]. They can also prevent nerve cell death caused by various insults, including nerve injury and brain trauma [11]. Unfortunately, these factors have some inevitable limitations such as short half-life as well as several adverse side effects due to their non-specific uptake after

systemic delivery, and therefore cannot be administered to patients for a long period of time [14]. Different approaches have been developed over the last years to overcome difficulties associated with systemic administration of NFs. The lack of effective therapies has brought new interest in the gene therapy approach.

Gene therapy can be defined as the intentional modulation of gene expression in specific cells to treat pathological conditions. Nowadays, almost any sequence in the genome and every RNA in the transcriptome has the potential to be modulated for therapeutic purposes through the introduction of exogenous nucleic acids into cells [15]. The goal is to deliver genetic information to a target cell, either to replace a defective function (monogenic disease), inhibit the expression of a certain protein or to introduce an additional function to treat or to prevent disease (as in a vaccine) [16]. In order to exhibit biological functions, the externally administered nucleic acids should reach the site of action in a biologically active form. However, nucleic acids are generally difficult to delivery in a systemic fashion due to their rapid clearance, limited serum half-life owing to nucleases degradation, lack of organ-specific distribution and low efficiency of cellular uptake [17, 18]. In an attempt to counteract this issue, nucleic acids are usually delivered into cells by means of vectors, which may be of viral or non-viral origin (**Figure 2**) [19].

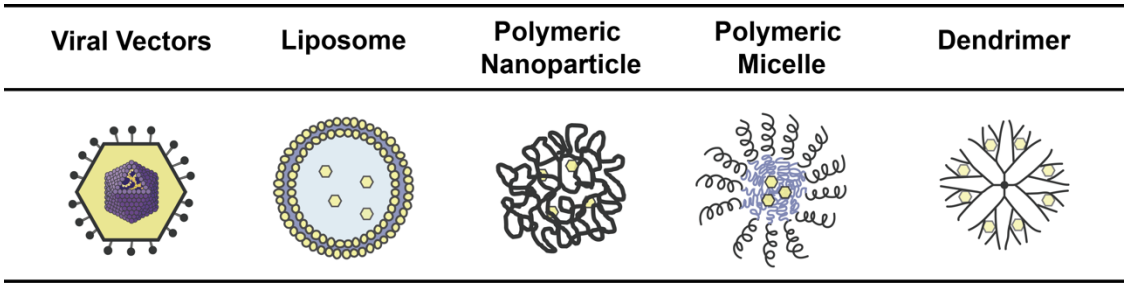

Figure 2. Schematic representation of the most widely used gene delivery vectors.

Viruses are highly evolved biological machines that efficiently gain access to host cells and exploit the cellular machinery to facilitate their replication. For most gene-therapy applications, ideal virus-based vectors harness the viral infection pathway but avoid the subsequent expression of viral genes that leads to replication and toxicity. This is achieved by deleting all, or some, of the coding regions from the viral genome, but leaving intact those sequences that are required for functions as packaging the vector

genome into the virus capsid or the integration of vector DNA into the host chromatin [16]. The most commonly used viral vectors are derived from retrovirus, adenovirus, and adeno-associated virus. Other viral vectors that have been less extensively used are derived from herpes simplex virus 1 (HSV-1), vaccinia virus, or baculovirus [20]. Despite their high efficiency to transfect cells, viral vectors pose safety concerns such as immunogenicity, insertional mutagenesis, limitation of the cargo size or the difficulty of large-scale production [21]. Thus, improving the design and biosafety of these vectors is a critical challenge for the future.

On the contrary, the most common used non-viral vectors for gene delivery are normally composed of cationic polymers or lipids, which are able to form ionic complexes with nucleic acids and possess the potential advantage of unrestricted cargo size, ease of preparation, low immunogenicity and potential for repeated administration [22]. Among these, polycationic polymers have been extensively investigated due to their versatility. They are able to interact electrostatically with negatively charged nucleic acids to form stable particles, termed polyplexes, with diameters that can be tuned to the order of nanometers. Physical properties of polymers such as rigidity, hydrophilicity, charge density, biodegradability and molecular weight can be adjusted to modulate nucleic acid-delivery properties such as nucleic acid binding, colloidal stability of ionic complexes, endosomal escape, vector unpacking, cytotoxicity and transfection efficiency [22]. Moreover, they are biocompatible and minimally immunogenic and cytotoxic, facts that can render such polymers a good alternative to viral or lipid mediated transfection [23].

Chitosan (CH) has been one of the most studied polymeric vectors for gene therapy, particularly for the delivery of plasmid DNA (pDNA), due to its biodegradability, biocompatibility and strong affinity with DNA [24]. CH is a linear polysaccharide consisting of repeating D-glucosamine and N-acetyl-D-glucosamine units, linked via (1-4) glycosidic bonds [25], and is a product derived from the alkaline N-deacetylation of chitin obtained from the exoskeleton of crustaceans like shrimp, the endoskeleton of squid or the cell walls of mushrooms [26]. Multiple studies have shown that the binding affinity of CH for DNA, the stability and the transfection efficiency of CH-DNA complexes are dependent on several parameters, including the polymer molecular weight and polydispersity, polymer degree of acetylation, DNA concentration, serum concentration

and pH of transfection medium, among other factors. The variation of these parameters can significantly influence the cellular uptake and endosomal escape of the complexes, and, subsequently, gene expression [27, 28]. Nevertheless, in comparison with poly(ethylene imine) (PEI), one of the gold-standard cationic polymers used for gene delivery, chitosan has lower transfection efficiency, since unlike PEI, the buffering capacity of CH is modest and is restricted to the pH interval between 5 and 7 [26]. Also, its low solubility at physiological pH hampered the progress of CH as a potential gene carrier for biomedical applications.

In an attempt to improve CH as a gene carrier and to enhance its transfection efficiency, various derivatives of CH have been synthesized. One of these generated derivatives was *N,N,N*-trimethyl chitosan (TMC). TMC is a partially quaternized derivative of CH and was first synthesized by Muzzarelli and Tanfani [29], to increase the solubility of CH at neutral and basic pH values [30]. Since it was first proposed, TMC has been widely used for different biomedical applications, including as an absorption enhancer and for drug and gene delivery. As TMC has fixed positive charges on its backbone, it can more effectively condense pDNA at physiologic pH, bringing about a 2.5 to 35-fold increase in the transfection efficiency compared to CH/pDNA complexes. However, TMC with high degrees of quaternization exerts stronger condensing capacity upon pDNA which deters intracellular gene dissociation, thus limiting the gene expression level [31].

A great advantage of non-viral delivery vectors is their unique tunable physicochemical characteristics, as the possibility to incorporate targeting elements into their structure that can efficiently bind to cell-surface receptors in target cells, in order to deliver and express genes in a specific fashion, without harming non-target cells and tissues [32, 33]. Different types of ligands such as glycosylated molecules, peptides, proteins or antibodies can be used in an active-targeting strategy depending on the location and/or cell/tissue properties [33]. When formulating a targeted non-viral gene delivery system, there are a number of factors to be considered that may have an effect on the overall efficiency of the delivery system, such as ligand density and positioning on the surface of the vector, vector size, and choice of targeting ligand. Vector ligand density should be optimized to ensure efficient binding to receptors [34, 35]. Furthermore, the binding of a ligand to its substrate may facilitate binding of neighboring receptors in a

thermodynamically favorable way [36]. In addition, the strategies used to link the targeting moieties to vectors, as well as many other factors including relative specificity, expression of target receptors, and physiological factors need to be considered in order to improve effectiveness and avoid interference or loss of biological activity.

In sum, the use of gene therapy holds great potential for future medicines for many applications, including neuronal regeneration. However, the reduced number of gene therapy products reaching the market is disappointing when one considers the number of research groups involved in the research and the clinical trials underway. It seems that until more suitable delivery systems become available, the potential of this field will never be reached.

References

1. Cashman, C. and A. Höke, "Mechanisms of distal axonal degeneration in peripheral neuropathies." Neurosci Lett, 2015. 596: p. 33-50.

2. Deumens, R., et al., "Repairing injured peripheral nerves: Bridging the gap." Progress in Neurobiology, 2010. 92(3): p. 245-276.

3. Head, K.A., "Peripheral Neuropathy: Pathogenic Mechanisms and Alternative Therapies." Alternative Medicine Review, 2006. 11(4): p. 294-329.

4. Weimer, L., "Medication-induced peripheral neuropathy." Curr Neurol Neurosci Rep, 2003. 3(1): p. 86-92.

5. Brewer, J., et al., *Chemotherapy-induced peripheral neuropathy: Current status and progress.*, in *Gynecol Oncol*. 2015.

6. Corrao, G., et al., "Lipid lowering drugs prescription and the risk of peripheral neuropathy: an exploratory case-control study using automated databases." J Epidemiol Community Health, 2004. 58(12): p. 1047-51.

7. Chiang, M., et al., "Progress in the treatment of small fiber peripheral neuropathy." Expert Rev Neurother, 2015. 15(3): p. 305-13.

8. Frostick, S., Q. Yin, and G. Kemp, "Schwann cells, neurotrophic factors, and peripheral nerve regeneration." Microsurgery, 1998. 18(7): p. 397-405.

9. Geuna, S., et al., "Tissue engineering and peripheral nerve reconstruction: an overview." Int Rev Neurobiol, 2013. 108: p. 35-57.

10. Boyd, J.G. and T. Gordon, "Neurotrophic Factors and Their Receptors in Axonal Regeneration and Functional Recovery After Peripheral Nerve Injury." Molecular Neurobiology, 2002. 27(3): p. 277-324.

11. Lim, S.T., M. Airavaara, and B.K. Harvey, "Viral vectors for neurotrophic factor delivery: A gene therapy approach for neurodegenerative diseases of the CNS." Pharmacological Research, 2010. 61(1): p. 14-26.

12. Gordon, T., "The role of neurotrophic factors in nerve regeneration." Neurosurg Focus, 2009. 26(2): p. E3.

13. Allodi, I., E. Udina, and X. Navarro, "Specificity of peripheral nerve regeneration: interactions at the axon level." Prog Neurobiol, 2012. 98(1): p. 16-37.

14. Thorne, R.G. and W.H. Frey, 2nd, "Delivery of neurotrophic factors to the central nervous system: pharmacokinetic considerations." Clin Pharmacokinet, 2001. 40(12): p. 907-46.

15. Yin, H., et al., "Non-viral vectors for gene-based therapy." Nat Rev Genet, 2014. 15(8): p. 541-55.

16. Bouard, D., N. Alazard-Dany, and F.L. Cosset, "Viral vectors: from virology to transgene expression." British Journal of Pharmacology, 2009. 157(2): p. 153-165.

17. Seow, Y. and M.J. Wood, "Biological Gene Delivery Vehicles: Beyond Viral Vectors." Molecular Therapy, 2009. 17(5): p. 767-777.

18. Nishikawa, M., S. Rattanakiat, and Y. Takakura, "DNA-based nano-sized systems for pharmaceutical and biomedical applications." Adv Drug Deliv Rev, 2010. 62(6): p. 626-632.

19. Johnson-Saliba, M. and D.A. Jans, "Gene Therapy: Optimising DNA Delivery to the Nucleus." Current Drug Targets, 2001. 2: p. 371-399.

20. Ponder, K.P., "Vectors in gene therapy." An introduction to molecular medicine and gene therapy, 2001: p. 77-112.

21. Xu, H., Z. Li, and J. Si, "Nanocarriers in gene therapy: a review." J Biomed Nanotechnol, 2014. 10(12): p. 3483-507.

22. Grigsby, C. and K. Leong, "Balancing protection and release of DNA: tools to address a bottleneck of non-viral gene delivery." J R Soc Interface, 2010. 7 Suppl 1: p. S67-82.

23. Borchard, G., "Chitosans for gene delivery." Adv Drug Deliv Rev, 2001. 52(2): p. 145-50.

24. Gomes, C.P., et al., "Translating chitosan to clinical delivery of nucleic acid-based drugs." MRS Bulletin, 2014. 39(01): p. 60-70.

25. Mao, S., W. Sun, and T. Kissel, "Chitosan-based formulations for delivery of DNA and siRNA." Advanced Drug Delivery Reviews, 2010. 62(1): p. 12-27.

26. Xu, Q., C.-H. Wang, and D.W. Pack, "Polymeric Carriers for Gene Delivery: Chitosan and Poly(amidoamine) Dendrimers." Current Pharmaceutical Design, 2010. 16: p. 2350-2368.

27. Moreira, C., et al., "Improving chitosan-mediated gene transfer by the introduction of intracellular buffering moieties into the chitosan backbone." Acta Biomaterialia, 2009. 5(8): p. 2995-3006.

28. Pires, L.R., et al., "Imidazole-grafted chitosan-mediated gene delivery: in vitrostudy on transfection, intracellular trafficking and degradation." Nanomedicine, 2011. 6(9): p. 1499–1512.

29. Muzzarelli, R.A.A. and F. Tanfani, "The N-permethylation of chitosan and the preparation ofN-trimethyl chitosan iodide." Carbohydr. Polym., 1985. 5: p. 297–307.

30. Jintapattanakit, A., et al., "Physicochemical properties and biocompatibility of N-trimethyl chitosan: effect of quaternization and dimethylation." Eur J Pharm Biopharm, 2008. 70(2): p. 563-71.

31. Zhao, X., et al., "Thiolated trimethyl chitosan nanocomplexes as gene carriers with high in vitro and in vivo transfection efficiency." J Control Release, 2010. 144(1): p. 46-54.

32. Warhler, R., S.J. Russell, and D.T. Curiel, "Engineering targeted viral vectors for gene therapy." Nature Reviews Genetics, 2007. 8: p. 573-587.

33. Rogers, M.L. and R.A. Rush, "Non-viral gene therapy for neurological diseases, with an emphasis on targeted gene delivery." J Control Release, 2012. 157(2): p. 183-9.

34. Gutoaia, A., et al., "Fine-tuned PEGylation of chitosan to maintain optimal siRNA-nanoplex bioactivity." Carbohydr Polym, 2016. 143: p. 25-34.

35. Rabanel, J.M., P. Hildgen, and X. Banquy, "Assessment of PEG on polymeric particles surface, a key step in drug carrier translation." J Control Release, 2014. 185: p. 71-87.

36. Yeo, Y., *Nanoparticulate Drug Delivery Systems: Strategies, Technologies, and Applications*. May 2013: John Wiley & Sons, Inc.

CHAPTER II

AIMS AND STRUCTURE OF THE THESIS

1. Aim of the Thesis

The main goal of the work described in this thesis was the development of a non-toxic, stable, targeted, efficient and simple nanoparticle (NP) that can specifically cargo DNA to neurons (**Figure 1**). The ultimate objective was to apply the developed nanoparticle as a vector of neurotrophic factor encoding genes, that can mediate gene delivery in the peripheral nervous system after a minimally invasive administration, towards the promotion of neurosurvival and neuroregeneration.

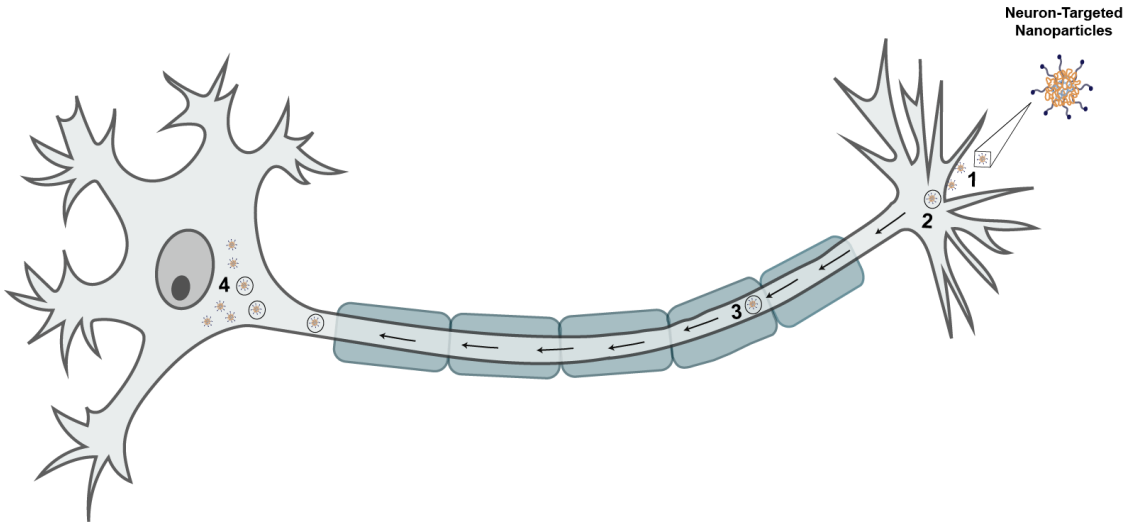

Figure 1. Schematic representation of the barriers that must be overcome by the developed vector for the optimal delivery of DNA into neurons. The developed neuron-targeted NPs will have to be specifically recognized by membrane receptors at the axon terminal of neurons (1) in order to be internalized into endocytic vesicles (2). Afterwards, the nanoparticles should reach the neuronal cell bodies through their active retrograde axonal transport (3). When present in the cell body, the nanoparticles have to surpass the endocytic barrier and be release from these vesicles into the cytoplasm (4). Finally, the gene of interest should reach the cell nucleus where it will exert its function.

In the design of a targeted NP-based system several points must be considered. Namely, the size and charge of the NP, its stability in physiological milieu, the nature, density and exposure of the targeting moieties, the delivery efficiency of the system, the duration and kinetics of the transgene expression and the toxicity profile.

As the starting material for the preparation of the targeted NP we have selected chitosan (CH).

Specific objectives for this work included:

a) the preparation and characterization of CH-based NPs with improved stability at physiologic conditions and optimized degradation kinetics;

b) tethering of a neuron targeting moiety to the NPs – here, we explored the non-toxic fragment of the tetanus toxin;

c) assessment of the interaction of the targeted NPs with neural cell populations and neural tissues by molecular recognition force spectroscopy, to probe neuronal specificity;

d) optimization of spacer length and protein density at the surface of the NPs towards achieving optimal cell binding and transfection efficiency in neuronal cells.

2. Structure of the Thesis

This thesis is divided into two parts, with a total of eight chapters and three appendices. In the first part of the thesis (Part I) a general introduction and a literature background is given to locate the reader on the field and support the proposed strategy. In the second part of the thesis (Part II) the explored methodology and obtained results are presented, and an overall discussion of the proposed strategy is provided.

In **Chapter III** we reviewed the most relevant work using CH-based vectors for the delivery of different nucleic acids, as well as data on the *in vivo* testing of these delivery systems [1]. Moreover, we additionally expressed our view on the barriers that might be hampering the translation of this knowledge into clinical practice and the challenges that need to be fulfilled for these promising vehicles to reach patients.

For gene therapy to advance, it is necessary the rational design of gene-delivery vectors able to address the individual rate-limiting steps identified along the gene-delivery pathway [2]. Most of these barriers are transversal to most cell types, although neurons have additional specifications such as a larger size and lack of division capacity. To achieve efficient neuronal gene delivery following a peripheral administration, vectors must mediate binding and internalization at axon terminals, undergo retrograde axonal transport, vesicular escape, and finally, in the case of plasmid DNA (pDNA) delivery, nuclear entry [3]. The different barriers for gene transfer into the nervous system are described in **Chapter IV**, including vector stability in the extracellular environment, tissue targeting, cellular binding and uptake, intracellular trafficking, endosomal escape, controlled vehicle unpacking and pDNA nuclear translocation. The presented state of the art also includes the main strategies used to target NPs to the nervous system, as well as the prospect of applying atomic force microscopy for the evaluation of NP specificity towards target cells and/or tissues.

The formation of stable and small-sized NPs is imperative to assure pDNA protection and colloidal stability in the extracellular environment, which ultimately will result in efficient cellular binding and uptake [4]. Therefore, in this work we explored the use of trimethyl chitosan (TMC), a CH derivative with increased stability at physiological pH. The quaternization of CH confers fixed positive charges to the polymer, which results in an increased solubility at a wider pH range [5]. To address other barriers adjacent to the transfection process, we aimed to optimize the biodegradation rate of the NPs core

to attain maximum internalization and transfection efficiency in neuronal cells. In the work described in **Chapter V**, we altered the biodegradation profile of TMC-based NPs by synthesizing TMC polymers with different degrees of acetylation, given rise to polymers with different profiles of enzymatic degradation. Afterwards, we took advantage of imaging flow cytometry, a high-throughput bioimaging technique, to unravel some critical aspects about NP formulation such as the distinction between internalized *versus* cell associated/adsorbed NPs, and even explore NP intracellular localization. Overall, our work provides novel information about the importance of vector degradation rate for gene delivery into cells, as a way to tune gene expression as a function of the desired application, and advances novel approaches to optimize NP formulation [6].

The delivery of therapeutic molecules by means of NP vectorization is a promising treatment strategy for many neurological diseases, since the introduction of therapeutic molecules into target cell populations can augment the natural survival and repair processes of the nervous system. Nevertheless, the ability to design NP delivery systems capable of selectively target their cargo to specific cell populations is still a major caveat in nanomedicine. One of the main challenges is the fact that each NP formulation needs to be precisely tuned to match the specificities of the target cell and route of administration. After identifying the acetylating degree that generates naked NPs with the best biological performance in terms of internalization and transfection efficiency, in **Chapter VI** we proceed with the development of neuron-targeted NPs. To provide the NPs with the ability to selective target neuronal cells, thiol groups were introduced into the TMC polymer. Subsequently, the NPs were further functionalized with the non-toxic and neurotropic carboxylic C-terminal fragment of the tetanus toxin heavy chain (HC), with proven efficacy both *in vitro* [7-9] and *in vivo* [10, 11], coupled to a poly(ethylene glycol) (PEG) spacer reactive for the thiol groups in the polymer. Afterwards, atomic force microscopy was used through the molecular recognition force spectroscopy (MRFS) mode to assess the specificity of the developed targeted NPs towards neuronal cell populations in biological samples of different complexity. The proposed methodology allowed us to evaluate in a precise fashion the specific interaction of each formulation with determined cell surface receptors. More significantly, by combining MRFS with fluorescent microscopy, one was able to probe

the NPs vectoring capacity in models of high complexity, such as primary mixed cultures, as well as specific subcellular regions in histological tissues [12].

Another critical parameter to take into consideration when formulating a targeted non-viral gene delivery system is the ligand density and exposure at the NP surface [13]. Most of the studies with targeted non-viral vectors rely on the use of PEG chains to coat the surface of nanocarriers to allow the grafting of targeting moieties and improve the physicochemical properties of these delivery systems. Still, to date there is no common agreement on the ideal PEG coverage-density or length to be used for optimum vector performance. Based on the above, in the work described in **Chapter VII** we aimed to optimize the ligand density and exposure at the surface of the previously described TMC NPs, to ensure maximum vector performance. To do so, HC was coupled to a 5 kDa PEG spacer (HC-PEG_{5k}) and grafted at different densities onto the NPs. By performing internalization and transfection studies on neuronal *versus* non-neuronal cell lines one was able to identify the ligand density that yielded a superior biological performance. Subsequently, and to enhance HC exposure and maximize cell-nanoparticle specific interaction, NPs containing different mixtures of HC-PEG_{5k} and a shorter size PEG spacer (2 kDa) at the same grafting density were produced. Our study showed that the precise adjustment of the PEG grafting density presents a significant impact in the biological performance of the developed NPs, both in terms of their internalization capacity as well as their transfection efficiency.

Finally, the concluding remarks, correlating the overall obtained results, as well as the perspectives for future research are presented in **Chapter VIII**.

The general outline for the developed work in this thesis is depicted in **Scheme 1**.

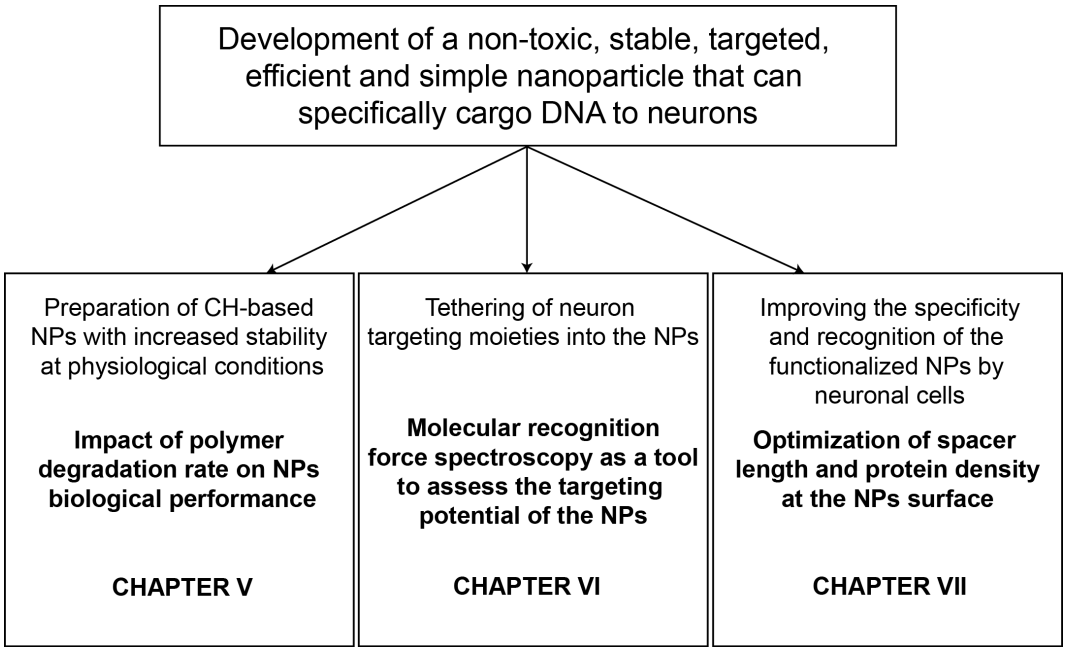

Scheme 1. Outline for the research work developed with the aim of producing functionalized nanoparticles for targeted gene delivery to the nervous system.

In the final part of this document a total of three appendices can be found. In Appendix I, a chapter with guidance for the implementation of MRFS for probing cell targeted NPs *in vitro* is presented. Although MRFS experiments are relatively straightforward to set up, there are stages such as sample preparation, AFM tips functionalization and data evaluation that are critical and of paramount importance to obtain suitable data. Taking this into consideration, in this chapter we describe in detail the protocol established by us, as well as valuable tips for the experimental design and data interpretation [14].

The *in vivo* application of the developed NPs in this work is shown in Appendix II. In this manuscript, our group proposes the use of neuron-targeted TMC-based NPs to mediate targeted gene delivery into peripheral neurons upon a peripheral and minimally invasive intramuscular administration. The NPs were prepared with a pDNA encoding for the brain-derived neurotrophic factor (BDNF) in a peripheral nerve injury model. We believe the obtained data in this work proves the efficacy of the proposed system in this thesis, opening new avenues for the treatment of nerve injury deriving from peripheral neuropathies based on the use of safe nanoparticle-mediated gene delivery strategies.

In Appendix III a short biography of the thesis author is presented, including a list of publications and participations in conferences.

References

1. Gomes, C.P., et al., "Translating chitosan to clinical delivery of nucleic acid-based drugs." MRS Bulletin, 2014. 39(01): p. 60-70.
2. Grigsby, C. and K. Leong, "Balancing protection and release of DNA: tools to address a bottleneck of non-viral gene delivery." J R Soc Interface, 2010. 7 Suppl 1: p. S67-82.
3. Bergen, J.M. and S.H. Pun, "Analysis of the intracellular barriers encountered by nonviral gene carriers in a model of spatially controlled delivery to neurons." J Gene Med, 2008. 10(2): p. 187-97.
4. Wiethoff, C.M. and C.R. Middaugh, "Barriers to nonviral gene delivery." J Pharm Sci, 2003. 92(2): p. 203-17.
5. Mourya, V.K. and N.N. Inamdar, "Trimethyl chitosan and its applications in drug delivery." J Mater Sci Mater Med, 2009. 20(5): p. 1057-79.
6. Gomes, C.P., et al., "A high-throughput bioimaging study to assess the impact of chitosan-based nanoparticle degradation on DNA delivery performance." Acta Biomater, 2016. 46: p. 129-140.
7. Oliveira, H., et al., "Targeted gene delivery into peripheral sensorial neurons mediated by self-assembled vectors composed of poly(ethylene imine) and tetanus toxin fragment c." Journal of Controlled Release, 2010. 143(3): p. 350-358.
8. Oliveira, H., et al., "Chitosan-based gene delivery vectors targeted to the peripheral nervous system." Journal of Biomedical Materials Research Part A, 2010. 95A(3): p. 801-810.
9. Lopes, C.D., et al., "Microfluidic-based platform to mimic the in vivo peripheral administration of neurotropic nanoparticles." Nanomedicine (Lond), 2016. 11(24): p. 3205-3221.
10. Lopes, C.D., et al., "In vivo targeted gene delivery to peripheral neurons mediated by neurotropic poly(ethylene imine)-based nanoparticles." Int J Nanomedicine, 2016. 11: p. 2675-83.
11. Lopes, C.D., et al., "BDNF gene delivery mediated by neuron-targeted nanoparticles is neuroprotective in peripheral nerve injury." Biomaterials, 2017. 121: p. 83-96.
12. Gomes, C.P., et al., "Atomic Force Microscopy as a Tool to Assess the Specificity of Targeted Nanoparticles in Biological Models of High Complexity." Adv Healthc Mater, 2017.
13. Gu, F., et al., "Precise engineering of targeted nanoparticles by using self-assembled biointegrated block copolymers." Proc Natl Acad Sci U S A, 2008. 105(7): p. 2586-91.
14. Gomes, C.P., et al., *Molecular recognition force spectroscopy for probing cell targeted nanoparticles in vitro*, in *Methods in Molecular Biology*, N. Santos and F. Carvalho, Editors. 2017, Springer. (*in press*)

CHAPTER III

TRANSLATING CHITOSAN INTO CLINICAL DELIVERY OF NUCLEIC ACID-BASED DRUGS

Translating Chitosan to Clinical Delivery of Nucleic Acid-based Drugs

Carla Pereira Gomes[1,2], Cátia Daniela Ferreira Lopes[1,3], Pedro Miguel Duarte Moreno[1], Aida Varela-Moreira[1,3], Maria José Alonso[4], Ana Paula Pêgo[1,2,5]

1 – INEB – Instituto de Engenharia Biomédica, Universidade do Porto, Rua do Campo Alegre, 823, 4150-180 Porto, Portugal

2 – Faculdade de Engenharia da Universidade do Porto, Rua Roberto Frias, s/n, 4200-465 Porto, Portugal

3 – Faculdade de Medicina da Universidade do Porto, Alameda Prof. Hernâni Monteiro, 4200-319 Porto, Portugal

4 – CIMUS Research Center, School of Pharmacy, University of Santiago de Compostela, Spain

5 – Universidade do Porto - Instituto de Ciências Biomédicas Abel Salazar (ICBAS), Rua Jorge Viterbo Ferreira 228, 4050-313 Porto, Portugal

Published in MRS Bulletin, Volume 39, 2014

1. Chitosan: Sources and Properties

Chitosan is a linear co-polymer of D-glucosamine and N -acetyl-D-glucosamine in a β -(1–4) linkage, in which glucosamine is the predominant repeating unit (**Figure 1**). The molar fraction of N-acetylated units defines the degree of acetylation (DA) of a given chitosan, expressed in molar percentage of N – acetylated units. Chitosan is soluble in lightly acidic aqueous solutions. At a pH lower than its pKa, ranging from ~ 6.5 to ~ 7, chitosan is a polycation, and at pH 4.0 and below, it is completely protonated [1]. The cationic character of chitosan under mildly acidic conditions and its ability to complex and condense nucleic acid-based molecules are the basis for its use as a transfection agent.

Chitosan is mostly obtained by deacetylation of chitin. The most commonly used sources of chitin are the exoskeleton of crustaceans and squids. The chitin present in squid pens is easier to deacetylate due to the absence of inter-sheet hydrogen bonding [2]. To conduct the deacetylation process with chitin from crustaceans, harsher conditions need to be applied, and the resulting chitosan typically has lower molecular weight. Consequently, this has been the preferred source of chitosan for use in nucleic acid delivery, as smaller and less disperse complexes can be formed when chitosan of lower molecular weight is used [3]. In either case, the fact that chitosan has an animal origin has raised some concerns, as it might be a potential source of allergens. More recently, chitosan isolated from the cell walls of mushrooms has become commercially available. As compared to chitosan obtained from marine animal resources, chitosan isolated from fungi cultured under controlled growing conditions presents higher reproducibility among batches and traceability [4], which makes it of interest for application in medical and pharmaceutical products. Irrespective of the original source, chitosan of ultrapure grade can now be obtained.

In addition to its ability to condense nucleic acid-based molecules and protect them from endonuclease degradation, a particular advantage of chitosan over other polycations proposed as non-viral vectors for nucleic acids relies on its low cytotoxicity and biodegradability. Besides chemical hydrolysis, enzymes can also mediate chitosan degradation *in vivo* [5]. Among these, lysozyme has been identified as the main one being involved in this process [6, 7]. It can hydrolyze partially N-acetylated chitosans, with the active site of the enzyme binding six sugar rings, being three consecutive N -

acetyl-D-glucosamine residues required for lysozyme catalytic activity [6]. As a consequence, the susceptibility of chitosan to lysozyme depolymerization depends not only on the DA but also on the distribution of N-acetylated units along the chitosan chains.

Further contributions to the field are expected when enzymatic production of chitosan will become readily available [8]. This will allow precise control over the resulting chain molecular weight, DA, and the distribution of the monomer units along the polymer backbone. Consequently, nanocomplex formation reproducibility and fine-tuning of biodegradation can be achieved, ultimately affecting the overall process of cell transfection.

2. Chitosan as a Vector for Nucleic Acid Delivery

Gene therapy is currently considered a strategy that provides cells with the genetic information required to produce specific therapeutic proteins or increase their overall expression levels, thus correcting or modulating specific pathologies. Moreover, the concept has been expanded to include specific regulation of gene expression through the use of short oligonucleotides targeting DNA or RNA, otherwise named as antisense gene therapy or oligonucleotide gene therapy.

Over the past several years, many attempts have been made to design non-viral vectors that could achieve the level of gene expression and specificity attained by viral vectors, while providing greater flexibility in terms of size of the transported nucleotide cargo, bypassing the immune system, and reducing safety concerns [9]. Among them, chitosan-based carriers have gained a great deal of attention for delivery of plasmid DNA (pDNA), small interference RNA (siRNA), and single-stranded oligonucleotides (ssON) (**Figure 2**). In the following sections, we present the state of the art of chitosan-based nanocarriers, focusing on their ability to deliver different types of nucleic acids.

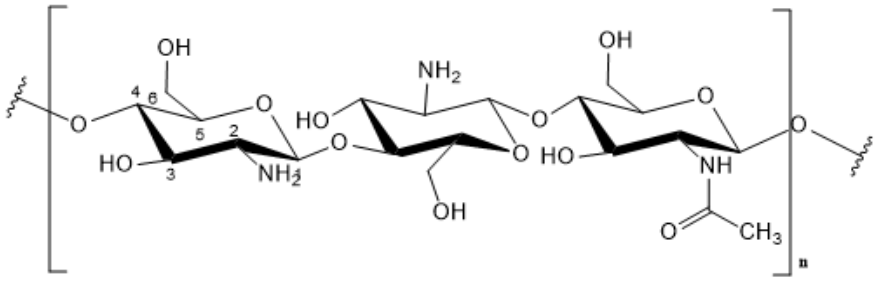

Figure 1. Chemical structure of partially deacetylated chitosan. a – D-glucosamine; b – *N*-acetyl D-glucosamine. Note: *n*, repetition unit.

2.1. Plasmid DNA

At the molecular level, pDNA can be considered to be a prodrug that, upon cellular internalization and nuclear entry, leads to the biosynthesis of a therapeutic protein [10] (**Figure 2a**). In addition to disease treatment, plasmids can be used as DNA vaccines for genetic immunization. DNA vaccines function through induction of immune response by introducing gene encoding antigens for specific pathogens [11]. pDNA is a double-stranded DNA molecule (1–200,000 base pairs) that can occur in three topological forms: the compact supercoiled form, the open circular form, and the linearized form.

Supercoiling arises from inherent properties of the DNA double helix to twist (turn) and writhe (turn over itself) and allows formation of a more compact molecule with implications for complex formation and transfection capabilities, also dependent on the type of vector used [12]. The US Food and Drug Administration (FDA) guidelines require the majority of pDNA (>80%) to be in its supercoiled form for application in pDNA vaccines for infectious disease indications [13].

There are a large number of reports describing the potential of chitosan and its derivatives for pDNA delivery [14]. Both chitosan-pDNA complexes [15] and chitosan-based nanocarriers prepared by ionic gelation [16] have been described for pDNA transfection. Overall, results revealed that transfection efficiency of chitosan-based delivery vehicles is dependent on several formulation parameters, such as chitosan molecular weight, DA, and stoichiometry (N/P ratio, moles of positive charges from amino groups to moles of negative charges from phosphate groups), among others [17]. Therefore, these parameters should be carefully considered and optimized when designing a pDNA delivery system. An in-depth review describing factors affecting pDNA delivery mediated by chitosan has been recently published [18].

Although chitosan has been proposed as an alternative to other non-viral vectors such as cationic liposomes or poly(ethylene imine) [19], it generally presents lower transfection efficiencies [20]. This difference could be attributed to its limited solubility at physiological pH as well as to its inefficient cellular uptake, endolysosome escape, and polyplex dissociation (**Figure 2b**). Consequently, several efforts are being made toward improving chitosan transfection efficiency by introducing different types of chemical modifications into the polymer backbone.

One common approach to enhance transfection efficiency is by improving chitosan solubility under physiological conditions. Chitosan grafted with PEI led to increased solubility, as well as improved transfection efficiency in relation to PEI alone [21]. Another strategy relies on the grafting of the poly(ethylene glycol) chain (PEGylation) to chitosan, which improves polymer solubility, yielding nanostructures that are more stable in the blood stream (extending their circulation time) and mediating transfection more efficiently [22]. The quaternization of chitosan by methylation of primary amine groups was also found to improve chitosan solubility and polyplex stability in physiological conditions [23].

In order to overcome the endosomal barrier (**Figure 2b**), conjugation of imidazole to chitosan has been explored to improve chitosan buffering capacity and endosomal escape [24, 25]. The introduction of hydrophobic moieties into the polymer backbone also led to more efficient endosomal escape [24] along with improvement of pDNA condensation capacity due to enhanced interaction between tethered hydrophobic domains and nucleic acids. Thiolation of chitosan also resulted in improvement of pDNA protection against degradation and formation of more stable complexes via establishment of disulfide bonds between chitosan chains. Additionally, in the reductive environment of the cytoplasm, there is an enhanced dissociation of pDNA from the polymer resulting in enhanced transgene expression [26, 27]. Finally, an amphiphilic modification of chitosan has also been attempted. Hydrophobic modification of chitosan with linoleic acid led to improved endonuclease protection ability, promoting cell binding and enhanced pDNA dissociation. Contrarily, introduction of poly(betamalic acid) via ester bonds led to enhanced water solubility, minimized non-specific protein adsorption, and facilitated pDNA unloading, resulting in an overall improved transfection efficiency [28].

As an alternative to chitosan backbone modification, the preparation of ionically cross-linked chitosan-TPP (tripolyphosphate) nanoparticles was also proposed [29]. Such systems were found to improve stability, achieving comparable gene expression levels to other efficient transfection agents. A more advanced system combines chitosan, TPP, and an additional poly/oligosaccharide such as hyaluronic acid [30] or beta-cyclodextrins [31].

While non-viral vectors can associate with most cell types via non-specific binding to the cell surface, specific targeting strategies based on receptor-ligand interactions are preferable to prevent widespread delivery and off-target effects. The incorporation of targeting moieties into the chitosan nanoparticles was found to modify the particle uptake, with the ligand/receptor interaction governing the internalization pathway and the subsequent intracellular trafficking [26, 32].

2.2. Small interfering RNA

siRNA are short, usually 19-21 base pair double-stranded synthetic RNA molecules, which elicit the degradation of messenger RNA (mRNA), thereby achieving down-regulation of a target gene through the mechanism of RNA interference (**Figure 2c**)

[33]. Due to its chemical nature, siRNA is highly sensitive to degradation by nucleases and unable to cross cellular membranes.

Being much smaller than pDNA, siRNA has far less charge density, possessing an inherently different structure and topology. These differences underlie the specificity of certain synthetic vectors in achieving efficient delivery with only one type of nucleic acid molecule. Chitosan-based vectors follow this rule, hence chemical and physical parameters need to be specifically optimized for siRNA delivery.

To the best of our knowledge, the first report on the use of chitosan-based nanoparticles for siRNA delivery was published in 2006 [34]. This study explored different methods of complexation (simple coacervation, ionic gelation, and adsorption to chitosan-TPP nanoparticles prepared by ionic gelation) using high molecular weight chitosans (110–470 kDa). The results showed that the molecular weight did not significantly influence transfection efficiency, although smaller particles were formed with the lowest molecular weight chitosan. The method of siRNA association, in turn, was relevant for transfection efficiency, with entrapment by ionic gelation being the most effective.

Recent reports highlight the effect of chitosan molecular weight on its interaction with siRNA and the transfection efficiency of the resulting complexes. However, the results are not definite yet. Some authors indicated that low molecular weight chitosan is not able to stably interact with siRNA merely because of insufficient electrostatic interactions between the two oppositely charged molecules. This effect was observed when 10 kDa chitosan (5% DA) [35] was compared to that of 35 kDa (fully deacetylated) [36]. In contrast, another paper showed that efficient silencing could be achieved with a chitosan of 12 kDa (8% DA) [37].

Overall, the conclusion at this point could be that increasing polymer molecular weight might not translate into further increases in performance [36, 38]. This could be explained by a productive interaction threshold between siRNA and the polymer chains, leading to sufficient condensation and intracellular dissociation capacity of the complexes. The previously mentioned examples also reveal that low DAs favor the interaction with siRNA and the overall vector performance. The use of chitosan with low DA is particularly crucial when preparing nanoparticles using the ionic complexation technique. In contrast, when using the ionic gelation technique, siRNA molecules,

besides establishing possible ionic interactions with chitosan, are physically entrapped during the particle formation process [29, 39].

A myriad of modifications in the polymer backbone, aimed at improving nanoparticle formation with siRNAs, have been explored. Similar to pDNA delivery, chitosan quaternization [40] and chitosan thiolation [41] have also been investigated. Hydrophobic modification of chitosan with tocopheryl (vitamin E) has also been achieved [42]. Other possible modifications include glycolchitosan, PEGylated chitosan, and guanidinylated chitosan, which have basically conferred improved stability, solubility, and cellular uptake resulting in enhanced transfection capabilities [43]. Another alternative for efficient encapsulation of siRNA combines PEGylated chitosan with hyaluronic acid and the process of nanoparticle formation induced by ionic gelation using TPP [44].

2.3. Single-stranded oligonucleotides

The therapeutic potential of single-stranded ONs (ssONs) was discovered in 1978, when Zamecnik and Stephenson reported that a DNA oligonucleotide complementary to the target RNA was able to inhibit virus replication in cell culture [45]. Soon after, the idea of achieving generalized blocking of RNA function through hybridization of ssONs with the RNA started to develop and with it the field of antisense oligonucleotides (AON). As with siRNAs, these molecules can be easily degraded and have difficulty entering cells. Attempts have been made to increase their stability by chemical modification and to maintain their effectiveness upon *in vivo* administration; however, the high amounts of ssONs needed to achieve a good response and the lack of specific cell targeting may raise some toxicity issues [46]. Thus, the development of appropriate delivery vectors is also critical in this context (**Figure 2d**). As in the case of siRNA, the small size and low charge density of the molecule poses a problem for complexation. Additionally, its single-stranded character confers a slight apolar characteristic to the molecule due to exposure of aromatic nitrogenous bases.

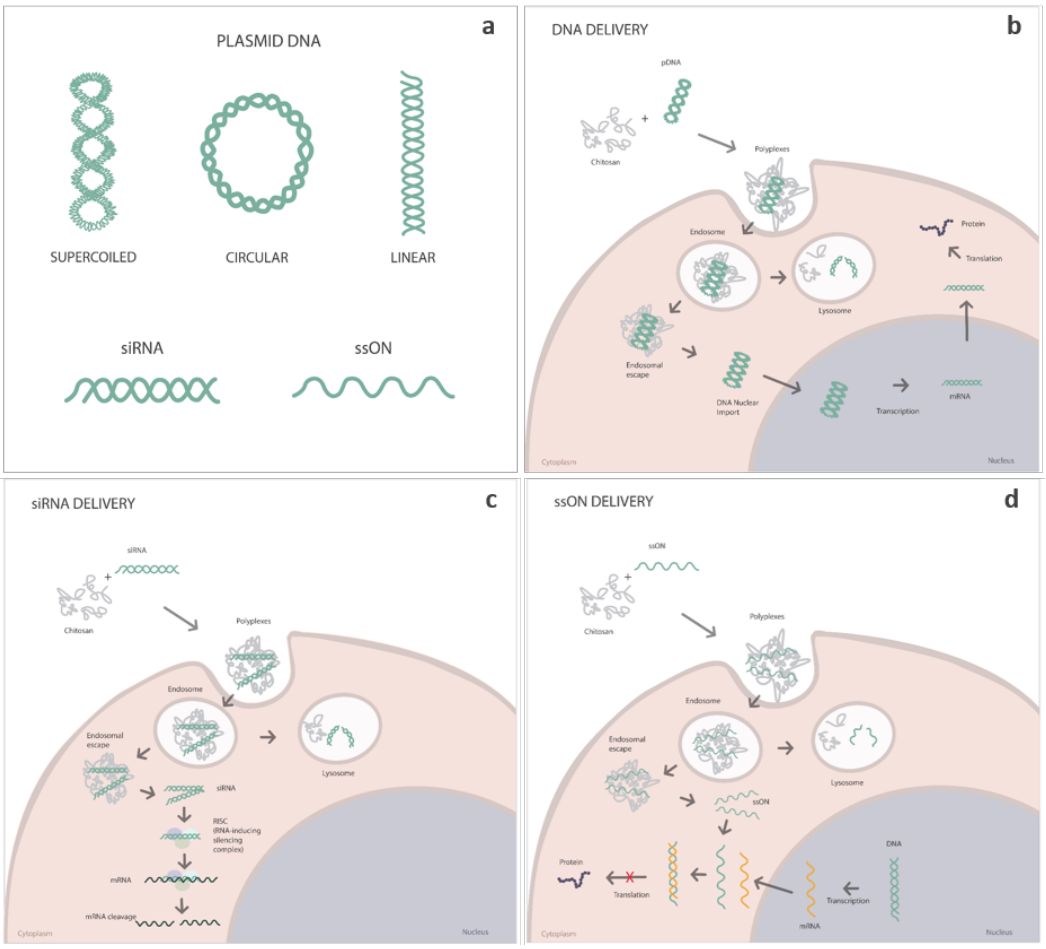

Figure 2. Schematic representation of the internalization of chitosan-nucleic acid nanoparticles and mechanisms of action of the different nucleic acids commonly used in gene therapy. After internalization, nanoparticles are trafficked along the endosomal network. Endosomes can mature into lysosomes via luminal acidification and recruitment of degradative enzymes, which target the vesicle contents for degradation. In order to access cytoplasmic or nuclear targets, nanoparticles must be capable of escaping from the endolysossomal pathway and make the nucleic acid of interest available. The schemes present the (a) different nucleic acids used in gene therapy and the mechanism of action of (b) Plasmid DNA (pDNA) – double stranded DNA capable of autonomous replication, (c) small interference RNA (siRNA) – short, double-stranded, synthetic RNA and (d) single-stranded oligonucleotides (ssONs). Note: mRNA, messenger RNA; RNase H, endoribonuclease H; miRNA, microRNA.

Although the number of reports on chitosan-based vectors for ssON delivery is still low, there are some approaches that have led to promising data. Chitosan nanocomplexes showed transfection activity in a model of intranasal application, even though very high amounts (100 μ g) were needed to achieve a response [47]. In another example, complexes of ssON with a galactose-modified chitosan resulted in an improved *in vitro* transfection efficiency as compared to the parent chitosan complexes [48]. Moreover, *in vivo* galactosylation of chitosan was found to vectorize high amounts of AON to

specific liver cells, which was seen as the major event leading to the increased efficiency of this vector.

The combination of chitosan with alginate for complexation of AON either by a lyophilization [49] or a pre-gelling method [50] has also led to interesting results. Indeed, chitosan-alginate nanoparticles prepared by lyophilization showed a capacity to transfect skin cells *in vivo* in an excisional wound model. Those prepared according to the pre-gelling method were found to control the AON release over a 50-hour period [51] and to transfect a human breast cancer cell line [52].

The delivery of AON from nanoparticles made by ionic gelation has also been reported in few studies [53]. A relevant example is the one showing that chitosan nanoparticles are useful carriers of AON for delivery into rat skin cells [54], with the authors suggesting the potential of this approach for topical application on human skin. More recently, the use of thiolated chitosan in order to facilitate the dissociation of the AON from the complex was also explored [55].

Overall, the information reported so far does not yet offer a comprehensive view of the most favorable properties for ssON delivery by chitosan. Considering the enormous potential for ssON-based therapeutics, a more detailed view on the use of chitosan with ssON is warranted.

3. In Vivo Application of Chitosan as a Vector for Nucleic Acid Delivery

Since initial proposals of chitosan as a nucleic acid delivery system, chitosan and its derivatives have been widely tested as nucleic acid carriers in animal models. The majority of the reported *in vivo* studies focus on the use of reporter gene models in order to evaluate biodistribution and transfection levels mediated by chitosan-pDNA complexes. Following these pioneering studies, there has been an increasing number of reports evaluating the efficacy of chitosan as a delivery carrier of therapeutic genes, namely in the fields of cancer, infections, and inflammatory diseases (**Table 1**).

Due to their mucoadhesive properties, chitosan-based nanoparticles have been applied in the development of strategies to treat diseases that affect mucosal surfaces, such as the gastrointestinal tract, lung, and eye. Kai and Ochiya reported successful oral delivery of the β -galactosidase reporter gene mediated by chitosan alone or N-acetylated to the intestine [56]. Others have reported similar findings in the gastric and intestinal mucosa. pDNA-loaded chitosan-based nanoparticles have also been explored in the field of respiratory diseases. An example is the work of Jiang *et al*., in which it was shown that aerosol delivery of pDNA producing small hairpin RNA, complexed to folate-chitosan-graft-PEI, specifically silenced the isoform 1 of the protein kinase B (Akt1) in lung tumor cells, resulting in lung tumorogenesis suppression [57].

Hyaluronic-chitosan nanoparticles made by ionic gelation have also been proposed for the delivery of nucleic acids to the ocular mucosa, which is a thin, continuous mucous membrane layer that lines the inner surface of the eyelids and eye surface [58]. In this case, the mucoadhesive properties of both polymers were combined with the CD44 targeting ability of hyaluronic acid, rendering the system very efficient for transfection of both the corneal epithelium and conjunctiva, ocular tissues that express this receptor. Another field of application has been mucosal administration of vaccines. For example, Roy *et al.* reported that oral immunization with pDNA vaccine-loaded chitosan nanoparticles led to successful immunological protection in a murine peanut allergy model [59].

Another pDNA vaccine encoding for the dense granule protein 1 (GRA1) has been proposed, intended to prevent *Toxoplasma gondii* infection. A significant immune

response against the encoded protein was observed after gastric administration of chitosan nanoparticles containing GRA1 pDNA to mice [60]. Nanovaccines have also been designed for intranasal administration. For example, a pDNA-loaded chitosan nanoparticle vaccine against the respiratory syncytial virus (RSV) infection was developed and tested in a murine model. The results showed an attenuation of pulmonary inflammation by induction of protective T helper 1 (Th1) cell type [61] and cytotoxic T lymphocyte responses [62] in BALB/c mouse strain.

The encouraging results of chitosan in delivering pDNA molecules drove interest in it as an attractive carrier for siRNA. Compared to *in vivo* pDNA delivery, research on siRNA delivery mediated by chitosan-based vectors is still in its infancy, the majority of current work being basic research involving model siRNA molecules. Delivery of siRNA for therapeutic purposes has recently started to receive increasing attention, with specific emphasis in the field of infectious diseases and cancer (Table I). One example is intranasal delivery of chitosan nanoparticles loaded with siRNA targeting the viral NS1 gene that encodes for a RSV nonstructural protein sequence with an important role in the virus replication process. The results showed a significant reduction of virus concentration (titers) in the lung and decreased pulmonary inflammation associated with RSV infection [63, 64]. On the other hand, in the field of cancer therapy, Pille *et al.* reported a 90% inhibition of tumor growth in a xenograft aggressive breast cancer model after intravenous administration of anti–Ras *homologous* A (Rho A) siRNA encapsulated in chitosan-coated polyisohexylcyanoacrylate nanoparticles [65].

Although being reported as one of the most promising nucleic acid carriers for clinical applications, so far chitosan-based nanoparticles have only been evaluated in pre-clinical settings. Therefore, much research is needed in order to advance toward the clinical development phase. This advancement is expected to be favored by the fact that several chitosan-based products are under clinical development, among them, an adjuvant for a Norwalk virus-like particle [66], whereas others, such as for wound dressing and as a dietary supplement, are already being marketed [66, 67].

Table 1. Overview of the main *in vivo* studies using chitosan-based nanoparticles to deliver plasmid DNA (pDNA) and small interference RNA (siRNA) molecules.

Application		Delivery system	Gene	Animal model	Administration route	Main findings	Ref.
Infection	*Toxoplasma gondii*	Chitosan/ pDNA	GRA1	C3H/HeN mice	Intragastric	Chitosan/GRA1pDNA vaccine resulted in high anti-GRA 1 antibodies, biased towards Th2 or mixed Th1/Th2 immune responses, whereas protective immune responses against *T. gondii* are clearly associated with Th1 type responses.	[60]
	CVB3	Chitosan/ pDNA	VP1	BALB/c (H-2d) mice	Intranasal	Chitosan/pcDNA3-VP1 induced CVB3-specific systemic immunity (humoral and cellular immune responses), and protected 42.9% mice from lethal CVB3 infection.	[68]
	Micobacterium tuberculosis	Chitosan/ pDNA	8 HLA-A2 0201-restricted T cell epitopes	HLA-A2 transgenic mouse model	Pulmonary	Induced maturation of dendritic cells and increased secretion of IFN-ɣ.	[69]
	RSV pulmonar infection	Chitosan/ pDNA	9 immunogenic RSV genes	RSV-infected BALB/c mice	Intranasal	Attenuated pulmonary inflammation induced by RSV infection; induced high levels of serum IgG and mucosal IgA antibodies; elevated lung specific production of IFN-ɣ.	[61]
		Chitosan/ pDNA	CTL epitope from the M2 protein of RSV	BALB/c mice	Intranasal and intradermal	The administration of chitosan-based nanoparticles (intranasal/ intradermal) induced virus-specific CTL responses in mice.	[62]
		Chitosan/ siRNA	siNS1	Fischer 344 rats	Intranasal	The delivery of siNS1 prior to RSV exposure was effective in reducing virus titters in the lung and in preventing the inflammation and airway hyper-responsiveness associated with the infection.	[64]
		Chitosan/ siRNA	siNS1	BALB/c mice	Intranasal	Mice treated intranasally with siNS1 nanoparticles before or after infection with RSV showed substantially decreased virus titers in the lung and decreased inflammation and airway reactivity.	[63]
	Severe acute respiratory syndrome coronavirus (SARS-CoV)	Biotinylated Chitosan-bfFp/pDNA	SARS-CoV nucleocapsid (N)	BALB/c mice	Intranasal and intramuscular	Intranasal administration of bfFp targeted chitosan-based nanoparticles along with anti-CD40 dendritic cells maturation stimuli enhanced magnitude of mucosal IgA as well as systemic IgG against N protein; The intramuscular route is superior for induction of systemic IgG responses compared with the intranasal route.	[70]
	Schistosoma mansoni	CHimi/pDNA Chitosan/ pDNA	Rho1-GTPase	C57BL6 mice	Oral	Immunization with chitosan-based nanoparticles resulted in 47% of protection against parasite infection; Oral immunization was not able to induce high levels of specific antibodies but induced high levels of the modulatory cytokine IL-10, resulting in a significative reduction of liver pathology.	[71]

Application		Delivery system	Gene	Animal model	Administration route	Main findings	Ref.
Allergy	Food allergy	Chitosan/ pDNA	Arah2	AKR/J mice	Oral	Immunized mice produced secretory IgA and serum IgG2a and showed a reduction in allergen-induced anaphylaxis.	[59]
	Allergy	Chitosan/ pDNA	Der p 1	BALB/cJ mice	Oral	Specific Der p 1 immune response was induced otherwise undetectable using parenteral route of administration.	[72]
	Allergic asthma	Chitosan/ pDNA	IFN-ɣ	STAT4-/- BALB/c mice	Intranasal	Chitosan/IFN-ɣ nanoparticles reduced the functional and immunological abnormalities associated with allergen sensitization; This effect is predominantly mediated via a STAT4 signaling pathway.	[73]
	Allergy	Chitosan/ pDNA	Der p 2	BALB/c mice	Oral	Specific Th1 immune responses were preferentially activated (induction of IFN-ɣ) and prevention of subsequent sensitization of Th2 cell-regulated specific IgE responses.	[1]
Cancer	Osteosar-coma	Chitosan/ pDNA	PEDF	Balb/c nude mice	Intratibial (cortex of the anterior tuberosity of tibiae)	Inhibition of tumor growth at the tibial site, less osteolysis, reduction of number and size of pulmonary metastases.	[75]
	Liver and colon cancer	Galactosylated chitosan/pDNA	IL -21 GM-SCF	BALB/c mice	Intravenously (tail vein)	The nanoparticles exhibited hepatocyte and passive tumor specificity, increased therapeutic efficacy, promoted leukocytes to aggregate in tumor tissues, and activated the cytotoxicity of natural killer (NK) cells and cytolytic T lymphocyte (CTL).	[76]
	Liver cancer	Chitosan-PEI-FQHPSF/ pDNA	IL-12	Ascite -bearing ICR mice	Intraperitoneal	The IL-12 expression significantly enhanced the anti-effect on ascites tumor-bearing ICR mice as compared with controls. Targeting specificity of the developed nanoparticle was demonstrated.	[77]
	Lung cancer	Chitosan-polyethyleneimin e-folate/shRNA	Akt1	A/J mice (Urethane-induced lung cancer)	Aerosol	Aerosol delivery of Akt1 shRNA suppressed lung tumorigenesis through the Akt signaling pathway.	[57]
	Prostate cancer	Chitosan/ siRNA	RXFP 1	Nude mice	Intratumoral	The targeted downregulation of human RXFP1 in prostate cancer cell xenografts resulted in significantly decreased tumor growth (decrease in cell proliferation and increase in apoptosis) and metastasis rate in nude mice.	[78]
	Ovarian Carcinoma	Chitosan/ siRNA	Src and Fgr	NCr-nu mice model of ovarian carcinoma (HeyA8-MDR)	Intravenously	Dual Src and Fgr silencing decreased angiogenesis, cell survival (increased apoptosis), and growth, consisting in an effective approach for treatment of ovarian carcinoma in animal models.	[79]
	Melanoma and breast cancer	Chitosan-hydrogel/ siRNA	TG2	NCr-nu mice models of melanoma (A375SM) and breast (MDA-MD231) cancer	Intratumoral	Chitosan-hydrogles carrying TG2-targeted siRNA significantly inhibited tumor growth in 72% in melanoma and 92% in breast cancer, without systemic side effects.	[2]

Application		Delivery system	Gene	Animal model	Administration route	Main findings	Ref.
Cancer	Hepatocellular carcinoma	Chitosan/shRNA	VEGF	ICR mice	Intratumoral and intravenously	The Chitosan/VEGF-shRNA complexes significantly inhibited VEGF expression of hepatocarcinoma cells and liver tumor tissues. The intratumoral or intravenous administration of Chitosan/VEGF-shRNA complexes demonstrated more effective suppression of tumor growth and angiogenesis compared with naked shRNA.	[81]
	Cancer	Thiolated glycol chitosan (TGC)/siRNA	VEGF	PC-3 -bearing mice	Intravenously	VEGF gene silencing; tumor growth inhibition reduced angiogenesis in tumors. No immune stimulation observed	[82]
Other	Hemophilia	Chitosan/pDNA	Factor VIII	FVIII exon 16 knock-out mice	Oral	FVIII was detected in both local and systemic tissues post administration. Treatment with of FVIII DNA-chitosan nanoparticles resulted in phenotypic correction in 13/20 mice	[83]
	Rheumatoid Arthritis	Chitosan/siRNA	TNF-α	C57BL/6J mice (collagen-induced Arthritic mice)	Intraperitoneal	The silencing of TNF-α resulted in minimal cartilage destruction and inflammatory cell infiltration.	[84]
	Diabetis mellitus	Chitosan/pDNA	GLP-1	Zucker diabetic fatty (ZDF) rat	Intravenously	Administration of nanoparticles resulted in 5-fold higher plasma levels of GLP-1 leading to a 3-fold increase in plasma insulin concentration when compared with untreated animals and to a normalization of blood glucose level up to 24 days after treatment	[85]
	Wound healing	Chitosan-Alginate/ASO	Smad 3	C57BL6 mice	Wound Dressing	The smad3 ASOs impregnated in polyelectrolyte complex (PEC) containing chitosan and sodium alginate provided reduced production of TGF-β1 via suppression of smad3 at cellular levels. Also, the healing process *in vivo* (suggested by wound closure and histological observation) was accelerated in comparison with controls.	[49]

GRA1: dense granule protein 1; CVB3: Coxsackievirus B3; HLA-A2: human leukocyte antigen serotype-A2; IFN-ɣ: Interferon-ɣ; RSV: Respiratory syncytial virus; CTL: Cytotoxic T lymphocyte; SARS-CoV: Severe acute respiratory syndrome coronavirus; bfFp: recombinant bifunctional fusion protein; Der p 1: *dermatophagoides pteronyssinus 1*; Der p 2: dermatophagoides pteronyssinus 2; STAT4: Signal Transducer and Activator of Transcription protein 4; PEDF: Pigment epithelium-derived factor; IL: Interleukin; shRNA: small hairpin RNA GM-SCF: Granulocyte-macrophage colony-stimulating factor; RXFP1: Relaxin family peptide receptor 1; TG2: tissue transglutaminase; VEGF: Vascular endothelial growth factor; TNF-α: Tumor necrosis factor- α; GLP-1: Glucagon-like peptide-1; TGF-β1: Transforming growth factor-β1; ASO – antisense oligonucleotide.

4. Translating Chitosan into the Clinic for Nucleic Acid Delivery: Progress and Challenges

The use of chitosan nanocarriers for gene therapy is largely documented, and there is now a considerable body of knowledge supporting this application. Notwithstanding, there are still no reports of marketed products or current clinical trials with chitosan-based vectors for *in vivo* administration of nucleic acids. While trying to bring such products from bench-to-bedside, a number of requisites must be taken into account. Important issues to be tackled are inherent to the use of nucleic acids as therapeutic molecules, namely the optimization of sequences to ensure robust gene expression while evading immune system surveillance (pDNA) or to minimize off-targets and reduce toxicity effects (ssONs and siRNA), as well as to determine therapeutic dosages. On the other hand, the proposed vector needs to fulfill its role as a carrier of the therapeutic agent. Some of the strategies being pursued to improve the efficiency of chitosan for nucleic acid delivery have been discussed in the previous sections. Most of the chitosan-related limitations are common to other vectors, as well as approaches being adopted to overcome these hurdles.

It is also important to consider that while chitosan is not currently listed as an excipient in any drug formulation approved by regulatory authorities, chitosan hydrochloride has been on the list of excipients of the European Pharmacopeia since 2002 [86] and in the US Pharmacopeia and The National Formulary since 2011 [87]. Moreover, chitosan (from shrimp and Aspergillus niger origin) is “generally recognized as safe” by the FDA as a direct ingredient in foods and beverages. Chitosan is also being used as a dietary supplement to reduce fat adsorption and in wound dressings [88], indicating that a good understanding of its topical and oral tolerance exists. In addition, there are a number of clinical trials reported by the FDA involving the use of chitosan for oral and nasal peptide/vaccine delivery where chitosan is being used as a vaccine adjuvant. In spite of this, there is still a need for standard guidelines describing the range of requirements, both for suppliers and product manufactures, of product quality and characterization methods [89]. The American Society for Testing and Materials (ASTM) is making a concerted effort to establish standard guidelines for tissue-engineered medical products and has recently dedicated one of these documents (F2103–11) to the characterization and testing of chitosan salts as starting materials for biomedical applications [90].

One must be aware that chitosan is not a single chemical entity but varies in compositional DA and distribution of the monomer units along the polymer backbone and molecular weight, depending on the source, extraction, and preparation method [89, 91]. For nucleic acid delivery, the polymer molecular weight and DA are very important parameters, as they will have an impact in terms of chain flexibility and the number of positive charges per chitosan molecule. Moreover, solubility, biodegradability, aggregation properties, and immune response will be affected by physicochemical properties of chitosan as well[92]. In this context, regulatory issues concerning polymer preparation and characterization methods will have to be addressed such that chitosan can successfully reach the clinic. In this respect, there are three main areas that must be dealt with: (1) polymer characterization and functionality, (2) product reproducibility between different batches, and (3) toxicology and long-term safety [92].

The ASTM guideline F2103–11 suggests the use of infrared spectroscopy (IR) and nuclear magnetic resonance (NMR) to correctly identify chitosan [90]. It also establishes limits of insoluble impurities, residual protein content, inorganic matter, and presence of heavy metals in the chitosan samples. The ASTM standard F2260–03 describes the methodology for determination of chitosan DA using ^{1}H-NMR [93]. It is based on the work of Vårum *et al.* and is valid for DA values from 50% down to 1% [94]. For molecular weight determination, a specific ASTM standard (F2602–08E011) has been published [95]. Several mobile phases are proposed for size exclusion chromatography, with many composed of not only acetic acid and sodium acetate, but also ammonium acetate. Finally, according to FDA specifications, the endotoxin content of chitosan samples should not exceed 5 EU/kg for non-intrathecal administration routes, in order for the material to be considered safe for biomedical applications [96].

The ASTM guidelines represent a promising attempt to surpass some of the difficulties listed previously. If properly followed, they should improve the manufacturing efficiency of chitosan-based products, with significant reduction in the cost of product development.

Another key issue to take into consideration is chitosan biodegradability. In the literature, multiple studies regarding chitosan processed in different forms (hydrogels, scaffolds, beads, or just in solution) have asserted this material as biodegradable. Most of these studies assess biodegradation upon variation of the polymer DA, since this parameter is

positively related with the rate of chitosan degradation. In spite of this, little is known about the degradation of chitosan in nanoparticle systems [97]. The extrapolation to nanoparticle biodegradation is not straightforward, because when the polymer is complexed with nucleic acids, the exposure of acetylated groups may not favor the degradation mediated by enzymes. Chellat and colleagues evaluated biodegradation of chitosan and chitosan complexed with xanthan (CH-X) (an anionic polysaccharide) in degradation media simulating gastric (containing pepsin) or intestinal fluids (containing pancreatin) and found that chitosan degradation was faster than CH-X microspheres [98]. To the best of our knowledge, *in vivo* degradation of chitosan nanoparticles containing nucleic acids has not been disclosed in the literature. It is worthwhile mentioning that this is a common limitation for most nanoparticulate systems.

5. Conclusions

This review highlights some of the most promising results involving the use of chitosan as a vector for nucleic acids, including examples already in pre-clinical trials that have been fueling the interest of the research community and manufacturers into use of this biopolymer. Chitosan has advantages over other non-viral carriers in terms of its nontoxicity and biodegradability. Another interesting feature widely explored is the mucoadhesive properties of chitosan, with impact on gastrointestinal, lung, and ocular applications.

While the field of gene therapy is still addressing many of the hurdles that have been hampering the widespread translation of nucleic acid-based therapies to the clinic, there are several products in clinical trials based on both viral and non-viral vectors supporting the high potential of such therapeutic strategies. Recently, two products successfully reached the market (Glybera® and Gendicine®) for the treatment of lipoprotein lipase deficiency and head and neck squamous cell carcinoma, respectively. Nevertheless, attaining safe and efficient delivery of the nucleic acid of interest is at the forefront of this quest, which makes chitosan and its derivatives attractive candidates.

While a number of issues that are common to all non-viral vectors remain to be addressed, there are a number of questions that are particular to chitosan. Many of these involve standardization of production and characterization methodology. While seemingly trivial, these issues have held back manufacturers and made comparison between studies difficult at times. Addressing these issues will certainly provide the basis for a deeper understanding of the behavior of this material in different biomedical settings, of which vectorization of nucleic acids is an example with great therapeutic potential. We believe that this will make pharmaceutical companies more secure to bring chitosan into clinical trials and finally to the market.

References

1. Sorlier P, Denuzière A, Viton C et al. "Relation between the degree of acetylation and the electrostatic properties of chitin and chitosan." Biomacromolecules. 2001(2):765-772.
2. Kurita K. Controlled functionalization of the polysaccharide chitin. Progress in Polymer science. 2001(26):1921-1971.
3. Köping-Höggård M, Vårum KM, Issa M et al. "Improved chitosan-mediated gene delivery based on easily dissociated chitosan polyplexes of highly defined chitosan oligomers."
4. Kannan M, Nesakumari M, Rajarathinam K et al. "Production and characterization of mushroom chitosan under solid-state fermentation conditions." Adv Biol Res. 2010(4):10-13.
5. He B, Wang L, Wang J et al. "Positive selection of three chitinase genes of the family 18 of glycoside hydrolases in mammals." Biologia. 2009(64):819-825.
6. Vårum KM, Myhr MM, Hjerde RJN et al. “In vitro degradation rates of partially N-acetylated chitosans in human serum.” Carbohydrate Research. 1997(299):99-101.
7. Vårum KM, Holme HK, Izume M et al. "Determination of enzymatic hydrolysis specificity of partially N-acetylated chitosans." Biochimica et Biophysica Acta (BBA)-General Subjects. 1996(1291):5-15.
8. Liu L, Liu Y, Shin H- et al. "Developing Bacillus spp. as a cell factory for production of microbial enzymes and industrially important biochemicals in the context of systems and synthetic biology." Applied microbiology and biotechnology. 2013(97):6113-6127.
9. Pêgo AP, Oliveira H, Moreno PM. "Biomaterial-Based Vectors for Targeted Delivery of Nucleic Acids to the Nervous System." Drug Delivery Systems: Advanced Technologies Potentially Applicable in Personalised Treatment. Springer; 2013. p. 185-224.
10. Uherek C, Wels W. "DNA-carrier proteins for targeted gene delivery." Advanced drug delivery reviews. 2000(44):153-166.
11. Johnston SA, Talaat AM, McGuire MJ. "Genetic immunization: what’s in a name." Archives of medical research. 2002(33):325-329.
12. Remaut K, Sanders NN, Fayazpour F et al. "Influence of plasmid DNA topology on the transfection properties of DOTAP/DOPE lipoplexes." Journal of controlled release. 2006(115):335-343.
13. Food and Drug Administration. Guidance: Drug Safety Information. FDA’s Communication to the Public. 2007
14. Mansouri S, Lavigne P, Corsi K et al. "Chitosan-DNA nanoparticles as non-viral vectors in gene therapy: strategies to improve transfection efficacy." European Journal of Pharmaceutics and Biopharmaceutics. 2004(57):1-8.
15. Lee KY, Kwon IC, Kim Y-H et al. "Preparation of chitosan self-aggregates as a gene delivery system." Journal of Controlled Release. 1998(51):213-220.
16. Gan Q, Wang T, Cochrane C et al. "Modulation of surface charge, particle size and morphological properties of chitosan–TPP nanoparticles intended for gene delivery." Colloids and Surfaces B: Biointerfaces. 2005(44):65-73.
17. Mao S, Sun W, Kissel T. "Chitosan-based formulations for delivery of DNA and siRNA." Advanced drug delivery reviews. 2010(62):12-27.
18. Buschmann MD, Merzouki A, Lavertu M et al. "Chitosans for delivery of nucleic acids." Adv Drug Deliv Rev. 2013(65):1234-1270.
19. Mao H-Q, Roy K, Troung-Le VL et al. "Chitosan-DNA nanoparticles as gene carriers: synthesis, characterization and transfection efficiency." Journal of controlled release. 2001(70):399-421.

20. Wong K, Sun G, Zhang X et al. "PEI-g-chitosan, a novel gene delivery system with transfection efficiency comparable to polyethylenimine in vitro and after liver administration in vivo." Bioconjugate chemistry. 2006(17):152-158.

21. Jiang X, Dai H, Leong KW et al. "Chitosan g PEG/DNA complexes deliver gene to the rat liver via intrabiliary and intraportal infusions." The journal of gene medicine. 2006(8):477-487.

22. Csaba N, Köping-Höggård M, Fernandez-Megia E et al. “Ionically crosslinked chitosan nanoparticles as gene delivery systems: effect of PEGylation degree on in vitro and in vivo gene transfer.” Journal of biomedical nanotechnology. 2009(5):162-171.,Mourya VK, Inamdar NN. “Trimethyl chitosan and its applications in drug delivery.” Journal of Materials Science: Materials in Medicine. 2009(20):1057-1079.

23. Kim TH, Ihm JE, Choi YJ et al. “Efficient gene delivery by urocanic acid-modified chitosan.” Journal of Controlled Release. 2003(93):389-402.

24. Moreira C, Oliveira H, Pires LR et al. “Improving chitosan-mediated gene transfer by the introduction of intracellular buffering moieties into the chitosan backbone.” Acta Biomaterialia. 2009(5):2995-3006.

25. Hu F-Q, Zhao M-D, Yuan H et al. “A novel chitosan oligosaccharide–stearic acid micelles for gene delivery: Properties and in vitro transfection studies.” International journal of pharmaceutics. 2006(315):158-166.

26. Oliveira H, Pires LR, Fernandez R et al. “Chitosan-based gene delivery vectors targeted to the peripheral nervous system.” J Biomed Mater Res A. 2010(95):801-810.

27. Lee D, Zhang W, Shirley SA et al. “Thiolated chitosan/DNA nanocomplexes exhibit enhanced and sustained gene delivery.” Pharm Res. 2007(24):157-167.

28. Wang B, He C, Tang C et al. “Effects of hydrophobic and hydrophilic modifications on gene delivery of amphiphilic chitosan based nanocarriers.” Biomaterials. 2011(32):4630-4638.

29. Csaba N, Köping-Höggård M, Alonso MJ. “Ionically crosslinked chitosan/tripolyphosphate nanoparticles for oligonucleotide and plasmid DNA delivery.” Int J Pharm. 2009(382):205-214.

30. de la Fuente M, Seijo B, Alonso MJ. “Design of novel polysaccharidic nanostructures for gene delivery.” Nanotechnology. 2008(19):075105.

31. Teijeiro-Osorio D, Remuñán-López C, Alonso MJ. “Chitosan/cyclodextrin nanoparticles can efficiently transfect the airway epithelium in vitro.” Eur J Pharm Biopharm. 2009(71):257-263.

32. Pérez-Martínez FC, Guerra J, Posadas I et al. “Barriers to non-viral vector-mediated gene delivery in the nervous system.” Pharm Res. 2011(28):1843-1858.,Chan P, Kurisawa M, Chung JE et al. “Synthesis and characterization of chitosan-g-poly(ethylene glycol)-folate as a non-viral carrier for tumor-targeted gene delivery.” Biomaterials. 2007(28):540-549.

33. Fire A, Xu S, Montgomery MK et al. “Potent and specific genetic interference by double-stranded RNA in Caenorhabditis elegans.” Nature. 1998(391):806-811.

34. Katas H, Alpar HO. “Development and characterisation of chitosan nanoparticles for siRNA delivery.” J Control Release. 2006(115):216-225.

35. Liu X, Howard KA, Dong M et al. “The influence of polymeric properties on chitosan/siRNA nanoparticle formulation and gene silencing.” Biomaterials. 2007(28):1280-1288.

36. Malmo J, Sørgård H, Vårum KM et al. “siRNA delivery with chitosan nanoparticles: Molecular properties favoring efficient gene silencing.” J Control Release. 2012(158):261-268.

37. Alameh M, Dejesus D, Jean M et al. “Low molecular weight chitosan nanoparticulate system at low N:P ratio for nontoxic polynucleotide delivery.” Int J Nanomedicine. 2012(7):1399-1414.

38. Holzerny P, Ajdini B, Heusermann W et al. “Biophysical properties of chitosan/siRNA polyplexes: profiling the polymer/siRNA interactions and bioactivity.” J Control Release. 2012(157):297-304.

39. Rojanarata T, Opanasopit P, Techaarpornkul S et al. “Chitosan-thiamine pyrophosphate as a novel carrier for siRNA delivery.” Pharm Res. 2008(25):2807-2814.

40. Dehousse V, Garbacki N, Jaspart S et al. “Comparison of chitosan/siRNA and trimethylchitosan/siRNA complexes behaviour in vitro.” Int J Biol Macromol. 2010(46):342-349.

41. Varkouhi AK, Verheul RJ, Schiffelers RM et al. “Gene silencing activity of siRNA polyplexes based on thiolated N,N,N-trimethylated chitosan.” Bioconjug Chem. 2010(21):2339-2346.

42. Noh SM, Han SE, Shim G et al. “Tocopheryl oligochitosan-based self assembling oligomersomes for siRNA delivery.” Biomaterials. 2011(32):849-857.

43. Ragelle H, Vandermeulen G, Préat V. “Chitosan-based siRNA delivery systems.” J Control Release. 2013(172):207-218.

44. Raviña M, Cubillo E, Olmeda D et al. “Hyaluronic acid/chitosan-g-poly(ethylene glycol) nanoparticles for gene therapy: an application for pDNA and siRNA delivery.” Pharm Res. 2010(27):2544-2555.

45. Zamecnik PC, Stephenson ML. “Inhibition of Rous sarcoma virus replication and cell transformation by a specific oligodeoxynucleotide.” Proc Natl Acad Sci U S A. 1978(75):280-284.

46. Straarup EM, Fisker N, Hedtjärn M et al. “Short locked nucleic acid antisense oligonucleotides potently reduce apolipoprotein B mRNA and serum cholesterol in mice and non-human primates.” Nucleic Acids Res. 2010(38):7100-7111.

47. Kim ST, Kim CK. “Water-soluble chitosan-based antisense oligodeoxynucleotide of interleukin-5 for treatment of allergic rhinitis.” Biomaterials. 2007(28):3360-3368.

48. Gao S, Chen J, Dong L et al. “Targeting delivery of oligonucleotide and plasmid DNA to hepatocyte via galactosylated chitosan vector.” Eur J Pharm Biopharm. 2005(60):327-334.

49. Hong HJ, Jin SE, Park JS et al. “Accelerated wound healing by smad3 antisense oligonucleotides-impregnated chitosan/alginate polyelectrolyte complex.” Biomaterials. 2008(29):4831-4837.

50. Gazori T, Khoshayand MR, Azizi E et al. “Evaluation of Alginate/Chitosan nanoparticles as antisense delivery vector: Formulation, optimization and in vitro characterization.” Carbohydrate Polymers. 2009(77):599-606.

51. Azizi E, Namazi A, Haririan I et al. “Release profile and stability evaluation of optimized chitosan/alginate nanoparticles as EGFR antisense vector.” Int J Nanomedicine. 2010(5):455-461.

52. Gazori, Haririan, Fouladdel et al. “Inhibition of EGFR expression with chitosan/alginate nanoparticles encapsulating antisense oligonucleotides in T47D cell line using RT-PCR and immunocytochemistry.” Carbohydrate Polymers. 2010(80):6-6.

53. Dung TH, Lee SR, Han SD et al. “Chitosan-TPP nanoparticle as a release system of antisense oligonucleotide in the oral environment.” J Nanosci Nanotechnol. 2007(7):3695-3699.

54. Ozbas-Turan S, Akbuga J, Sezer AD. “Topical application of antisense oligonucleotide-loaded chitosan nanoparticles to rats.” Oligonucleotides. 2010(20):147-153.

55. Talaei F, Azizi E, Dinarvand R et al. “Thiolated chitosan nanoparticles as a delivery system for antisense therapy: evaluation against EGFR in T47D breast cancer cells.” Int J Nanomedicine. 2011(6):1963-1975.

56. Kai E, Ochiya T. “A method for oral DNA delivery with N-acetylated chitosan.” Pharm Res. 2004(21):838-843.

57. Jiang HL, Xu CX, Kim YK et al. “The suppression of lung tumorigenesis by aerosol-delivered folate-chitosan-graft-polyethylenimine/Akt1 shRNA complexes through the Akt signaling pathway.” Biomaterials. 2009(30):5844-5852.

58. de la Fuente M, Seijo B, Alonso MJ. “Novel hyaluronic acid-chitosan nanoparticles for ocular gene therapy.” Investigative ophthalmology & visual science. 2008(49):2016-2024.,de la Fuente M, Seijo B, Alonso MJ. “Bioadhesive hyaluronan-chitosan nanoparticles can transport genes across the ocular mucosa and transfect ocular tissue.” Gene Therapy. 2008(15):668-676.

59. Roy K, Mao HQ, Huang SK et al. “Oral gene delivery with chitosan--DNA nanoparticles generates immunologic protection in a murine model of peanut allergy.” Nat Med. 1999(5):387-391.

60. Bivas-Benita M, Laloup M, Versteyhe S et al. “Generation of Toxoplasma gondii GRA1 protein and DNA vaccine loaded chitosan particles: preparation, characterization, and preliminary in vivo studies.” Int J Pharm. 2003(266):17-27.

61. Kumar M, Behera AK, Lockey RF et al. “Intranasal gene transfer by chitosan-DNA nanospheres protects BALB/c mice against acute respiratory syncytial virus infection.” Hum Gene Ther. 2002(13):1415-1425.

62. Iqbal M, Lin W, Jabbal-Gill I et al. “Nasal delivery of chitosan-DNA plasmid expressing epitopes of respiratory syncytial virus (RSV) induces protective CTL responses in BALB/c mice.” Vaccine. 2003(21):1478-1485.

63. Zhang W, Yang H, Kong X et al. “Inhibition of respiratory syncytial virus infection with intranasal siRNA nanoparticles targeting the viral NS1 gene.” Nat Med. 2005(11):56-62.

64. Kong X, Zhang W, Lockey RF et al. “Respiratory syncytial virus infection in Fischer 344 rats is attenuated by short interfering RNA against the RSV-NS1 gene.” Genet Vaccines Ther. 2007(5):4.

65. Pille JY, Li H, Blot E et al. “Intravenous delivery of anti-RhoA small interfering RNA loaded in nanoparticles of chitosan in mice: safety and efficacy in xenografted aggressive breast cancer.” Hum Gene Ther. 2006(17):1019-1026.

66. Barbosa MA, Pêgo AP, Amaral IF. Chitosan. In: Ducheyne P, Hutmacher DW, Kirkpatrick J et al., editors. Comprehensive Biomaterials. London, UK: Elsevier; 2011. p. 221-237.

67. Shaji J, Jain V, Lodha S et al. “Chitosan: A Novel Pharmaceutical Excipient.” International Journal of Pharmaceutical and Applied Sciences 1. 2010

68. Xu W, Shen Y, Jiang Z et al. “Intranasal delivery of chitosan-DNA vaccine generates mucosal SIgA and anti-CVB3 protection.” Vaccine. 2004(22):3603-3612.

69. Bivas-Benita M, van Meijgaarden KE, Franken KL et al. “Pulmonary delivery of chitosan-DNA nanoparticles enhances the immunogenicity of a DNA vaccine encoding HLA-A*0201-restricted T-cell epitopes of Mycobacterium tuberculosis.” Vaccine. 2004(22):1609-1615.

70. Raghuwanshi D, Mishra V, Das D et al. “Dendritic cell targeted chitosan nanoparticles for nasal DNA immunization against SARS CoV nucleocapsid protein.” Mol Pharm. 2012(9):946-956.

71. Oliveira CR, Rezende CM, Silva MR et al. “Oral vaccination based on DNA-chitosan nanoparticles against Schistosoma mansoni infection.” ScientificWorldJournal. 2012(2012):938457.

72. Chew JL, Wolfowicz CB, Mao HQ et al. “Chitosan nanoparticles containing plasmid DNA encoding house dust mite allergen, Der p 1 for oral vaccination in mice.” Vaccine. 2003(21):2720-2729.

73. Kumar M, Kong X, Behera AK et al. “Chitosan IFN-gamma-pDNA Nanoparticle (CIN) Therapy for Allergic Asthma.” Genet Vaccines Ther. 2003(1):3.

74. Li GP, Liu ZG, Liao B et al. “Induction of Th1-type immune response by chitosan nanoparticles containing plasmid DNA encoding house dust mite allergen Der p 2 for oral vaccination in mice.” Cell Mol Immunol. 2009(6):45-50.

75. Dass CR, Contreras KG, Dunstan DE et al. “Chitosan microparticles encapsulating PEDF

plasmid demonstrate efficacy in an orthotopic metastatic model of osteosarcoma." Biomaterials. 2007(28):3026-3033.

76. Cheng M, Li Q, Wan T et al. "Synthesis and efficient hepatocyte targeting of galactosylated chitosan as a gene carrier in vitro and in vivo." J Biomed Mater Res B Appl Biomater. 2011(99):70-80.

77. Zhao QQ, Hu YL, Zhou Y et al. "Gene-carried hepatoma targeting complex induced high gene transfection efficiency with low toxicity and significant antitumor activity." Int J Nanomedicine. 2012(7):3191-3202.

78. Feng S, Agoulnik IU, Truong A et al. "Suppression of relaxin receptor RXFP1 decreases prostate cancer growth and metastasis." Endocr Relat Cancer. 2010(17):1021-1033.

79. Kim HS, Han HD, Armaiz-Pena GN et al. "Functional roles of Src and Fgr in ovarian carcinoma." Clin Cancer Res. 2011(17):1713-1721.

80. Han HD, Mora EM, Roh JW et al. "Chitosan hydrogel for localized gene silencing." Cancer Biol Ther. 2011(11):839-845.

81. Huang Z, Dong L, Chen J et al. "Low-molecular weight chitosan/vascular endothelial growth factor short hairpin RNA for the treatment of hepatocellular carcinoma." Life Sci. 2012(91):1207-1215.

82. Lee SJ, Huh MS, Lee SY et al. "Tumor-homing poly-siRNA/glycol chitosan self-cross-linked nanoparticles for systemic siRNA delivery in cancer treatment." Angew Chem Int Ed Engl. 2012(51):7203-7207.

83. Bowman K, Sarkar R, Raut S et al. "Gene transfer to hemophilia A mice via oral delivery of FVIII-chitosan nanoparticles." J Control Release. 2008(132):252-259.

84. Howard KA, Paludan SR, Behlke MA et al. "Chitosan/siRNA nanoparticle-mediated TNF-alpha knockdown in peritoneal macrophages for anti-inflammatory treatment in a murine arthritis model." Mol Ther. 2009(17):162-168.

85. Jean M, Alameh M, Buschmann MD et al. "Effective and safe gene-based delivery of GLP-1 using chitosan/plasmid-DNA therapeutic nanocomplexes in an animal model of type 2 diabetes." Gene Ther. 2011(18):807-816.

86. Europe CO. Chitosan Hydrochoride. European Pharmacopeia. Strasbourg: 2002.

87. NF USPC. "Chitosan." 2011(29):5361-5365.

88. Boateng JS, Matthews KH, Stevens HN et al. "Wound healing dressings and drug delivery systems: a review." J Pharm Sci. 2008(97):2892-2923.

89. Struszczyk MH. "Global Requirements for Medical Applications of Chitin and its Derivatives." Monograph XI. 2006

90. F2103 ASTMS. "Standard Guide for Characterization and Testing of Chitosan Salts as Starting Materials Intended for Use in Biomedical and Tissue-Engineered Medical Product Applications." 2011

91. Varma AJ, Deshpande SV, Kennedy JF. "Metal complexation by chitosan and its derivatives: a review." Carbohydrate Polymers. 2004(55):77-93.,Bansal V, Sharma PK, Sharma N et al. "Applications of Chitosan and Chitosan Derivatives in Drug Delivery." Advances in Biological Research. 2011(5):28-37.

92. Buschmann MD, Merzouki A, Lavertu M et al. "Chitosans for delivery of nucleic acids." Adv Drug Deliv Rev. 2013

93. 03(2012)e1 ASTMSF. "Standard Test Method for Determining Degree of Deacetylation in Chitosan Salts by Proton Nuclear Magnetic Resonance (1H NMR) Spectroscopy." 2012

94. Varum KM, Anthonsen MW, Grasdalen H et al. "Determination of the degree of N-acetylation

and the distribution of N-acetyl groups in partially N-deacetylated chitins (chitosans) by high-field n.m.r. spectroscopy." Carbohydr Res. 1991(211):17-23.

95. F2602-2008e1 ASTMS. "Standard Test Method for Determining the Molar Mass of Chitosan and Chitosan Salts by Size Exclusion Chromatography with Multi angle Light Scattering Detection (SEC MALS)." 2008

96. USA/FDA Guidelines. "Guidance for Industry - Pyrogen and Endotoxins Testing." 2012

97. Pires LR, Oliveira H, Barrias CC et al. "Imidazole-grafted chitosan-mediated gene delivery: in vitro study on transfection, intracellular trafficking and degradation." Nanomedicine (Lond). 2011(6):1499-1512.

98. Chellat F, Tabrizian M, Dumitriu S et al. "Study of biodegradation behavior of chitosan-xanthan microspheres in simulated physiological media." J Biomed Mater Res. 2000(53):592-599.

CHAPTER IV

OVERCOMING THE BARRIERS TOWARDS SUCCESSFUL GENE DELIVERY TO THE PERIPHERAL NERVOUS SYSTEM

1. Biological Barriers for Gene Delivery into Neurons

The efficient delivery of therapeutic nucleic acids to neurons has the potential to address the molecular cause of not only peripheral neuropathies but also many other conditions affecting the nervous system such as neurodegenerative diseases or spinal cord injuries [1-3].

Efficient non-viral vectors for gene delivery need to overcome multiple extra- and intracellular barriers after administration, before nucleic acids could reach the cell cytoplasm or nucleus, in the case of siRNA and single stranded oligonucleotides or plasmid DNA (pDNA) delivery, respectively (**Figure 1**). Most of these barriers are transversal to most cell types, including neuronal cells. **Table 1** summarizes some of the key aspects that require optimization before efficient gene transfer (pDNA) mediated by non-viral vectors can be achieved, in particular by cationic polymeric systems.

Besides these, neurons have other features such as larger cellular processes (neurites) and lack of division capacity, that constitute additional barriers for nucleic acids delivery. In a clinical scenario, a minimally invasive peripheral administration is preferred over direct injection into the nervous tissue. However, due to the elongated morphology of neuronal projections, the intracellular transport of non-viral vectors in neurons is one of the most challenging routes for nucleic acids delivery. A non-invasive peripheral administration implies the delivery of nanomedicines to the distal ends of axon or dendrites, where these vectors should be internalized and undergo retrograde transport towards the neuronal cell body, where the nucleic acids should escape into the cytoplasm (siRNA or oligonucleotides) or undergo nuclear entry (pDNA) [4].

Because of their specific properties, neurons are considered one of the most difficult cell types to transfect [5] and, therefore, there is a need to develop more efficient non-viral vectors before they can be broadly used for neuronal gene therapy.

The following sections will review strategies that have been explored to overcome some of these limitations.

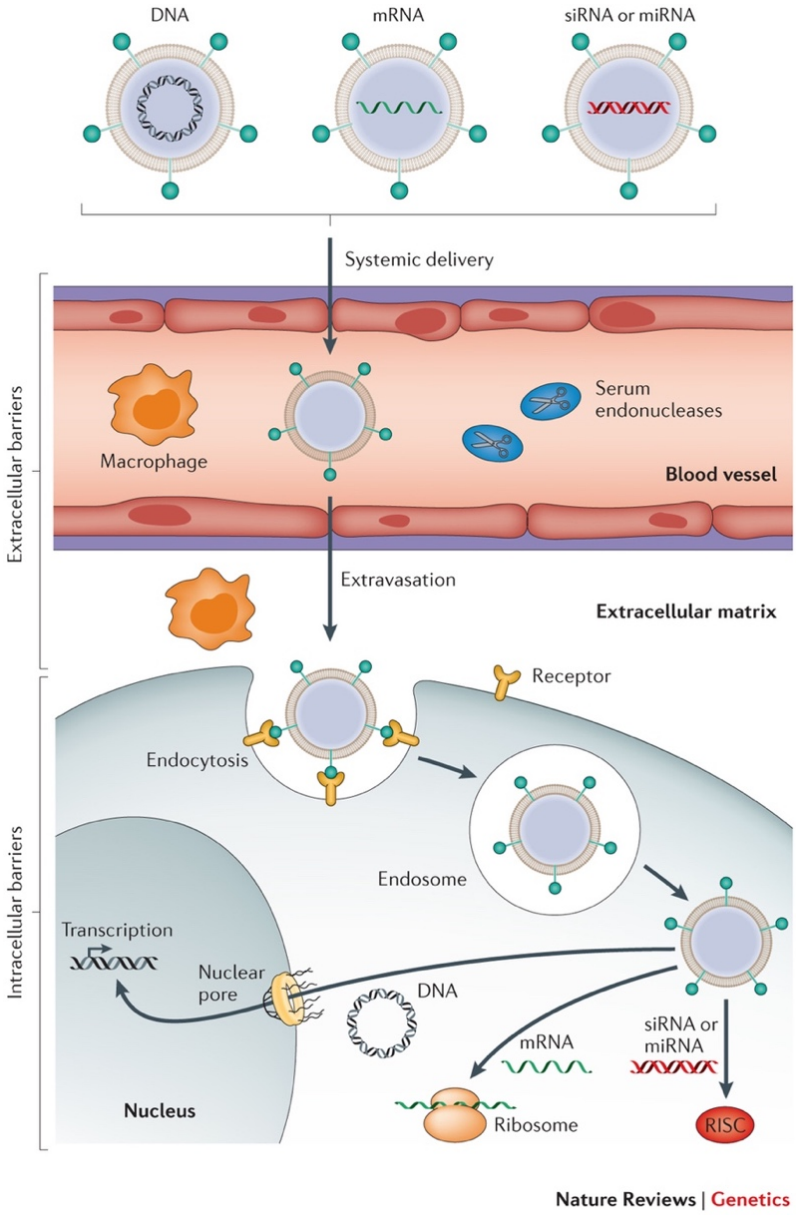

Figure 1. Barriers to successful *in vivo* delivery of nucleic acids using non-viral vectors. Various non-viral vectors can be used to deliver DNA, mRNA and short double-stranded RNA, including small interfering RNA (siRNA) and microRNA (miRNA) mimics. These vectors need to prevent degradation by serum endonucleases and evade immune detection (which could be achieved by chemical modifications of nucleic acids and encapsulation of vectors). They also need to avoid renal clearance from the blood and prevent nonspecific interactions (using polyethylene glycol (PEG) or through specific characteristics of the particles). Moreover, these vectors need to extravasate from the bloodstream to reach target tissues (which requires certain characteristics of particles and specific ligands), and mediate cell entry and endosomal escape (by specific ligands and key components of carriers). siRNA and miRNA mimics must be loaded into the RNA-induced silencing complex (RISC), whereas mRNA must bind to the translational machinery. DNA has to be further transported to the nucleus to exert its activity. Reprinted by permission from Macmillan Publishers Ltd: Nature Review Genetics ([6]), copyright (2014).

Table 1. Main barriers for gene delivery and possible strategies to overcome them exploring cationic polymers as vector systems (adapted from [7]**).**

Extracellular Delivery	
Degradation of pDNA by serum nucleases	DNA condensation or encapsulation with cationic polymers
Nonspecific interactions (of the pDNA/carrier) with blood components	Surface shielding of the vector with hydrophilic polymers
Rapid renal clearance	Control of particle size in combination with surface shielding
Intracellular Delivery and Persistence of Gene Expression	
Particle uptake by cells	Use of specific targeting ligands to enhance receptor-mediated endocytosis of the particles
Endosomal escape	Polycationic “proton sponges” (e.g. poly(ethylene imine, PEI) Use of co-transfection agents such as chloroquine Imidazole-containing polymers Use of membrane-disruptive peptides
Transport from the cytosol into the nucleus	Small and cationic particles to enhance cytosolic migration Nuclear localization signal peptides

1.1. Extracellular barriers

An imperative aspect that is common to all routes of administration is the ability of the delivery system to be stable in the extracellular environment, which may present a number of barriers such as nucleases, proteases, the immune and scavenger systems or adverse pH conditions [8]. The stability of non-viral delivery systems in the extracellular milieu, such as intercellular or intravascular spaces, is related to the chemical stability of the nucleic acids as well as the physical stability of the delivery system. The existence of nucleases in the extracellular environment results in a rapid degradation of the nucleic acids, which can be at least partially overcome by either complexing and condensing them with a variety of polycations or by its encapsulation within a vector system, thereby protecting them from degradation. However, although delivery vectors may have the ability to protect the nucleic acids from endonuclease

attack, the vectors themselves can also be susceptible to recognition and clearance, as well biodegradation.

Another problem regarding the stability of cationic polymer-nucleic acid complexes (polyplexes) is related to its aggregation potential. For most systems employing cationic polymers, aggregation is frequently observed, especially for complexes prepared near charge neutrality. Large aggregates can be formed that cannot transverse cell membranes and may become lodged in microvascular/extracellular networks or accumulate in organs of the mononuclear phagocyte system such as the liver or spleen [9]. However, highly cationic systems can also manifest reduced colloidal stability, owing to electrostatic interactions with endogenous negatively charged molecules, such as glycosaminoglycans, serum albumin, and other extracellular proteins [10]. Further to this, the excess of positive charges can induce damage of cellular membranes and apoptosis [11]. Thus, a balance must be reached in the design of a delivery vector regarding its surface charge.

The hydrophilic polymer poly(ethylene glycol) (PEG) has been used to shield the charge of polymeric particles [12-15], reducing their aggregation, binding with serum proteins or other extracellular proteins, whilst evading the immune system [16]. Although there are successful attempts to develop alternative polymers to PEG, such as poloxamer [17], poly(vinyl alcohol) [18], poly(amino acid)s [19], and poly(saccharide)s [20], PEG is still the most widely used material. PEGylation, however, has been shown to reduce internalization of untargeted polyplexes and to influence intracellular trafficking of the particles [21].

1.2. Intracellular barriers

Being able to surpass the extracellular barriers and reach the target cell is not the only hurdle faced by non-viral gene delivery systems. The nature of conventional gene therapy requires the genetic material to be transcribed by the cell, which requires delivery to the nucleus or, in the case of siRNA or single stranded oligonucleotides, to the cytoplasm. There are several intracellular barriers that may hamper the delivery of nucleic acids into their site of action, including the overpass of the cellular membrane, escape from the endo-lysosome pathway and the active transport of pDNA to the nucleus.

1.2.1. Cellular uptake

The route followed by non-viral gene delivery vectors may differ in the cases in which the vector does or does not have targeting moieties. In the case of non-targeted vectors, these are thought to mediate transfection via a multistage process that includes either hydrophobic or cationic binding (through electrostatic interactions with the anionic cell surface proteoglycans) to the cell membrane and subsequent entry into the cytoplasm. Morphological studies using light and electron microscopy suggest that following the electrostatic adsorption of positively charged polyplexes to the negatively charged plasma membrane, the process of clathrin-dependent endocytosis is predominantly responsible for the cellular uptake of the complexes [22]. Direct fusion with the cell membrane and/or fluid phase endocytosis may also contribute to the cellular uptake of the complexes. Both size and composition of these complexes might determine the mechanism of internalization. Large polyplexes (200-500 nm) enter the cell by clathrin-independent endocytosis (caveolae or macropinocitosys routes) while the smaller ones (<200 nm) are internalized via coated pits through clathrin-mediated endocytosis (CME). Cell surface properties and endocytic activity of the specific cell type also influence the contribution of various internalization pathways in the uptake of the complexes.

The incorporation of targeting moieties in the vector design is expected to modify the particle uptake, with the ligand-receptor interaction governing the internalization pathway and the subsequent intracellular route [23]. The major types of targeting ligands include high affinity small molecules, peptides, aptamers and antibodies [24]. In receptor-mediated endocytosis, which occurs mostly through CME, the plasma-membrane region containing the receptor-ligand complex undergoes endocytosis into vesicles known as clathrin-coated pits, which are transported via microtubules of the cell cytoplasm deeper into the cell, where they form endosomes [25].

Different internalization pathways also influence the fate of the vector once inside the cell. As a result, many efforts have been made to elucidate the mechanisms involved in cellular uptake in order to improve the efficiency of gene therapy [26].

1.2.2. Intracellular trafficking and endosomal escape

Once internalized, the intracellular vesicles carrying these vectors fuse with organelles of the endocytic compartment. Endosomal entrapment constitutes one of the major limiting steps to efficient gene delivery. The endosomal compartment provides cells a way of regulating what enters and leaves the cell and, therefore, any material within the endosome can be either recycled to the cell membrane or progressed to lysosomes [27]. Initially, non-viral vectors are found in vesicles known as early endosomes, which are characterized by their peripheral location in the cell and a slightly acidic luminal pH. The inability of non-viral vectors to escape the endosomal compartment presumably results in their trafficking via late endosomes to lysosomal compartments where the nucleic acids are eventually degraded. Therefore, efficient endosomal escape is necessary for effective delivery [10].

The mechanisms involved in endosomal release of nucleic acids by vectors containing cationic polymers are still not well understood and have also been found to be vector dependent. One hypothesis is based on the idea that a physical disruption of the negatively charged endosomal membrane occurs on direct interaction with the cationic polymer. Such a mechanism has been proposed for both PAMAM dendrimers and poly(L-lysine) (PLL) [28]. Conflicting studies have reported an ability of PEI to disrupt the membrane of isolated lysosomes [29] and bacterial cells [30] but not red blood cells [31], suggesting that the physical properties of target membranes at least partially control the extent of disruption. An alternative hypothesis to explain endosomal disruption by cationic polymers with ionizable amine groups has been known as the ‘‘proton sponge’’ hypothesis [32]. Endosomal membranes possess a vacuolar-type H^+ - ATPase (V-ATPase) that transports protons against a gradient into the endosome resulting in acidification of the compartment. When an ionizable polymer such as PEI is present in endosomes, it is proposed that the Donnan effect causes protonation of the polymer on proton flux into the endosomal lumen and pulls chloride ions and water in, which causes swelling and ultimately, osmotic lysis.

Additional pharmacological agents have been used in conjunction with polyplexes to enhance endosomal release of nucleic acids. Chloroquine (CQ) has been the most commonly used *in vitro* lysosomotropic agent. It is a weak base that enters the lysosomes and becomes protonated under acidic environment. Depending on the

concentration of CQ, it can have different functions. At low concentrations, it may act as an inhibitor to endosome acidification, impeding the accumulation of free protons in the endosome, preventing its maturation and, ultimately, reducing the extent of nucleic acid degradation. At high concentrations (normally applied in *in vitro* studies), it will lead to the accumulation of counter ions to protons in endosomes, resulting in the endosomal swelling and rupture [33, 34]. Relatively high concentrations of glycerol, sucrose or poly(vinylpyrrolidone) (PVP) have also been demonstrated to increase transgene expression presumably by causing osmotic lysis of endosomes. Peptides with pH-dependent membrane lytic activity have also been shown to enhance endosomal escape of pDNA [22].

1.2.3. *Plasmid DNA nuclear entry*

After endosomal escape, pDNA must access the nucleus. In order to reach the nucleus in neuronal cells the particles must reach the cell body, which in neuronal cells might also imply the retrograde transport of the non-viral vectors from the neurite terminals to the cell body. Wang *et al.* demonstrated the ability of PEI/pDNA complexes to undergo internalization within axon terminals in the tongue and retrograde transport back to neuronal soma in the brain stem [35]. Using particle tracking, it was also possible to directly observe retrograde transport of labeled PEI/DNA complexes in live primary neurons [36], and TMC-based NPs in neurons from dissociated dorsal root ganglia cultures [37]. However, the movement observed in most systems is due to transport within endosomes, which are known to acidify and degrade their contents upon arrival at the microtubule-organizing center. In gene delivery systems that effectively bypass degradation by releasing their cargo from early endosomes, transport within the cytoplasm is likely to be a major rate-limiting step due to limited diffusion of particles. Diffusion of pDNA in the cytoplasm has been found to be substantially slower than that observed in dilute solution [38]. For pDNA longer than 2000 base pairs, the diffusion coefficient in the cytosol is <1% of that in water, suggesting a substantial diffusional barrier. This decreased mobility has been ascribed to molecular crowding of the plasmid, but may also reflect an increased viscosity of the cytoplasm. As expected, the diffusion coefficient of pDNA in the cytoplasm is inversely related to the size of the plasmid, suggesting smaller plasmids may be more desirable. In addition to the

considerable diffusional barrier for pDNA in the cytosol, the presence of calcium-sensitive cytosolic nucleases poses a significant metabolic barrier as well [39].

Cells have developed a highly complex transport infrastructure that conveys diffusion-limited cargo along cytoskeletal filaments. Microtubule-based transport is critical for neuronal function since it allows communication between the cell body and axon. For retrograde transport toward the nucleus, dynein is the primary minus end-directed motor [40], and several viruses take advantage of this retrograde transport system for delivery of viral proteins and nucleic acids to the nucleus. The fact that viral particles, which are similar in size to non-viral gene carriers, recruit the dynein motor for assisted retrograde transport validates the need to develop non-viral vectors that can also actively recruit the retrograde motor machinery for efficient delivery to neurons.

Given the post-mitotic nature of neurons, the nuclear import of therapeutic pDNA is an important prerequisite for efficient transgene expression. Clearly, the ability of viruses to efficiently deliver genetic material into host cell nuclei has not yet been successfully reproduced in non-viral systems. There have been numerous attempts to incorporate nuclear localization signal (NLS) peptides into non-viral gene carriers as a means to promote nuclear import [41]. However, a consensus regarding how to most effectively incorporate NLS peptides into non-viral vehicles has not been reached. Furthermore, attempts to improve non-viral gene delivery to post-mitotic cells by incorporating NLS peptides have resulted in modest increases in gene expression at best. Consequently, nuclear entry remains one of the most challenging barriers hindering the development of non-viral gene carriers in applications requiring delivery to post-mitotic cells [40].

2. Targeting Neuronal Cells

Targeted gene therapy is a strategy that consists in creating vectors that can achieve restricted cell populations. It aims at increasing the specificity and safety of gene therapy, avoiding vector diffusion to untargeted organs and cells. While non-viral vectors can associate with most cell types via nonspecific binding to the cell surface, neuron-specific targeting strategies based on receptor-ligand interactions are preferable when designing a neuronal targeted delivery system to prevent widespread delivery to off-target cells. Cell specific gene delivery is of great importance for gene therapy particularly in a sophisticated system like the nervous system, which is

composed of various subtypes of neurons with specific physiological functions. Neurons express several different classes of receptors, including neuropeptide, neurotrophin, and neurotoxin receptors [40]. Targeting moieties corresponding to each of these classes of receptors have been tested in non-viral delivery systems. As an early example of a neuron-targeted polyplex, Martinez-Fonget *et al*. conjugated neurotensin, a 12-amino acid neuropeptide, to PLL, and demonstrated targeted uptake in cultured cells [42].

Various strategies have been described for targeting polymer-based gene carriers to either TrkA or the $p75^{NTR}$ receptors. Zeng *et al.* formulated ternary complexes by electrostatic association of pDNA, low molecular weight PEI, and the nerve growth factor loop 4 hairpin motif. These complexes mediated specific gene transfer into cultured cells expressing the TrkA receptor as well as into DRG *in vivo*, while minimizing the toxicity caused by nonspecific uptake of large amounts of higher-molecular weight PEI [43]. In addition to targeting receptors expressed by specific neuronal populations, it would be ideal to target receptors whose upregulation corresponds to specific disease or injury states. To demonstrate this strategy, Barati *et al.* conjugated an antibody that binds to the $p75^{NTR}$ neurotrophin receptor (MC192) to PLL-based polyplexes and demonstrated transgene expression in targeted neurons in models of peripheral nerve injury [44].

As a final class of neuron-targeting ligands, neurotoxins have been exploited for their ability to efficiently capture cellular internalization machinery as a mean to invade targeted neurons. Of particular interest is the tetanus toxin (TeNT). When applied intramuscularly, TeNT binds to the pre-synaptic neuron terminals, and after internalization is trafficked to the cell body by retrograde axonal transport, thus allowing the possibility of delivery by a minimally invasive method [45]. The purified, non-toxic carboxylic terminal fragment from TeNT (HC), which is responsible for TeNT cell binding and retrograde axonal transport, has been conjugated to PLL [46], PEI [45, 47] and chitosan [48] as means to direct polyplexes into cell lines expressing the relevant receptors. More recently, Liu *et al.* identified a 12-amino acid peptide, Tet1, that mimics the receptor binding properties of HC [49]. Park *et al.* conjugated this peptide to PEI and demonstrated specific uptake of Tet1-modified PEI/DNA polyplexes by PC-12 cells [50].

The success of a targeting strategy depends on the conjugation chemistry, the length of spacer between ligand and polyplex, the ligand–receptor binding strength, and the number of targeting ligands per polyplex. A variety of common crosslinking chemistries have been used to attach targeting ligands to the polymers, including covalent bonds and biotin–streptavidin [33]. Care must be taken, however, to ensure that the ligand–receptor interaction is not perturbed by conjugation. There also exists a balance between the specific targeting interactions and nonspecific electrostatic binding to the cell surface. Cell uptake and gene expression were found to be specific only within a narrow window of polymer/DNA ratios near electroneutrality. Finally, there is typically an optimal ligand valency, due to saturation of both receptor binding and the cell's internalization machinery [33]. Efficient cell-specific targeting therefore requires careful optimization of the various parameters that affect cell-surface binding. Therefore, the possibility to measure the interaction between the conjugated ligand in the nanoparticles with its respective receptors in the target cells is of great importance.

2.1. Atomic force microscopy as a tool to tailor targeted nanoparticles

The use of tailored gene delivery systems has become increasingly important in the development of novel medical therapies and pharmaceutical products. Their incorporation into pharmaceutical formulations may promise enhanced biodistribution and pharmacokinetic properties, increasing the efficacy of a therapeutic product and potentially reducing unwanted side effects [51]. However, the ability to design nanoparticle delivery systems capable of selectively target their payloads to specific cell populations is still a major caveat in nanomedicine. One of the main hurdles is the fact that each nanoparticle formulation needs to be precisely tuned to match the specificities of the target cell and route of administration. Also, the optimal ligand density allowing maximum cell-specific interaction is a critical issue in the tailoring of targeted systems, but the optimization of this parameter implies tedious and time-consuming *in vitro* studies. Thus, technologies that enable the analysis of the specific interaction of these nanomedicines with their target cellular population at the molecular level and under biological relevant conditions are still eagerly awaited to advance new therapeutic delivery approaches into potential new therapies [51].

In this context, atomic force microscopy (AFM) has emerged as a powerful characterization platform, providing valuable insight that may have major implications for nanoparticle design and development. Owing to its capacity to allow observation and manipulation of biosurfaces under physiological conditions, AFM has revolutionized the way in which researchers explore biological structures at the single-molecule level [34].

AFM is a well-known high-resolution surface topography technique with nanometer resolution that allows the measurement of piconewton forces associated with single molecules, thereby providing fundamental insights into the molecular basis of biological phenomena. Moreover, by means of molecular recognition force spectroscopy (MRFS), the AFM cantilever offers the possibility to predict the efficiency of the nanoparticles interaction with target cells, being used as a biosensing system to assess the natural intermolecular interactions between ligands and receptors present in biological membranes [51-53].

Interaction forces between (i.e. intermolecular) and within (i.e. intramolecular) biomolecules determine their structure, dynamics, and function. The intermolecular binding strength of ligand–receptor pairs is pivotal for many biological processes such as receptor signaling and immune system protection (e.g. antibody-antigen complexes) [35]. For measurements associated with intermolecular protein–ligand binding strengths, the ligand can be attached to the AFM tip (**Figure 2**) and the protein attached to the substrate surface (or vice versa). The procedure requires bringing the AFM tip into contact with the surface so as to form a receptor–ligand complex [36]. Linear PEG chains are frequently used to attach one or a few sensor molecules to the tip, with the advantage that PEG is chemically and physically inert, allowing for rapid and free reorientation of the sensor molecule when the AFM tip approaches the surface. Thus, even a single sensor molecule on the tip can properly recognize its cognate molecule on the target surface. Furthermore, the 6–8 nm long PEG linker facilitates data analysis in molecular recognition experiments because the nonlinear elasticity of PEG stretching allows for easy discrimination of specific unbinding events (which are preceded by a characteristic nonlinear stretching curve) from nonspecific tip adhesion [35].

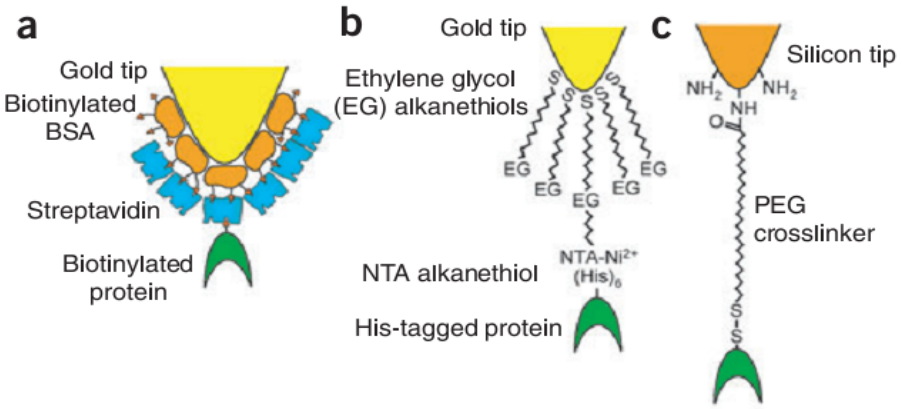

Figure 2. Schematics of surface chemistries commonly used for modifying AFM tips for molecular recognition force spectroscopy. (a) Physisorption of proteins such as Biotinylated BSA; (b) Chemisorption of alkanethiols on gold; (c) Covalent coupling of silanes on silicon oxide. Proteins are coupled to the tip via a heterobifunctional PEG crosslinker (Reprinted from [37]).

Interaction forces of tip-bound ligands and surface-immobilized receptors are measured in force-distance cycles (**Figure 3**). When the AFM tip is retracted from the substrate surface, the force required for dissociation (i.e. the unbinding force), defined as the rupture force at the moment of sample separation, can be subsequently recorded and measured by pulling on the complex until the interaction bond breaks. Such experiments allow for estimation of unbinding forces, dissociation rate constants and bonding widths of the binding pockets [37]. In addition, it can provide insight into the molecular dynamics of a ligand recognition process by varying the loading rate of the force appliance. Since the force required to separate a ligand from its specific binding site is different from the force needed to remove a non-specifically bound ligand, this technique allows the recognition of specific interactions between biomolecules.

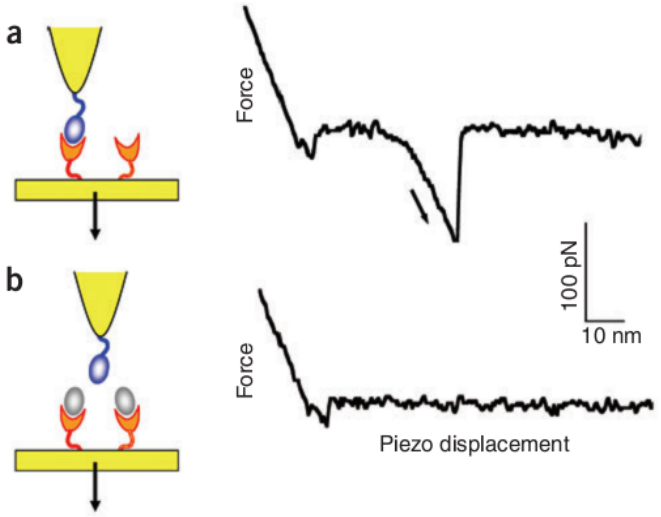

Figure 3. Measurement of molecular recognition interaction forces. (a) Typical force-displacement curve obtained upon retracting (down arrow) a functionalized AFM tip. Force-displacement curves are obtained from raw 'voltage-displacement' curves using the sensitivity of the AFM detector and the cantilever spring constant. The curve shows an unbinding force of about 100 pN, attributed to the rupture of the ligand-receptor pair. The unbinding event is accompanied by a nonlinear elongation force reflecting essentially the stretching of the flexible spacer. (b) Blocking experiment demonstrating that the 100 pN unbinding force is not observed when the measurements are performed in the presence of blocking agents. (Reprinted from [37]).

Taking advantage of this functionality, Oliveira *et al.* has previously proposed the use of MRFS as a screening tool for the optimization of the density of targeting moieties toward improving receptor-specific binding of NPs to neuronal cells in simple cell culture systems [53]. The obtained data allowed them to determine the optimal targeted nanoparticle formulation regarding neuronal cell internalization and transfection and to obtain new insights into the ligand-receptor mechanism. It remained to be established if the proposed methodology could be applied in models of higher complexity and biological relevance, which offers an additional challenge, in order to expand the impact and applicability of this technique.

Another advantage of AFM is the possibility to combine it with optical microscopy. Optical imaging techniques enable the spectroscopic discrimination of different species in a biological sample. In particular, fluorescence microscopy has proven to be a powerful tool for selective and specific visualization of labeled molecules down to the single molecule level, rendering it possible to follow cellular processes and monitor the dynamics of living cell components. The advantages of AFM and fluorescence

microscopy complement each other, and the combination of the two techniques allows a more detailed characterization of cellular structures and processes [37], which can be of critical importance for its application in models of higher biological complexity, with different cellular populations.

3. Conclusions

Previous studies of the mechanisms involved in non-viral gene delivery collectively suggest that the efficiency of the process can be controlled by the physicochemical properties of the delivery system. More information is necessary, however, to fully understand the relative contribution of each step to the overall delivery process. Finally, the effect of the physical and chemical properties of the various non-viral delivery systems on the efficiency of each step must be adequately comprehended and integrated because vector optimization to improve the efficiency of one step in the process may be detrimental to the effectiveness of another.

References

1. Bowers, W.J., D.F. Howard, and H.J. Federoff, "Gene therapeutic strategies for neuroprotection: implications for Parkinson's disease." Exp Neurol, 1997. 144(1): p. 58-68.
2. Blits, B. and M.B. Bunge, "Direct gene therapy for repair of the spinal cord." J Neurotrauma, 2006. 23(3-4): p. 508-20.
3. Federici, T. and N.M. Boulis, "Gene-based treatment of motor neuron diseases." Muscle Nerve, 2006. 33(3): p. 302-23.
4. Bergen, J.M. and S.H. Pun, "Analysis of the intracellular barriers encountered by nonviral gene carriers in a model of spatially controlled delivery to neurons." J Gene Med, 2008. 10(2): p. 187-97.
5. Washbourne, P. and A.K. McAllister, "Techniques for gene transfer into neurons." Current Opinion in Neurobiology, 2002. 12(5): p. 566-573.
6. Yin, H., et al., "Non-viral vectors for gene-based therapy." Nat Rev Genet, 2014. 15(8): p. 541-55.
7. Boeckle, S. and E. Wagner, "Optimizing Targeted Gene Delivery: Chemical Modification of Viral Vectors and Synthesis of Artificial Virus Vector Systems." The AAPS Journal, 2006. 8(4): p. 731-742.
8. Belting, M., S. Sandgren, and A. Wittrup, "Nuclear delivery of macromolecules: barriers and carriers." Adv Drug Deliv Rev, 2005. 57(4): p. 505-27.
9. Laga, R., et al., "Polymer coatings for delivery of nucleic acid therapeutics." J Control Release, 2012. 161(2): p. 537-53.
10. Wiethoff, C.M. and C.R. Middaugh, "Barriers to nonviral gene delivery." J Pharm Sci, 2003. 92(2): p. 203-17.
11. Moghimi, S.M., et al., "A two-stage poly(ethylenimine)-mediated cytotoxicity: implications for gene transfer/therapy." Mol Ther, 2005. 11(6): p. 990-5.
12. Essa, S., J.M. Rabanel, and P. Hildgen, "Effect of polyethylene glycol (PEG) chain organization on the physicochemical properties of poly(D, L-lactide) (PLA) based nanoparticles." Eur J Pharm Biopharm, 2010. 75(2): p. 96-106.
13. Germershaus, O., et al., "Gene delivery using chitosan, trimethyl chitosan or polyethylenglycol-graft-trimethyl chitosan block copolymers: establishment of structure-activity relationships in vitro." J Control Release, 2008. 125(2): p. 145-54.
14. Monck, M.A., et al., "Stabilized plasmid-lipid particles: pharmacokinetics and plasmid delivery to distal tumors following intravenous injection." J Drug Target, 2000. 7(6): p. 439-52.
15. Jokerst, J.V., et al., "Nanoparticle PEGylation for imaging and therapy." Nanomedicine, 2011. 6(4): p. 715–728.
16. D'Souza A, A. and R. Shegokar, "Polyethylene glycol (PEG): a versatile polymer for pharmaceutical applications." Expert Opin Drug Deliv, 2016. 13(9): p. 1257-75.
17. Morille, M., et al., "Long-circulating DNA lipid nanocapsules as new vector for passive tumor targeting." Biomaterials, 2010. 31(2): p. 321-9.
18. Takeuchi, H., et al., "Polymer coating of liposomes with a modified polyvinyl alcohol and their systemic circulation and RES uptake in rats." J Control Release, 2000. 68(2): p. 195-205.
19. Metselaar, J.M., et al., "A novel family of L-amino acid-based biodegradable polymer-lipid conjugates for the development of long-circulating liposomes with effective drug-targeting capacity." Bioconjug Chem, 2003. 14(6): p. 1156-64.

20. Haidar, Z.S., R.C. Hamdy, and M. Tabrizian, "Protein release kinetics for core-shell hybrid nanoparticles based on the layer-by-layer assembly of alginate and chitosan on liposomes." Biomaterials, 2008. 29(9): p. 1207-15.

21. Mishra, S., "PEGylation significantly affects cellular uptake and intracellular trafficking of non-viral gene delivery particles." European Journal of Cell Biology, 2004. 83(3): p. 97-111.

22. Lechardeur, D. and G.L. Lukacs, "Intracellular Barriers to Non-Viral Gene Transfer." Current Gene Therapy, 2002. 2: p. 183-194.

23. Pêgo, A.P., H. Oliveira, and P.M. Moreno, *Biomaterial-Based Vectors for Targeted Delivery of Nucleic Acids to the Nervous System*, in *Drug Delivery Systems: Advanced Technologies Potentially Applicable in Personalised Treatment*, J. Coelho, Editor. 2013, Springer Netherlands: Dordrecht. p. 185-224.

24. Yameen, B., et al., "Insight into nanoparticle cellular uptake and intracellular targeting." J Control Release, 2014. 190: p. 485-99.

25. El-Sayed, A. and H. Harashima, "Endocytosis of gene delivery vectors: from clathrin-dependent to lipid raft-mediated endocytosis." Mol Ther, 2013. 21(6): p. 1118-30.

26. Stewart, M.P., et al., "Challenges in carrier-mediated intracellular delivery: moving beyond endosomal barriers." Wiley Interdiscip Rev Nanomed Nanobiotechnol, 2016. 8(3): p. 465-78.

27. Billiet, L., et al., "Gene transfer by chemical vectors, and endocytosis routes of polyplexes, lipoplexes and lipopolyplexes in a myoblast cell line." Biomaterials, 2012. 33(10): p. 2980-90.

28. Zhang, Z.Y. and B.D. Smith, "High-generation polycationic dendrimers are unusually effective at disrupting anionic vesicles: membrane bending model." Bioconjug Chem, 2000. 11(6): p. 805-14.

29. Klemm, A.R., D. Young, and J.B. Lloyd, "Effects of polyethyleneimine on endocytosis and lysosome stability." Biochem Pharmacol, 1998. 56(1): p. 41-6.

30. IM, H., et al., "Polyethyleneimine is an effective permeabilizer of gram-negative bacteria." Microbiology, 1997. 143(Pt 10): p. 3193–3199.

31. Kichler, A., et al., "Polyethylenimine-mediated gene delivery: a mechanistic study." J Gene Med, 2001. 3(2): p. 135-44.

32. Boussif, O., et al., "A versatile vector for gene and oligonucleotide transfer into cells in culture and in vivo: polyethylenimine." Proc Natl Acad Sci U S A, 1995. 92(16): p. 7297-301.

33. Erbacher, P., et al., "Putative Role of Chloroquine in Gene Transfer into a Human Hepatoma Cell Line by DNA/Lactosylated Polylysine Complexes." Experimental Cell Research, 1996. 225(1): p. 186-194.

34. Ciftci, K. and R.J. Levy, "Enhanced plasmid DNA transfection with lysosomotropic agents in cultured fibroblasts." International Journal of Pharmaceutics, 2001. 218(1): p. 81-92.

35. Wang, S., et al., "Transgene expression in the brain stem effected by intramuscular injection of polyethylenimine/DNA complexes." Mol Ther, 2001. 3(5 Pt 1): p. 658-64.

36. Suk, J.S., et al., "Quantifying the intracellular transport of viral and nonviral gene vectors in primary neurons." Exp Biol Med (Maywood), 2007. 232(3): p. 461-9.

37. Lopes, C.D., et al., "Microfluidic-based platform to mimic the in vivo peripheral administration of neurotropic nanoparticles." Nanomedicine (Lond), 2016. 11(24): p. 3205-3221.

38. Lukacs, G.L., et al., "Size-dependent DNA mobility in cytoplasm and nucleus." J Biol Chem, 2000. 275(3): p. 1625-9.

39. Pollard, H., et al., "Ca2+-sensitive cytosolic nucleases prevent efficient delivery to the nucleus of injected plasmids." J Gene Med, 2001. 3(2): p. 153-64.

40. Bergen, J.M., et al., "Nonviral approaches for neuronal delivery of nucleic acids." Pharm Res, 2008. 25(5): p. 983-98.

41. van der Aa, M.A., et al., "The nuclear pore complex: the gateway to successful nonviral gene delivery." Pharm Res, 2006. 23(3): p. 447-59.

42. Martinez-Fong, D., et al., "Neurotensin-SPDP-poly-L-lysine conjugate: a nonviral vector for targeted gene delivery to neural cells." Brain Res Mol Brain Res, 1999. 69(2): p. 249-62.

43. Zeng, J.M., X. Wang, and S. Wang, "Self-assembled ternary complexes of plasmid DNA, low molecular weight polyethylenimine and targeting peptide for nonviral gene delivery into neurons." Biomaterials, 2007. 28(7): p. 1443-1451.

44. Barati, S., et al., "GDNF gene delivery via the p75(NTR) receptor rescues injured motor neurons." Exp Neurol, 2006. 202(1): p. 179-88.

45. Oliveira, H., et al., "Targeted gene delivery into peripheral sensorial neurons mediated by self-assembled vectors composed of poly(ethylene imine) and tetanus toxin fragment c." Journal of Controlled Release, 2010. 143(3): p. 350-358.

46. Knight, A., et al., "Non-viral neuronal gene delivery mediated by the HC fragment of tetanus toxin." Eur J Biochem, 1999. 259(3): p. 762-9.

47. Lopes, C.D., et al., "In vivo targeted gene delivery to peripheral neurons mediated by neurotropic poly(ethylene imine)-based nanoparticles." Int J Nanomedicine, 2016. 11: p. 2675-83.

48. Oliveira, H., et al., "Chitosan-based gene delivery vectors targeted to the peripheral nervous system." Journal of Biomedical Materials Research Part A, 2010. 95A(3): p. 801-810.

49. Liu, J.K., et al., "A novel peptide defined through phage display for therapeutic protein and vector neuronal targeting." Neurobiology of Disease, 2005. 19(3): p. 407-418.

50. Park, I.K., et al., "Neuron-specific delivery of nucleic acids mediated by Tet1-modified poly(ethylenimine)." J Gene Med, 2007. 9(8): p. 691-702.

51. Lamprecht, C., P. Hinterdorfer, and A. Ebner, "Applications of biosensing atomic force microscopy in monitoring drug and nanoparticle delivery." Expert Opin Drug Deliv, 2014. 11(8): p. 1237-53.

52. Muller, D.J. and Y.F. Dufrene, "Atomic force microscopy: a nanoscopic window on the cell surface." Trends Cell Biol, 2011. 21(8): p. 461-9.

53. Oliveira, H., et al., "Molecular Recognition Force Spectroscopy: A New Tool to Tailor Targeted Nanoparticles." Small, 2011. 7(9): p. 1236-1241.

PART 2

CHAPTER V

A HIGH-THROUGHPUT BIOIMAGING STUDY TO ASSESS THE IMPACT OF NANOPARTICLE DEGRADATION ON DNA DELIVERY PERFORMANCE

A High-Throughput Bioimaging Study to Assess the Impact of Chitosan-based Nanoparticle Degradation on DNA Delivery Performance

Carla Pereira Gomes[a,b,c,‡], Aida Varela-Moreira[a,b,d,‡,#], Victoria Leiro[a,b], Cátia Daniela Ferreira Lopes[a,b,d], Pedro Miguel Duarte Moreno[a,b], Ana Paula Pêgo[a,b,c,e,,*]

[a]INEB – Instituto de Engenharia Biomédica, Universidade do Porto, Rua Campo Alegre 823, 4150-180 Porto, Portugal
[b]i3S – Instituto de Investigação e Inovação em Saúde, Universidade do Porto, Rua Alfredo Allen 208, 4200-135 Porto, Portugal
[c]Faculdade de Engenharia da Universidade do Porto, R. Dr. Roberto Frias, 4200-465 Porto, Portugal
[d]Faculdade de Medicina da Universidade do Porto, Alameda Prof. Hernâni Monteiro, 4200 – 319 Porto, Portugal
[e]ICBAS – Instituto de Ciências Biomédicas Abel Salazar, Universidade do Porto, Rua de Jorge Viterbo Ferreira 228, 4050-313 Porto, Portugal

[‡]These authors contributed equally to this work

[#]Present Address: Laboratory of Clinical Chemistry and Haematology (LCKH), University Medical Center, Heidelberglaan 100, 3584 CX Utrecht, The Netherlands

Published in Acta Biomaterialia, Volume 46, 2016

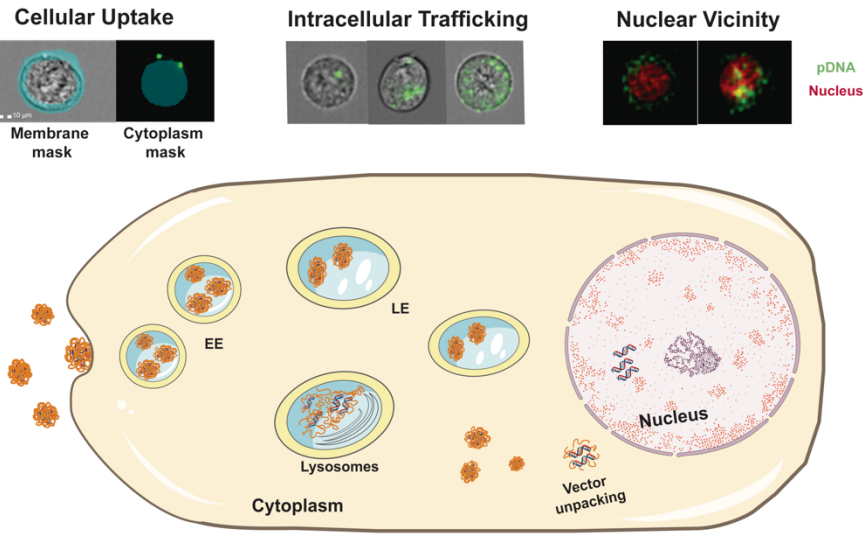

Abstract

By using imaging flow cytometry as a powerful statistical high-throughput technique we investigated the impact of degradation on the biological performance of trimethyl chitosan (TMC)-based nanoparticles (NPs). In order to achieve high transfection efficiencies, a precise balance between NP stability and degradation must occur. We altered the biodegradation rate of the TMC NPs by varying the degree of acetylation (DA) of the polymer (DA ranged from 4 to 21%), giving rise to NPs with different enzymatic degradation profiles. While this parameter did not affect NP size, charge or ability to protect plasmid DNA, NPs based on TMC with an intermediate DA (16%) showed the highest transfection efficiency. Subsequently, by means of a single quantitative technique, we were able to follow, for each tested formulation, major steps of the NP-mediated gene delivery process – NP cell membrane association, internalization and intracellular trafficking, including plasmid DNA transport towards the nucleus. NP cytotoxicity was also possible to determine by quantification of cell apoptosis. Overall, the obtained data revealed that the biodegradation rate of these NPs affects their intracellular trafficking and, consequently, their efficiency to transfect cells. Thus, one can use the polymer DA to modulate the NPs towards attaining different degradation rates and tune their bioactivity according to the desired application. Furthermore, this novel technical approach revealed to be a valuable tool for the initial steps of nucleic acid vector design.

Statement of Significance

By changing the biodegradation rate of trimethyl chitosan-based nanoparticles (NPs) one was able to alter the NP ability to protect or efficiently release DNA and consequently, to modulate their intracellular dynamics. To address the influence of NP degradation rate in their transfection efficiency we took advantage of imaging flow cytometry, a high-throughput bioimaging technique, to unravel some critical aspects about NP formulation such as the distinction between internalized versus cell-associated/ adsorbed NP, and even explore NP intracellular localization. Overall, our work provides novel information about the importance of vector degradation rate for gene delivery into cells, as a way to tune gene expression as a function of the desired application, and advances novel approaches to optimize nanoparticle formulation.

1. Introduction

The remarkable advances in molecular medicine and biology observed within the last decades have led to the development of promising therapeutic tools to be applied in the regenerative medicine field. These include the generation of nucleic acid-based approaches to correct defective proteins or to induce the expression of therapeutic proteins *in situ* [1]. An efficient gene vector has to be safe and capable of mediating the expression of the gene of interest for a sustained period of time, in a sufficiently large population of cells, to produce the desired biological effect. Due to their safer profile, non-viral vectors have drawn significant attention for regenerative medicine applications [2]. Among these, cationic polymers have been extensively explored, both *in vitro* and *in vivo*, for nucleic acid delivery as a result of their cationic nature, which favors both the interaction with nucleic acids and cell membranes [3, 4].

Chitosan (CH) is a cationic polymer that has been widely explored as a gene delivery vector [5]. However, despite being biocompatible and biodegradable, its poor solubility in physiological conditions has limited its widespread application. More recently, a CH derivative – trimethyl chitosan (TMC) – has been proposed for its improved solubility in a wide pH range [6]. Due to the quaternized amine groups, TMC has fixed positive charges, which enables the establishment of electrostatic interactions between the polymer and the negatively charged nucleic acids even at physiological pH [7, 8]. Previously, we have shown that the degradation profile of CH influences the biological activity of the resulting DNA-CH nanoparticles (NPs), namely in terms of their efficiency to transfect cells. Moreover, we established that the enzymatic degradation of the CH-based NPs was correlated with the polymer degree of acetylation (DA) [9]. Consequently, we advanced that the modulation of the NP degradation profile could be an advantageous tool for the development of unique gene delivery vectors, in which one can tune the release rate of a gene of interest. Remain to be established if degradation is also a key parameter in the context of TMC NP-mediated plasmid DNA (pDNA) delivery.

In this study, we took advantage of imaging flow cytometry as a high-throughput technique to evaluate the impact of the degradation rate of TMC-based NPs on their performance as a pDNA vector. The accurate quantification of NP cellular internalization, although critical for the clinical application of gene delivery systems, has

been a challenge for many years [10, 11]. The accurate evaluation of NP uptake is difficult due to the strong adsorption of certain nanomaterials onto the cellular membranes. The most common methods used for NP internalization evaluation are flow cytometry or microscopy-based techniques, however, both of them have limitations. While the high-throughput nature of traditional flow cytometry generates robust statistical data, it lacks spatial resolution, making the distinction between internalized from membrane-adsorbed NPs a challenge. Attempts to solve this problem have included the destruction of membrane-associated NPs followed by their removal through washes [13] or the measurement of fluorescence in the presence and absence of fluorescence quenchers with selective permeation characteristics [14, 15], among others. However, these methods are specific for certain types of NPs and/or fluorophores, making comparisons of data between studies difficult [11, 16]. Hence, “internalization” data can be misleading in terms of its impact on transfection efficiency. By combining both techniques, imaging flow cytometry provides an accurate high-throughput robust analysis tool of fluorescent signal intensities and spatial relationships between different structures and cellular features thus providing a reliable statistical quantification of NPs internalization [12-14]. Besides NP internalization kinetics, here we were capable to infer about NP intracellular behavior through the quantification of the number of nanoparticle-loaded vesicles (NLV) per cell at different time-points. Moreover, we were able to evaluate the proximity of the internalized NPs to the cell nuclei, a parameter of great importance, as it can be associated to the NP transfection efficiency. In this way, with the use of a single technique, we assessed some of the most crucial parameters to the process of optimization of NP formulation.

2. Materials and Methods

2.1. Polymers purification

Trimethyl chitosan (TMC) derived from ultra-pure chitosan was supplied by Kytozyme (Belgium) (lot VIHA0013-157). TMC was purified by filtration and dialysis, as previously described [15]. The original chitosan (CH), also provided by Kytozyme (Belgium) (lot VIHA0018-019), was purified by precipitation according to a previously established protocol [16].

2.2. TMC deacetylation and re-acetylation

The purified TMC was deacetylated as previously described [17]. Briefly, the purified polymer was dissolved in a concentrated sodium hydroxide (NaOH) solution (47% w/v) and left to react for 2 h at 110°C under a silicon bath. Next, the solution was placed under an ice bath and HCl with the same molarity as NaOH (11 M) was added drop wise for neutralization. The resulting polymer was dialyzed for three days against deionized water and then freeze dried (Labconco, USA). TMC with a higher DA was obtained by re-acetylation of deacetylated TMC accordingly to a previously described procedure [18]. The reaction was performed using acetic anhydride as acetylating agent and 1,2-propanediol as co-solvent. The molar ratio of acetic anhydride per free amine groups added was of 0.18 and was extrapolated from an graphic described elsewhere [18], considering 20% the aimed percentage of acetylation. The acetylated polymer was precipitated by addition of methanol/diethyl ether (2:1), recovered by centrifugation and washed three times with ethanol. Subsequently, the polymer was dialyzed and freeze dried as described above.

2.3. Polymer characterization

Proton nuclear magnetic resonance (^{1}H-NMR) was performed to evaluate polymer degree of acetylation (DA) and TMC degree of quaternization (DQ). All polymer samples were dissolved in D_2O (5 mg.ml^{-1}) at 60 ºC overnight and further analysed in a digital spectrometer (Bruker Advance III 400, UK) at room temperature (RT) with a total of 200 scans. The % DA was calculated according to Mourya *et al.* [6] and the % of DQ was calculated following the equation reported by Curti and Campana-Filho [19]. Gel permeation chromatography (GPC) was used to determine polymer molecular weight. The modular system employed was composed by an isocratic pump +

autosampler + vacuum degasser module (Viscotek GPC Max VE 2001 GPC solvent / sample module), a viscometer/right angle laser light scattering (RALLS) dual detector (T60 Viscotek), and a refractive index detector (K-5002 Knaeur) operating at the same wavelength as the RALLS detector (670 nm). Separations were performed in a set of PL aquagel-OH mixed columns. Measurements were performed in 0.33 M $NaCH_3COOH$ / 0.28 M CH_3COOH eluent at a flow rate of 1 $ml.min^{-1}$. Sample concentration in a 0.1–0.2% (w/v) range and an injection volume of 100 µl were applied. Dextran and pullulan were used as broad and narrow standards, respectively. All measurements were performed in triplicate, at RT. Endotoxin levels of the purified polymer extracts were assessed using the Limulus Amebocyte Lysate Assay (QCL-1000, Cambrex Bio Science, USA), following the manufacturer instructions.

2.4. Plasmid DNA

The pDNA used encoded for the enhanced Green Fluorescent Protein and Luciferase (eGFP and Luc; pCMV-eGFPLuc, 6.7 kb, Invitrogen) genes. Plasmid was produced in a DH5α competent *E. coli* strain and purified using an EndoFree Plasmid Giga Kit following the manufacturer instructions (Qiagen, Germany). Plasmid concentration and purity were assessed by UV spectroscopy (Nanodrop 1000, Thermo Scientific, USA). Only plasmid solutions with an absorbance (260/280 nm) ratio comprised between 1.8 and 2.0 were used.

2.5. Nanoparticle preparation

TMC polymers were allowed to hydrate overnight in 5 mM HCl aqueous solution at a final concentration of 0.5% (w/v). Afterwards, 40 mM HEPES with 10% (w/v) glucose, pH 7.4 was added in order to attain a final solution at 0.25% (w/v) in 20 mM HEPES with 5% (w/v) glucose, pH 7.4. CH solutions were prepared in 5 mM acetate buffer, pH 5.5, as previously described [20]. Subsequently, solutions were filter sterilized and final polymer concentration was assessed by a colorimetric assay using Cibacron® Brilliant Red (Sigma-Aldrich, USA), as previous described [15]. NPs were prepared by mixing, while vortexing, equal volumes of pre-heated (55°C for 10 min, Thermomixer®) pDNA solution (1 $mg.ml^{-1}$) and either CH (0.1% (w/v)) or TMC solutions (0.25% (w/v)). CH- and TMC-based NPs were allowed to stabilize for 15 min at RT before further use. NPs were prepared with 4 µg of pDNA at N/P molar ratios ranging from 1 to 18 to assess the best ratio regarding transfection efficiency in ND7/23 cells (**Supplementary Figure**

S1). The N/P ratio refers to the amount of positive moles from the polymer (N) (primary amine groups for CH and quaternized amine groups for TMC) to moles of pDNA phosphate groups (P). Since the TMC_{16} NPs presented a higher performance at the N/P ratio of 15, this ratio was chosen for all experiments throughout the study.

2.6. Determination of average hydrodynamic size and zeta potential

Nanoparticle hydrodynamic mean diameter and zeta potential were determined using a Zetasizer Nano Zs (Malvern Instruments, UK) following the manufacturer instructions. NPs were prepared as mentioned above and then diluted 6 times in Dulbecco's Modified Eagle Medium (DMEM) with GlutamaxTM, 10% (v/v) heat inactivated (55ºC) foetal bovine serum (FBS) and 1% (v/v) penicillin/streptomycin, all supplied by Gibco (Thermo Fisher Scientific, USA), and left to stabilize for 30 min prior to NP size and surface charge determination, using a high concentration cell (ZEN1010, Malvern Instruments, UK). CH and TMC-based NP size and surface charge were also measured in 5 mM acetate buffer pH 5.5 and 20 mM HEPES buffer with 5% (w/v) glucose pH 7.4, respectively (**Supplementary Table S1**). Size measurements were performed at 25°C at a 173° scattering angle in the automatic mode, and the mean hydrodynamic diameters were determined by cumulant analysis (Z-average mean). The calculated zeta potential of the NPs was determined by laser Doppler velocimetry (LDV) and phase analysis light scattering (M3-PALS) at 25°C. The software used was DTS Nano version 7.11, supplied by the manufacturer (Malvern Instruments, UK).

2.7. pDNA condensation efficiency and nanoparticle stability

Plasmid DNA condensation efficiency was assessed through the SYBR Gold® (Life Technologies, Thermo Fisher Scientific, USA) exclusion assay. NPs were prepared with a pDNA concentration of 25 $ng.\mu l^{-1}$ (in a final volume of 100 µl). Afterwards, 20 µl of NPs were added to a black-walled 96-well plate (Greiner bio-one) containing 198 µl of either their buffer of preparation (testing their ability to condense pDNA after preparation) or in complete DMEM medium (to investigate NP stability in cell culture conditions). Finally, 2 µl of a 10,000x diluted (Tris-acetate-EDTA – TAE Buffer) SYBR® Gold solution was added to each well in order to reach a final volume of 200 µl. After 10 min incubation with continuous plate mixing, fluorescence was measured (λ_{exc} = 485 nm, λ_{em} = 540 nm). A pDNA standard curve was performed in each experiment, using

a series of pDNA dilutions (**Supplementary Figure S2**). The amount of free pDNA (not complexed with the polymer) for each well was calculated based on the equation obtained by the linear regression of the pDNA standard curve. Results are expressed as relative percentage of complexation where 100% means pDNA is totally complexed with polymer in NPs, and 0% means that all pDNA is free (not complexed with the polycation). Samples with the same mass ratio of polymer without DNA were used as control in order to subtract any polymer background fluorescence.

2.8. Nanoparticle enzymatic degradation study

Nanoparticle enzymatic degradation was assessed by an indirect method, previously set up by our team [9]. CH or TMC-based NPs were prepared with a fixed mass ratio, independently of the polymer DA, and incubated with lysozyme in the presence of a fluorogenic substrate – 4-methylumbelliferyl b-D-*N,N´,N´´*-triacetylchitotrioside (MU-$[GlcNAc]_3$). The enzyme substrate was previously dissolved in CH_3COONa (1 M, pH = 5.5):H_2O:dimethylformamide (1:1:1) in a 96-well plate. Then, lysozyme (from chicken egg white, Sigma-Aldrich, USA) was added to each well and incubated at 37°C, 70 rpm. The freshly prepared NPs were added in order to obtain a final molar ratio of 3.5:0.45:1.2 (lysozyme:substrate:NPs). After 1, 2, 4, 8 or 12 h of reaction, NaOH was added at a final concentration of 0.05 M to stop the reaction and the fluorescence resultant of substrate enzymatic degradation was measured (λ_{exc} = 360 nm; λ_{em} = 455 nm). Results are expressed as relative fluorescence percentage normalized to the positive control (maximum fluorescence emission by the fluorogenic substrate).

To compare the degradation kinetics of the developed formulations, a non-linear fitting of the degradation data was performed by using the one phase decay equation model with the GraphPad Prism 6.0 software. By using this fitting model, we were able to infer about the rate constant of NPs degradation (*k*), expressed in reciprocal values of the X axis time units. Additionally, the degradation span (difference between initial time and plateau) was also computed and expressed as % of fluorescence.

2.9. Cell culture

For the *in vitro* assays, a sensorial neuron cell line model was used. The ND7/23 (mouse neuroblastoma (N18 tg 2) x rat dorsal root ganglion neuron hybrid) cell line was obtained from ECACC. The cells were routinely cultured in complete DMEM medium

(with serum and antibiotics) and maintained at 37°C in a 5% CO_2 humidified incubator. Cells were routinely tested for mycoplasma by standard PCR.

2.10. Transfection studies

ND7/23 cells were seeded into 24-well plates at a cell density of 2 x 10^4 viable cells per cm^2, 24 h prior to incubation with NPs. TMC-based NPs were prepared at N/P ratio of 15 with 2 µg of pDNA per cm^2 and suspended in complete DMEM medium (with serum and antibiotics), in a 1:6 dilution prior to addition to cells. NPs based on poly(ethylene imine) with 25 kDA (Sigma-Aldrich) were prepared at N/P ratio of 3 using the same amount of pDNA as the TMC-based NPs. Lipofectamine® 2000 (ThermoFisher Scientific) was used according to the manufacturer instructions. 24 h post-incubation the cell media was removed, and 1 ml of fresh complete DMEM medium was added to each well. Cells were incubated for an additional 48 h period, with daily renewing of the culture media. In the transfection studies using chloroquine (CQ), a final concentration of 100 µM of the reagent was used. CQ was added to cells 20 h post NP incubation to promote endolysosomal escape of NPs. Four hours after addition of CQ to cells, cell medium was replaced with fresh medium and cells were incubated for an additional 48 h period, with daily renewing of the culture media. At the defined time point (72 h post-incubation with NPs), cells were trypsinized and processed for flow cytometry for eGFP expression determination. Twenty thousand gated events were taken for each replicate and analysed using FACS Calibur flow cytometer (BD Biosciences). The resulting data was analysed using FlowJo software (version 10, FLOWJO, LLC). Untreated cells were used as negative control.

2.11. Nanoparticles internalization and intracellular localization studies by imaging flow cytometry

Cells were seeded into 6-well TCPS plates (Greiner bio-one) at a cell density of 2 x 10^4 cells per cm^2 24 h prior to incubation with NPs in complete DMEM medium, as previously described. pDNA was labelled with YOYO®-1 (Invitrogen) as indicated by the manufacturer. CH or TMC-based NPs were prepared at N/P ratio of 15 with 2 µg of pDNA per cm^2 and incubated with cells from 0.5 h to 24 h, at 37°C. Afterwards, cells were trypsinized, fixed with 4% paraformaldehyde (PFA) and centrifuged to obtain a pellet of about 10^5 cells in 50 µl. Cell images were acquired using an ImageStream^X

multispectral imaging flow cytometer (Amnis, EDM Millipore, Darmstadt, Germany), collecting 10,000 events per sample at 40x magnification. A 488 nm wavelength laser was used to excite YOYO®-1 and DRAQ5™. The fluorescence images were collected using the 480−560 nm and 660–745 nm spectral detection channels, respectively. For double stained cells, single stained controls were used to compensate fluorescence between channel images on a pixel-by-pixel basis. Cell images were analysed using IDEAS® image-analysis software version 6.0 (Amnis, EDM Millipore, Germany). To discriminate internalized *versus* membrane-associated NPs, a mask representing the whole cell was defined by the bright-field image, and an internal mask (cytoplasm) was defined by eroding the whole cell mask by 5 pixels (each pixel being equivalent to 0.5 μm). The external region was determined by dilating the mask by 2 pixels and subtracting the internal mask (cytoplasm), which results in the mask for the cell membrane. Comparison of the fluorescence detected inside the internal mask with the whole cell fluorescence enabled the determination of the internalization score (IS). These values were calculated using the IDEAS® software, as previously described [12].

The number of nanoparticle-loaded vesicles (NLV) per cell was determined using images acquired with the Extended Depth of Field [21]. To determine the number of NLV per cell, a mask was created in order to identify the fluorescence intensity peaks at least 4-fold greater than the background. The number of individual vesicles in a cell was enumerated using the Spot Count feature from IDEAS® software, and plotted in frequency histograms. To assess NLV proximity to the nuclear vicinity, the degree of pixel intensity correlation between the labelled pDNA and nuclear DNA of each cell was analysed. For this purpose, cells were incubated with DRAQ5™ (6.25 μM) (BioStatus, UK) prior to acquisition on the imaging flow cytometer. Nuclear proximity was also evaluated from 0.5 h to 24 h. To measure the presence of YOYO®-1 in the nuclear vicinity, the Similarity feature of IDEAS® software was used [22]. In order to identify the pixels from nucleus, a nuclear mask was created by the user taking into account the fluorescent intensity of DRAQ5™ in its respective detection channel. Gating for nuclear localization events was decided based on visual inspection of histogram bins; the translocation gate was the same for each sample within an experiment.

2.12. Transmission electron microscopy

Cells were seeded as previously described for internalization studies. pDNA and TMC were labelled with FluoroNangold™ and Quantum Dots (QDs), respectively. pDNA was biotinylated with Label IT® Biotin Labelling Kit (Mirus Bio, USA) according to the manufacturer's instructions. Subsequently, biotinylated pDNA was reacted with Streptavidin-FluoroNanogold™ (Nanoprobes, USA) according to the manufacturer's instructions. TMC was conjugated with QD705 bearing a carboxylic via EDC (Sigma-Aldrich, USA) as coupling agent. Briefly, TMC solution (10 $mg.ml^{-1}$ in PBS) was activated by adding EDC at the mole ratio of 567:1 (EDC:TMC). Afterwards, carboxyl-QD705 solution (Life Technologies, USA) (final concentration of 0.09 µM) was slowly added to the activated TMC and stirred for 2 h at RT in the dark. Unconjugated QDs were removed by centrifugation at 10,000 rpm for 10 min using an ultrafiltration filter tube (MWCO: 30 kDa, Millipore, USA). The purified TMC-QD solution was stocked at 4 °C until further use.

2.13. Apoptosis analysis by imaging flow cytometry

ND7/23 cells were seeded in 6-well plates, as previously described. After 24 h, cells were incubated with CH or TMC-based NPs at N/P ratio of 15 in the presence of complete DMEM medium (with serum and antibiotics). Twenty-four hours later, cells were fixed with 4% PFA, washed three times with PBS and incubated with fluorescent DNA-binding dye DRAQ5™ and imaged on the ImageStream^X system, collecting 10,000 events per sample at 40x magnification. A 488 nm wavelength laser was used to excite DRAQ5™ and the fluorescence images were collected using the 660–740 nm spectral detection channel. Apoptotic cells were identified using two standard image-based features from the IDEAS® software: Area and Spot Small Total. Untreated cells were used as negative control.

2.14. Cell metabolic activity assay

To determine cell viability, a resazurin-based assay was used [23]. After 4 h of incubation at 37°C, 200 µl of medium was transferred to a black-walled 96-well plate (Greiner bio-one) and fluorescence was measured (λ_{exc} = 530 nm, λ_{em} = 590 nm). Cell viability was assessed 72 h after incubation of NPs with cells. Results are expressed as percentage of metabolic activity of treated cells relative to untreated cells.

2.15. Statistical analysis

Statistical analysis was performed using GraphPad Prism 6.0. Results are presented as mean ± standard deviation (SD) of at least three independent experiments. The D'Agostino-Pearson omnibus test was used to confirm the Gaussian distribution of data. Afterwards, one or two-way ANOVA with different post-tests for multiple comparison analysis were used as mentioned in each figure. Results were considered statistically significant when $p<0.05$.

3. Results

3.1. Polymer characterization

In order to investigate the influence of polymer DA on the degradation profile of the TMC-based NPs, the original purified TMC was deacetylated and then re-acetylated. The unmodified CH (starting material for the TMC synthesis) was used as control. The results obtained from the polymer characterization are presented in **Table 1**. As expected, the original TMC polymer presented a DA value similar to the unmodified CH, which was 16%. After TMC chemical modification, a final DA value of 4% was achieved for the deacetylated polymer, whereas for the re-acetylated polymer, a value around 21% was attained.

Table 1. Polymer characteristics in terms of molecular weight, degree of acetylation (DA) and degree of quaternization (DQ).

Polymer	Mn^a ($x10^3$ $g.mol^{-1}$)	Mw^a ($x10^3$ $g.mol^{-1}$)	Mw/Mn^a	DA^b (%)	DQ^b (%)
CH_{16}	37.3 ± 5.9	55.5 ± 7.4	1.49	16.1 ± 0.2	---
TMC_4	---	---	---	3.5 ± 0.2	29.7 ± 3.2
TMC_{16}	43.3 ± 5.0	71.3 ± 8.9	1.65	15.7 ± 0.9	30.1 ± 4.6
TMC_{21}	44.7 ± 9.1	68.9 ± 6.1	1.54	20.6 ± 0.5	32.4 ± 3.9

All polymers were purified and characterized. [a]Average number and average weight molecular weight, as well as the polymer polydispersity index (Mw/Mn) were determined by gel permeation chromatography (n=3 ± standard deviation (SD)). [b]Degree of *N*-acetylation and quaternization were assessed by ^{1}H-NMR (n=3 ± SD) (^{1}H-NMR spectra in Supplementary Figure S3).

The average number molecular weight (Mn) of the purified materials was found to be 43.3 ± 5.5 kDa for TMC_{16} and 37.3 ± 5.9 kDa for CH_{16}. The selection of this Mn was based on previous studies that have shown that chitosan's with an intermediate Mn are better suited for pDNA gene delivery, as chitosan-based polymers with molecular weight ≥ 17 kDa form more compact NPs and better protect pDNA from endonuclease degradation; on the other hand, a Mn value above 50 kDa has shown to hinder the release of pDNA from the polymer matrix [24]. GPC analysis confirmed that the applied reaction conditions for TMC modification did not lead to the hydrolysis of the polymeric chains, as no statistically significant differences were found between the deacetylated and re-acetylated polymer (TMC_{21}) and the original one (TMC_{16}). Endotoxin levels from

the polymer extracts were found to be < 0.1 EU.ml^{-1}, respecting the US Department of Health and Human Services guidelines for implantable devices [25].

3.2. Nanoparticle physicochemical characterization

The physicochemical properties of CH or TMC-based NPs were evaluated in terms of hydrodynamic average size, polydispersity index (PdI), surface charge (zeta potential) and pDNA condensation efficiency. For the as prepared NPs, no significant differences were observed in terms of size, PdI and surface charge (see **Supplementary Table S1**), with all NPs presenting average sizes below 205 nm, low PdI values (< 0.2) and positive surface charges (≥ 15 mV). To mimic cell culture conditions, NP average size, PdI and surface charge were evaluated after a 6-fold dilution in complete DMEM medium (pH 7.4). Under these conditions, all the produced TMC-based NPs remained stable, presenting sizes below 191 nm, independently of the polymer DA (**Table 2**).

Table 2. Physicochemical characterization of CH- and TMC-based nanoparticles.

Polymer	Hydrodynamic size[a] (d.nm)	Polydispersity index[a] (PdI)	Zeta-potential[b] (mV)	pDNA condensation efficiency[c] (%)
CH_{16}	397 ± 67$^{\#\#}$	0.560 ± 0.24$^{\#\#}$	-0.9 ± 1.5$^{\#\#\#}$	45.7 ± 3.7$^{\#\#\#}$
TMC_4	184 ± 30	0.219 ± 0.15	+11.2 ± 2.3	94.9 ± 2.9
TMC_{16}	191 ± 22	0.238 ± 0.04	+10.8 ± 1.2	93.6 ± 0.3
TMC_{21}	188 ± 16	0.221 ± 0.11	+10.1 ± 2.0	90.1 ± 1.2

All NPs were prepared at N/P ratio of 15. Average size, polydispersity index, zeta-potential and pDNA condensation efficiency of CH- and TMC-based NPs. [a]NP average hydrodynamic sizes and PdI were measured by dynamic light scattering; [b]Mean surface charge of NPs based on zeta-potential measurements. Both size and surface charge measurements were performed in complete DMEM medium (with 10% (v/v) FBS), pH 7.4 (n=3 ± SD). [c]Percentage of pDNA condensed into NPs after incubation in complete DMEM medium assessed by SYBR® Gold (n=3 ± SD). Statistical differences are presented as: $^{\#}p<0.05$, $^{\#\#}p<0.01$ and $^{\#\#\#}p<0.001$ for CH_{16} vs other TMC NPs.

On the contrary, CH_{16} NPs presented a significantly higher average hydrodynamic size (~400 nm) and PdI (> 0.5). TMC-based NPs also maintained their positive surface charge with zeta-potential values above 10 mV, whereas CH_{16} NPs surface charge was close to neutrality (-0.9 mV). Moreover, the intensity *versus* size profile obtained before (acetate or HEPES buffer) and after NPs dilution in DMEM medium with serum clearly showed that CH NPs do not present the same colloidal stability as TMC-based NPs in

cell culture conditions (**Figure 1**). In the case of TMC-based NPs, no significant differences were seen in the size profiles before and after NPs dilution in medium with serum (**Figure 1b**). On the contrary, in the case of CH NPs an increase of the maximum intensity peak width and a shift toward increased sizes was seen, with the appearance of a small peaks between 1,000 and 10,000 nm, which indicates the presence of polymer agglomerates (**Figure 1a**).

We next assessed the efficiency of CH_{16} and TMC-based polymers to condense pDNA by incubating the NPs in the presence of a nucleic acid intercalating dye (SYBR® Gold, Invitrogen). To the best of our knowledge, this is the first time that SYBR® Gold is used as a quantitative measurement for the assessment of the NPs ability to condense nucleic acids. The obtained results show that once prepared, all polymers were able to complex approximately 90% of the pDNA (**Supplementary Table S2**). However, after incubation in complete DMEM medium CH_{16} NPs release about half of the initially complexed pDNA. Contrariwise, TMC-based NPs remain stable and maintain all the originally complexed pDNA (**Table 2**).

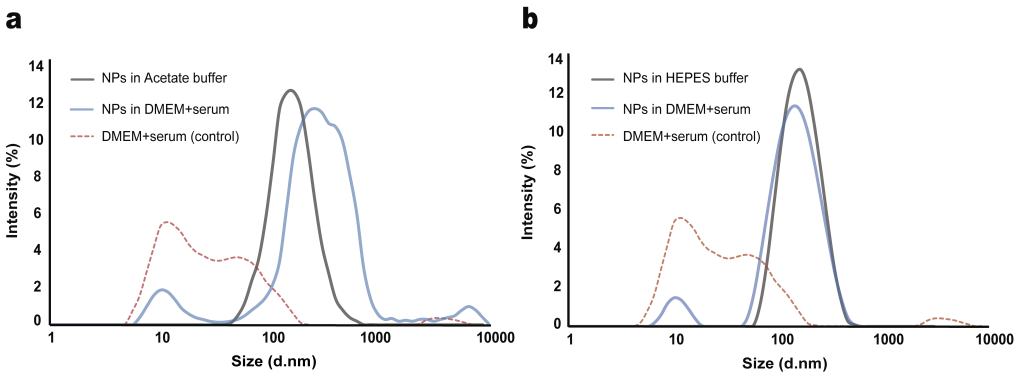

Figure 1. Stability of CH- and TMC-based nanoparticles in different media. Size distribution of (a) CH or (b) TMC NPs in their respective preparation buffer and after dilution (1:6) in complete DMEM medium. The graphic of TMC_4 NPs (b) is representative of all the different TMC NPs tested. The profile of DMEM with serum and no NPs (control) is presented in order to discriminate protein-related aggregates.

3.3. Nanoparticle enzymatic degradation and transfection efficiency

To evaluate the biodegradation of TMC-based NPs, a lysozyme-based assay previously setup by our team was used in which the competition for lysozyme between a fluorogenic substrate (MU-$[GlcNAc]_3$) and the NPs under investigation is explored [9]. First, we compared the biodegradation profile of TMC_{16} and CH_{16} NPs (prepared with

the same polymer mass). As depicted in **Figure 2a**, after incubation of NPs in the presence of MU-$[GlcNAc]_3$ for a 12-hour period, a decrease in the fluorescence intensity is observed for both formulations. At the time point of 2 h, a statistically significant fluorescence reduction is observed in the case of TMC_{16} NPs, however, after this time period no statistical differences were observed between the two polymeric NPs. This data indicates that while TMC_{16} NPs degrade to the same extent as the CH_{16} NPs, the former degrade at a slightly higher rate in the initial hours of reaction, indicating that the complexation of the polymer with the NAs does not alter the biodegradation behaviour of the polymers. Using this model, a significant lower degradation rate (*k*) for CH_{16} NPs was determined, when compared to TMC_{16} NPs. However, the degradation span is similar between both formulations. These results were also corroborated by fitting the data with the exponential decay equation model (**Figure 2c**). Afterwards, we evaluated the influence of polymer DA on TMC-based NP biodegradation. Enzymatic degradation of TMC NPs with different DA was also evaluated for a 12 h incubation period with lysozyme (**Figure 2b**). As previously reported for CH NPs [9], TMC-based NP enzymatic degradation is influenced by the polymer DA. A positive correlation between polymer DA and NP degradation rate as well as degradation span was observed (**Figure 2c**). Among the tested TMC-based polymers, TMC_4 NPs were the ones that degraded at a slower rate and to the lowest extent, while TMC_{21} showed the opposite results. Furthermore, with the time course of the degradation study a plateau value was reached for all formulations. This effect is probably related to the fact that at least 3-4 acetylated units are required in the hexameric binding pocket for lysozyme to allow enzymatic cleavage [26]. Since these domains are destroyed through cleavage of the glycosidic bond [26, 27], degradation by lysozyme occurs till a certain molecular weight depending on the DA of the polymer [28].

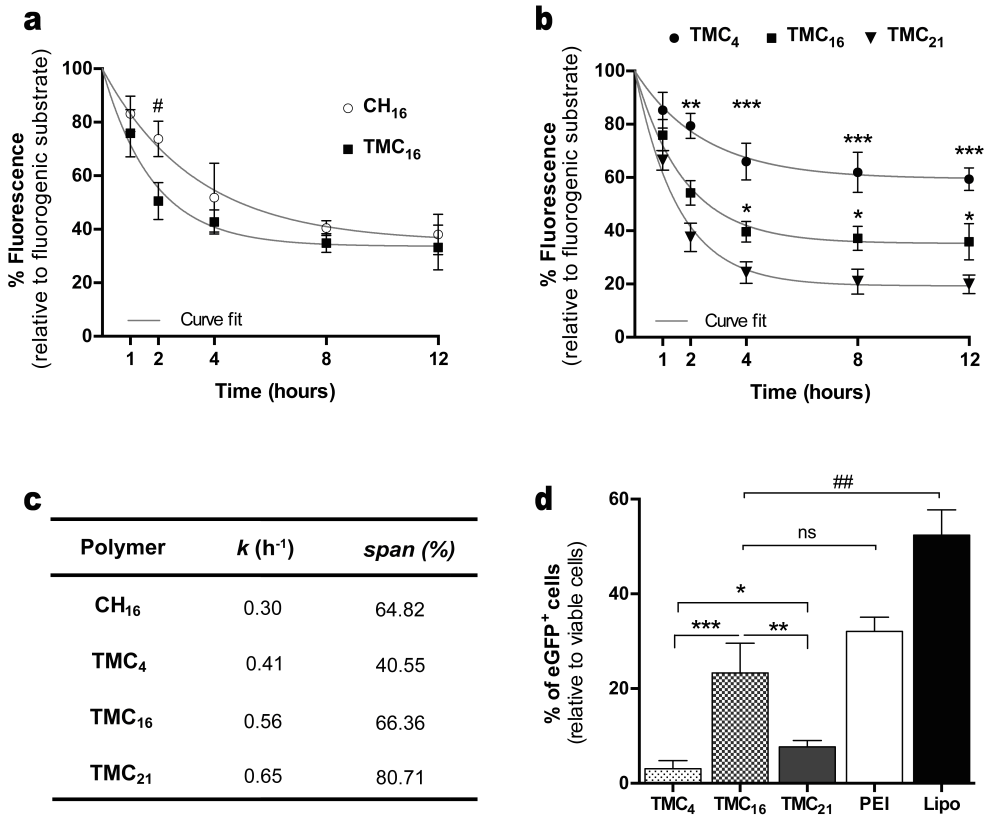

Polymer	*k* (h^{-1})	*span (%)*
CH_{16}	0.30	64.82
TMC_4	0.41	40.55
TMC_{16}	0.56	66.36
TMC_{21}	0.65	80.71

Figure 2. Effect of polymer DA on NPs biodegradation and transfection efficiency. Extent of MU-$[GlcNAc]_3$ hydrolysis after incubation with lysozyme in the presence of (a) CH_{16} or TMC_{16} NPs or (b) TMC-based NPs, for a period of 12 h. The results are expressed as relative fluorescence of the substrate cleavage by lysozyme without the NPs (positive control). A student's t-test was used to determine the statistical difference between CH_{16} and TMC_{16}. Two-way ANOVA analysis of variance with Tukey's post-test was used for comparisons between all TMC-based NPs. Statistical differences are presented as: no symbol $p > 0.05$; $^{\#}p < 0.05$ when comparing CH_{16} to TMC_{16}; $*p < 0.05$ and $**p < 0.01$, $***p < 0.001$ when comparing TMC_{16} and TMC_4 with TMC_{21} NPs, respectively. (c) Table with the degradation rate (k) and degradation span (% of fluorescence) of all NP formulations, obtained through the fitting of the degradation data with the one phase decay equation model (grey line in a and b). (d) The transfection efficiency of TMC- based NPs was evaluated 72 h post-transfection. The percentage of cells expressing eGFP was assessed by flow cytometry. Poly(ethylene imine) (PEI) and Lipofectamine® 2000 (Lipo) were used as positive controls. Each bar represents the mean of four independent experiments ± SD. One-way ANOVA analysis of variance with Tukey's post-test was used for comparisons between conditions. Statistical differences are presented as: $*p<0.05$, $**p<0.01$ and $***p<0.001$ for comparisons between TMC-based NPs; ns = $p>0.05$ and $^{\#\#}p<0.01$ when comparing TMC_{16} with PEI or Lipo, respectively.

Unlike other polymeric vectors that have endosomal buffering capacity and act as proton sponges, in the case of chitosan-based vectors their buffering capacity is limited and their degradation products (oligo- and monosaccharides) are the entities responsible for the increase in osmolarity, which results in water influx and subsequent

swelling and rupture of vesicular membranes [29, 30]. Since chitosan degradation strongly influences the ability of chitosan-based vectors to release pDNA, we next evaluated the impact of TMC-based NPs degradation rate on their biological performance as gene transfer vectors (**Figure 2d**). Among TMC polymers, TMC_{16} presented a statistically significant higher percentage of transfected cells (**Figure 2d**). TMC_4 and TMC_{21} showed to be less efficient, transfecting only 3% and 8% of cells, respectively. The transfection activity was also determined as the eGFP fluorescence level fold increase relative to untreated cells (**Supplementary Figure S4**). Similarly, the TMC_{16} NP formulation was the one to mediate the highest eGFP expression. Poly(ethylene imine) (PEI) with 25 kDa (Sigma-Aldrich) and Lipofectamine® 2000 (ThermoFisher Scientific), both well-known and widely used commercial available transfecting agents, were used as positive controls (**Figure 2d**). We did not observe any significant differences when comparing the transfection efficiency of TMC_{16} with PEI (both polymeric NPs). On the contrary, the use of Lipofectamine® 2000 resulted in a ~1.5 fold change in the percentage of transfected cells, when comparing to TMC_{16} NPs. Nonetheless, the use of this lipid-based commercial agent resulted in a statistically significant increase in cellular toxicity (**Supplementary Figure S5**). The percentage of ND7/23 cells transfected using naked pDNA (without any vector) was virtually zero, presenting similar values to those of the negative control (untreated cells).

3.4. Nanoparticle internalization profile and kinetics

To understand the extent of the impact of biodegradation on transfection efficiency we further proceeded with the study of the intracellular trafficking pathway of the developed NPs. By using imaging flow cytometry instead of conventional flow cytometry, we aimed at gaining quantitative information on the number of cells with internalized NPs as a function of time, as well as on the NA cargo present in each cell treated with different NP formulations. For this purpose, pDNA was fluorescently labeled with YOYO®-1 (Invitrogen). For the distinction between the percentage of cells with internalized NPs (cytoplasm) *versus* the ones that were YOYO®-1 positive (cytoplasm and membrane-associated NPs), a mask representing the whole cell was defined by the bright-field image, and an internal mask was set by eroding the whole cell mask by 5 pixels (2.5

μm) in order to eliminate the fluorescent signal resulting from membrane-associated NPs (**Figure 3a**).

The results from the uptake studies (**Figure 3b**) showed considerable differences between CH- and TMC-based NPs. Moreover, it showed significantly differences between the percentage of YOYO®-1 positive cells (white bars) and the percentage of cells with internalized pDNA (patterned bars) for all formulations. In the case of TMC-based NPs, as early as 0.5 h after NP incubation, more than 80% of cells were positive for YOYO®-1, a value that kept unaltered with time.

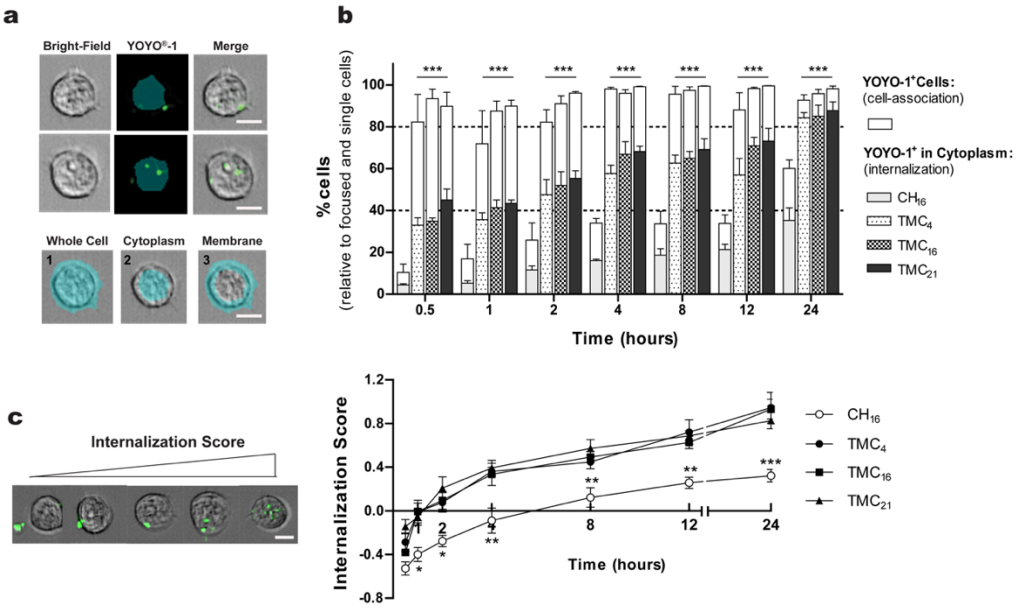

Figure 3. Evaluation of nanoparticle internalization kinetics. (a) Examples of images captured by ImageStream^X in bright-field, YOYO®-1 (green) and their overlays (scale bars: 10 μm). Masks (cyan blue) were created to fit the whole cell (1), cell cytoplasm (2) and membrane (3 = 1–2). YOYO®-1 images are represented with the cell cytoplasm mask, to distinguish internalized versus membrane associated NPs. (b) Percentage of ND7/23 cells positive for YOYO®-1 after incubation with CH or TMC-based NPs from 0.5 to 24 h. The difference between cells with associated NPs (white bars) and cells that had internalized NPs (patterned bars) is shown. (c) The internalization score (IS) – ratio between the fluorescence intensity inside cell to the fluorescence intensity of the entire cell – was also evaluated from 0.5 to 24 h, as a function of NPs internalization kinetics. Representative images of cells with NPs (green) in the extra- or intracellular compartment (scale bar: 10 lm). All data was acquired from at least three independent experiments ± SD. Two-way ANOVA analysis of variance with Bonferroni's post-test was used for comparisons between polymers. Statistical differences are presented as: no symbol $p > 0.05$; *$p<0.05$, **$p<0.01$ and ***$p<0.001$.

However, by discriminating the cells with labelled pDNA in the cell cytoplasm, one can find that the amount of pDNA internalized steadily increased over time. At 0.5 h, already

40% of cells internalized NPs, a value that significantly increased to more than 80% after 24 h of contact. The similar internalization behaviour observed among TMC NPs is not unexpected since no significant differences were observed in terms of size or surface charge between NP formulations. The internalization process of CH-based NPs was found to be less efficient. Independently of the time point, the percentage of YOYO®-1 positive cells was lower and, even after a 24 h incubation the total amount of cells which effectively internalized pDNA was only 35% of the total cell population. This behaviour can possibly be ascribed to differences on NP net charge. At physiological pH, CH NPs present a charge close to neutrality (**Table 2**), which may hamper the process of NP cell association and internalization. Moreover, these NPs presented higher average sizes and lower colloidal stability in relation to the TMC-based NPs, which might also negatively influence the internalization process.

The internalization score (IS), defined as the ratio of fluorescence intensity inside the cell to the total fluorescence intensity of the cell [31], was also calculated. A positive value of IS corresponds to a cell with mostly internalized NPs, whereas a negative IS value corresponds to a cell with mostly membrane-associated NPs. The mean values of IS for CH and TMC-based NPs along the 24 h internalization study are presented in **Figure 3c**. From 1 h of incubation onwards, statistically significant different IS values were found for CH_{16} and TMC-based NPs. In the case of CH_{16} NPs, only after 8 h of incubation with cells was reached a positive IS value, while cells treated with TMC-based NPs present positive IS values after 2 h of contact. No significant differences were observed among the TMC-based NPs tested, indicating that the polymer DA did not altered the kinetics of the internalization process.

Overall these results further corroborate that CH NPs are not as efficiently internalized by the cells as TMC NPs, indicating that CH_{16} NPs are not only internalized by a lower number of cells but also at a lower rate.

3.5. Cellular distribution of nanoparticle-loaded vesicles

An additional advantage of using imaging flow cytometry is the possibility to quantify the number of nanoparticle-containing vesicles per cell, as well as to localize molecules of interest in intracellular compartments or its vicinity. Although imaging flow cytometry lacks resolution for single NP identification, it enables the detection of NP clusters within individual vesicles (endosomes or lysosomes) inside the cell, the so-called

nanoparticle-loaded vesicles (NLV) [32]. Masking of the cell images allowed cluster identification (representative images in **Figure 4a**) and transformation of the intensity histograms to NLV count distributions (**Figure 4b**). By following this parameter as a function of time, we were able to gain further insights on NP distribution and intracellular trafficking after internalization.

Three groups with low (**Figure 4c**), medium (**Figure 4d**) or high (**Figure 4e**) number of NLV were gated among the cells that internalized NPs. The obtained results reveal that for TMC NPs, already after 1 h of incubation, a high percentage of cells (> 40%) had a high number of NLV (> 11 per cell) (**Figure 4e**). Contrariwise, in the case of CH NPs, the percentage of cells with high NLV was significantly lower (~ 2-fold). Moreover, while in the case of TMC NPs the percentage of cells with high number of NLV is decreasing with time, suggesting that these NPs are being released from the vesicles where they are entrapped, in the case of CH this percentage is increasing along the 24 h study.

Regarding the TMC-based NPs, it was observed an increase in the percentage of cells with low number of NLV and a decrease in the percentage of cells with high number of NLV. However, the observed variations were different among TMC polymers (**Figure 4f**). The percentage of cells with medium number of NLV increased in the case of TMC_4 and TMC_{21} NPs, whereas for TMC_{16} NPs it remains constant. After 24 h, more than 50% of cells incubated with TMC_{16} NPs presented a low number (< 4) of NLV, whereas for the other formulations the majority of cells had between 5 and 10 NLV per cell. These results suggest that TMC_{16} NPs are somehow being more efficiently released from the endolysosomal compartment, which may explain their higher transfection efficiency. To further confirm this hypothesis and infer about the amount of NPs localized in endo- or lysosomes, a transfection assay in the presence of chroloquine (CQ), a well-known disruptor of the endolysosomal vesicles, was performed (**Supplementary Figure S6**).

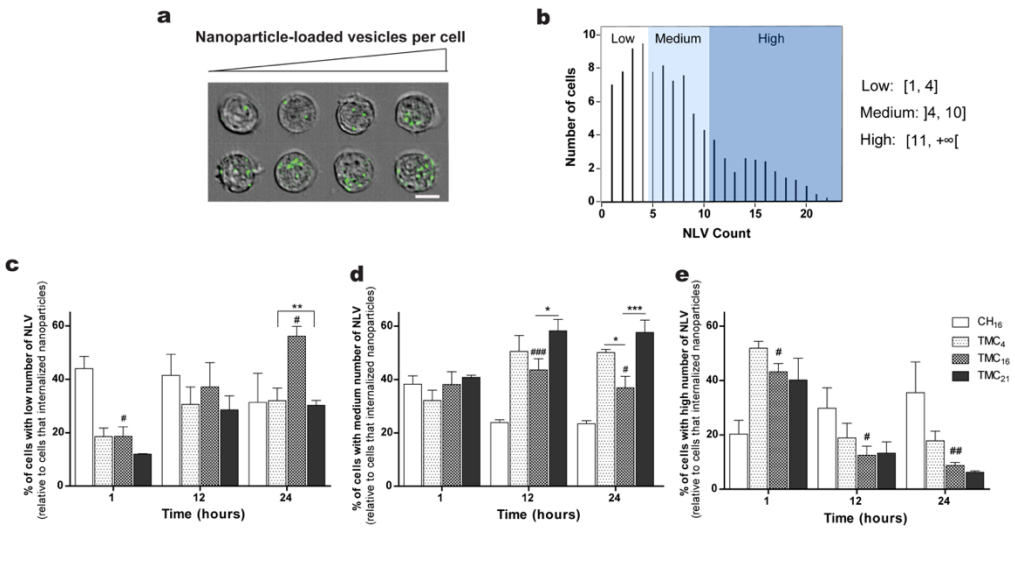

f

Evolution of the number of NLV per cell throughout the 24 h study				
	CH_{16}	TMC_4	TMC_{16}	TMC_{21}
Low	↓ 0.7	↑ 1.7	↑↑ 3.0	↑↑ 2.5
Medium	↓ 0.6	↑ 1.6	— 1.0	↑ 1.4
High	↑ 1.8	↓↓ 0.4	↓↓ 0.2	↓↓ 0.2

Figure 4. Quantification of the number of nanoparticle-loaded vesicles (NLV) per cell as a function of time of incubation. (a) Example of cells acquired from imaging flow cytometry (bright-field) with increasing number of NLV (YOYO®-1 – green; scale bar: 10 µm). (b) Histogram of NLV frequency obtained from IDEAS® software analysis with the gated regions of interest. The percentage of cells that internalized NPs with low (c), medium (d), and high (e) number of NLV were considered. (f) Table summarizing the distribution of the number of NLV per cell depending on the NPs tested along the 24 h. The fold-increase or decrease along the study (value from 24 h/value from 1 h) is shown. Each bar represents the mean of at least three independent experiments ± SD. Two-way ANOVA analysis of variance with Bonferroni's post-test was used for comparisons between polymers. Statistical differences are present as: no symbol $p>0.05$, *$p<0.05$, **$p<0.01$ and ***$p<0.001$, when comparing TMC_{16} to other TMC polymers; $^{\#}p<0.05$, $^{\#\#}p<0.01$ and $^{\#\#\#}p<0.001$ when comparing TMC_{16} with CH_{16}.

After NPs incubation with cells for 20 h, CQ was added in a final concentration of 100 µM for a total period of 4 h. The obtained results confirm that both TMC_4 and TMC_{21} NP formulations end up entrapped in the endocytic compartment, as their incubation in the presence of CQ resulted in a ~5-fold increase in their cell transfection efficiency. TMC_{16} NPs also suffered from an increase in transfection efficiency after CQ incubation, although this increment was only of 1.8-fold. Moreover, no significant differences were found in the transfection efficiency of TMC_{16} *versus* TMC_{21} NPs after incubation with CQ, which clearly indicates that the previous observed differences arise from TMC_{21} less effective escape from the endolysosomal pathway. This difference

may result from the different degradation rates of the developed NPs, being an intermediate rate of degradation necessary for an increased protection of pDNA during the endolysossomal pathway and/or a more efficient escape of the NPs from the endocytic vesicles.

To validate the assumption that the NPs under study are trafficked through the endolysosomal compartment, transmission electron microscopy of the cells incubated for 4 h with TMC-based NPs was performed (**Supplementary Figure S7**).

3.6. Nanoparticle-loaded vesicles localization in the nuclear vicinity

The percentage of cells with NLV in the vicinity of the cell nucleus was determined from 0.5 to 24 h incubation with NP formulations prepared with YOYO®-1 labelled pDNA and subsequent staining of cell nuclei with DRAQ5™ (**Figure 5a**). The similarity feature of the IDEAS® software was applied in the quantification of the extent of pDNA nuclear translocation. This allows the quantification of the correlation between two spectrally distinct images of a single cell and is derived from the Pearson's correlation coefficient of the pixels' intensities of the image pair [22]. The similarity score was calculated for cells both positive for YOYO®-1 and DRAQ5™ (**Figure 5b**). The positive region on YOYO®-1/DRAQ5™ similarity histograms represents the region of images that correlate positively (**Figure 5c**). Using this analytical approach, we were able to assess the variations regarding the localization in the nuclear vicinity of the NPs under study. Over the 24 h study, one observed for all tested NPs a steady increase in the number of cells with NLV localized in the perinuclear region (data not shown), supporting the described movement of the endocytic vesicles towards the microtubule-organizing centre close to the cell nucleus [33]. After 24 h of incubation, cells treated with CH_{16} NPs presented the lower extent of NLV in the nuclear vicinity (**Figure 5d**). Since at this time point around 35% of cells that internalized CH_{16} NPs have a high number of NLV, these results indicate that only one third of these NLV are being transported to the nuclear vicinity. The remaining NLV could be either in the transport pathway towards the nuclei vicinity or being recycled to the cell membrane [34]. In the case of TMC-based NPs, the data indicates that NLV localization in the nuclear region was maximum for the TMC_{16} NPs, more than 30% of internalized pDNA being in the nuclear vicinity, although no significant differences were found between the polymers with the highest DA (TMC_{16} and TMC_{21}).

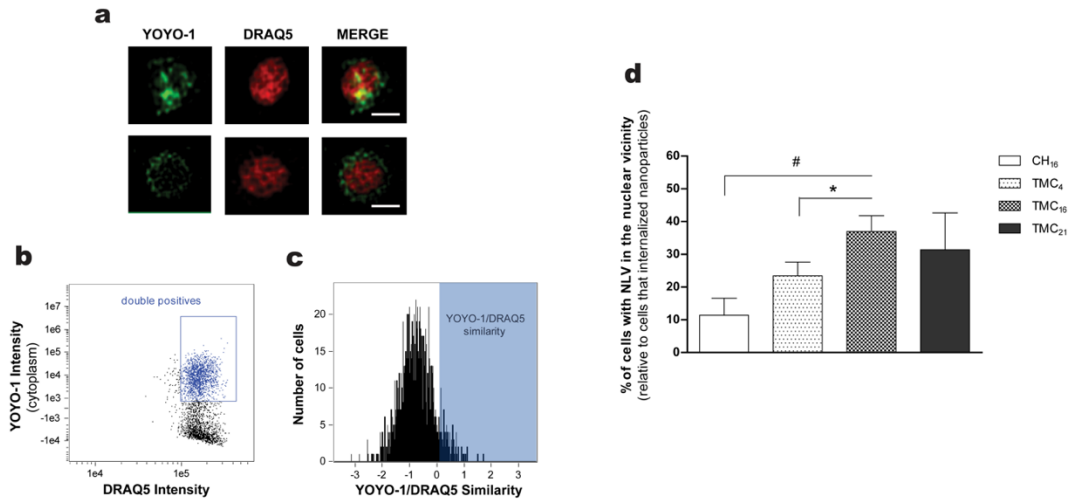

Figure 5. Determination of the percentage of cells with nanoparticle-loaded vesicles (NLV) present in the nuclear vicinity. (a) Representative images acquired by imaging flow cytometry. The fluorescence images collected using the 480–560 nm (YOYO®-1 – green) and 660–740 nm (DRAQ5™ – red) spectral detection channels and their composite images are showed (scale bars: 10 μm). (b) Cells positive for both fluorescent dyes were selected; (c) Histogram of frequency of the similarity feature from IDEAS® software. Cells with similar YOYO®-1/DRAQ5™ image pairs were gated; (d) Percentage of cells with NLV localized in the nuclear vicinity 24 h post-incubation with CH or TMC-based NPs. Each bar represents the mean of at least three independent experiments ± SD. Two-way ANOVA analysis of variance with Bonferroni's post-test was used for comparisons between polymers. Statistical differences are present as: no symbol $p>0.05$, *$p<0.05$, when comparing TMC_{16} to other TMC polymers; #$p<0.05$ when comparing TMC_{16} with CH_{16}.

Bishop and co-workers have also reported an approximately percentage of pDNA nuclear association between 10 and 40, depending on the amount of time that the cells (gliobastoma cells derived from human primary brain cancer) were exposed to the NPs [35]. Also, the NLV quantification in the nuclear vicinity corroborate the transfection efficiency data, since the NPs that mediate the arrival of higher amount of NA to the nuclear vicinity are also the most efficient to transfect cells.

3.7. Nanoparticle cytotoxicity

Another important consideration to take into account when designing a non-viral gene delivery vector concerns their safety profile. Taking advantage of the nuclear labelling with DRAQ5™, we were also able to evaluate cell apoptosis 24 h post-incubation with the NPs by imaging flow cytometry (**Figure 6**). A consistent distinguishing feature of the apoptotic process is nuclear condensation and DNA fragmentation. Apoptotic nuclei stained with fluorescent DNA intercalating dyes typically produce small, fragmented,

highly textured nuclear images (**Figure 6a**). Because of this characteristic morphology, apoptotic nuclei are ideally suited for analysis with this technique [36, 37].

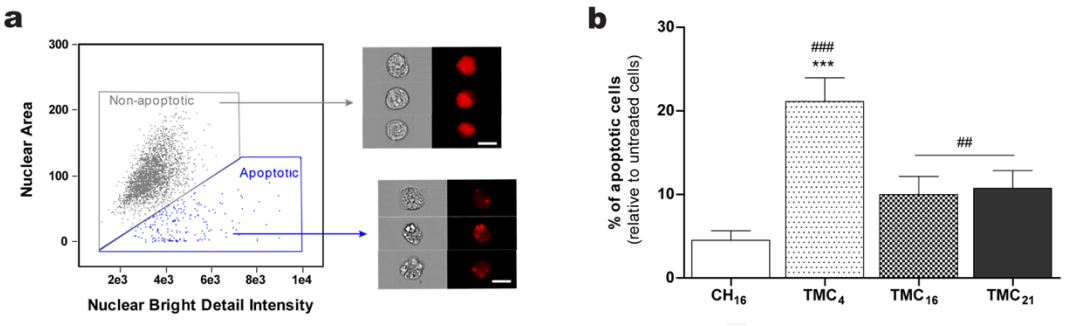

Figure 6. ND7/23 cell apoptosis upon incubation with CH- or TMC-based nanoparticles. (a) Gated regions of non-apoptotic and apoptotic cells and their representative images: bright-field and nuclear region (DRAQ5^{TM} fluorescent red) (scale bars: 10 μm); (b) Percentage of apoptotic cells relative to negative control (untreated cells) after 24 h incubation with CH- or TMC-based nanoparticles. Each bar represents the mean of three independent experiments ± SD. One-way ANOVA analysis of variance with Bonferronis's Multiple Comparison post-test. Statistical differences are present as: no symbol $p>0.05$; ***$p<0.001$ when comparing to other TMC NPs; $^{\#\#}p<0.01$ and $^{\#\#\#}p<0.01$ when comparing to CH_{16} NPs.

CH_{16} NPs had a negligible effect on cell apoptosis (no statistical differences were observed in relation to untreated cells). For the cells treated with the TMC-based NPs, a significant increase in cell apoptosis was observed, TMC_4 NPs being the ones causing the highest detrimental effect, although it only affected approximately 20% of cells (**Figure 6b**).

The results from imaging flow cytometry are in accordance with the data obtained from the cytotoxic evaluation based on the determination of metabolic activity by a resazurin-based method (**Supplementary Figure S5**). The metabolic activity of the cells was measured 72 h after transfection and the most detrimental effect corresponded to a 29% decrease in cell viability for cells treated with TMC_4 NPs. This effect may be a consequence of the higher amount of positively charged moieties present in this polymer or due to an increased NP accumulation inside the cells, since these NPs have also the lowest biodegradation capacity.

4. Discussion

The presented data disclose important information regarding how NP extracellular and intracellular stability impacts the overall transfection process. When it comes to the design of non-viral gene delivery vehicles, a high number of extra- and intracellular obstacles must be overcome, and therefore it is particularly important to coordinate various functionalities of the polymeric vehicles in order to enhance their transfection efficiency. In a recent study, Bishop *et al* have described cellular uptake as the limiting barrier for efficient non-viral vectors gene delivery [35], and therefore the formation of stable and small sized NPs is imperative to assure pDNA protection and colloidal stability in the extracellular environment and allow an efficient cellular binding and uptake [38]. The results obtained in this study support previous findings showing that TMC-based NPs present higher stability and pDNA condensation capacity at physiological conditions, compared to CH NPs [39], both important factors for the multistep process of gene transfection.

Nonetheless, these parameters are not sufficient to meet all the premises necessary for the design of efficient gene delivery vectors. One of the most important requirements for gene transfer consists in the arrival of therapeutically relevant amount of intact pDNA to the nucleus of a target cell. If NP release from NLV and subsequent pDNA unpacking occurs too slowly or are impaired, the latter will not be accessible to the transcriptional machinery and will eventually be lost or diluted in processes like exocytosis or mitosis. On the contrary, if release occurs too promptly, or if the polyplex is not stable enough to resist endonuclease access, the pDNA will became susceptible to degradation prior reaching its final cellular target [35, 40]. Therefore, an ideal vector would provide total protection of complexed pDNA from degradation prior to releasing it efficiently near or within the nucleus of a target cell. On the other hand, many of the polymeric features that contribute to pDNA protection also hamper its release once NPs are inside the cell, the polymer ability to protect and efficiently release pDNA being inversely related. Various strategies have been tried to design vectors able to trigger pDNA release at the right time and space but, to the best of our knowledge, little attention has been paid to the contribution of vector degradation to this process. From our point of view, pDNA availability is highly dependent on NPs disassemble and, consequently, polymer degradation. TMC biodegradation has been described in solution by Verheul and co-workers [41], who found that TMC degradation by lysozyme

is also positively correlated with the polymer DA. However, to the best of our knowledge, the biodegradation of a TMC-based nanoparticulate system was never assessed before. In fact, the extrapolation to NP biodegradation is not straightforward, since when the polymer is complexed with nucleic acids the exposure of acetylated groups may not favour/allow the degradation mediated by enzymes. To address this question, we altered the biodegradation rate of the TMC NPs by deacetylation and re-acetylation of the polymer, giving rise to NPs with different enzymatic degradation profiles, while not affecting the NP size, charge or ability to protect pDNA. This proved to have an impact on the intracellular dynamics, which resulted in a significantly different transfection ability of the proposed NPs.

Taken together, these results suggest that biodegradation is a key feature for the overall transfection process and that a polymer with an intermediate DA is necessary to assure a compromise between NP stability and NA release intracellularly. These data are in accordance with previous reports that state that chitosan-based polyplexes with an optimal pDNA binding strength allow for efficient intracellular unpacking. On the contrary, excessively stable polyplexes release pDNA more slowly and less efficiently resulting in decreased levels of transgene expression [42]. To understand the extent of the impact on transfection efficiency of the polymer DA variations and, consequently, biodegradation, we further proceeded with the study of the intracellular trafficking pathway of the developed NPs. By using imaging flow cytometry instead of conventional flow cytometry we aimed at gaining quantitative information on the number of cells with internalized NPs as a function of time, as well as on the NA cargo present in each cell treated with different NP formulations. Furthermore, with the use of a single technique, we were able to assess *in vitro* the major parameters necessary for an efficient gene delivery system, from cellular uptake to pDNA transport towards nuclear vicinity, including vector toxicity. This technique was found to be a great tool for the initial steps of vector design and optimization. Moreover, due to its high-throughput nature, it allowed to accurately disclose otherwise imperceptible differences between formulations. To the best of our knowledge, this was the first time that imaging flow cytometry was used to infer about NP trafficking through the endocytic pathway, by means of the quantification of the NLV per cell, without the use of additional intracellular markers. The quantification of the percentage of cells with DNA in the nuclear vicinity by imaging flow cytometry was also a novel experimental approach explored by us.

5. Conclusions

In sum, our work provides novel information about the importance of vector degradation rate for gene delivery into cells as a way to tune gene expression in function of the desired application, and advances novel approaches to optimize nanoparticle formulation.

Taking advantage of imaging flow cytometry, a high- throughput technique with unique features that combines the statistical strength of flow cytometry with image acquisition of every event, we were able to unravel some critical aspects for NP formulation and contribute to the design of more efficient nucleic acid delivery vectors.

Ultimately, the development of an efficient non-viral gene delivery vector will depend on the combination of intelligent material design with innovative imaging techniques, which would facilitate the rational design of these formulations.

Acknowledgements

The work was financed by Portuguese funds through FCT (Fundação para a Ciência e a Tecnologia) in the framework of the projects UID/BIM/04293/2013, PTDC/CTM-NAN/115124/2009 and PTDC/CTM-NAN/3547/2014. CP Gomes, CDF Lopes and PMD Moreno acknowledge FCT for their scholarships (SFRH/BD/ 79930/2011, SFRH/BD/77933/2011 and SFRH/BPD/108738/2015, respectively). Authors acknowledge the Bioimaging Center for Biomaterials and Regenerative Therapies of INEB (b.IMAGE) for the support with Imaging Flow Cytometry and the Biointerfaces and Nanotechnology Service (INEB-i3S) for size and zeta potential analysis.

Supplementary Information

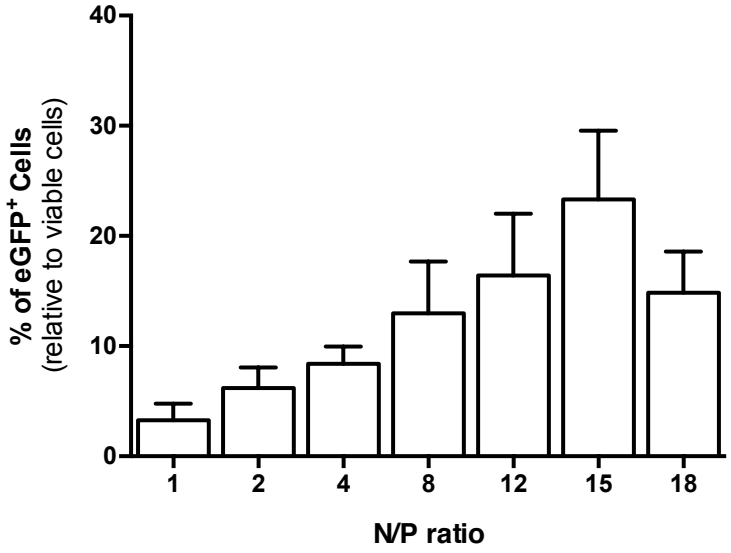

Figure S1. Transfection efficiency of TMC_{16} nanoparticles assessed in ND7/23 cells. The transfection efficiency of TMC_{16} NPs prepared at N/P ratios ranging from 1 to 18 was evaluated 72 h post-transfection. The percentage of viable cells expressing eGFP was assessed by flow cytometry. Each bar represents the mean of three independent experiments ± SD.

Table S1. CH- and TMC-based nanoparticles average size, polydispersity index and zeta potential after preparation.

Polymer	Hydrodynamic size[a] (d.nm)	Polydispersity index (PdI)[a]	Zeta potential[a] (mV)
CH_{16}	206 ± 12	0.219 ± 0.03	+19.6 ± 3.2
TMC_4	187 ± 22	0.210 ± 0.05	+15.1 ± 4.2
TMC_{16}	189 ± 29	0.187 ± 0.02	+20.7 ± 2.2
TMC_{21}	196 ± 21	0.193 ± 0.06	+17.5 ± 0.5

All NPs were prepared at N/P ratio of 15. [a]Nanoparticle average hydrodynamic sizes, PdI and mean zeta potential based on dynamic light scattering measurements were performed after NPs preparation in 5 mM acetate buffer, pH 5.5 (CH NPs) or 20 mM HEPES buffered solution with 5% (w/v) glucose, pH 7.4 (TMC NPs) (n=3 ± SD). No statistical differences were found between all tested NPs.

a

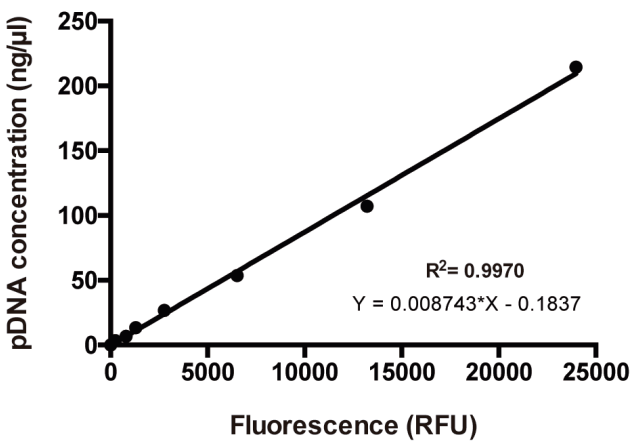

b

DNA Standard Curve		
pDNA (ng.µl^{-1})	RFU	RFU without blank
0	111	0
3.35	348	237
6.7	909	798
13.4	1409	1298
26.8	2888	2777
53.6	6638	6527
107.2	13326	13215
214.4	24090	23979

Figure S2. Plasmid DNA quantification by means of a SYBR® Gold based assay. (A) Representative plasmid DNA (pDNA) standard curve obtained after pDNA consecutive dilutions. The line obtained through linear regression of the data is represented in the graphic in black, as well as the R square and the linear equation. (B) Table with the spectroscopy data obtained after incubating pDNA with SYBR® Gold for 10 min and measuring the emitted fluorescence. RFU = Relative fluorescence units.

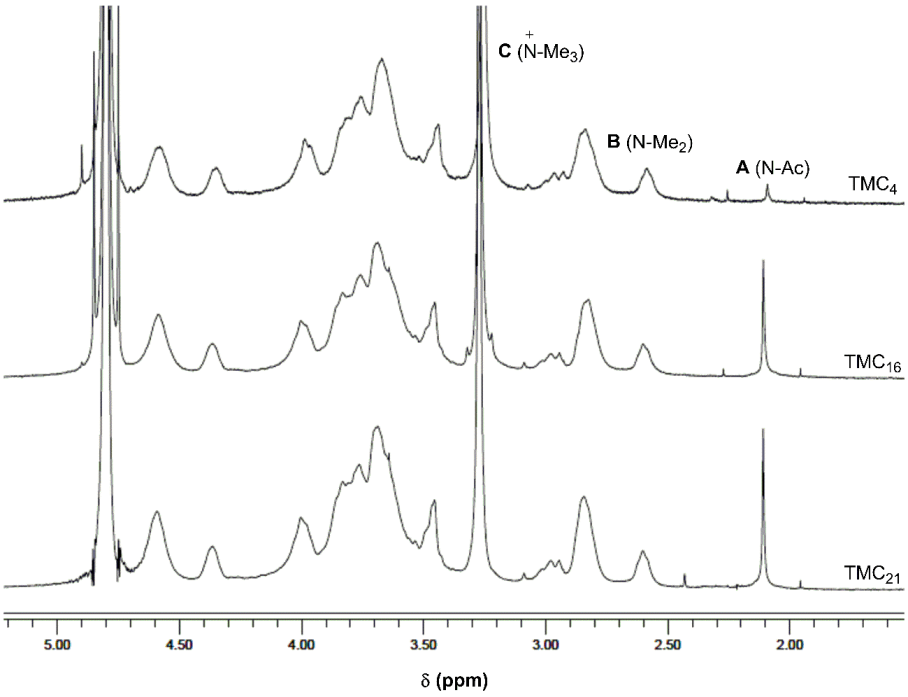

Figure S3. ^{1}H-NMR spectra of the original (TMC_{16}), deacetylated (TMC_4) and re-acetylated (TMC_{21}) trimethyl chitosans (400 MHz, in D_2O). Signal A corresponds to the acetyl group (N-Ac) of TMC. The degree of acetylation (DA) for TMC polymers was determined by integration of appropriate signals: A (N-Ac), B (N-Me_2) and C (N-Me_3) in the ^{1}H-NMR spectra, and calculated following the equation reported by Curti and Campana-Filho (S. P. J Macromol Sci Pure 2006**,** A43, (3), 555-572).

Table S2. Nanoparticle pDNA condensation efficiency.

Polymer code	pDNA condensation efficiency[a] (%)
CH_{16}	92.5 ± 6.7
TMC_4	87.3 ± 8.9
TMC_{16}	91.6 ± 2.3
TMC_{21}	89.1 ± 4.8

[a]All NPs were prepared at N/P ratio of 15. The percentage of pDNA condensed into NPs was assessed by SYBR® Gold after NP preparation and incubation for 10 min in 5 mM acetate buffer, pH 5.5 (for CH NPs) or 20 mM HEPES buffered solution with 5% (w/v) glucose, pH 7.4 (for TMC NPs) (n=3 ± SD). No statistical differences were found between all tested NPs.

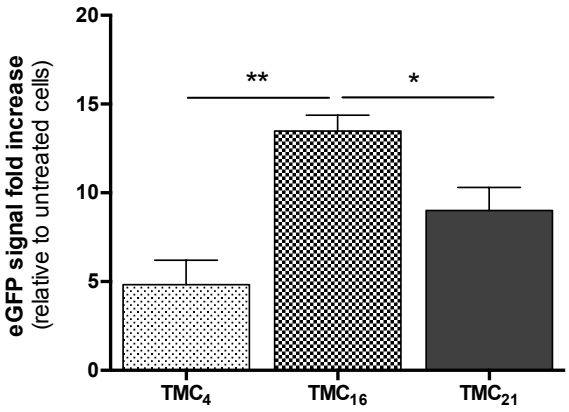

Figure S4. Effect of polymer DA on eGFP fluorescent levels after ND7/23 cells transfection with TMC-based nanoparticles. Fluorescent levels of eGFP were analyzed 72 h post-incubation of cells with TMC-based NPs. Untreated cells were used as control. eGFP fluorescence levels were evaluated in the FL1 channel and a total of twenty thousand gated events were collected. The results are expressed as eGFP signal fold increase, following the ratio: (eGFP geometric mean of treated cells – eGFP geometric mean of untreated cells)/eGFP geometric mean of untreated cells. Each bar represents the mean ± SD of four independent experiments. One-way ANOVA analysis of variance with Bonferroni's post-test was used for comparisons between polymers. Statistical differences are presented as: no symbol p>0.05, *p<0.05 and **p<0.01.

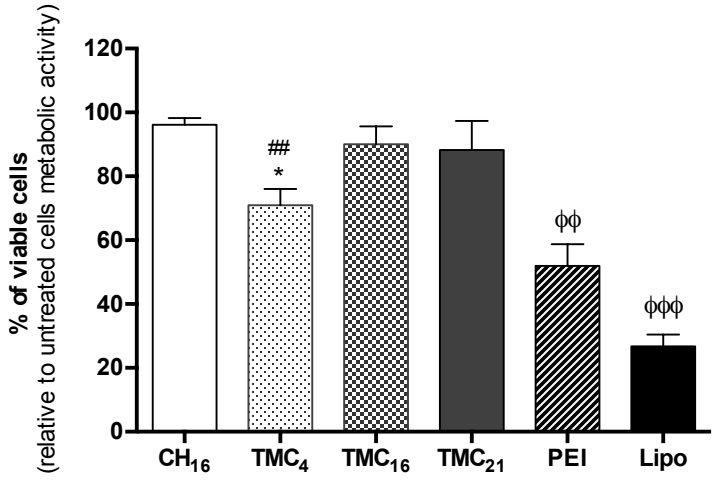

Figure S5. Cellular cytotoxicity upon incubation with CH_{16} or TMC-based nanoparticles. Cellular viability was assessed 72 h after ND7/23 cells incubation with NPs by the resazurin reduction method. Results are expressed as percentage relative to untreated cells. Each bar represents the mean of three independent experiments ± SD. One-way ANOVA analysis of variance with Bonferronis's Multiple Comparison post-test was performed. Statistical differences are present as: no symbol p>0.05; *p < 0.05 when comparing to other TMC NPs; $^{\#\#}$p<0.01 when comparing to CH_{16} NPs; $^{\phi\phi}$p<0.01 and $^{\phi\phi\phi}$p<0.001 when comparing PEI and Lipo with TMC_{16}, respectively.

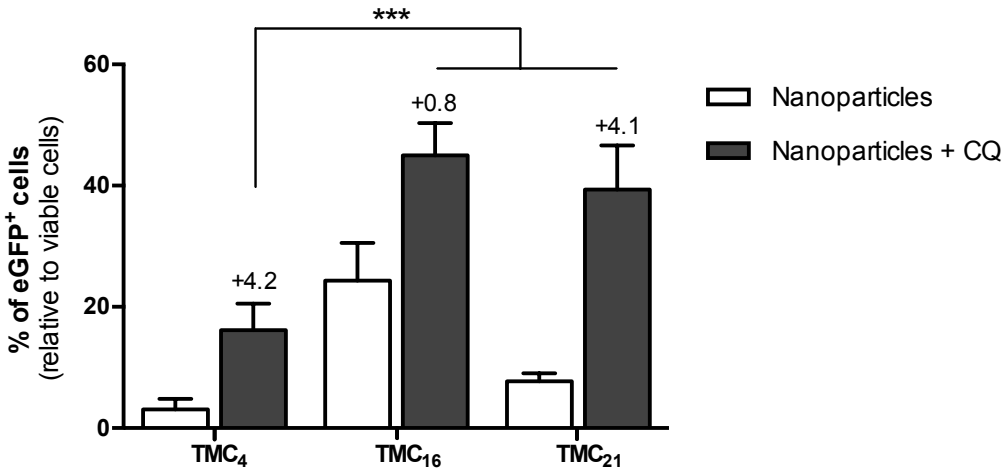

Figure S6. Comparison between transfection efficiency of TMC-based NPs assessed in ND7 cells untreated or treated with chloroquine. Chloroquine (CQ) was added at a final concentration of 100 μM to cells after a 20-hour period of incubation with NPs. After 4 hours, cell medium was exchanged with fresh one. Cells were further incubated for an additional 48-hour period, before being processed for flow cytometry. Results from cell transfection in the presence (black bars) or absence (white bars) of chloroquine are shown. Each bar represents the mean of at least three independent experiments ± SD. The positive effect of CQ in the transfection efficiency of the respective NPs is indicated by the fold change in the number of transfected cells above each bar. Two-way ANOVA analysis of variance with Tukey's multiple comparison post-test was performed. Statistical differences between cells incubated with NPs and CQ (black bars) are presented as: no symbol $p>0.05$, ***$p<0.001$.

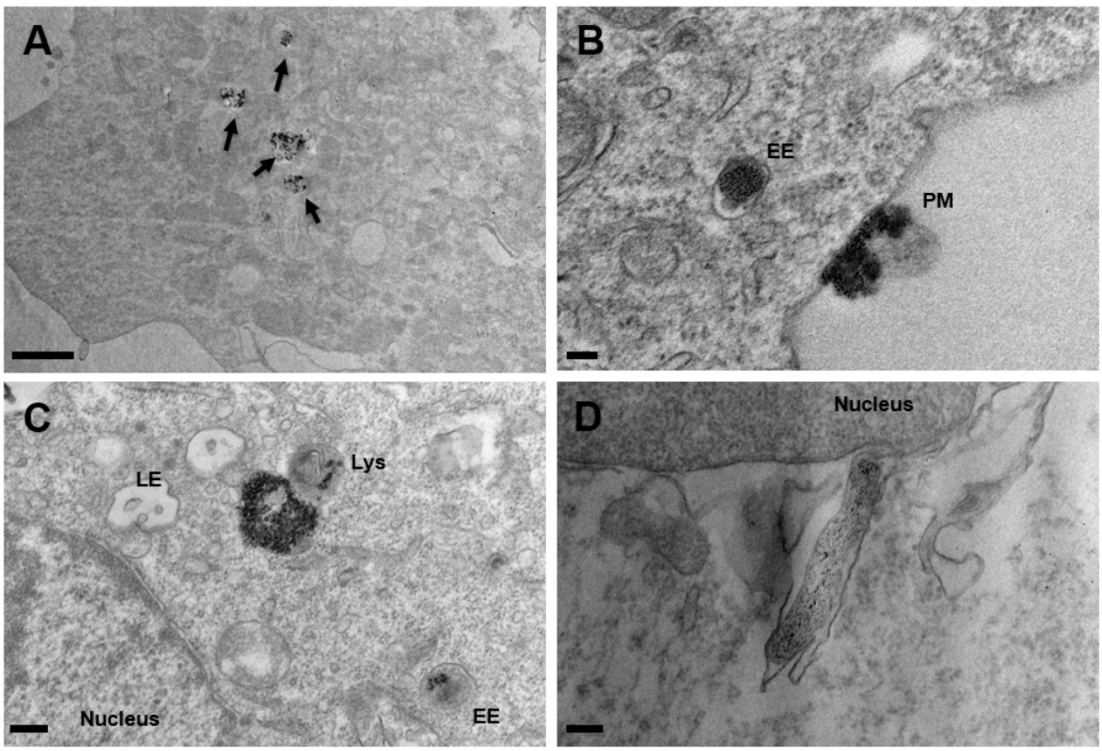

Figure S7. Ultrastructural analysis of TMC_{16} NPs intracellular trafficking assessed by transmission electron microscopy. Electron micrographs of ND7/23 cells incubated with TMC_{16}-QDs/pDNA-gold labelled NPs for 4 h confirm the internalization of NPs via the endocytic pathway, mainly in the form of intracellular clusters within vesicles. (a) ND7/23 cells fixed and imaged without contrast agent to avoid artifacts (control). Arrows indicate the presence of the labeled NPs in endocytic organelles. (b-d) After incubation with NPs, ND7/23 cells were fixed and treated with contrast agent to enhance cell intracellular features. The labeled NPs were found in the extracellular matrix attached to the plasma membrane (b), inside early endocytic vesicles (b-c), in the multivesicular lysosomes (Lys) (c) and in the nuclear vicinity (d). PM: Plasma membrane; EE: Early endosomes; LE: Late endosomes; Lys: Lysosomes. Scale bars: (a) 1 μm; (b) 100 nm; (c-d) 200 nm.

References

1. Verma, I.M. and M.D. Weitzman, "Gene therapy: twenty-first century medicine." Annu Rev Biochem, 2005. 74: p. 711-38.
2. Goodwin, T. and L. Huang, "Nonviral vectors: we have come a long way." Adv Genet, 2014. 88: p. 1-12.
3. Smedt, S.C.D., J. Demeester, and W.E. Hennink, "Cationic Polymer Based Gene Delivery Systems." Pharm Res, 2000. 17(2): p. 113-126.
4. Kirtane, A.R. and J. Panyam, "Polymer nanoparticles: Weighing up gene delivery." Nature nanotechnology, 2013. 8(11): p. 805-806.
5. Gomes, C.P., et al., "Translating chitosan to clinical delivery of nucleic acid-based drugs." MRS Bulletin, 2014. 39(01): p. 60-70.
6. Mourya, V.K. and N.N. Inamdar, "Trimethyl chitosan and its applications in drug delivery." J Mater Sci Mater Med, 2009. 20(5): p. 1057-79.
7. Thanou, M., et al., "Quaternized chitosan oligomers as novel gene delivery vectors in epithelial cell lines." Biomaterials, 2002. 23(1): p. 153-9.
8. Kean, T., S. Roth, and M. Thanou, "Trimethylated chitosans as non-viral gene delivery vectors: Cytotoxicity and transfection efficiency." Journal of Controlled Release, 2005. 103(3): p. 643-653.
9. Pires, L.R., et al., "Imidazole-grafted chitosan-mediated gene delivery: in vitrostudy on transfection, intracellular trafficking and degradation." Nanomedicine, 2011. 6(9): p. 1499–1512.
10. Gottstein, C., et al., "Precise quantification of nanoparticle internalization." ACS Nano, 2013. 7(6): p. 4933-45.
11. Lopes, C., M. Gomez-Lazaro, and A. Pêgo, "Seeing is believing but quantifying is deciding." Nanomedicine (Lond), 2015. 10(15): p. 2307-10.
12. Vranic, S., et al., "Deciphering the mechanisms of cellular uptake of engineered nanoparticles by accurate evaluation of internalization using imaging flow cytometry." Part Fibre Toxicol, 2013. 10: p. 2.
13. Phanse, Y., et al., "Analyzing cellular internalization of nanoparticles and bacteria by multi-spectral imaging flow cytometry." J Vis Exp, 2012(64): p. e3884.
14. Marangon, I., et al., "Localization and relative quantification of carbon nanotubes in cells with multispectral imaging flow cytometry." J Vis Exp, 2013(82): p. e50566.
15. Moreno, P.M., et al., "Delivery of Splice Switching Oligonucleotides by Amphiphilic Chitosan-Based Nanoparticles." Mol Pharm, 2016. 13(2): p. 344-56.
16. Moreira, C., et al., "Improving chitosan-mediated gene transfer by the introduction of intracellular buffering moieties into the chitosan backbone." Acta Biomaterialia, 2009. 5(8): p. 2995-3006.
17. Mima, S., et al., "Highly Deacetylated Chitosan and Its Properties." Journal of Applied Polymer Science, 1983. 28(6): p. 1909-1917.
18. Vachoud, L., N. Zydowicz, and A. Domard, "Formation and characterisation of a physical chitin gel." Carbohydr Res, 1997. 302(3-4): p. 169-177.
19. Curti, E. and S.P. Campana-Filho, "Viscosity behavior of chitosan and N,N,N-trimethylchitosan chloride salts in acid-free aqueous solution." Journal of Macromolecular Science-Pure and Applied Chemistry, 2006. A43(3): p. 555-572.

20. Oliveira, H., et al., "Chitosan-based gene delivery vectors targeted to the peripheral nervous system." Journal of Biomedical Materials Research Part A, 2010. 95A(3): p. 801-810.

21. Ortyn, W.E., et al., "Extended depth of field imaging for high speed cell analysis." Cytometry A, 2007. 71(4): p. 215-31.

22. George, T.C., et al., "Quantitative measurement of nuclear translocation events using similarity analysis of multispectral cellular images obtained in flow." J Immunol Methods, 2006. 311(1-2): p. 117-29.

23. O'Brien, J., et al., "Investigation of the Alamar Blue (resazurin) fluorescent dye for the assessment of mammalian cell cytotoxicity." Eur J Biochem, 2000. 267(17): p. 5421-6.

24. Huang, M., et al., "Transfection efficiency of chitosan vectors: effect of polymer molecular weight and degree of deacetylation." J Control Release, 2005. 106(3): p. 391-406.

25. Administration, U.S.F.a.D., *Guidance for Industry - Pyrogen and Endotoxins Testing*, U.S.D.o.H.a.H. Services, Editor. 2012, U.S. Department of Health and Human Services

26. Nordtveit, R.J., K.M. Vårum, and O. Smidsrød, "Degradation of fully water-soluble, partially N-acetylated chitosans with lysozyme." Carbohydrate Polymers, 1994. 23(4): p. 253-260.

27. Pangburn, S., P. Trescony, and J. Heller, "Lysozyme degradation of partially deacetylated chitin, its films and hydrogels." Biomaterials, 1982. 3(2): p. 105-108.

28. Ren, D., et al., "The enzymatic degradation and swelling properties of chitosan matrices with different degrees of N-acetylation." Carbohydrate Research, 2005. 340(15): p. 2403-2410.

29. Koping-Hoggard, M., et al., "Chitosan as a nonviral gene delivery system. Structure-property relationships and characteristics compared with polyethylenimine in vitro and after lung administration in vivo." Gene Therapy, 2001. 8(14): p. 1108-1121.

30. Wattiaux, R., et al., "Endosomes, lysosomes: their implication in gene transfer." Advanced Drug Delivery Reviews, 2000. 41(2): p. 201-208.

31. Yan, Y., et al., "Particles on the Move: Intracellular Trafficking and Asymmetric Mitotic Partitioning of Nanoporous Polymer Particles." ACS Nano, 2013. 7(6): p. 5558–5567.

32. Summers, H.D., et al., "Statistical analysis of nanoparticle dosing in a dynamic cellular system." Nat Nanotechnol, 2011. 6(3): p. 170-4.

33. Ross, J.L., M.Y. Ali, and D.M. Warshaw, "Cargo transport: molecular motors navigate a complex cytoskeleton." Current Opinion in Cell Biology, 2008. 20(1): p. 41-47.

34. Hofmann, D., et al., "Mass Spectrometry and Imaging Analysis of Nanoparticle-Containing Vesicles Provide a Mechanistic Insight into Cellular Trafficking." ACS Nano, 2014. 8(10): p. 10077–10088.

35. Bishop, C.J., et al., "Quantification of cellular and nuclear uptake rates of polymeric gene delivery nanoparticles and DNA plasmids via flow cytometry." Acta Biomater, 2016. 37: p. 120-30.

36. Zuba-Surma, E.K., et al., "The ImageStream System: a key step to a new era in imaging." Folia Histochemica et Cytobiologia, 2007. 45(4): p. 279-290.

37. Zuba-Surma, E.K. and M.Z. Ratajczak, "Analytical capabilities of the ImageStream cytometer." Methods Cell Biol, 2011. 102: p. 207-30.

38. Wiethoff, C.M. and C.R. Middaugh, "Barriers to nonviral gene delivery." J Pharm Sci, 2003. 92(2): p. 203-17.

39. Germershaus, O., et al., "Gene delivery using chitosan, trimethyl chitosan or polyethylenglycol-graft-trimethyl chitosan block copolymers: establishment of structure-activity relationships in vitro." J Control Release, 2008. 125(2): p. 145-54.

40. Grigsby, C. and K. Leong, "Balancing protection and release of DNA: tools to address a bottleneck of non-viral gene delivery." J R Soc Interface, 2010. 7 Suppl 1: p. S67-82.

41. Verheul, R.J., et al., "Influence of the degree of acetylation on the enzymatic degradation and in vitro biological properties of trimethylated chitosans." Biomaterials, 2009. 30(18): p. 3129-35.

42. Strand, S.P., et al., "Molecular design of chitosan gene delivery systems with an optimized balance between polyplex stability and polyplex unpacking." Biomaterials, 2010. 31(5): p. 975-87.

CHAPTER VI

ATOMIC FORCE MICROSCOPY AS A TOOL TO ASSESS THE SPECIFICITY OF TARGETED NANOPARTICLES IN BIOLOGICAL MODELS OF HIGH COMPLEXITY

Atomic Force Microscopy as a Tool to Assess the Specificity of Targeted Nanoparticles in Biological Models of High Complexity

Carla Pereira Gomes[1,2,3], Cátia Daniela Ferreira Lopes[1,2,4], Michael Leitner[5], Andreas Ebner[5], Peter Hinterdorfer[5], and Ana Paula Pêgo[1,2,3,6,*]

1 – INEB – Instituto de Engenharia Biomédica, Universidade do Porto

2 – i3S – Instituto de Investigação e Inovação em Saúde, Universidade do Porto, Rua Alfredo Allen 208, 4200-135 Porto, Portugal

3 – Universidade do Porto – Faculdade de Engenharia, R. Dr. Roberto Frias, 4200-465 Porto, Portugal

4 – Universidade do Porto – Faculdade de Medicina, Alameda Prof. Hernâni Monteiro, 4200-319 Porto, Portugal

5 – Institute of Biophysics, Johannes Kepler University, Gruberstraße 40, 4020 Linz, Austria

6 – ICBAS – Instituto de Ciências Biomédicas Abel Salazar, Universidade do Porto, Rua de Jorge Viterbo Ferreira 228, 4050-313 Porto, Portugal

Published in Advanced Healthcare Materials, Volume 6, 2017

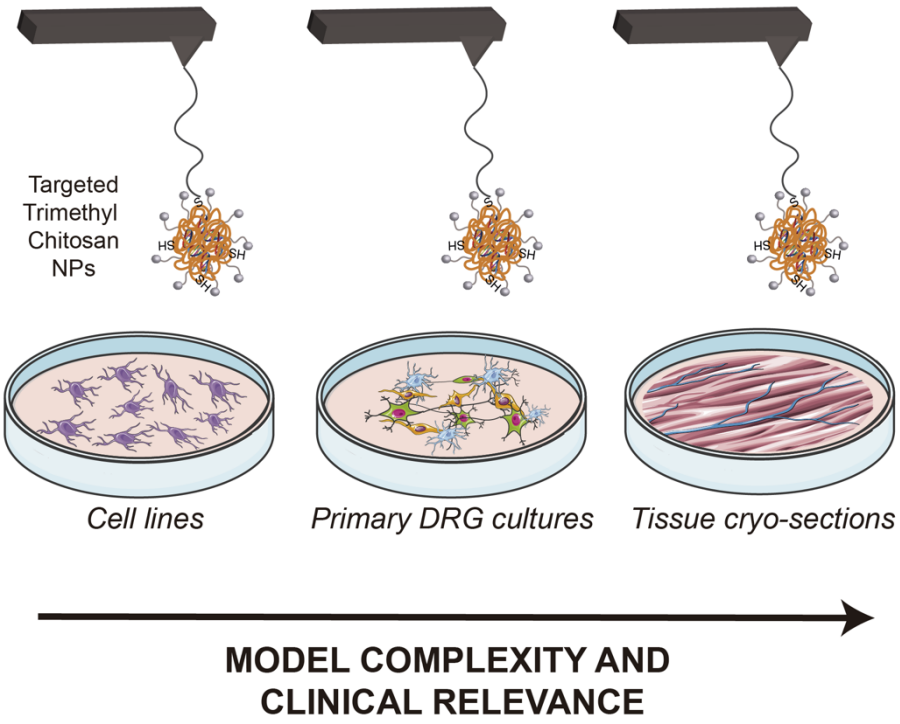

Abstract

The ability to design nanoparticle delivery systems capable of selectively target their payloads to specific cell populations is still a major caveat in nanomedicine. One of the main hurdles is the fact that each nanoparticle formulation needs to be precisely tuned to match the specificities of the target cell and route of administration. In this work, molecular recognition force spectroscopy (MRFS) is presented as a tool to evaluate the specificity of neuron-targeted trimethyl chitosan nanoparticles to neuronal cell populations in biological samples of different complexity. The use of atomic force microscopy tips functionalized with targeted or non-targeted nanoparticles made it possible to assess the specific interaction of each formulation with determined cell surface receptors in a precise fashion. More importantly, the combination of MRFS with fluorescent microscopy allowed to probe the nanoparticles vectoring capacity in models of high complexity, such as primary mixed cultures, as well as specific subcellular regions in histological tissues. Overall, this work contributes for the establishment of MRFS as a powerful alternative technique to animal testing in vector design and opens new avenues for the development of advanced targeted nanomedicines.

.

1. Introduction

One of the biggest challenges in medicine is to improve our ability to efficiently and precisely deliver therapeutic molecules to a desired target. The mean by which a drug is delivered could have a significant impact on its efficacy. The majority of drugs present an optimal concentration range within which maximum benefit is derived, and concentrations above or below these limits will more likely produce toxicity, having no therapeutic advantage [1]. Another critical issue consists in the remarkable difficulty of many therapeutic molecules in overcoming biological barriers [2]. In this regard, the emergence of nanomedicine opens new therapeutic opportunities for bioactive molecules that cannot be used effectively as conventional drug formulations [3, 4]. Vectorizing these molecules by means of nanoparticle (NP) based structures has revolutionized the field of drug formulation and delivery, as these carrying systems present unique tunable physicochemical properties that allow to protect drugs from degradation and clearance, prevent harmful side-effects and improve bioavailability by providing controlled or timed drug release [5-7]. Moreover, the attractiveness of these nanomaterials is that they can be also designed for targeted drug delivery at a specific disease site, improving the uptake of their payload and safety profile, ultimately resulting in an increased therapeutic index [8].

In the last decades, research in nanomedicine has strongly focused on the use of specific ligands to be conjugated onto the NPs surface when aiming at increasing NP selectivity and specificity [9]. Nevertheless, the fact that each NP formulation needs to be precisely tuned to match the specificities of the target cell population and route of administration is time consuming and implies cumbersome testing, both *in vitro* and *in vivo*. Thus, technologies that enable the screening and characterization of a large number of candidates under biologically relevant conditions are still eagerly awaited [10].

In this context, atomic force microscopy (AFM) has emerged as a powerful characterization platform, providing valuable insights that may have major implications for targeted NP design and development [11]. AFM is a well-known high-resolution surface topography technique with nanometer resolution under physiological conditions. Furthermore, in addition to topographical imaging, the AFM cantilever offers the possibility to be used as a biosensing system, as it can be functionalized with

different (bio)structures to prove their interactions with specific receptors, either isolated, reconstituted or in native biological samples. As a result, AFM has evolved from a mere physical microscopy technique into a standard method in pharmaceutical and life sciences, becoming a multifunctional molecular toolkit [11, 12].

Taking advantage of this functionality, our group has previously proposed the use of molecular recognition force spectroscopy (MRFS) as a screening tool for the optimization of the density of targeting moieties towards improving receptor-specific binding of NPs to neuronal cells in simple cell culture systems [13]. It remained to be established if the proposed methodology could be applied in models of higher complexity and biological relevance, to expand the impact and applicability of the technique.

In this work, we aimed at testing the specificity of gene carrying trimethyl chitosan (TMC) NPs actively targeted towards neuronal populations in complex biological models, that include *in vitro* heterogeneous primary neural cell cultures and innervated histological tissue sections, by MRFS. To promote the NP selective targeting towards neuronal cells, TMC NPs functionalized with the non-toxic and neurotropic carboxylic C-terminal fragment of the tetanus toxin heavy chain (HC), with proven efficacy both *in vitro* [14, 15] and *in vivo* [16, 17], were used.

To the best of our knowledge, this is the first report showing the application of force spectroscopy using primary cultures composed of mixed cell populations and/or histological tissue sections for the evaluation of NP vectoring capacity. We believe that our data validate MRFS as a valuable tool for the design and characterization of the targeting potential of new formulations that ultimately will lead to the appearance of more robust and advanced nanomedicines, regardless of the desired application and biological target. Furthermore, MRFS can be assumed as a promising alternative screening method to animal experimentation.

2. Materials and Methods

2.1. Synthesis of partially thiolated TMC

Trimethyl chitosan (TMC) derived from ultra-pure chitosan was supplied by Kytozyme (Belgium) (lot VIHA0013-157) and purified by filtration and dialysis, as previously described [18, 19]. Further details on polymer characterization are described in the Supplementary Materials and Methods (SMM).

Thiolated TMC (TMC_{SH}) was synthesized by the immobilization of thiol groups from 2-iminothiolane on the primary amino groups of the polymer, as described elsewhere [15, 17]. The resulting powders were stored at -20 ºC until further use. Determination of polymer thiol content was performed based on the Ellman's assay [20] (see SMM).

2.2. Nanoparticle preparation and characterization

TMC_{SH}-plasmid DNA NPs were prepared through self-assembly by mixing, while vortexing, equal volumes of pDNA and TMC_{SH} solutions (in 20 mM HEPES buffered saline (HBS) with 5% (w/v) glucose solution, pH 7.4). Nanocomplexes were prepared at a molar ratio of quaternized amine groups (N) to moles of pDNA phosphate groups (P) – N/P molar ratio – of 8. TMC_{SH} NP core (naked NPs; **Figure 1a**) were left to stabilize for 15 min before further use or functionalization. For NP functionalizatifon, TMC_{SH}-pDNA nanocomplexes were incubated for 24 h (37ºC, 1,000 rpm) with either a 5 kDa MeO-PEG-MAL (Sigma-Aldrich) (non-targeted – nT NPs) (**Figure 1b**) or with the PEG-modified HC fragment (targeted – Tg NPs) (**Figure 1c**). Details for the preparation of PEG-HC can be found in the SMM.

All formulations (naked, nT and Tg NPs) were characterized in terms of size, polydispersity index (PdI) and zeta potential using a Zetasizer Nano Zs (Malvern Instruments). The Smoluchowski model was applied for zeta potential determination and the cumulant analysis was used for average particle size determination. Ten µg of pDNA was used to prepare the tested formulations. All measurements were performed in triplicate, at 25°C.

For pDNA condensation efficiency evaluation, the previously described SYBR® Gold (Life Technologies, Thermo Fisher Scientific) exclusion assay was used [19]. This assay enables the measurement of free pDNA, due to SYBR® Gold binding to free nucleic acids (not complexed into NPs). Results are expressed as relative percentage

of complexation, where 100% means pDNA is totally complexed with polymer in NPs, and 0% means that all pDNA is free (not complexed with the polycation). Samples with the same mass ratio of polymer without pDNA were used as control to subtract any polymer background fluorescence.

2.3. Internalization studies in cell lines:

ND7/23 (mouse neuroblastoma N18 tg 2)×rat dorsal root ganglion neuron hybrid), NIH 3T3 (mouse embryonic fibroblast) and RN22 (immature rat Schwann) cells were seeded into 24-well plates (Greiner bio-one), 24 h prior to incubation with NPs. TMC-based NPs were prepared at N/P ratio of 8 using 2 µg of pDNA per cm^2 and suspended in complete Dulbecco's modified Eagle medium (DMEM) (with serum and antibiotics). To assess the NP internalization profile, NPs were prepared as described above using YOYO®-1 labelled pDNA. After an incubation period of 2 h in the presence of NPs, cells were incubated with trypan blue to quench any external fluorescence and subsequently trypsinized and processed for flow cytometry. Twenty thousand gated events were taken for each replicate and analyzed using a FACS Calibur flow cytometer (BD Biosciences). The resulting data was analyzed using FlowJo software (version 10, FLOWJO, LLC). Untreated cells were used as negative control.

2.4. Internalization studies in DRG primary cultures

Primary dissociated dorsal root ganglia (DRG) cells were seeded and cultured in complete neuron culture medium as mentioned in SMM. After two days in culture, TMC-based NPs loaded with YOYO®-1 pDNA were added to the cells. Naked, nT or Tg NPs were prepared at an N/P ratio of 8 using 2 µg of pDNA per cm^2 and suspended in complete neuron culture medium (with serum and antibiotics). After an incubation period of 2 h, cells were washed with phosphate buffered saline (PBS) twice and subsequently fixed with 4% (w/v) PFA for 10 min at 37ºC. Afterwards, a protocol for neuron discrimination was conducted (see SMM). For identification of cell nuclei, 100 µl of a 2 µg mL^{-1} HCS CellMask™ Orange Stain (Molecular Probes®) solution was added to each coverslip and incubated with cells for 30 min at RT, protected from light. After washing with PBS, cells were imaged using a laser scanning confocal microscope Leica TCS SP5 II (Leica Microsystems, Germany) with the HC PL APO Lbl. Blue 63x/1.40 oil objective. For each treatment group, a total of 20 fields were randomly

selected for representative imaging. All images were acquired with the same laser intensity to allow for qualitative and semi-quantitative comparison between the different NPs profile of cellular association/uptake. Images were acquired from two independent experiments.

2.5. HC conjugation with quantum dots

HC was conjugated to Qdot® 705nm ITK™ carboxyl quantum dots (Invitrogen), according to a previously described protocol [21]. Briefly, 50 µL of the Qdot stock solution (8 µM) was diluted by adding 400 µL of 0.01 M phosphate buffer, pH 8.5 containing 20 µL of 1-ethyl-3-(3-dimethylaminopropyl)carbodiimide (EDC) at 1 mg mL^{-1}, and mixed at RT for 10 min in the dark. HC (20.5 µL of 3.3 mg mL^{-1} stock solution) in 0.1M phosphate buffer, pH 8 was then added to the reaction mixture, thus giving a molar ratio of 3HC:1Qdot. After 2 h of constant stirring at RT in the dark, the HC-Qdots conjugate (hereafter designated as HC-QDs) solution was washed and concentrated using a ultracentrifugal filter with a 30 kDa cut-off membrane (Millipore) to a final protein concentration of 1.5 µM.

2.6. Identification of HC receptors with HC-QDs

ND7/23, NIH 3T3 and RN22 cells were plated at a final density of 2.0, 2.5 and 2.0 x 10^4 viable cells per cm^2 on glass coverslips coated with poly-*d*-lysine (PDL) and plated in a 24-well plate. DRG primary cells were isolated and cultured as described above. After 48 h, cells were incubated at 4ºC for 10 min and then washed three times with cold PBS before a 30 min incubation with HC-QDs at a final concentration of 5 µg mL^{-1} in 0.1% (w/v) BSA in PBS, at 4 ºC. In the case of ND7/23 cells, a control was performed with a 10 min incubation of unlabeled HC (50 µg mL^{-1}) prior to the incubation with HC-QDs. Afterwards, cells were washed with cold PBS three times and then fixed with 4% (w/v) PFA prepared in PBS for 15 min at RT. After washing twice with cold PBS, cells were permeabilized for 5 min with Triton X-100 0.1% (v/v) prepared in PBS and incubated with 1% (w/v) BSA for 1 h. All cell lines were then incubated with phalloidin 488 (Invitrogen) prepared in 1% (w/v) BSA solution (1:100) for 1 additional hour for cytoplasmic staining.

2.7. Tissue section preparation and labelling with HC-QDs

Gastrocnemius muscles and sciatic nerves were collected from a young adult B6 mouse. Tissues were fixed in 4% (w/v) PFA overnight at 4ºC and cryopreserved in a 30% (w/v) sucrose solution (Sigma-Aldrich). Cryo-sections of gastrocnemius muscles (50 µm-thick) and sciatic nerve (16 µm-thick) were obtained in a cryostat (HM550, Microm) and collected in 0.01 mg mL^{-1} PDL-coated 35 mm glass bottom dishes (10 mm microwell diameter, MatTek).

Frozen sections of gastrocnemius muscles were double stained for the post-synaptic marker α-bungarotoxin and βIII tubulin, to allow the identification of neuromuscular junctions (NMJ). In brief, tissue sections were blocked for 1 h at RT with 5% (v/v) normal goat serum in PBS containing 0.3% (v/v) Triton X-100 and incubated with the primary monoclonal antibody mouse anti-βIII tubulin (1:1,000, Promega) overnight at 4 °C. After washing in PBS, tissue sections were incubated for 90 min at RT with a secondary antibody rabbit anti-mouse Alexa Fluor® 488 conjugate (Molecular Probes®; 1:1000), α-bungarotoxin – tetramethylrhodamine conjugate (Molecular Probes®; 1:200) and HC-QDs, all diluted in blocking buffer.

2.8. AFM tip functionalization

Silicon nitride AFM cantilevers with 0.01-0.03 N m^{-1} nominal spring constant (Bruker AFM Probes, MSCT) were amino functionalized as previously described [22], using a gas-phase silanization method with (3-aminopropyl)triethoxysilane (APTES, Sigma-Aldrich). The attachment of HC to the AFM tip surface was attained using a heterobifunctional PEG spacer, acetal-PEG-NHS (PEG_{18}) (**Figure 2d**), as previously described [23]. Briefly, the amino-functionalized tips were incubated for 2 h in 0.5 mL of a 6.6 mg mL^{-1} acetal-PEG-NHS solution in chloroform (Sigma-Aldrich) with 2% (v/v) triethylamine (Sigma-Aldrich) at RT. After washing the tips three times in fresh chloroform and drying them in a N_2 flux, the AFM tips were incubated for 10 min in 1% (v/v) citric acid (Sigma-Aldrich) in water to convert the acetal group into an aldehyde group. Afterwards, the protein was coupled to the tips by incubating 100 µL of HC in PBS at 0.2 mg mL^{-1} containing 2 µL of a 1 M $NaCNBH_3$ solution (Sigma-Aldrich). Then, ethanolamine hydrochloride solution (5 µL, 1 M, pH 8; Sigma-Aldrich) was added and the incubation proceeded for 10 min at RT. This procedure allows for the blockage of

any unreacted aldehyde groups. Finally, the functionalized tips were rinsed three times with filtered PBS and kept in this solution at 4 ºC until further use.

The functionalization of AFM tips with the developed TMC-based NPs was attained through the use of a MAL-PEG-NHS spacer (PEG_{18}) (**Figure 2e**), as previously described [13].

2.9. Molecular recognition force spectroscopy (MRFS) studies

All measurements were carried out on a PicoPlus 5500 AFM instrument (Keysight Technologies, USA). Force–distance cycles (approach-retraction cycles) were performed at RT by using HC fragment- or NP-functionalized AFM tips.

Force spectroscopy studies using ND7/23, NIH 3T3 or RN22 fixed cells (4% (w/v) PFA, 20 min) cultured on PDL-coated glass coverslips and mounted on a standard fluid cell on the AFM scanner were performed in PBS at RT. Force–distance cycles were recorded at a 2,000 nm s^{-1} pulling rate. The loading rate was varied via the rate of piezo expansion (pulling speed in z-direction), which was adjusted by means of sweep duration time and scan range for trace and retrace. To provide an insight into the loading rate dependence of the HC or NPs on their cell receptors, pulling speeds from 50 to 4000 nms^{-1} were used. To evaluate the specificity of the measured events, surface receptor blockage was accomplished by incubating cells with free HC at 0.1 mg mL^{-1} in PBS for 1 h prior acquisition of further FDC.

For the correct positioning of the functionalized AFM tips when performing MRFS studies on DRG primary cultures and histological tissue sections, a combined setup where the AFM sample stage (PicoPlus 5500) is mounted to the body of an inverted widefield fluorescence microscope (Axio Observer Z1, Zeiss) was used.

2.10. Data analysis of force-distance cycles

For each dataset, at least 10 cells or 3 tissue samples were probed with several independent HC or NP functionalized AFM-tips. Up to 2,000 force–distance cycles were recorded at each cell/tissue location and the tip position was changed by a few hundred nanometers every 100 curves to ensure that the binding events were statistically appropriate. Data analysis (cantilever spring constants and force-distance cycle

analysis) was performed using in-house algorithms implemented in MATLAB (MathWorks). The spring constants of the cantilevers were determined by using the thermal noise method [24, 25]. Empirical force distributions of the rupture forces of unbinding events (PDF) were calculated as previously described [26]. Unspecific adhesions were not valued as rupture events.

3. Results

3.1. Polymer characterization

Trimethyl chitosan (TMC) with an average number molecular weight (Mn) of 43.3 kDa, a degree of acetylation of 15.7% and a quaternization degree of 30.1% was used [19]. To attain nanoparticle neurotropism, our group has been exploring the tethering of a pegylated HC fragment at the NPs surface [15-17, 27]. Consequently, thiol groups were introduced into the trimethyl chitosan (TMC) polymer backbone (TMC_{SH}) by a previously described method [15, 17]. During TMC_{SH} complexation with plasmid DNA, the presence of thiol pending groups further contributes to the crosslinking of the polycation, stabilizing the resulting complexes, and allows the subsequent functionalization of the NPs. The total amount of thiol groups grafted to the polymer was 149.1 ± 15.8 μmoL g^{-1}, as determined by the Ellman's assay [20], corresponding to 4.7 ± 0.5 % substitution of TMC primary amines by thiol groups.

3.2. Nanoparticle preparation and characterization

Polymer-plasmid DNA binary complexes, hereafter referred to as naked NPs (**Figure 1a**), were prepared by coacervation, as a result of the electrostatic interaction between the positively charged polymer and the negatively charged plasmid DNA (pDNA). After NP stabilization at room temperature (RT) for 20 min, the NPs were further functionalized by attachment of 5 kDa PEG chains with a terminal methyl oxide group (**Figure 1b**) or HC-PEG conjugates (**Figure 1c**), to yield non-targeted (nT) or targeted (Tg) NPs, respectively. Transmission electron microscopy images of each formulation are presented in (**Figure 1d-f**). To confirm the presence of the non-toxic carboxylic fragment of the tetanus toxin (HC) at the NP surface, the Tg NPs were functionalized with HC modified with Qdot® 705nm ITK™ carboxyl quantum dots (Invitrogen; further details in materials and methods) – hereafter designated as HC-QDs.

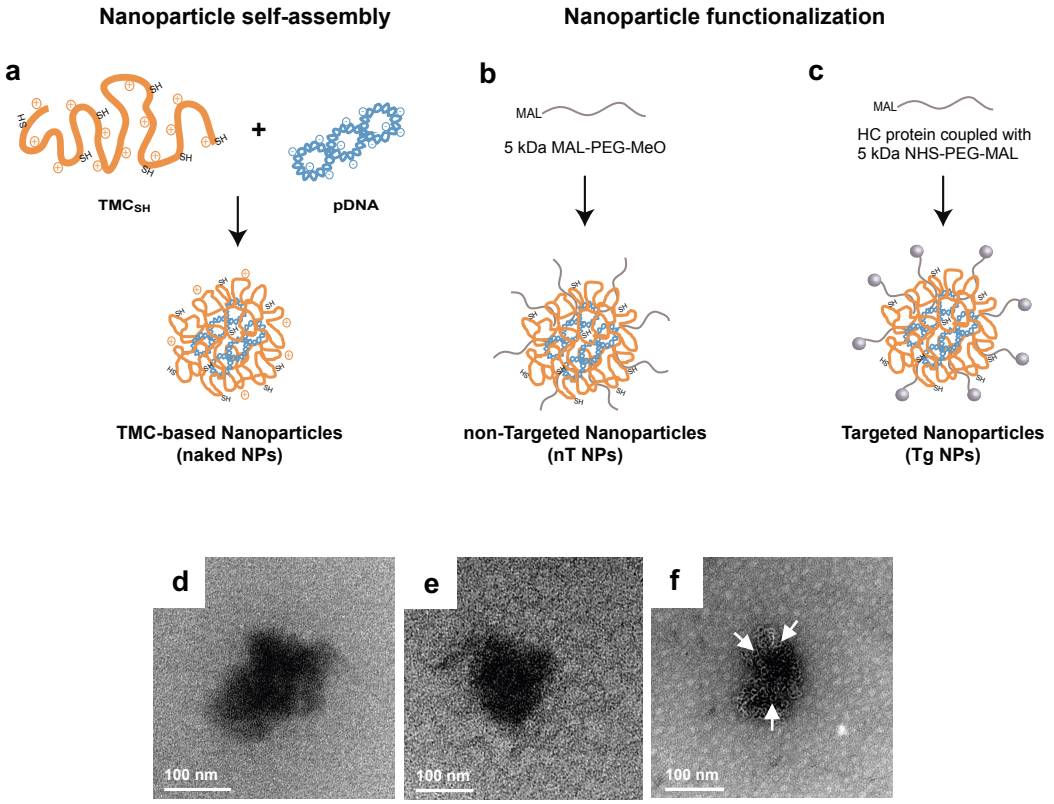

Figure 1. Preparation and characterization of trimethyl chitosan-based nanoparticles by transmission electron microscopy. Schematic representation for the preparation of trimethyl chitosan (TMC) nanoparticles: the core of the NPs was prepared by coacervation as a result of the electrostatic interaction between the (a) polymer and plasmid DNA (naked NPs) and afterwards NPs were functionalized either with (b) a 5 kDa MAL-PEG-MeO chains (nT NPs) or with (c) the HC protein coupled to a 5 kDa NHS-PEG-MAL spacer (Tg NPs). Transmission electron microscopy micrographs of suspended (d) naked, (e) nT or (f) Tg NPs samples. Tg NPs were prepared using HC-QDs (arrows) to distinguish the protein at the NP surface.

After preparation, all NPs were characterized in terms of mean average diameter size, polydispersity index (PdI) and zeta-potential (surface charge) by dynamic light scattering. The ability of the developed NPs to efficiently condense pDNA was also measured, using a method previously setup by us [19]. The obtained data from the NP characterization (**Table 1**) show that naked NPs presented significant higher average sizes (> 220 nm) when compared to the functionalized ones (< 180 nm). In agreement, the PdI values were also significant higher ($p<0.05$) for the naked NPs, when compared to the other formulations. This effect is ascribed to the presence of the PEG spacer at the surface of functionalized NPs, that contributes to the observed reduction of particle size [28]. Regarding the zeta potential, the addiction of the PEG molecules to the NPs surface led to a reduction in the NP zeta potential between +2 and +5 mV, depending

on the presence or absence of the HC protein, respectively. Since HC is a positively charged protein at the pH of the NP preparation (pH 7.4), the slight higher zeta potential value of the Tg NPs in relation to the nT ones was to be expected. Regarding the NPs ability to condense pDNA, all formulations presented condensation efficiencies above 91%, showing that NPs functionalization did not alter their ability to maintain their cargo.

Table 1. TMC-based nanoparticles physicochemical characterization.

Nanoparticle formulation	Size (nm)[a]	Polydispersity Index (PdI)[a]	Zeta potential (mV)[a]	pDNA condensation efficiency (%)[b]
Naked	222.0 ± 8.1	0.281 ± 0.037	+21.5 ± 0.5	93.3 ± 5.2
non-Targeted	179.9 ± 9.4	0.177 ± 0.015	+16.9 ± 0.3	90.8 ± 7.4
Targeted	167.3 ± 11.2	0.219 ± 0.029	+19.4 ± 0.2	92.5 ± 4.9

[a)]NPs average diameter size, PdI and surface charge (zeta potential) were determined by dynamic light scattering in 20 mM HEPES buffered saline (HBS) with 5% (w/v) glucose solution, pH 7.4; [b)]pDNA condensation efficiency was determined by SYBR® Gold exclusion assay in complete DMEM medium with serum and antibiotics, pH 7.4.

3.3. Nanoparticle specificity towards neuronal vs. non-neuronal cell lines

The HC fragment is responsible for the tetanus toxin neurospecific binding to polygangliosides present at the neuronal cellular membrane (being GT1b the most predominant) that leads to the consequent toxin internalization and retrograde transport [29, 30]. Firstly, the binding specificity of the purified HC fragment towards selected neuronal (ND7/23) and non-neuronal cell lines (RN22 and NIH 3T3) was determined to confirm the validity of the chosen cell lines as *in vitro* models for the determination of the Tg NPs neuro-specificity. The HC protein was modified with quantum dots (HC-QDs) and incubated with the three selected cell lines at 4 ºC to allow ligand-receptor interaction but inhibit protein internalization. The obtained results (**Figure 2**) show that the HC-QDs specifically bind to the neuronal cell line (ND7/23) (**Figure 2a)**, as no interaction was observed between the HC-QDs and the control lines of schwannoma (RN22) and fibroblasts (NIH 3T3) cells (**Figure 2b** and **Figure 2c**, respectively). To further confirm the specificity of the binding of the HC-QDs to the neuronal line, a pre-incubation of cells with a 100-fold excess of unlabeled HC was performed prior to the

incubation with the QD modified HC, resulting in a significant drop of the observed fluorescent signal (data not shown). These results are in accordance with our previous findings, in which we have compared the HC binding profile to ND7/23 and NIH 3T3 cell lines using HC labelled with rhodamine [14]. After validation of the selected cell lines, we proceeded with the MRFS studies to assess the specificity of the different developed NP formulations towards the cell lines under testing. A heterobifunctional PEG_{18} linker was used to tether both, the HC fragment (via an acetal group) (**Figure 2d)** and the NPs (via a maleimide group) (**Figure 2e**) to an AFM tip. Representative force-distance curves (FDC) obtained for naked, nT or Tg NPs in ND7/23 cells are shown in **Figure 2f-h**. When performing MRFS with naked NPs, independently of the cell line, the occurrence of multiple unbinding events was observed. These result from non-specific low force (< 20 pN) electrostatic interactions established between the positively charged NPs (Table 1, zeta potential data) and the negatively charged cell membrane. In contrast, most of the FDC obtained with the nT NPs did not present any unbinding events. On the other hand, the nT NPs are coated with PEG molecules, which offer a stealth effect and avert the interaction of these NPs with the cellular membrane. Consequently, most of the FDC resulting from the interaction of these NPs with cells did not present unbinding events of any kind (unspecific adhesion forces, electrostatic interactions or specific events), independently of the cell line tested. The same result was observed in the FDC obtained with the Tg NPs probed against the non-neuronal cell lines. Unsurprisingly, the acquisition of FDC with Tg NPs in ND7/23 cells presented single molecule unbinding events, comparable to those obtained with the HC-functionalized AFM tips (data not shown). Such occurrences were followed by a distinctive non-linear force signal due to the elastic extension of the PEG linker present at the AFM tip surface, which allowed for the distinction of specific rupture events from unspecific adhesions [31]. The analysis of the specific rupture events in a dataset of hundreds of FDC yields a force histogram that can be represented as a calculated probability density functions (PDF), according to Baumgartner *et al,* allowing the determination of the most probable rupture force for the ligand-receptor pair [26]. Representative PDFs for the interaction between the HC fragment and the different cell lines under testing are shown in **Figure 2i**. The interaction between the HC fragment and ND7/23 cells presented a monomodal distribution peak around 30 pN with a binding probability (BP) of 16.6%. In contrast, the interaction of the HC fragment with the non-

neuronal cell lines (RN22 and NIH 3T3) resulted in a multimodal distribution with a low empirical probability density function and a BP value of 3.5 and 4.8%, respectively. To attest that the measured forces resulted from the specific ligand-receptor pair interaction, ND7/23 cells surface receptors were blocked using free HC (1 mg mL^{-1}) prior acquisition of FDC, which resulted in a significant drop of the BP from 16.6 to 4.4% ($p<0.001$). In **Figure 2j** is presented the PDF graphic resulting from the Tg and nT NPs probing against the ND7/23 cell line. The Tg NPs presented a distribution peak similar to the one obtained for the HC fragment, with a comparable BP value (17.8%). After cell surface blockage with free HC, this value significantly decreased to 5.8%, proving the specificity of this interaction. On the other hand, the use of AFM tips holding nT NPs yielded a statistically significant lower BP value (3.7%) when compared to the tips with Tg NPs. The different BP values given from the measurement of the interactions between both Tg and nT NPs with the different cell lines is showed in **Figure 2k**, each dot corresponding to the acquisition of approximately 2,000 FDC in a given cell. Despite the statistically significant difference observed in the BP between these two NP systems towards the neuronal cell line, no statistical differences were observed between the two formulations in the non-neuronal cell lines. Moreover, the BP of the Tg NPs is significantly higher for the neuronal cell line than the non-neuronal cells ($p<0.001$).

Finally, to support the data obtained through the MRFS studies, we assessed the internalization profile of these formulations by flow cytometry. Briefly, cells were incubated with the different TMC-based NPs containing YOYO®-1 labelled pDNA for 2 hours and afterwards the percentage of cells with internalized NPs was quantified (**Figure 2l**). In order to remove the external fluorescent signal (adsorbed NPs), cells were incubated with trypan blue and washed before FACS analysis. The obtained results were in line with the MRFS data, showing a significant decrease in the internalization of the Tg NPs for both non-neuronal cell lines (RN22 and NIH 3T3), when compared to the naked NP formulation ($p<0.001$ and $p<0.05$, respectively). Moreover, while the incubation with the nT NPs led to a decrease in the internalization extent, independently of the cell line tested, the Tg NPs were internalized into a high percentage of neuronal cells (> 90%), confirming their specific tropism towards this cell line.

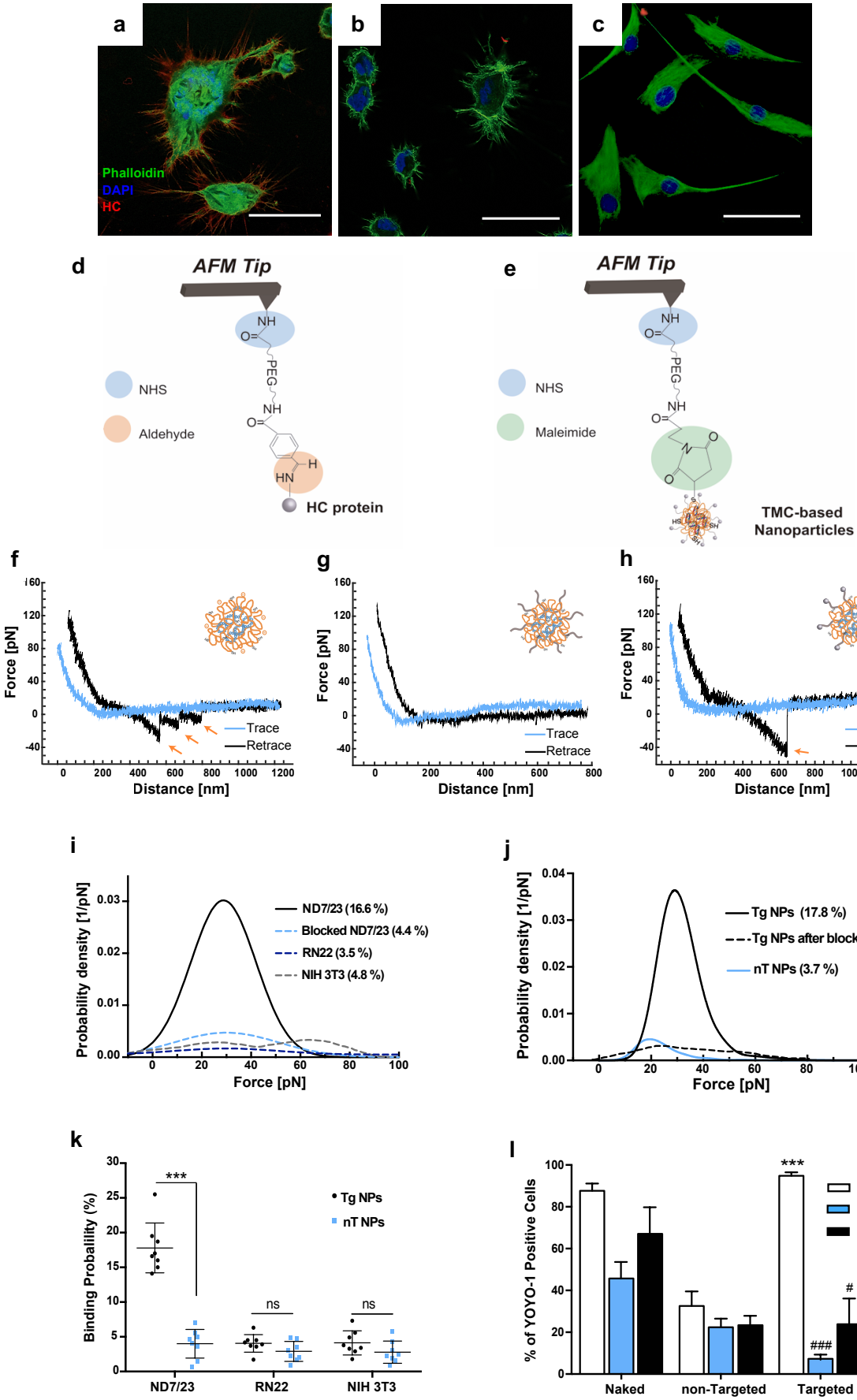
a
b
c
Phalloidin
DAPI
HC
d
AFM Tip
NHS
Aldehyde
PEG
HC protein
e
AFM Tip
NHS
Maleimide
PEG
TMC-based
Nanoparticles
f
g
h
Force [pN]
Distance [nm]
Trace
Retrace
i
Probability density [1/pN]
Force [pN]
ND7/23 (16.6 %)
Blocked ND7/23 (4.4 %)
RN22 (3.5 %)
NIH 3T3 (4.8 %)
j
Probability density [1/pN]
Force [pN]
Tg NPs (17.8 %)
Tg NPs after blocking (5.8 %)
nT NPs (3.7 %)
k
Binding Probaility (%)
Tg NPs
nT NPs
***
ns
ns
ND7/23
RN22
NIH 3T3
l
% of YOYO-1 Positive Cells
ND7/23
RN22
NIH 3T3
***
###
#
Naked
non-Targeted
Targeted

Figure 2. Evaluation of functionalized TMC-based nanoparticles specificity towards neuronal-like cells. Representative images of HC-QDs (red) binding to (a) ND7/23, (b) RN22 and (c) NIH 3T3 cells at 4 ºC; the cytoplasm and nuclei of cells were labelled with Phalloidin (green) and DAPI (blue), respectively (scale bars: 25 μm). Schematic representation of the chemical tethering strategy used to bind (d) the HC fragment or (e) TMC-based NPs (naked, nT or Tg) to an AFM tip via heterobifunctional PEG spacers. Representative force-distance curves obtained in ND7/23 cells for (f) naked, (g) nT and (h) Tg NPs; the presence of unbinding events is denoted by the orange arrays. The probability density function (PDF) of rupture forces showing specificity proof for (i) HC- and (j) NP-functionalized AFM tips; controls were performed by surface blocking with free HC (0.1 mg mL^{-1}) for 1 h; the unbinding probability for each condition is presented inside parentheses. (k) Comparison between the binding probability of nT and Tg NPs in neuronal (ND7/23) and non-neuronal (RN22 and NIH 3T3) cell lines, each dot representing a different data set, corresponding to 1,000-2,000 force-distance curves. The non-parametric multiple t test analysis was used for comparisons between both formulations in the different cell lines: $^{***}p<0.001$. (l) Percentage of YOYO®-1 positive cells after incubation with TMC-based NPs containing labelled plasmid DNA for 2 h; each bar represents the mean of three independent experiments ± SD; the non-parametric multiple t-test analysis was used for comparison between formulations: $^{***}p<0.001$ for comparison between nT and Tg NPs; $^{\#}p<0.05$ and $^{\#\#\#}p<0.001$ when comparing naked with Tg NPs.

3.4. Nanoparticle specificity for neurons in heterogeneous primary neuronal cultures

Following the determination of the binding specificity of the developed NPs in single-cell culture systems, we further proceeded our studies in an in vitro model of higher complexity using primary dissociated DRG mixed cell cultures. These cultures are composed by the heterogeneous collection of cells that is present in the sensory ganglia that lie in the intervertebral foramina. Importantly, the culture reflects the diverse population of cells that constitute a DRG and the isolated sensory neurons retain features observed in vivo (e.g. the capacity to extend neurites). Besides DRG neurons, they are mainly constituted by Schwann cells, satellite cells and fibroblasts.

The HC fragment binding affinity and natural tropism to this mixed cell population was investigated using the previously modified HC-QDs. For neuronal cell identification, DRGs were co-labelled with the anti-βIII tubulin antibody (pan-neuronal marker). All cellular nuclei present in the culture were identified by DAPI staining. Representative images are shown in **Figure 3a-d**. One can observe the preferential binding of HC-QDs to neuronal cell bodies (white arrows), as well as neuronal axons, with negligible labelling being observed around the nuclei of non-neuronal cells. We next proceeded with the determination of the specificity of the HC fragment and the developed NP formulations towards the cells present in the DRG cultures by MRFS studies. By

combining fluorescent microscopy with AFM, one was able to distinguish neuronal (βIII tubulin positive cells) from non-neuronal cells and to locate the AFM tip above the cell type that we wanted to probe. The data obtained from the acquisition of FDC in both neuronal and non-neuronal cells with AFM tips functionalized with either the HC fragment, nT and Tg NPs is depicted in **Figure 3e**. As observed with the cell lines, FCD acquired with tips bearing naked NPs presented multiple bindings resulting from non-specific interactions (data not shown). The BP obtained following the interaction between HC-functionalized AFM tips and neuronal cells was of 29%, which was significantly higher than the value attained in the non-neuronal cells (16%; $p<0.001$). Similar results were obtained for the AFM tips functionalized with Tg NPs, once again proving the targeted vectoring capacity of these NPs. AFM tips functionalized with nT NPs presented a BP of 11%, independently of the cell type being tested ($p>0.05$).

Representative PDF for the interaction between the nT or Tg NPs and specific cells from DRG cultures is shown in **Figure 3f.** Except for the interaction between Tg NPs with neuronal cells from DRGs, all tested conditions showed a multimodal distribution of forces with low binding probabilities. Contrariwise, measurements between Tg NPs and neuronal cells resulted in the appearance of three peaks in the force PDF, having as the most probable force 30 pN with two other force peaks around 60 and 90 pN. For this ligand-receptor pair, most of FDCs present single rupture events, although multiple consecutive rupture events also occurred. **Figure 3g** shows the distribution of rupture events per curve for a representative dataset of a neuronal cell probed with an AFM tip functionalized with Tg NPs, having a total BP of 26.7%. A maximum of 3 consecutive events were observed, although the majority of the FDC with unbinding events only presented one event per curve (~ 70%).

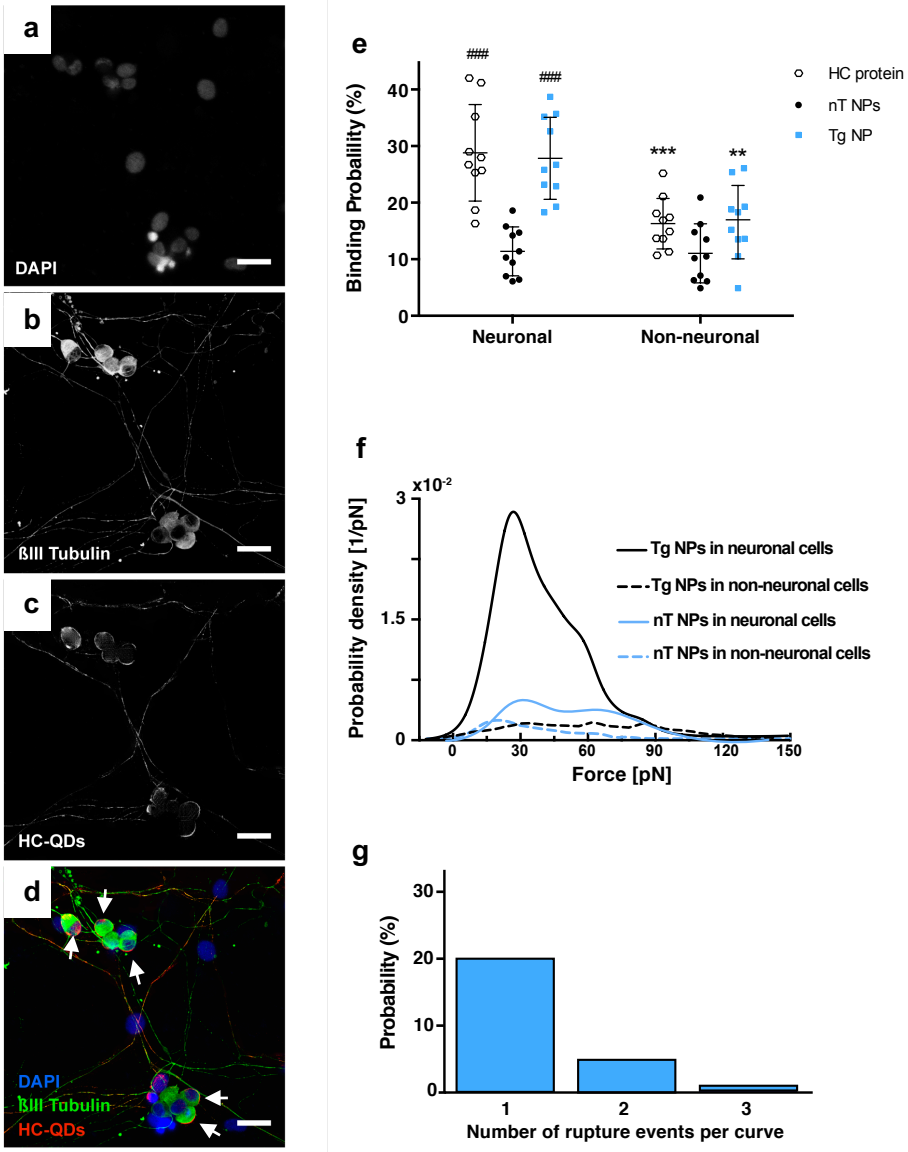

Figure 3. Binding specificity of functionalized TMC-based nanoparticles in primary dissociated dorsal root ganglia (DRG) cultures. (a-d) Representative images for the HC binding pattern in DRG primary cultures; (a) nuclei from all cells present in culture labelled with DAPI, (b) neuronal cells stained for ßIII tubulin and (c) HC-QDs binding pattern after incubation for 30 min at 4ºC; (d) all merged channels, with nuclei (blue), DRG neurons (green) and HC-QDs labelling (red; arrows); scale bars: 25 µm. (e) Comparison between the binding probability of AFM tips functionalized with HC, nT or Tg NPs in neuronal *versus* non-neuronal cells present in the DRG cultures; each dot represents a different data set, corresponding to 1,000-2,000 force-distance curves. The non-parametric multiple t test analysis was used for comparisons between formulations in the different cell lines: $^{###}p<0.001$, when comparing HC or Tg NPs to the nT NPs in neuronal cells; $^{**}p<0.01$ and $^{***}p<0.001$, when comparing each formulation in different cell types (neuronal *versus* non-neuronal). (f) Probability density function (PDF) of rupture forces for AFM tips functionalized with nT and Tg NPs in different cell types. (g) Representative binding statistics of one neuronal cell probed with an AFM tip functionalized with Tg NPs, where the total binding probability was 26.7%.

To validate these data, we further assess the cellular association profile of the developed NPs in primary DRG cultures by confocal microscopy (**Figure 4**). NPs loaded with YOYO®-1-labelled pDNA were incubated with cells for 2 hours. Afterwards, cells were stained for ßIII tubulin and were incubated with a dye that stained the cytoplasm and nuclei of all cells in culture – the HCS Cell Mask™ (Thermo Fisher Scientific). This approach allowed for the distinction of NPs preferentially associated to neurons or to non-neuronal cell types.

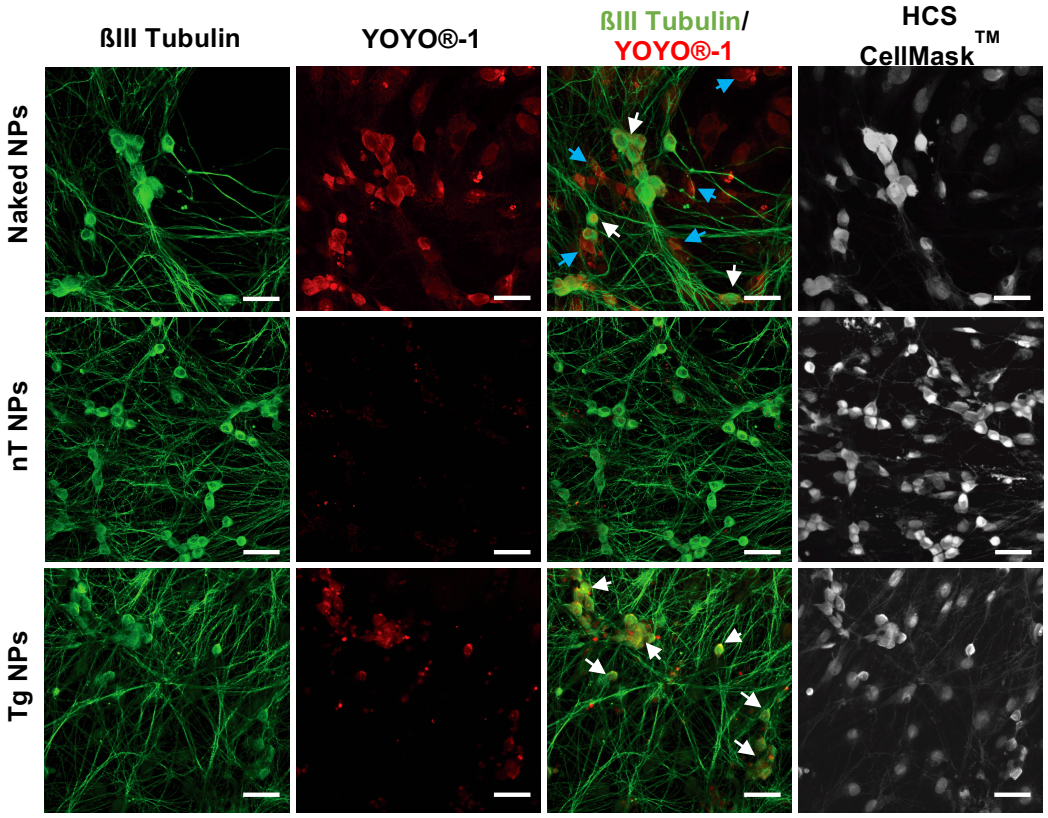

Figure 4. Cellular association of TMC-based nanoparticles to primary dissociated DRG cultures. Representative images of DRG cells incubated with naked, nT or Tg NPs loaded with YOYO®-1-labelled plasmid DNA. For neuronal cell identification, cells were immunostained for ßIII tubulin (green). The NP cargo is identified in red (YOYO®-1). HCS Cell Mask™ (nucleus and cytoplasm stain) was used to identify all cells (neuronal and non-neuronal) present in culture. The white arrows were used to identify NPs uptaken/associated to neuronal cells while the blue arrows label NPs uptaken/associated to non-neuronal cells. All images were acquired with the same laser intensity and contrast settings to allow for qualitative and semi-quantitative comparison between the different NPs profile of cellular association/uptake. Scale bars: 25 µm.

The obtained results corroborated the previous findings attained by MRFS. From the analysis of the images, one can observe that the naked NPs associate to all types of

cells, irrespective of their origin. On the other hand, the nT NPs had minimal association to any cell type present in culture, explained by the stealth effect of the PEG molecules on the NP surface. As determined by MRFS, the Tg NP presented preferential tropism to the DRG neurons, confirming their specificity towards this cell type.

3.5. Nanoparticle targeting capacity towards specific cellular regions in histological sections

The expression and exposure of cellular surface receptors is strongly influenced not only by the cell type but also by the cell-cell cross-talk and the extracellular microenvironment. For that reason, the extrapolation of the results from NP characterization and uptake studies *in vitro* to an *in vivo* scenario is neither easy nor straightforward. In this context, we hypothesized that AFM could be a suitable tool to investigate the targeting capacity of NPs in a model that more closely resembles the *in vivo* scenario and, therefore, expected to be more clinically relevant. So, we next evaluated the interaction between the developed NPs and histological tissue sections. To the best of our knowledge, this is the first time that force spectroscopy studies with NPs were performed in this type of samples.

As our team is working towards the design of gene delivery vectors capable to target peripheral nerves after a minimal invasive peripheral administration (**Figure 5a)**, we next assessed the binding specificity of the developed NPs towards histological sections of the innervated gastrocnemius muscle (site of administration) and the sciatic nerve (final target). Moreover, by taking advantage of the use of fluorescence microscopy combined with AFM, we were able to precisely position the AFM tip to perform MRFS in the subcellular regions of interest. After analyzing the biding profile of HC-QDs in the histological tissue sections (**Figure 5b-c)**, a broad labelling was observed in the sciatic nerve cryo-section, as expected. Contrariwise, in the gastrocnemius muscle sections, HC-QDs fluorescent signal was only found at the neuromuscular junctions (NMJ) in co-localization with the ßIII tubulin staining, with no signal being detected in the muscle tissue.

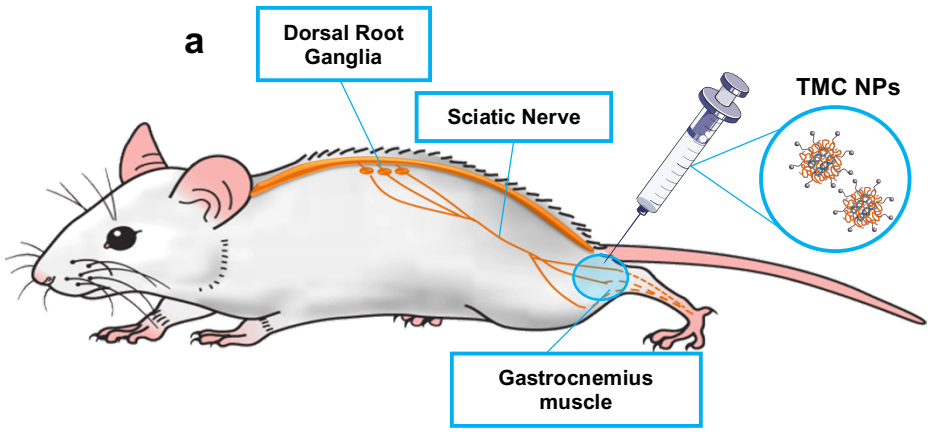
a
Dorsal Root Ganglia
Sciatic Nerve
TMC NPs
Gastrocnemius muscle

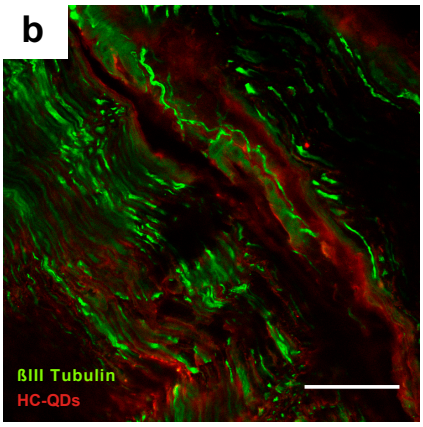
b
ßIII Tubulin
HC-QDs

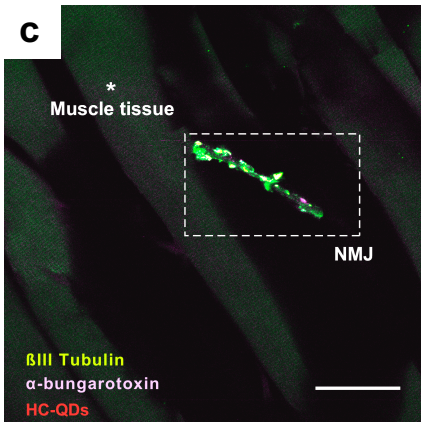
c
*
Muscle tissue
NMJ
ßIII Tubulin
α-bungarotoxin
HC-QDs

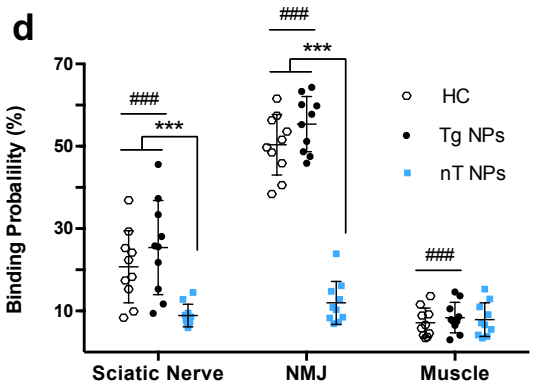
d
Binding Probability (%)
70
50
30
10
###
***
###
***
###
HC
Tg NPs
nT NPs
Sciatic Nerve
NMJ
Muscle

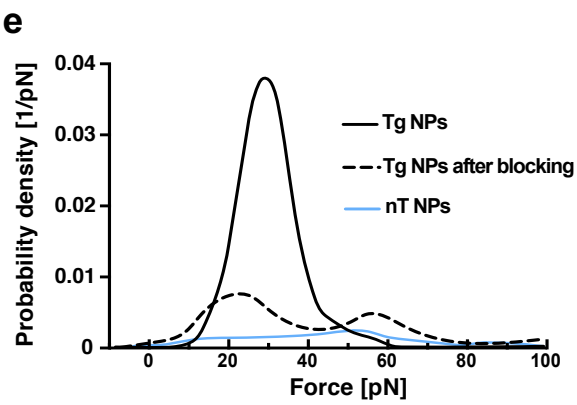
e
Probability density [1/pN]
0.04
0.03
0.02
0.01
0
0
20
40
60
80
100
Force [pN]
Tg NPs
Tg NPs after blocking
nT NPs

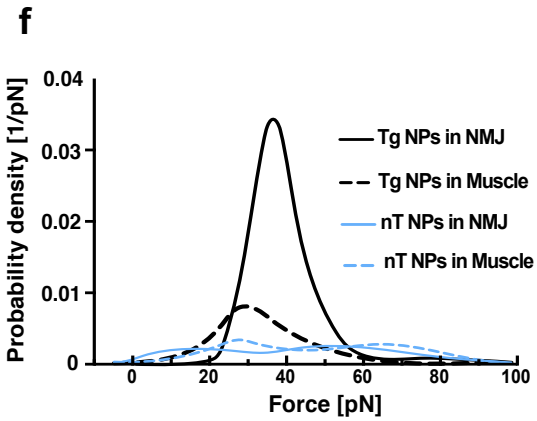
f
Probability density [1/pN]
0.04
0.03
0.02
0.01
0
0
20
40
60
80
100
Force [pN]
Tg NPs in NMJ
Tg NPs in Muscle
nT NPs in NMJ
nT NPs in Muscle

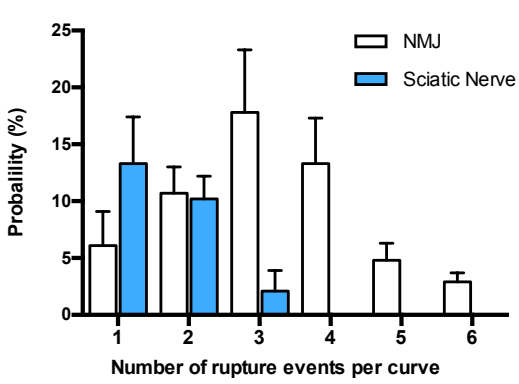
g
Probability (%)
25
20
15
10
5
0
1
2
3
4
5
6
Number of rupture events per curve
NMJ
Sciatic Nerve

Figure 5. Binding specificity of functionalized TMC-based nanoparticles in histological tissue samples. a) Schematic representation of the proposed minimal invasive peripheral administration of the developed Tg NPs in an *in vivo* model. Representative images of HC-QDs binding pattern in tissue cryo-sections of b) sciatic nerve and c) gastrocnemius muscle; the frozen tissue sections were both labeled for βIII tubulin (green) for neuronal identification and the gastrocnemius muscles were further stained with the postsynaptic marker α-bungarotoxin (purple) to allow the identification of neuromuscular junctions (NMJ); HC-QDs labeling is identified in red; scale bars: 50 μm. d) Comparison between the binding probability of AFM tips functionalized with HC, nT or Tg NPs in specific cellular regions in the relevant histological sections, each dot representing a different data set. The nonparametric multiple t-test analysis was used for comparisons between formulations in the different cell lines: ***$p < 0.001$, when comparing the nT NPs binding probability to HC or Tg NPs in the same cellular region; $^{###}p < 0.001$, when comparing HC and Tg NPs binding probability between different cellular regions (sciatic nerve vs NMJ vs muscle). Probability density function (PDF) of rupture forces considering the interaction between the functionalized NPs and the e) sciatic nerve and (f) gastrocnemius muscle tissue cryo-sections; controls were performed by surface blocking with free HC (0.1 mg mL^{-1}) for 1 h.

We then performed MRFS in determined cellular sub-populations of the tissue samples. FDC using NP-functionalized AFM tips were acquired in the sciatic nerve (regions labelled for ßIII tubulin), muscle tissue (no labelling) and NMJ (positive for ßIII and the post-synaptic marker α-bungarotoxin). The comparison between the BP of HC-, nT- or Tg NPs-functionalized tips in the referred cellular regions are presented in **Figure 5d.** Both HC and Tg NPs tips presented comparable results ($p>0.05$), with an average BP between 20-26% in the sciatic nerve. These values were identical to the ones previously obtained with the cellular models here tested (ND7/23 cells and primary neurons), confirming these as good models for testing the specificity of neuron-target NPs. Interestingly, these values were significantly higher ($p<0.001$) in the NMJ, with a BP between 50-55%, and significantly dropped to a BP around 8% in the case of muscle tissue probing ($p<0.001$). Once again, the BP of the nT NPs did not significantly differ among the different cellular regions being tested (8-13%). Moreover, after analysis of the PDF from the interaction between nT and Tg NPs in the sciatic nerve (**Figure 5e**) and in the NMJ **(Figure 5f**), one can observe that only the Tg NPs present monomodal peak distributions, with higher force probabilities around 30-40 pN. Moreover, in the FCD acquired with Tg NPs tips in the NMJ a maximum of 6 consecutive events were observed contrary to the FDC from the sciatic nerve were the occurrence of multiple events was significantly lower (**Figure 5g**) ($p<0.001$).

3.6. Loading rate dependence for HC- or nanoparticle-receptor complexes in models of different complexity

The most probable rupture force obtained for the different datasets (showed in the PDF histograms) is not a unitary value, as it depends on the time scale of the measurement [32]. A receptor-ligand bond present a limited duration that is even shorter when an external force is applied to the bond, owing to thermal activation. In fact, the thermal energy of the surrounding solution also makes bonds break, which is essential for rendering possible time-controlled regulation of ligand-stimulated processes [33]. When a bond is pulled faster than its spontaneous dissociation rate, the ligand-receptor unbinding force depends not only on the molecules themselves but also on the loading rate established for the experiment [11, 34]. In the case of a single energy barrier, the unbinding force rises with the logarithm of the loading rate in a linear fashion, yielding the natural kinetic off-rate constant (k_{off}) that defines the lifetime of the bond in absence of any applied force, as well as the energetic barrier length scale ($x_ß$). To determine the loading rate dependence of both the HC fragment and the HC-functionalized NPs (Tg NPs) in the biological models under testing, unbinding forces were evaluated at various retraction velocities (300 to 2,000 nm s^{-1}). The most probable rupture forces were then plotted against the logarithm of the actual loading rate (r). The loading rate was then computed by multiplying the retraction velocity by the effective spring constant (k_{eff}), which can be inferred from the slope of the FDC at rupture [35].

The loading rate dependence for the interaction between HC or Tg NPs in ND7/23 cells, primary cell cultures or tissue histological samples are shown in **Figure 6a**, **6b** and **6c**, respectively. For each dataset, a continuous curve with a linear slope was found, fitting the described theory. The obtained values of $x_β$ and k_{off} did not significantly varied among the tested conditions (**Table 2**) ($p>0.05$). The fact that both HC or HC-functionalized NPs present identical rupture forces, independently of whether they were tested in cells or tissue samples, indicates that the functionalization of these NPs did not alter the binding kinetics between HC and its cellular receptors, and moreover, that no significance differences were observed among the different models tested.

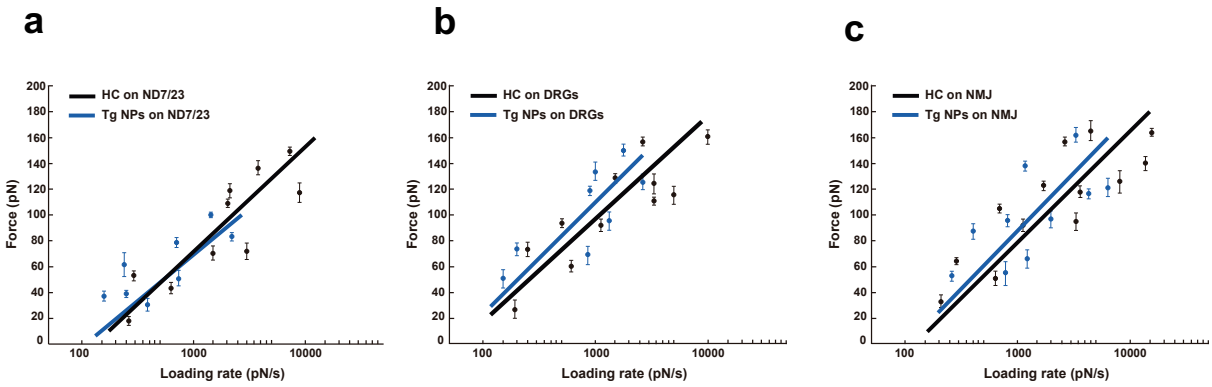

Figure 6. Loading rate dependence of HC fragment *versus* HC-functionalized TMC nanoparticles. Fitting of the measured unbinding forces at different loading rates considering the interaction between the HC fragment (black line) or Tg NPs (blue line) and a) ND7/23 cells, b) DRG primary cultures, and c) neuromuscular junctions (NMJ) in histological tissue sections.

Table 2. Kinetic parameters for HC fragment *versus* Tg NPs interaction with different biological models.

	$x_{ß}$ [Å][a]	k_{off} [s^{-1}][b]
HC on ND7/23	1.17 ± 0.03	7.48 ± 0.38
Tg NPs on ND7/23	1.33 ± 0.45	6.97 ± 0.40
HC on DRGs	2.43 ± 0.39	7.81 ± 0.24
Tg NPs on DRGs	2.24 ± 0.22	7.49 ± 0.31
HC on NMJ	2.15 ± 0.19	7.33 ± 0.50
Tg NPs on NMJ	1.48 ± 0.31	6.52 ± 0.26

[a]Energy barrier width and [b]kinetic off-rate

4. Discussion

Tailored drug-delivery systems have become increasingly important in the development of novel medical therapies and pharmaceutical products [11]. Interestingly, regardless of the substantial preclinical research efforts into developing actively targeted drug delivery systems, these technologies are still lacking in approved products and in clinical trials [36].

In addition to providing high-resolution topographical images of sample surfaces, AFM can be used to explore receptor ligand interactions at the molecular scale. Moreover, the possibility of tailoring the AFM probe with different chemical groups and individual molecules, coupled with the ability to carry out measurements under near-physiological conditions, made this approach ideal for the pharmaceutical and life sciences [37]. To date, most MRFS studies were performed either on receptors isolated on surfaces or using fixed or live cells. However, this approach is not representative of what happens in an *in vivo* setting. The microenvironment of a cell is complex and is composed by other cells (either of the same origin or different), extracellular matrix components, fluids and various molecular factors derived from these. The feedback loops of a cell and its surrounding are indispensable for cellular homeostasis and highly influences cell behavior, including the expression of certain molecules at the cellular membrane [38].

Taking this into consideration, the main goal of this study was to propose a methodology to assess the specificity of neuron-targeted NPs towards biological models of higher complexity and clinical relevance. For this, we exploited the presence of thiol groups at the surface of the previously developed neuron-targeted TMC-based NPs to stably attach them to an AFM tip and probe them against cell lines, heterogeneous primary cell cultures and histological tissue sections of clinically relevant sites of administration. As these NPs already proved to have neural tropism, they represent a good tool to validate MRFS throughout the different biological models under testing.

Our results show the selective binding and internalization of the Tg NPs towards the neuronal cell line (ND7/23 cells), in opposition to fibroblasts or Schwann cells (NIH 3T3 or RN22 cells, respectively). More importantly, the Tg NP selectivity towards neuronal cells was reinforced when these were tested in a more complex cell culture system as the DRG primary cultures. Furthermore, in this model, a higher frequency of multiple unbinding events was observed, pointing to a higher abundance of HC receptors

expression than on the ND7/23 cell line. These results are in accordance to other studies that have reported a high expression level of the ganglioside family of receptors in DRGs, specially the GT1b receptors – around 85% in small and > 90% in medium and large DRG neurons in rat, mice or human tissues (as determined by immunohistochemistry) [39]. Moreover, the expression of GT1b was found to be superior in the neuronal cell bodies and nerve termini, compared to peripheral nerve trunks [40]. This could explain our results, as the data acquired for neuronal cells present in the DRG primary cultures was obtained from performing FDC in neuronal cell bodies. In contrast, the nT NPs presented a statistically significant lower BP, independently of being probed against neuronal or non-neuronal cells. Moreover, the data from confocal microscopy validate the obtained results from MRFS, where the selective binding of Tg NPs towards neuronal cells could be observed. Overall, this set of results validate the use of AFM to evaluate NP neuronal vectoring capacity in both cell lines and DRG primary cultures, and allowed us to obtain new insights into HC receptor expression levels in both systems.

As the ultimate goal of the development of this NP system is to obtain a vector to be administered *in vivo* via a minimal invasive route, we further evaluated the vectoring capacity of the neuron-targeted TMC NPs in histological tissue sections of clinically relevant sites of administration. Our results showed similar results of binding probability and forces for FDC acquired in the sciatic nerve, when compared to the results obtained in neuronal cells from the primary DRG cultures. We would expect to have a slight increase in the binding probability as the binding of HC-QDs to this tissue sample is very abundant around the axonal extensions. However, when performing MRFS in a histological cryo-section of the sciatic nerve, one has to consider that some regions of the nerve trunk present in the tissue section will be myelinated and, therefore, the neuron cell membrane will not be exposed. This also justifies the higher variance of binding probability values observed (ranging from 9.4 to 45.6%). Nevertheless, in the innervated NMJ from gastrocnemius muscle sample, a statistically significant high percentage of unbinding events per tip was observed, confirming that this is a suitable tissue for the peripheral administration of the NPs. Also, our data show that in the NMJ the HC receptors density is very high as the majority of the FDC obtained in these specimens presented between 2 to 4 unbinding events, explained by the interaction of multiple HC moieties present at the surface of the probed NP. This can be either GT1b

receptors or other types of gangliosides, which can also interact with the HC fragment. However, and since the binding forces are identical between each unbinding event, we believe that these unbinding events result from the higher density of the GT1b receptors in this region. The specificity of this interaction was proven through the acquisition of FDC in the muscle, with both Tg and nT NPs, where a significant drop of the BP was observed.

We further determined the rupture forces between the HC or Tg NPs and the different biological models and, as expected, found a logarithmic dependence of the rupture force with increasing loading rates. This behavior is in accordance with a well-established theory for receptor-ligand interaction [32], proving once more the specificity of the observed unbinding events. Moreover, no significant differences were found between rupture forces or the kinetics of ligand-receptor interaction between the tested NPs and the HC protein (independently of the model tested). This result assures that the neuron-targeting effect of the TMC-based NPs is being mediated by the HC molecules exposed at the NP surface through the used PEG spacer.

In summary, this biotechnological study shows the feasibility of the proposed method for the development and characterization of targeted nanomedicines in different biological models.

5. Conclusion

The development of techniques able to correctly evaluate NP vectoring capacity is in emergent need. Moreover, it is important to have a reliable method that allows reproducible and comparable results independently of the model being tested (isolated cell lines, heterogeneous cellular cultures or tissue samples) to fasten the development of these nanoparticulate systems. We believe that MRFS has the potential to be used as a screening and characterization tool that will fasten comparative investigations of different drug-delivery systems and targeting agents. Moreover, by combining fluorescent microscopy with AFM force spectroscopy one is able to correlate the specific interactions of the ligand-receptor pair in specific cells of heterogeneous primary cultures or cellular regions of histological sections. As this technology allows for the evaluation of native biological samples under physiological conditions, it could be used to assess cell targeting regardless of the desired application.

Acknowledgments

The authors would like to acknowledge the Bioimaging Center for Biomaterials and Regenerative Therapies of INEB (b.IMAGE) for the support with atomic force and confocal microscopy, Centro de Materiais da Universidade do Porto (CEMUP) for NMR analysis and the Biointerfaces and Nanotechnology Service (INEB-i3S) for nanoparticle size and zeta potential analysis. The work was financed by Portuguese funds through FCT (Fundação para a Ciência e a Tecnologia) in the framework of the projects UID/BIM/04293/2013, PTDC/CTM-NAN/115124/2009 and PTDC/CTM-NAN/3547/2014. CP Gomes and CDF Lopes acknowledge FCT for their PhD scholarships SFRH/BD/79930/2011 and SFRH/BD/77933/2011, respectively.

Supplementary Materials and Methods

Polymer characterization

Polymer molecular weight was determined by gel permeation chromatography (GPC). Measurements were performed in 0.33 M $NaCH_3COOH$ / 0.28 M CH_3COOH eluent at a flow rate of 1 mL min^{-1}. The average number molecular weight of the starting material was found to be 43.3 ± 5.0 kDa. The degree of acetylation (DA) and degree of quaternization (DQ) were assessed by proton nuclear magnetic resonance (^{1}H-NMR). Polymer samples were dissolved in D_2O (5 mg mL^{-1}) at 60ºC overnight and further analyzed in a digital spectrometer (Bruker Avance III 400) at room temperature (RT) with a total of 200 scans. The % DA was calculated according to Mourya *et al* [41] and the % of DQ was calculated following the equation reported by Curti and Campana-Filho [42], and were found to be 15.7 ± 0.9 and 30.1 ± 4.6 %, respectively. Endotoxin levels of the purified polymer extracts were assessed using the Limulus Amebocyte Lysate Assay (QCL-1000, Cambrex) and were found to be < 0.1 EU mL^{-1}, respecting the US Department of Health and Human Services guidelines for implantable devices [43].

Determination of polymer thiol content

The degree of polymer thiolation was quantified with 5,5-dithio-bis-(2-nitrobenzoic acid) (DTNB, Ellman's reagent) [20]. The amount of free thiol groups grafted to the polymer was determined based in a previously described protocol [44]. Briefly, DTNB was dissolved in 0.1 M sodium phosphate buffer, pH 8 at a final concentration of 100 µg mL^{-1}. The polymer samples were dissolved in the same solution at a final concentration of 2.5 mg mL^{-1}. Then, 20 µL of the polymer solution was mixed with 180 µL of DTNB reagent solution in a microplate and after incubation of 15 min at RT the absorbance was measured at a wavelength of 405 nm (Spectra Max GeminiXS, Molecular Devices). Cysteine standards were used to calculate the amount of free thiol moieties in the polymer. The degree of thiolation was calculated using the estimated average molecular weight per glucosamine unit.

Transmission electron microscopy (TEM)

The morphology of TMC-based NPs was characterized by TEM. Briefly, 10 µL of the nanoparticle suspension was placed on a grid, treated with sodium phosphotungstate, and observed in a TEM Zeiss 902 A. To assess the presence and distribution of the PEGylated HC at the NPs surface, the targeted NPs were prepared with HC conjugated to Qdot® 705nm ITK^{TM} carboxyl quantum dots (QDs) (Invitrogen) before its complexation with the polymer. The resulting NPs were adsorbed on a grid and imaged by TEM, without any further treatment.

Plasmid DNA

The plasmid DNA (pDNA) used encoded for the enhanced Green Fluorescent Protein and Luciferase (eGFP and Luc; pCMV-eGFPLuc, 6.7 kb, Invitrogen) genes. Plasmid was produced in a DH5α competent *E. coli* strain transformed with the respective plasmid under the cytomegalovirus (CMV) promoter. Subsequently, pDNA purification was performed using an EndoFree Plasmid Giga Kit following the manufacturer instructions (Qiagen). Plasmid concentration and purity were assessed by ultraviolet spectroscopy (Nanodrop 1000, Thermo Scientific). Only plasmid solutions with an absorbance (260/280 nm) ratio comprised between 1.8 and 2.0 were used.

Tetanus toxin production and modification

The non-toxic carboxylic fragment (HC) of the tetanus neurotoxin (TeNT) was produced recombinantly using the BL21 *E. coli* strain and subsequently purified as described by Sinha *et al*.[29] The plasmid encoding for the HC fragment was a kind offer from Prof. Neil Fairweather (King's College, UK). Successively, the obtained HC fragment was covalently linked to a bifunctional 5 kDa PEG spacer (JenKem Technology) holding a N-hydroxysuccinimide (NHS) and a maleimide (MAL) end group, as previously described.[14, 15] The amount of reactive MAL groups in the HC protein was determined using a modified Ellman's assay,[14, 15] and found to be 2.1 ± 0.4 mol PEG/HC.

Cells

Cell lines: ND7/23 (mouse neuroblastoma (N18 tg 2)×rat dorsal root ganglion neuron hybrid; selected as a sensorial peripheral nervous system cell model), NIH 3T3 (mouse embryonic fibroblast) and RN22 (immature rat Schwann) cell lines (all obtained from ECACC) were routinely cultured in Dulbecco's Modified Eagle Medium (DMEM) with Glutamax, supplemented with 10% (w/v) fetal bovine serum (FBS) (heat inactivated at 57°C for 30 min) and 1% PS (10,000 U mL^{-1} penicillin and 10,000 µg mL^{-1} streptomycin), all supplied by Gibco®, and maintained at 37°C in a 5% CO_2 humidified incubator. Cells were routinely tested for mycoplasma by standard PCR. For molecular recognition force spectroscopy studies, cells were seeded in 22 mm diameter glass coverslips previously coated with 0.01 mg mL^{-1} poly(D-lysine) (PDL, molecular weight 30 – 70 kDa, Sigma-Aldrich) for 1 hour at 37ºC before mounting on the AFM sample plate. Cells were seeded to achieve a confluence state around 60% in order to be able to acquire force-distance cycles on isolated cells.

Primary dorsal root ganglia (DRG) cultures: Primary embryonic rat DRG neurons were isolated from Wistar embryo rats (E18). Briefly, rat embryos were dissected in Hank´s buffer solution (Sigma-Aldrich) and enzymatically treated with 1.25% (w/v) collagenase type II (Gibco®) at 37°C for 90 minutes. Subsequently, collagenase was removed and DRGs washed three times in DMEM followed by sequential mechanical dissociation with 1,000 µL and 200 µL pipette tips. Viable cells were counted using the trypan blue (0.4% (w/v), Sigma-Aldrich) exclusion assay. Dissociated DRG neurons were seeded at a density of 6.4 x 10^4 viable cells per cm^2 in 35 mm glass bottom petri dishes (10 mm well diameter, MatTek) previously coated with 0.01 mg mL^{-1} of poly(D-lysine) (PDL, molecular weight 30 – 70 kDa, Sigma-Aldrich) overnight at 37°C. Cells were cultured in complete neuron culture medium constituted by DMEM/Ham´s F12 with GlutaMAX™ (DMEM/F12), 1% PS, 25 ug mL^{-1} fungizone, 2% (v/v) B27 supplement (all from Gibco®) and 50 ng mL^{-1} of nerve growth factor (NGF) 7S (Calbiochem®, Millipore) in a humidified incubator at 37°C supplied with 5% CO_2. After two days in culture, cells were washed with phosphate buffered saline (PBS) and subsequently fixed with 4% (w/v) paraformaldehyde (PFA). In the supplementary information, is described the protocol for neuronal discrimination as well as the purity of the cultures. To discriminate neurons from non-neuronal cells present in culture, fixed cells were immunostained against βIII tubulin, a neuron-specific microtubule marker, using the monoclonal antibody mouse

anti-βIII tubulin (1:1,000; Promega) and nuclei were stained with 0.1 μg mL^{-1} 4',6-diamidino-2-phenylindole (DAPI) (Sigma-Aldrich). Non-neuronal cells were identified solely by nuclei staining. This DRG neuron isolation protocol resulted in 72% of neuron purity at 48 hours post-seeding, determined by the % of neurons (βIII tubulin positive) in relation to the total number of cells in culture.

Animal experimentation

All experiments using animals were carried out with the permission of the local animal ethical committee in accordance with the EU Directive (2010/63/EU) and Portuguese law (DL 113/2013). The experimental protocol (reference 421/000/000/2013) was approved by the ethics committee of the Portuguese official authority on animal welfare and experimentation (*Direção-Geral de Alimentação e Veterinária*).

References

1. Reddy, P.D. and D. Swarnalatha, "Recent Advances in Novel Drug Delivery Systems." International Journal of PharmTech Research, 2010. 2(3): p. 2025-2027.
2. Tosi, G., B. Ruozi, and D. Belletti, "Nanomedicine: the future for advancing medicine and neuroscience." Nanomedicine (Lond), 2012. 7(8): p. 1113-6.
3. Wang, A.Z., F. Gu, and O.C. Farokhzad, "Biofunctionalized targeted nanoparticles for therapeutic applications." Expert Opin. Biol. Ther, 2008. 8(8): p. 1063-1070.
4. Emerich, D.F. and C.G. Thanos, "The pinpoint promise of nanoparticle-based drug delivery and molecular diagnosis." Biomolecular Engineering, 2006. 23(4): p. 171-184.
5. Arachchige, M., Y. Reshetnyak, and O. Andreev, "Advanced targeted nanomedicine." J Biotechnol, 2015. 202: p. 88-97.
6. Debbage, P., "Targeted drugs and nanomedicine: present and future." Curr Pharm Des, 2009. 15(2): p. 153-72.
7. Curtis, C., et al., "Systems-level thinking for nanoparticle-mediated therapeutic delivery to neurological diseases." Wiley Interdiscip Rev Nanomed Nanobiotechnol, 2017. 9(2): p. e1422.
8. Kumar Khanna, V., "Targeted delivery of nanomedicines." ISRN Pharmacol, 2012. 2012: p. 571394.
9. Vyas, S.P., A. Singh, and V. Sihorkar, "Ligand-receptor-mediated drug delivery: an emerging paradigm in cellular drug targeting." Crit Rev Ther Drug Carrier Syst, 2001. 18(1): p. 1-76.
10. Kamaly, N., et al., "Targeted polymeric therapeutic nanoparticles: design, development and clinical translation." Chem Soc Rev, 2012. 41(7): p. 2971-3010.
11. Lamprecht, C., P. Hinterdorfer, and A. Ebner, "Applications of biosensing atomic force microscopy in monitoring drug and nanoparticle delivery." Expert Opin Drug Deliv, 2014. 11(8): p. 1237-53.
12. Muller, D.J. and Y.F. Dufrene, "Atomic force microscopy: a nanoscopic window on the cell surface." Trends Cell Biol, 2011. 21(8): p. 461-9.
13. Oliveira, H., et al., "Molecular Recognition Force Spectroscopy: A New Tool to Tailor Targeted Nanoparticles." Small, 2011. 7(9): p. 1236-1241.
14. Oliveira, H., et al., "Targeted gene delivery into peripheral sensorial neurons mediated by self-assembled vectors composed of poly(ethylene imine) and tetanus toxin fragment c." Journal of Controlled Release, 2010. 143(3): p. 350-358.
15. Lopes, C.D., et al., "Microfluidic-based platform to mimic the in vivo peripheral administration of neurotropic nanoparticles." Nanomedicine (Lond), 2016. 11(24): p. 3205-3221.
16. Lopes, C.D., et al., "In vivo targeted gene delivery to peripheral neurons mediated by neurotropic poly(ethylene imine)-based nanoparticles." Int J Nanomedicine, 2016. 11: p. 2675-83.
17. Lopes, C.D., et al., "BDNF gene delivery mediated by neuron-targeted nanoparticles is neuroprotective in peripheral nerve injury." Biomaterials, 2017. 121: p. 83-96.
18. Moreno, P.M., et al., "Delivery of Splice Switching Oligonucleotides by Amphiphilic Chitosan-Based Nanoparticles." Mol Pharm, 2016. 13(2): p. 344-56.
19. Gomes, C.P., et al., "A high-throughput bioimaging study to assess the impact of chitosan-based nanoparticle degradation on DNA delivery performance." Acta Biomater, 2016. 46: p. 129-140.

20. Ellman, G.L., "Tissue sulfhydryl groups." Arch Biochem Biophys, 1959. 82(1): p. 70-7.

21. Chakraborty, S., et al., "Cholera toxin B conjugated quantum dots for live cell labeling." Nano Lett, 2007. 7(9): p. 2618-26.

22. Ebner, A., P. Hinterdorfer, and H. Gruber, "Comparison of different aminofunctionalization strategies for attachment of single antibodies to AFM cantilevers." Ultramicroscopy, 2007. 107(10-11): p. 922-7.

23. Wildling, L., et al., "Linking of sensor molecules with amino groups to amino-functionalized AFM tips." Bioconjug Chem, 2011. 22(6): p. 1239-48.

24. Butt, H.-J. and M. Jaschke, "Calculation of thermal noise in atomic force microscopy." Nanotechnology, 1995. 6(1): p. 1.

25. Hutter, J. and J. Bechhoefer, "Calibration of atomic force microscopy cantilevers." Rev. Sci. Instrum, 1993. 66: p. 1868-1873.

26. Baumgartner, W., P. Hinterdorfer, and H. Schindler, "Data analysis of interaction forces measured with the atomic force microscope." Ultramicroscopy, 2000. 82(1): p. 85-95.

27. Oliveira, H., et al., "Chitosan-based gene delivery vectors targeted to the peripheral nervous system." Journal of Biomedical Materials Research Part A, 2010. 95A(3): p. 801-810.

28. Germershaus, O., et al., "Gene delivery using chitosan, trimethyl chitosan or polyethylenglycol-graft-trimethyl chitosan block copolymers: establishment of structure-activity relationships in vitro." J Control Release, 2008. 125(2): p. 145-54.

29. Sinha, K., et al., "Analysis of mutants of tetanus toxin HC fragment: ganglioside binding, cell binding and retrograde axonal transport properties." Molecular Microbiology, 2000. 37(5): p. 1041-1051.

30. Herreros, J., G. Lalli, and G. Schiavo, "C-terminal half of tetanus toxin fragment C is sufficient for neuronal binding and interaction with a putative protein receptor." Biochem. J., 2000. 347: p. 199-204.

31. Hinterdorfer, P., et al., "Detection and localization of individual antibody-antigen recognition events by atomic force microscopy." Proceedings of the National Academy of Sciences, 1996. 93(8): p. 3477-3481.

32. Evans, E. and K. Ritchie, "Dynamic strength of molecular adhesion bonds." Biophys J, 1997. 72(4): p. 1541-55.

33. Hinterdorfer, P. and Y.F. Dufrêne, "Detection and localization of single molecular recognition events using atomic force microscopy." Nature Methods, 2006. 3(5): p. 347-355.

34. Kienberger, F., et al., "Molecular Recognition Imaging and Force Spectroscopy of Single Biomolecules." Acc. Chem. Res., 2006. 39(29-36).

35. Evans, E. and K. Ritchie, "Strength of a weak bond connecting flexible polymer chains." Biophys J, 1999. 76(5): p. 2439-47.

36. Anselmo, A.C. and S. Mitragotri, "Nanoparticles in the clinic." Bioengineering & Translational Medicine, 2016. 1: p. 10-29.

37. Variola, F., "Atomic force microscopy in biomaterials surface science." Physical chemistry chemical physics : PCCP, 2015. 17(5): p. 2950-9.

38. Ludwig, T., et al., "Probing cellular microenvironments and tissue remodeling by atomic force microscopy." Pflugers Arch, 2008. 456(1): p. 29-49.

39. Gong, Y., et al., "Localization of major gangliosides in the PNS: implications for immune neuropathies." Brain : a journal of neurology, 2002. 125(Pt 11): p. 2491-506.

40. Massaad, C.A., et al., "Fluorescently-tagged anti-ganglioside antibody selectively identifies peripheral nerve in living animals." Scientific reports, 2015. 5: p. 15766.

41. Mourya, V.K. and N.N. Inamdar, "Trimethyl chitosan and its applications in drug delivery." J Mater Sci Mater Med, 2009. 20(5): p. 1057-79.

42. Curti, E. and S.P. Campana-Filho, "Viscosity behavior of chitosan and N,N,N-trimethylchitosan chloride salts in acid-free aqueous solution." Journal of Macromolecular Science-Pure and Applied Chemistry, 2006. A43(3): p. 555-572.

43. FDA/USA Administration., *Guidance for Industry - Pyrogen and Endotoxins Testing*, 2012, U.S. Department of Health and Human Services: United States.

44. Verheul, R.J., S.v.d. Wal, and W.E. Hennink, "Tailorable Thiolated Trimethyl Chitosans for Covalently Stabilized Nanoparticles." Biomacromolecules, 2010. 11: p. 1965–1971.

CHAPTER VII

FINE TUNING NEURONAL TARGETING OF NANOPARTICLES BY ADJUSTING THE LIGAND GRAFTING DENSITY AND COMBINING PEG SPACERS OF DIFFERENT LENGTH

Fine tuning neuronal targeting of nanoparticles by adjusting the ligand grafting density and combining PEG spacers of different length

Carla Pereira Gomes[1,2,3], Victoria Leiro[1,2], Cátia Daniela Ferreira Lopes[1,2,4] and Ana Paula Pêgo[1,2,3,5]

1 – INEB – Instituto de Engenharia Biomédica, Universidade do Porto

2 – i3S – Instituto de Investigação e Inovação em Saúde, Universidade do Porto, Porto, Portugal

3 – Faculdade de Engenharia da Universidade do Porto, R. Dr. Roberto Frias, 4200-465 Porto, Portugal

4 – Faculdade de Medicina da Universidade do Porto, Alameda Prof. Hernâni Monteiro, 4200-319 Porto, Portugal

5 – ICBAS – Instituto de Ciências Biomédicas Abel Salazar, Universidade do Porto, Rua de Jorge Viterbo Ferreira 228, 4050-313 Porto, Portugal

Manuscript submitted for publication

Abstract

Poly(ethylene glycol) (PEG) has been extensively used to coat the surface of nanocarriers to improve their physicochemical properties and allow the grafting of targeting moieties. Still, to date there is no common agreement on the ideal PEG coverage-density or length to be used for optimum vector performance. In this study, we aimed to investigate the impact of both PEG density and length on the vectoring capacity of neuron-targeted gene-carrying trimethyl chitosan nanoparticles. The non-toxic fragment from the tetanus toxin (HC) was coupled to a 5 kDa heterobifunctional PEG (HC-PEG_{5k}) reactive for the thiol groups inserted into the polymer backbone and grafted at different densities onto the nanoparticles. Internalization and transfection studies on neuronal versus non-neuronal cell lines allowed to determine the PEG density of 2 mol% of PEG chains per mol of primary amine groups as the one with superior biological performance. To enhance HC exposure and maximize cell-nanoparticle specific interaction, NPs containing different ratios of HC-PEG_{5k} and 2 kDa methoxy-PEG at the same grafting density were produced. By intercalating HC-PEG_{5k} with methoxy-PEG_{2k} we attained the best performance in terms of internalization (higher payload delivery into cells) and transfection efficiency, using twice lower amount of HC. This outcome highlights the need for fine-tuning of PEG-modified nanoparticles towards the achievement of optimal targeting.

1. Introduction

The primary goal of nanomedicine is to improve clinical outcomes [1]. Towards this end, one of the major challenges in the field is the ability to develop formulations with high efficacy and selectivity towards a desired target. The possibility of engineering nanoparticles (NPs) with appropriate surface chemistries allows for the partitioning of the therapeutic molecules toward the diseased tissues, increasing the payload delivery in the desired areas of action and limiting unwanted side effects [1-3].

In recent years, we have witnessed the development of an enormous array of systems designed to fulfill these demands. Among all nanocarriers, polymer-based NPs offer significant advantages over other platforms for targeted delivery of drugs, proteins or nucleic acids. Polymeric materials have emerged as a major class of controlled release systems due to their unique physicochemical properties that can be readily manipulated [4]. As a result of this versatility, polymer-based NPs can be formulated to deliver a high range of biomolecules, to allow grafting of different types of ligands into their matrices as well as to be biodegradable. This allows for the tailoring of NPs to achieve active targeting properties that will render them adaptable to multiple clinical settings, with improved efficacy and safety [1, 5].

To promote active targeting, researchers have been using different molecules that possess high affinity towards a unique molecular signature to direct the binding of NPs to receptors differentially expressed on (diseased) tissues or cells, such as antibodies, protein and protein fragments, small molecules, peptides or aptamers [3, 6]. One of the most popular strategy for NP surface grafting of targeting moieties has been through the use of poly(ethylene glycol) (PEG) as a spacer [7]. The addition of this hydrophilic polymer serves different purposes. Other than serving as an intermediate linker/spacer to connect the desired targeting moieties onto NPs, PEG is expected to render these with “stealth” properties, decreasing biofouling by plasma proteins and non-specific immune clearance, and to contribute to the exposure of the targeting moieties at their surface. However, the use of a too dense PEG layer will hinder NP cellular uptake and endosomal escape [8]. This phenomenon is recognized as the “PEG dilemma” [9], and consists in achieving the right balance of PEGylation in order to effectively avoid undesired interactions with extracellular components, without compromising cellular uptake by the desired cell population [8, 10].

Our team has been working on the development of a suitable NP to vectorize therapeutic genes to peripheral neurons in a targeted fashion, after a peripheral and minimally invasive administration. For this, we have chosen trimethyl chitosan (TMC) as starting material due to its suitable properties for non-viral gene delivery, namely its biocompatibility and low toxicity, easiness of chemical modification, plasmid DNA (pDNA) condensation efficiency and good solubility at physiological conditions [11, 12]. So far, the obtained results are very promising, as we were able to design a NP with improved stability and adequate degradation kinetics at physiological conditions [12] that is able to specifically interact with neurons [13] and upon internalization suffer retrograde transport [14]. Moreover, in an *in vivo* setup these NPs were able to accelerate the recovery of a crushed nerve by preventing nerve degeneration and enhancing nerve regeneration in a specific fashion [15]. Hereupon, we went further in optimizing the targeting ligand exposure at the NP surface, as this is a feature of paramount importance to promote maximum cell interaction and NP biological performance.

To date, few studies have considered fundamental aspects for targeted NP design such as the effect of the PEG chain length, flexibility and conformation on ligand-receptor interactions. Both the targeting ligand density and PEG conformation at the NP surface – brush or mushroom-like – should be tightly balanced to achieve NP maximum cell interaction and internalization [10]. In fact, the PEGylation of NPs with identical single chains could hinder the ligand free motion, particularly at high PEG densities, resulting in a reduced accessibility of the ligands towards their cellular receptors [16].

Based on the above, the main goal of the present study was first to determine the optimal ligand grafting density and exposure at the surface of polymeric biodegradable NPs, in order to achieve optimal vectoring capacity towards neuron-like cells. For this, we compared in a systematic manner the physicochemical properties and the internalization and transfection efficiency of TMC NPs grafted with the non-toxic and neurotropic C-terminal fragment of the tetanus toxin heavy chain (HC) through the covalent attachment of a 5 kDa PEG spacer (PEG_{5k}) at different densities. After establishing the optimal grafting density, we further investigated the effect of the PEG chain organization on the ligand exposure at the neuron-targeted NPs surface

by testing mixed ratios of a HC-tethered PEG (HC-PEG_{5k}) and a shorter methoxy-terminated PEG chain of 2 kDa (MeO-PEG_{2k}). To determine the best NP formulation in terms of cell-specific interaction, we took advantage of imaging flow cytometry, an advanced bioimaging technique with powerful statistical power [12] that allowed us to evaluate the impact of the fine-tuning functionalization of the developed NPs on their internalization and pDNA delivery in different cell lines.

With this work, we show the importance of determining the right PEGylation grafting density and targeting moiety exposure as key parameters for the development of effective targeting non-viral nanocarriers.

2. Materials and Methods

2.1. Trimethyl chitosan purification and characterization

Trimethyl chitosan (TMC) derived from ultra-pure chitosan produced from *Agaricus bisporus* mushrooms, was provided by Kytozyme (lot VIHA0013-157, Belgium). Prior to use, the polymer was purified by filtration and dialysis and characterized as previously described [12]. The molecular weight was determined by gel permeation chromatography to be 43.3 ± 5.0 $kg.mol^{-1}$. Acetylation and quaternization degrees were calculated by ^{1}H-Nuclear Magnetic Resonance spectroscopy and found to be 15.7 ± 0.9% and 30.1 ± 4.6%, respectively. Endotoxin levels of the purified polymer extracts were assessed using the Limulus Amebocyte Lysate Assay (QCL-1000, Cambrex Bio Science, USA), following the manufacturer instructions and were found to be < 0.1 $EU.mL^{-1}$, respecting the US Department of Health and Human Services guidelines for implantable devices [17].

2.2. Synthesis of thiolated trimethyl chitosan (TMCSH)

Partially thiolated TMC (TMC_{SH}) was prepared by reaction between the primary amino groups of purified polymer and 2-iminothiolane, as previously described [14]. Briefly, TMC was dissolved in HEPES buffer (20 mM, pH 7.4) at 5 $mg.mL^{-1}$. Then, 2-iminothiolane·HCl (Sigma-Aldrich, USA) was added in order to attain a theoretical modification of 10% of the polymer primary amines and the pH of the resulting solution adjusted to 8 with NaOH. The reaction mixture was saturated with argon and magnetically stirred at room temperature (RT) for 6 h. The resulting solution was dialyzed for 3 days against 5 mM HCl at 4ºC. Thereafter, the dialyzed solution was frozen at -80ºC and lyophilized for 3 days, yielding the TMC_{SH} as a white powder, which was stored at -20ºC until further use.

2.3. Determination of polymer thiol content

The amount of reduced/free thiol groups grafted to the TMC was determined spectrophotometrically using the Ellman's reagent (5,5-dithio-bis-(2-nitrobenzoic acid), DTNB; Sigma-Aldrich, USA) as previously described [14, 18]. An amount of 155.3 ± 10.1 $\mu mol.g^{-1}$, corresponding to 4.8 ± 0.3% functionalization of TMC primary amines with 4-mercaptobutan-1-iminium (holding the thiol groups), was achieved.

2.4. Plasmid DNA

The pDNA used encoded for the enhanced green fluorescent protein (eGFP) and luciferase (pCMV-eGFPLuc, 6.7 kb, Invitrogen, USA) genes. Plasmid was produced in a DH5α competent *E. coli* strain transformed with the respective plasmid under the cytomegalovirus (CMV) promoter. Subsequently, pDNA purification was performed using an EndoFree Plasmid Giga Kit following the manufacturer instructions (Qiagen, Germany). Plasmid concentration and purity were assessed by ultraviolet spectroscopy (Nanodrop 1000, Thermo Scientific, USA). Only plasmid solutions with an absorbance ratio (260/280 nm) comprised between 1.8 and 2.0 were used.

2.5. HC production, purification and modification

The HC fragment was produced recombinantly using the BL21 *E. coli* strain as previously described by Sinha *et al.* [19]. The plasmid encoding for the HC fragment, together with a coding sequence for six histidines in the N-terminal, was a kind offer from Prof. Neil Fairweather (King's College, UK). The purified HC fragment was covalently linked to a 5 kDa heterobifunctional PEG spacer bearing a N-hydroxysuccinimide (NHS) ester and a maleimide (MAL) end groups (JenKem Technology, USA) as described elsewhere [15, 18]. Briefly, amine groups from HC fragment reacted with the succinimidyl ester group (NHS) through stable amide bonds. To assess the degree of HC modification, the amount of reactive MAL groups linked to the HC protein was determined using a modified Ellman's assay [18, 20], and found to be 1.9 ± 0.4 mol PEG/mol HC. Hereafter, the HC functionalized with PEG-MAL will be designated as HC-PEG_{5k}.

2.6. Nanoparticle preparation

2.6.1. Nanoparticle core

Polymer-pDNA nanocomplexes were prepared by mixing, while vortexing, equal volumes of pDNA and TMC_{SH} solutions (both in 20 mM HEPES buffered saline (HBS) with 5% (w/v) glucose solution, pH 7.4). TMC_{SH} NPs core were let to stabilize for 15 min at RT before further functionalization. Nanocomplexes with different molar ratios of quaternized amine groups (N) to moles of DNA phosphate groups (P) – N/P ratio – were prepared.

2.6.2. Nanoparticle functionalization

After NP core preparation and stabilization, NPs were either functionalized to produce non-targeted NPs (nT NPs) by grafting a 5 kDa methoxy-PEG-MAL (MeO-PEG_{5k}, Sigma-Aldrich, USA), or to generate neuron-targeted NPs (Tg NPs), by grafting HC-PEG_{5k} (HC-PEG_{5k}-MAL) into the NPs.

For the ligand density optimization, NPs functionalized with PEG in 1, 2 or 4 mol% of the TMC primary amino groups were produced (MeO-PEG_{5k} or HC-PEG_{5k}; see **Scheme 1**). For the ligand exposure optimization, mixtures of HC-PEG_{5k} and a 2 kDa MeO-PEG-MAL (MeO-PEG2k, JenKem Technology, USA) were used at 1:1, 2:1 and 1:2 molar proportion (HC-PEG_{5k}:MeO-PEG_{2k}; see **Scheme 2**). After addition of any of the molecules (PEGs and HC-PEG) mentioned above, the NPs were left at 37 ºC and 800 rpm overnight (Thermomixer®, Eppendorf®, Germany), before further use.

2.7. Determination of nanoparticles hydrodynamic size and zeta potential

Complexes were prepared as described above. Eight µg of pDNA was used for each formulation. The zeta potential and size of the complexes were assessed using a Zetasizer Nano Zs (Malvern, UK) following the manufacturer's instructions. The Smoluchowski model was applied for zeta potential determination and cumulant analysis was used for mean particle size determination. All measurements were performed in triplicate, at 25 °C.

2.8. Plasmid DNA condensation efficiency and polyplexes stability in physiological conditions

Plasmid DNA condensation efficiency was assessed through the SYBR® Gold exclusion assay, as previously described [12]. This assay enables the measurement of free pDNA, due to SYBR® Gold binding to free nucleic acids (not complexed into NPs). Both binary and ternary complexes were prepared and further diluted in the respective preparation buffer to assess the ability to complex nucleic acids. Furthermore, polyplexes stability under physiological conditions was evaluated. For this purpose, the complexes were incubated in Dulbecco's Modified Eagle Medium (DMEM) medium with Glutamax, supplemented with 10% (w/v) fetal bovine serum (FBS) (heat inactivated at 57 ºC for 30 min) and 1% Pen/Strep (10,000 $U.ml^{-1}$

penicillin and 10,000 µg.ml^{-1} streptomycin) (all supplied by Gibco®, Thermo Fisher Scientific, USA).

The assay was performed through addition of complexes with a 10-fold dilution in the mentioned solutions in a black-walled 96-well plate (Greiner Bio-One, Austria) with SYBR® Gold solution. After 10 min incubation with continuous plate mixing, fluorescence was measured (λ_{exc} = 485 nm, λ_{em} = 540 nm, Synergy Mx Microplate Reader (BioTek, USA)). Results are expressed as relative percentage of complexation, where 100% means pDNA is totally complexed with polymer in NPs, and 0% means that all pDNA is free (not complexed with the polycation). Polymer solutions with the same polymer concentration were used as control to subtract any polymer background fluorescence.

2.9. Cellular internalization studies by conventional flow cytometry

ND7/23 (mouse neuroblastoma (N18 tg 2)×rat dorsal root ganglion neuron hybrid), NIH 3T3 (mouse embryonic fibroblast) and RN22 (rat schwannoma) cells (all obtained from ECACC) were seeded into 24-well tissue culture polystyrene (TCPS) plates (Greiner Bio-One, Austria) at a cell density of 4 x 10^4, 5 x 10^4 and 3 x 10^4 viable cells per cm^2, respectively. All cells were cultured in DMEM medium with Glutamax supplemented as described above, 24 h prior incubation with NPs. pDNA was labelled with YOYO®-1 (Invitrogen, USA) as indicated by the manufacturer. Tg and nT NPs were prepared at different N/P ratios (2 to 12) using 2 µg of pDNA per cm^2 and incubated with cells for 2 h, at 37 ºC. After the incubation period, cells were thoroughly washed with cold phosphate buffered saline (PBS) to stop the internalization process and incubated with 0.4% (w/v) Trypan Blue® for 10 min to quench any extracellular fluorescence signal. Afterwards, cells were washed and then processed for being examined by flow cytometry using a FACS Calibur™ flow cytometer (BD Biosciences, USA). A total of 20,000 gated events were collected for each condition. The resulting data was analyzed using FlowJo® software (version 10, FLOWJO, LLC). Untreated cells were used as negative control.

2.10. Cellular internalization studies by imaging flow cytometry

ND7/23, NIH 3T3 and RN22 cells were seeded into 12-well TCPS plates (Greiner Bio-One, Austria) at a cell density of 4 x 10^4, 5 x 10^4 and 3 x 10^4 viable cells per cm^2,

respectively, 24 h prior incubation with NPs. pDNA was labelled with YOYO®-1 (Invitrogen, USA) as indicated by the manufacturer. Neuron-targeted NPs were prepared at N/P ratio of 8 with 2 µg of pDNA per cm^2 and incubated with cells for 2 h, at 37 °C.

Afterwards, cells were trypsinized, fixed with 4% (w/v) formaldehyde in PBS and centrifuged to obtain a pellet of about 10^5 cells in 50 µL. Cell images were acquired using an ImageStreamX multispectral imaging flow cytometer (Amnis Corporation – Millipore, Germany), collecting 10,000 events per sample at 40x magnification. A 488 nm wavelength laser was used to excite YOYO®-1. The fluorescence images were collected using the 480−560 nm spectral detection channel. Cell images were analyzed using IDEAS image-analysis software (Amnis Corporation – Millipore, Germany). Cells within the focal plane were first selected using a two-dimensional plot of image contrast versus root-mean-squared (rms) gradient. Gating on bivariate plot of aspect ratio versus cell area was further used to isolate a population of single cells.

To discriminate NPs inside cells from the ones associated to the cell membrane, cellular masks were created to separate two regions of the cells – internal (cytoplasm) and external (membrane), as previously described [12]. The number of nanoparticle-loaded vesicles (NLV) per cell was determined by using images acquired using the Extended Depth of Field (EDF) filter [21]. To determine the number of NLV per cell, a mask was created in order to identify the fluorescence intensity peaks at least 4-fold greater than the background. The number of individual vesicles in a cell was enumerated using the Spot Count feature from IDEAS® image-analysis software version 6.0 (Amnis, EDM Millipore, Germany), and plotted in frequency histograms.

2.11. Transfection studies

ND7/23, NIH 3T3 and RN22 cells were seeded into 24-well TCPS plates (Greiner Bio-One, Austria) at a cell density of 4 x 10^4, 5 x 10^4 and 3 x 10^4 viable cells per cm^2, respectively, 24 h prior incubation with NPs. Cell medium was refreshed prior addition of the NPs. 24 h post-transfection the cell media was removed, and 0.5 ml of fresh complete DMEM medium was added to each well. Cells were incubated for an additional 48 h period, with daily renewing of the culture media. At 72 h post-incubation, cells were trypsinized and processed for flow cytometry for eGFP

expression determination. Twenty thousand gated events were taken for each replicate and analyzed as described above. Untreated cells were used as negative control.

2.12. Nanoparticle cytotoxicity

To determine cell viability, a resazurin-based assay was used [22]. Briefly, 72 h after incubation with NPs, a sterile 0.1 $mg.ml^{-1}$ solution of resazurin (Sigma-Aldrich, USA) in PBS was added to each well to a final 10% (v/v) concentration. After 4 h of incubation at 37 °C, 200 µl of medium was transferred to a black-walled 96-well plate (Greiner Bio-One, Austria) and fluorescence was measured (λ_{exc} = 530 nm, λ_{em} = 590 nm). Results are expressed as percentage of metabolic activity of treated cells relative to untreated cells.

2.14. Statistical analysis

Statistical analysis was performed using GraphPad Prism 7.0. Results are presented as mean ± standard deviation (SD) of at least two independent experiments, each one with three technical replicates. The D'Agostino-Pearson omnibus test was used to confirm the Gaussian distribution of data. Afterwards, the appropriate statistical test was used, as mentioned in each figure. Results were considered statistically significant when $p<0.05$.

3. Results

3.1. Assessment of the PEGylation density impact on nanoparticle physicochemical properties

TMC-based NPs were prepared at different N/P ratios and functionalized with different densities (1, 2 or 4 mol% of the primary amino groups in the polymer) of either HC-PEG_{5k} (Tg NPs) or methoxy-PEG_{5k} (MeO-PEG_{5k}; nT NPs) (**Scheme 1**). The quantity of PEG per NP was calculated as a function of the number of moles of primary amine groups (mol%) of the total polymer present in each N/P ratio. All prepared NPs presented a pDNA condensation efficiency between 85 and 90% (data not shown). **Figure 1** summarizes the physicochemical characteristics of Tg and nT NPs functionalized at different densities with the respective PEG.

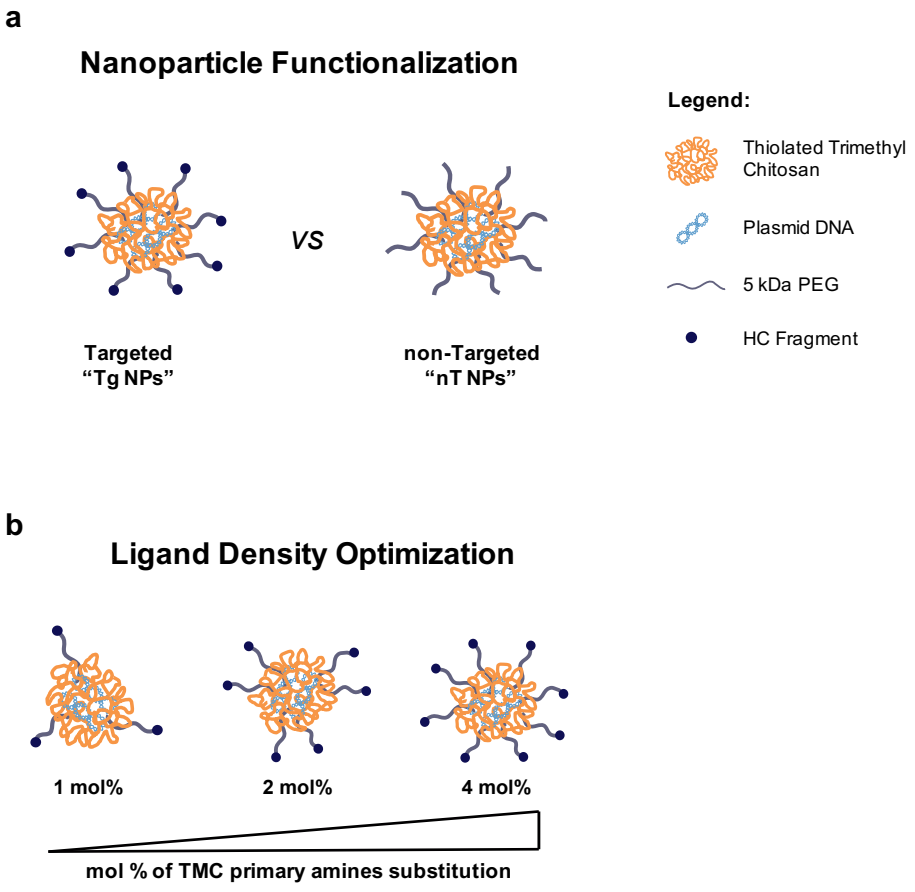

Scheme 1. Schematic representation of the functionalization of TMC-based nanoparticles. a) TMC-based NPs were functionalized either with HC coupled to a 5 kDa heterbifunctional PEG spacer (N-hydroxysuccinimide-PEG-maleimide; HC-PEG_{5k}) to produce neuron-targeted NPs (Tg NPs) or with the 5 kDa methoxy-PEG-maleimide (MeO-PEG_{5k}) spacer (nT NPs, non-Targeted NPs). b) The prepared NPs were functionalized with increasing amounts of HC-PEG_{5k} or MeO-PEG_{5k}, with the charged amount of PEG per NP being shown below each formulation.

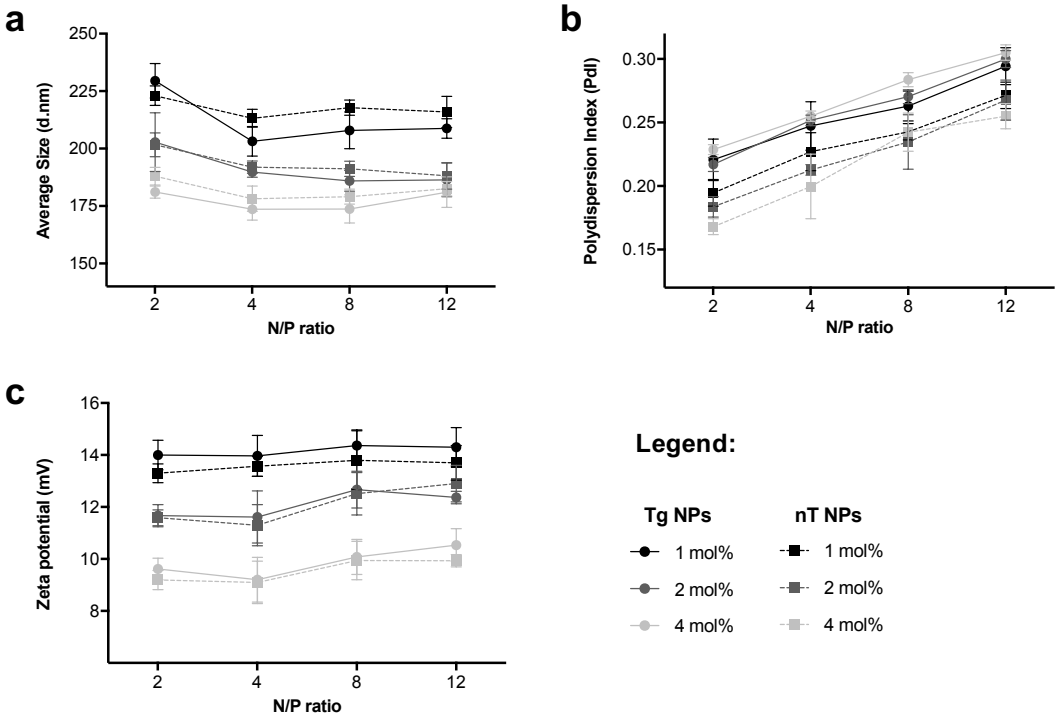

Figure 1. Physicochemical characterization of functionalized TMC NPs as a function of N/P ratio and PEG density. TMC-based NPs prepared at different N/P ratios were functionalized with increasing amounts of HC-PEG_{5k} (Tg NPs) or MeO-PEG_{5k} (nT NPs). a) Average hydrodynamic sizes, b) polydispersity index and c) zeta potential were measured by dynamic light scattering in PBS, pH 7.4 at 25 °C. Results from three independent experiments are represented as mean ± SD. Statistical differences between Tg and nT NPs were assessed through the multiple t test analysis.

All formulations presented unimodal size distribution by dynamic light scattering (DLS) (data not shown). As illustrated in **Figure 1a**, for both formulations, the higher the degree of PEGylation, the smaller the NPs average diameter size, independently of the N/P ratio tested. Among all, NPs bearing 4 mol% of PEG (with or without HC) were the ones with the smallest sizes (~170 to 190 nm) ($p<0.01$ when compared to 1 mol% NPs). Also, the NPs prepared at N/P ratio of 2, particularly those with lower PEGylation densities (1 and 2 mol%), exhibited statistical significant higher average sizes ($p<0.05$). Above this N/P ratio (N/P > 2), the NPs size did not increase significantly with the N/P ratio, which means that the size is not significantly altered by the increment in the polymer mass and respective percentage of PEGylation. Moreover, no significant differences were found in the mean diameter size between nT and Tg NPs, showing that HC functionalization does not influence the NP average hydrodynamic sizes.

In contrast, higher N/P ratios led to a concomitant raise in the PdI values, for all formulations tested (**Figure 1b**). Moreover, Tg NPs presented significantly higher PdI values ($p<0.05$) when compared to the nT NPs, independently of the ligand density at the surface of the NPs. The higher variability can be the consequence of the protein fragment grafting, which may not be incorporated always at the same orientation onto the NPs surface. Regardless, all formulations tested presented PdI values below 0.3, which is within the range of commonly PdI values obtained for chitosan-based NPs [23].

The surface charge of the developed NPs was also evaluated. As expected, higher degrees of PEGylation led to lower zeta-potential values (**Figure 1c**), independently of the presence of HC ($p<0.01$ comparing 1 with 4 mol% NPs at all N/P ratios tested; $p<0.05$ when comparing the grafting densities of 1 with 2 mol% or 2 with 4 mol%). For each percentage of PEG functionalization (with or without HC), no significant differences were found from NPs prepared at different N/P ratios (from 2 to 12). Moreover, all prepared NPs presented a cationic surface charge (from +8 to +14 mV) indicating a good colloidal stability.

3.2. Determination of optimal HC-PEG$_{5k}$ density for cell-specific internalization and transfection efficiency

The effect of HC-PEG$_{5k}$ density on the NPs ability to be internalized by cells was studied by flow cytometry on ND7/23 (neuron-like cell line), NIH 3T3 (fibroblasts) and RN22 (Schwann cell line) cells. The results obtained after a 2 h incubation period of the cells with formulations prepared at different N/P ratios and ligand grafting densities are presented in **Figure 2a**, where the distribution of the intensity of YOYO®-1-labelled pDNA per cell is reported for each cell line tested (for the data regarding the percentage of YOYO®-1 positive cells after NP incubation please refer to the **Supplementary Table S1**). For the nT NPs, a clear inverse trend is observed between the amount of PEG grafted into NPs and the cellular pDNA intensity ($p<0.05$, when comparing all formulations - 1 to 4 mol% of PEGylation). This trend seems to be independent of the NPs N/P ratio or the cell line under testing. In the case of the Tg NPs, there is an evident difference between the pDNA intensity in neuronal *versus* non-neuronal cell lines. In the neuronal cells, a higher accumulation of pDNA per cell is observed as the N/P ratio increases that plateaus at N/P ratio 8.

Contrary to the observed trend in the case of nT NPs, in the case of the Tg formulations we observed that the higher ligand grafting densities are the ones that result in higher cellular uptake efficiencies in neuronal cells, independently of the N/P ratio ($p<0.01$). Moreover, one can notice that the Tg NPs prepared at N/P ratio of 8 yielded the higher pDNA cellular uptake in the neuronal cell line with the lowest internalization in the fibroblasts and Schwann cells and therefore, this formulation represents a good candidate to maximize the neuronal targeted vectoring capacity of the proposed NPs.

Based on the above, we moved to analyze the effect of the HC-PEG_{5k} density on the transfection efficiency of TMC-based NPs prepared at the N/P ratio of 8 (**Figure 2b**). Corroborating the data acquired from the flow cytometry study (**Figure 2a**) a similar trend was obtained for the nT NPs, where higher PEG_{5k} grafting densities led to a reduced percentage of transfected cells. The observed difference was identical to all cell lines tested, with a reduction of approximately 2-fold in the transfection efficiency from 1 to 4 mol% in nT NPs ($p<0.05$). The Tg NPs presented a similar trend when incubated with the non-neuronal cell lines (NIH 3T3 and RN22), although not as pronounced ($p>0.05$). Indeed, no statistical differences were found between the transfection efficiencies of nT *versus* Tg formulations at compared grafting densities in the non-neuronal cell lines. In contrast, when incubated with the neuronal cells (ND7/23), a distinct tendency was observed for the Tg NPs.

While the incubation with NPs bearing 1 mol% of HC-PEG_{5k} resulted in a lower percentage of transfected cells (~15%) when compared to their equivalent nT NPs, at the grafting density of 2 mol% HC-PEG_{5k} this percentage was significantly improved to approximately 40% of the total cell population ($p<0.01$). The higher grafting density (4 mol%) exhibited an intermediate capacity of transfection, with ~ 26% of transfected cells ($p<0.05$).

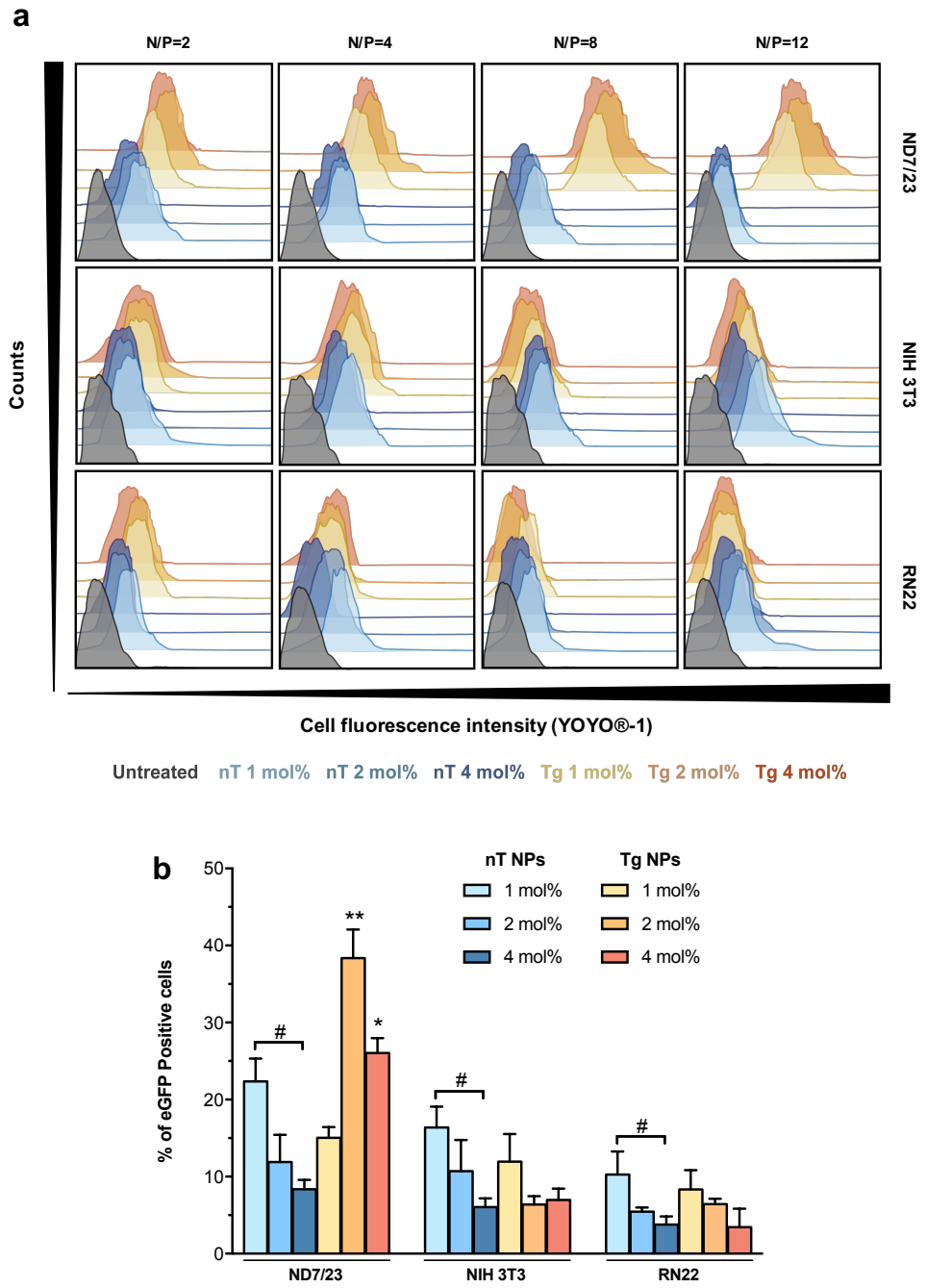

Figure 2. Extent of cellular uptake and transfection efficiency of Targeted (Tg) *versus* non-Targeted (nT) TMC NPs. a) Cellular uptake: representative flow cytometry distributions showing the intensity of pDNA fluorescence among ND7/23, NIH 3T3 and RN22 cells after a 2h incubation with TMC-based NPs prepared with labelled (YOYO®-1) pDNA at different N/P ratios; untreated cells were used as control. b) Transfection efficiency: the percentage of viable cells expressing eGFP was analyzed by flow cytometry 72 h post-incubation with the different formulations; untreated cells were used as control. Each bar represents the mean of three independent experiments ± SD. Statistical differences were assessed through the multiple t test analysis and are represented as: *$p<0.05$ and **$p<0.01$ for comparisons among Tg NPs; $^{\#}p<0.05$ for comparisons among nT NPs; no symbol = $p>0.05$.

3.3. Preparation of targeted NPs with hetero PEG brushes

To investigate the effect of PEG spacer length on ligand exposure towards achieving maximum targeting performance, we next compared Tg NPs functionalized with single length HC-PEG$_{5k}$ (**Scheme 2a**) with NPs prepared using a PEGylation "cocktail" that consisted of mixed ratios of PEG spacers of different length (**Scheme 2b**). For this, shorter PEG molecules (MeO-PEG$_{2k}$) were tethered to NPs along with HC-bound longer PEGs (HC-PEG$_{5k}$).

For the subsequent analysis, all NPs were prepared at the same N/P ratio (N/P = 8) and using the same grafting density of 2 mol% of TMC primary amine groups, as this was previously shown to be the one mediating the best biological performance (neuronal targeting and transfection).

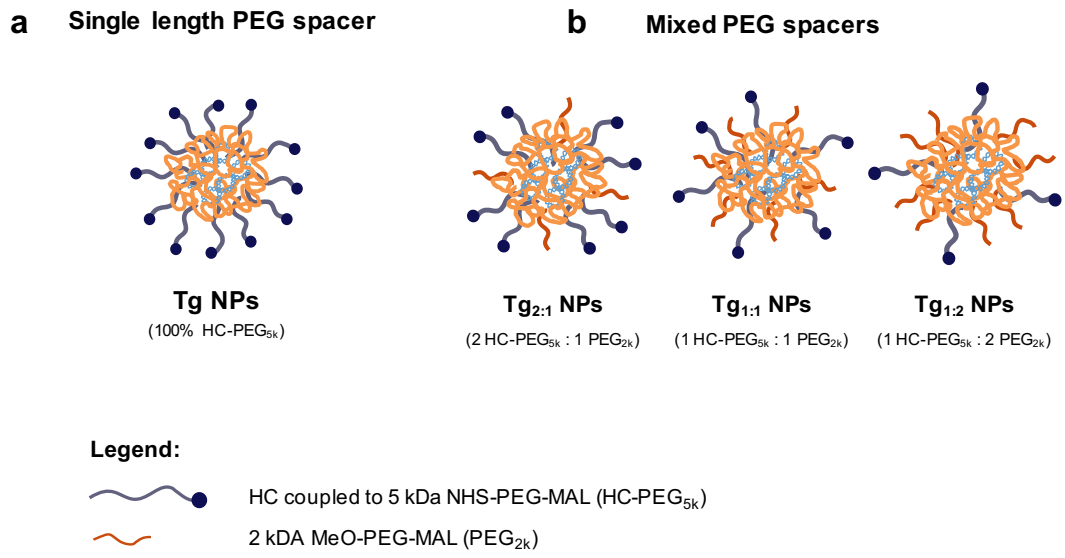

Scheme 2. Schematic representation of the preparation of functionalized hetero PEG-neuron-targeted TMC NPs. To optimize the exposition of HC at the NPs surface, TMC NPs were prepared at N/P 8 using 2 mol% of a) HC-PEG$_{5k}$ alone or b) in combination with a shorter length PEG spacer (MeO-PEG$_{2k}$), given rise to NPs with molar different ratios of HC-PEG$_{5k}$ and MeO-PEG$_{2k}$.

The results from the physicochemical characterization of the produced NPs are presented in **Table 1**. As can be observed, no differences were found in terms of average size, PdI or zeta potential values among all tested formulations ($p>0.05$). This is not a surprising result, as the N/P ratio and grafting density, two major contributors for NPs physicochemical properties, were not altered between formulations.

Table 1. Physicochemical characterization of neuron-targeted NPs functionalized with different molar ratios of HC-PEG$_{5k}$/Meo-PEG$_{2k}$.

Formulation	Size (nm)	Polydispersity index (PdI)	Zeta-potential (mV)
Tg NPs	186 ± 18	0.27 ± 0.09	+12.7 ± 1.2
Tg$_{2:1}$ NPs	191 ± 24	0.26 ± 0.21	+11.4 ± 2.1
Tg$_{1:1}$ NPs	179 ± 15	0.26 ± 0.05	+13.2 ± 1.9
Tg$_{1:2}$ NPs	184 ± 10	0.29 ± 0.11	+10.3 ± 0.8

All NPs were prepared at N/P ratio of 8 and a final PEG grafting density of 2 mol% of TMC primary amine groups. Average hydrodynamic sizes, polydispersity index and zeta potential were measured by dynamic light scattering in PBS, pH 7.4 at 25 °C. Results from three independent experiments are represented as mean ± SD.

3.4. Evaluation of internalization and payload delivery of neuron-targeted NPs functionalized with hetero PEG brushes

Subsequently, we evaluated the performance of the different NP formulations in terms of internalization and payload delivery to the three cell lines under testing. Although by conventional flow cytometry, no differences could be observed in terms of internalization between all targeted formulations (NPs prepared at the same N/P ratio and ligand grafting densities, bearing different molar ratios of HC-PEG$_{5k}$:PEG$_{2k}$; **Supplementary Table S2**), when performing the internalization study exploring imaging flow cytometry we could find significant differences in the behavior of the tested NPs. The use of this technique allowed us to clearly distinguish between internalized (**Figure 3a**) versus membrane-bound NPs (**Figure 3b**) [12, 24]. In this particular case, where we are evaluating the importance of very precise NP design on the overall transfection process, the use of this advanced bioimaging technique was of paramount importance.

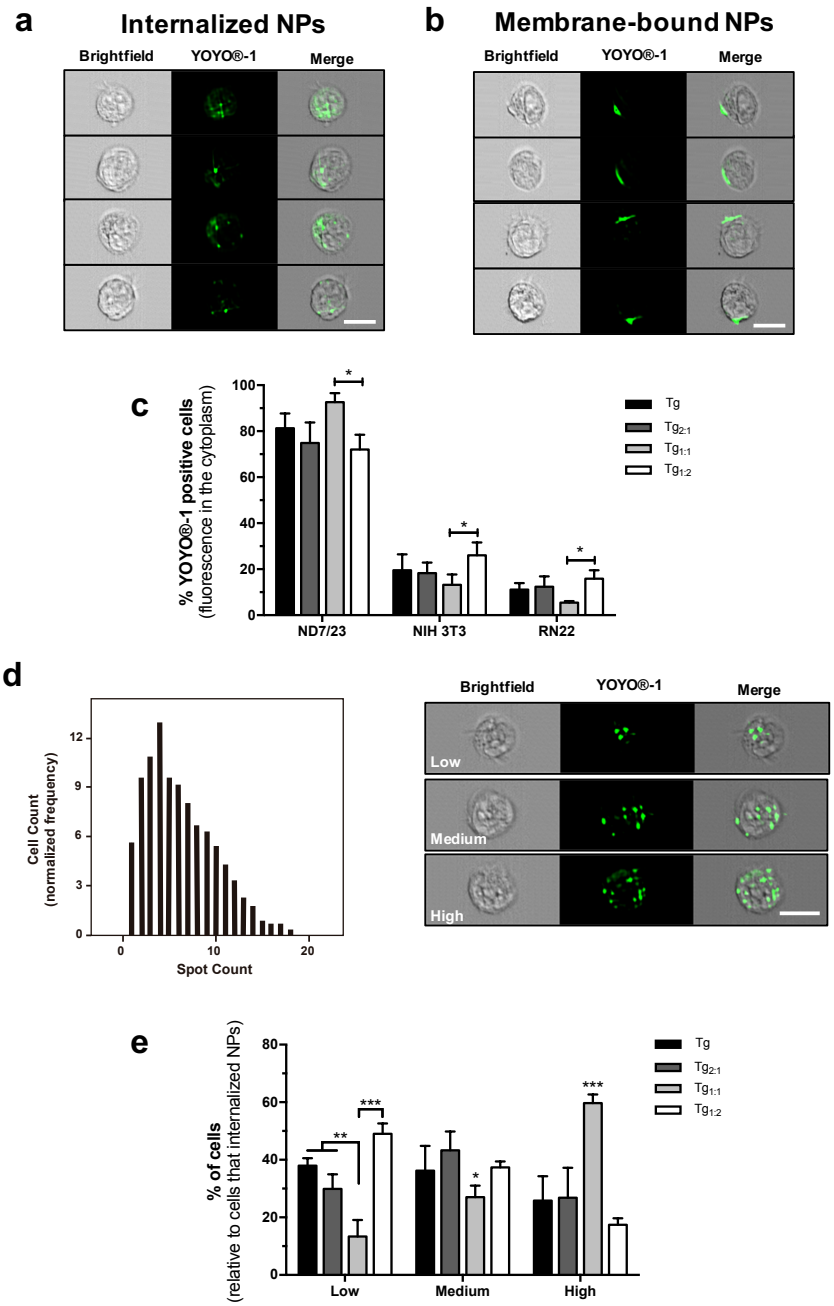

Figure 3. Efficiency of cellular uptake and payload delivery mediated by neuron-targeted TMC NPs with different ratios of HC-PEG$_{5k}$:MeO-PEG$_{2k}$ in neuronal *versus* non-neuronal cell lines. Representative bright-field, YOYO®-1 (green fluorescence) and their overlays (scale bars: 10μm) images acquired on ImageStream^X for ND7/23 cells that a) have internalized YOYO®-1 labelled-pDNA or b) have YOYO®-1 labelled-pDNA associated with the cellular membrane. c) Percentage of ND7/23, NIH and RN22 cells positive for YOYO®-1 after a 2 h incubation with the different NP formulations. d) Histogram of NLV frequency obtained from IDEAS® software analysis and respective representative images of cells from the different gated regions (low, medium and high number of NLVs). e) Percentage of ND7/23 cells that had internalized low, medium or high amount of NLVs after a 2 h incubation with the different NP formulations containing YOYO®-1 labelled-pDNA. All data is represented as a mean of three independent experiments ± SD. Multiple t test analysis was used for comparisons between formulations. Statistical differences are presented as: *p<0.05, **p<0.01 and ***p<0.001.

As depicted in **Figure 3c**, a statistical significant difference was found in the percentage of neuronal cells that had internalized NPs (>72%), compared to the non-neuronal cells (<26%) ($p<0.001$). This result indicates that these NPs are being preferentially internalized by the neuronal population, corroborating the previous data obtained by conventional flow cytometry (**Figure 2a**). When comparing the internalization efficiency in neuronal cells among the different tested formulations, no significant differences were found, with exception for the comparison between $Tg_{1:1}$ and $Tg_{1:2}$ NPs ($p<0.05$), having the latter a poor performance in contrast with the former. Moreover, $Tg_{1:2}$ NPs were also more internalized in the non-neuronal cells when in comparison to $Tg_{1:1}$.

As no major differences were found between the different NP formulations in terms of internalization efficiency, we next evaluated the payload delivery efficiency into neuronal cells. For this, we used another feature of the imaging flow cytometry analysis software (IDEAS®, Amnis Corporation, Germany) to assess the number of nanoparticle-loaded vesicles (NLV) per cell (**Figure 3d**), a methodology previously described by us [12]. By quantifying the number of NP clusters within individual vesicles (endosomes or lysosomes), one can infer about the efficiency of each formulation to delivery their payload into cells, through the determination of the intracellular distribution of NLVs.

Three groups with low (≤ 4), medium (> 4 and < 9) or high (≥ 10) number of NLV per cell were gated among the cells that had internalized NPs (**Figure 3e**). The results clearly show that the $Tg_{1:1}$ NPs were the ones with the best performance among all formulations, with ~60% of the cell population having 10 or more NLVs per cell, and only 13% of cells with low number of NLVs. The Tg and $Tg_{2:1}$ NPs presented similar performances, with the majority of the population having a medium number of NLVs, and less than 30% of cells with 10 or more NLVs. As observed in the internalization data, the $Tg_{1:2}$ NPs were the ones that not only internalized in a lower percentage of cells but also that presented the lower amount of payload delivery, since the bulk population that internalized these particles (~50%) presented a maximum of 4 NLVs per cell. Altogether, these results indicate that, despite the similarities found in terms of internalization efficiency, the $Tg_{1:1}$ NPs were able to deliver a higher payload

amount to cells, leading to the presence of a higher concentration and accumulation of pDNA.

3.5. Transfection efficiency of neuron-targeted NPs functionalized with hetero PEG brushes

The transfection mediated by neuron-targeted NPs prepared with mixed ratios of different length PEG spacers (N/P ratio of 8 and PEG grafting density ratio of 2 mol% per primary amine group) was assessed. The different cell lines under study were incubated for 24 h with the prepared formulations and the transfection efficiency assessed 48 h post-incubation by quantifying the number of positive cells for eGFP by flow cytometry. The results (**Figure 4**) show a marked difference in the number of eGFP positive cells when NPs were incubated with neuronal (ND7/23) or non-neuronal cells (NIH 3T3 and RN22). All formulations presented a similar behavior when incubated with non-neuronal cells, with a maximum of 11% of the total population being transfected in the case of $Tg_{1:2}$ NPs. In contrast, the percentage of neuronal cells being transfected was significantly higher than the non-neuronal cells ($p<0.001$). Among the neuronal population, the formulation that achieved the highest percentage of transfected cells was the $Tg_{1:1}$ NPs, leading to the expression of eGFP in more than half of the cell population (~53% of transfected cells; $p<0.01$). These results are in accordance with the previous findings observed in imaging flow cytometry, as these NPs revealed to be the most efficient to deliver their payload into neuronal cells.

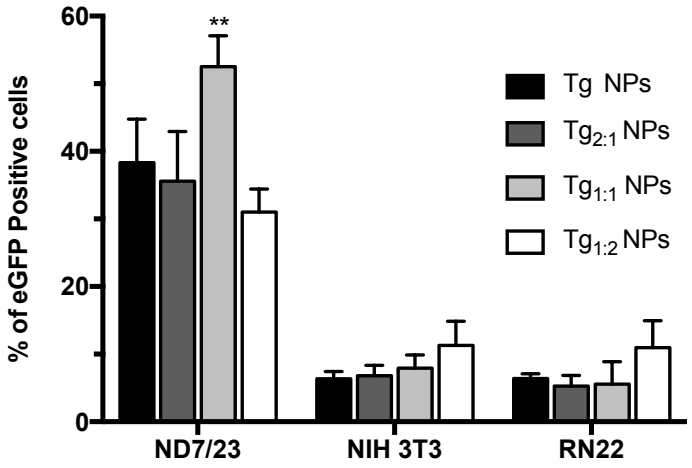

Figure 4. Transfection efficiency of neuron-targeted TMC-based NPs with different ratios of HC-PEG$_{5k}$:MeO-PEG$_{2k}$ in neuronal *versus* non-neuronal cell lines. The transfection efficiency of the different Tg NPs was evaluated 72 h post-transfection through the quantification of the percentage of cells expressing eGFP by flow cytometry. Untreated cells were used as control. Each bar represents the mean of three independent experiments ± SD. Statistical differences are presented as: **p<0.01, when comparing the different NP formulations transfection efficiency in the ND7/23 cells.

To exclude the possibility of any interference related to cell viability in the transfection results, we also evaluated the metabolic activity of these cells after incubation with all formulations under testing (**Supplementary Figure S1**). The results showed that none of these formulations presented a significant cytotoxic effect in the different cell types tested.

4. Discussion

For more than two decades PEG has been the polymer of choice for surface modification of particulate drug/gene carriers to provide improved pharmacological properties and to allow for the preparation of targeted delivery systems [25]. The PEG layer may have different roles in a particle biological fate, and all of them depend on its surface grafting density. PEG coatings are known to prevent aggregation and to stabilize NPs in media with physiological salt concentration by steric and hydration repulsions [25]. The resistance to non-specific absorption of plasmatic proteins is one of the most important determinant of NP fate once administered in the host [26]. High resistance to protein adsorption leads to a decreased uptake by the mononuclear phagocytose system, decreased degradation and elimination rate leading to a longer half-life in the extracellular compartments, which in turn influences NPs pharmacokinetic parameters. Resistance to protein adsorption may also improve targeting capabilities by preventing obstruction by steric hindrance of ligand recognition [27, 28]. The PEG layer present on NP surfaces can also improve drug or nucleic acids encapsulation by providing a physicochemical barrier to payload escape, and it might additionally affect drug/nucleic acid release pattern [29]. On the other hand, excessive PEGylation degrees can lead to a strong inhibition of cellular uptake and to a less efficient interaction and binding with target receptors, as target recognition of ligand molecules located at the surface of a PEGylated NP are also dependent on the density and thickness of the PEG layer and the positioning of the ligand [25].

Taking this into account, in this work we aimed to determine the optimal PEG grafting density and ligand exposure at the surface of TMC-based NPs, in order to achieve maximum vectoring capacity towards neuronal cells. After establishing the grafting density, we further investigated the effect of the PEG chain organization on the ligand exposure at the neuron-targeted NPs surface by testing mixed ratios of a HC-tethered PEG (HC-PEG_{5k}) and a short free PEG chain of 2 kDa (MeO-PEG_{2k}).

Initially, we evaluated the effect of the HC-PEG_{5k} grafting density on the NPs physicochemical properties, such as size and zeta potential. Our data indicate that the increase in PEG grafting density is inversely correlated to NPs size, as with increasing PEGylation a reduction in the NPs dimensions was observed. A similar behavior was

previously reported for similar PEG lengths in other polymeric NPs [30-34]. This result can be explained considering that the structure of the PEG layer is strongly influenced by the chain length. Specifically, it has been suggested that longer chain PEGs (such as 5 kDa) interact via short-range van der Waals attraction and inter-chain hydrogen bonding, producing chain entanglement, that results in a condensation of the size of the outer layer that will, ultimately, lead to NPs with smaller hydrodynamic size [35]. The increase in PEG density also prompted a decrease in zeta potential. As this has been observed independently of the N/P ratios tested, it can be inferred that this effect arises from the spatial shielding of the polymer positive surface charges by the PEG chains.

Subsequently, we determined the percentage of HC-PEG grafting density that mediated higher internalization into neuronal cells. The amount of cellular uptake was monitored by flow cytometry using YOYO®-1 labelled pDNA. Our data revealed that the highest uptake was obtained for NPs with a N/P ratio of 8 and higher grafting densities (2 and 4 mol% of primary amines in the polymer). In contrast, for nT NPs, increasing the PEG density consistently reduced the uptake efficiency, as described by others [8]. This data is in accordance with previous findings reported by us, where we observed the preferentially binding of HC-functionalized NPs towards neuronal populations in biological models of different complexity [13], and their more efficient retrograde transport towards the neuronal cell body [14]. Therefore, we have confidence that the higher payload delivery obtained from the incubation of Tg NPs with neuronal cells results from the receptor-mediated internalization promoted by the interaction between HC and the ganglioside receptors present in this neuronal cell line.

When considering a PEGylated NP, it is believed that the PEG will extend away from the particle. However, as deGennes proposed, there are two regimens for polymers attached to a surface, depending on their grafting density [36] – if the density is too low, the polymer is said to be in a “mushroom-like” conformation, where the PEG chains will bend toward the surface; on the contrary, if the grafting density is high enough, the polymers are said to be in the “brush-like” regimen, and the PEG molecules will be extended away from the surface (**Scheme 3**). The molecular weight of the polymer, as well as its grafting density will determine the degree of surface

coverage and distance between graft sites [36, 37], and will ultimately affect the exposure of the targeting moiety and the NPs targeting efficiency. In addition, following cellular binding and internalization, NPs need to efficiently release their payload into the cytoplasm. This critical step is dependent on several parameters such as the endosomal protonation of chitosan, which will promote the entry of counter ions into the endosome, increasing ionic concentration and hence water influx that will contribute to endosomal rupture (proton sponge effect) [38, 39], the ability of the polymer to unfold from a collapsed state into an extended conformation after protonation of the amine groups (umbrella effect) [40] and its biodegradation rate [12]. All these outcomes are influenced by the degree of PEGylation.

From our data, it seems that for these TMC-based NPs an intermediate PEG grafting density of 2 mol% is ideal to promote the best PEG conformation in order to better expose the HC fragment at the surface, resulting in the right balance between NP stability and receptor-mediated internalization, and consequently, transfection efficiency.

Having determined the best ligand density for cellular uptake and transfection efficiency, we next investigated how to enhance HC exposure and motion at the NPs surface to achieve the best biological performance and specificity towards neuronal cells. The ability of the targeting moiety to present free motion at the nanocarrier surface is of critical importance for optimal active targeting. If grafted at a high density, the PEG molecules could reduce the ligand motility and freedom of association to its receptor, due to the steric repulsive (or crowding) effect derived from neighboring PEG chains [41] (**Scheme 3**).

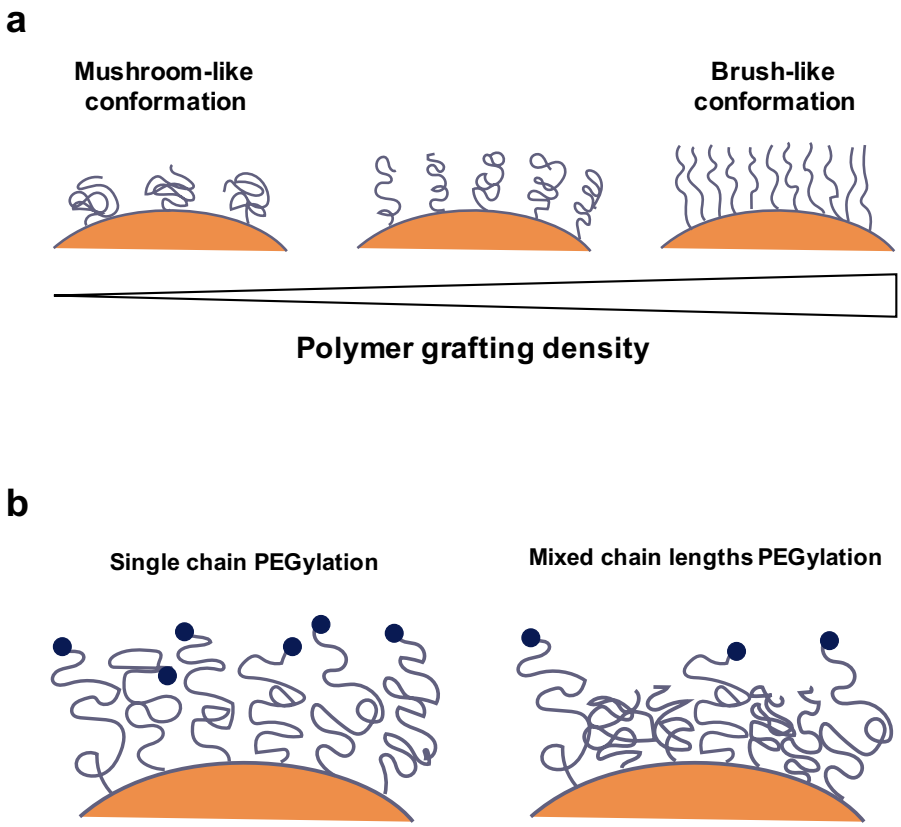

Scheme 3. Effect of spacer grafting density and length on conformation and ligand exposition.

To overcome this hurdle, we generated NPs containing hetero PEG brushes by using a longer HC-linker PEG (5 kDa) and a free shorter PEG (2 kDa) as a filler molecule, at different mixed molar ratios. All the produced NPs presented similar physicochemical properties, as their N/P ratio and PEG grafting densities were kept constant.

Afterwards, their target towards neuron-like cells was systematically evaluated in terms of internalization and payload delivery efficiency through imaging flow cytometry. The obtained data revealed the $Tg_{1:1}$ NPs as the formulation with the best biological performance in terms of payload delivery into target cells, as well as transfection efficiency. Moreover, this formulation performed even better than the formulation with 100% of HC-PEG_{5k}, which present the double amount of HC protein functionalized into NPs. These results suggest that the filling effect of shorter PEG chains is more critical for the right ligand exposure and consequent binding ability of these NPs than the fed amount of ligand-installed PEG chains, which can be explained by considering that the binding ability of ligand functionalized NPs is

determined by the number of receptor-accessible ligand molecules, as previously shown in a pilot study by Ishii *et al.* [16].

Altogether, the results herein reported suggest that the mobility of ligands, as well as their density, are crucial for the multivalent binding ability of ligand-functionalized NPs, and thus should be carefully design according to the desired application.

5. Conclusions

In summary, our study showed that precise adjustment of the PEG grafting density presented a significant impact on the biological performance of the developed NPs, either in terms of their internalization capacity as their transfection efficiency. This outcome emphasizes the need for the fine-tuning of PEG-modified NPs to attain optimal pDNA specifically delivery and bioactivity, as well as endorse the critical importance for the spatial control of the targeting moieties for the successful development of the next-generation nanomedicines.

Acknowledgements

The work was financed by Portuguese funds through FCT (Fundação para a Ciência e a Tecnologia) in the framework of the projects UID/BIM/04293/2013, PTDC/CTM-NAN/115124/2009 and PTDC/CTM-NAN/3547/2014. CP Gomes and CDF Lopes acknowledge FCT for their PhD scholarships (SFRH/BD/79930/2011 and SFRH/BD/77933/2011, respectively). V Leiro acknowledges the support of the project NORTE-01-0145-FEDER-000012, financed by Norte Portugal Regional Operational Programme (NORTE 2020), under the PORTUGAL 2020 Partnership Agreement, through the European Regional Development Fund (ERDF).

Supplementary Information

Table S1. Percentage of YOYO®-1 positive cells after incubation with nT or Tg NPs functionalized at different grafting densities.

1 mol% grafting density						
	ND7/23		NIH 3T3		RN22	
N/P ratio	nT NPs	Tg NPs	nT NPs	Tg NPs	nT NPs	Tg NPs
2	38.3 ± 2.4	75.8 ± 3.8	30.1 ± 4.2	37.7 ± 3.9	19.4 ± 1.3	26.7 ± 5.2
4	35.8 ± 3.8	77.4 ± 3.7	35.4 ± 3.9	37.3 ± 3.3	25.1 ± 2.8	22.8 ± 4.3
8	36.3 ± 1.9	91.3 ± 7.3	30.3 ± 4.4	29.1 ± 6.2	18.9 ± 3.8	19.3 ± 2.2
12	22.4 ± 4.2	89.7 ± 5.1	55.8 ± 6.3	42.5 ± 7.6	24.8 ± 2.7	18.3 ± 3.6
2 mol% grafting density						
	ND7/23		NIH 3T3		RN22	
N/P ratio	nT NPs	Tg NPs	nT NPs	Tg NPs	nT NPs	Tg NPs
2	35.5 ± 3.8	86.4 ± 7.3	28.7 ± 2.8	40.3 ± 6.1	18.4 ± 2.6	28.5 ± 2.0
4	35.4 ± 2.7	91.2 ± 8.5	32.8 ± 2.3	39.9 ± 5.6	21.3 ± 2.1	20.2 ± 3.3
8	31.2 ± 2.5	98.8 ± 3.2	29.4 ± 3.4	22.6 ± 3.4	16.8 ± 1.9	10.1 ± 0.9
12	21.5 ± 3.1	95.4 ± 5.2	48.5 ± 5.5	41.4 ± 2.7	29.3 ± 1.5	17.8 ± 0.5
4 mol% grafting density						
	ND7/23		NIH 3T3		RN22	
N/P ratio	nT NPs	Tg NPs	nT NPs	Tg NPs	nT NPs	Tg NPs
2	30.5 ± 2.5	85.3 ± 6.1	26.2 ± 3.2	44.6 ± 2.1	18.6 ± 1.8	23.3 ± 3.1
4	26.5 ± 3.6	81.3 ± 7.7	28.4 ± 2.9	45.7 ± 4.4	18.3 ± 1.3	21.0 ± 3.6
8	24.3 ± 2.9	94.5 ± 4.3	28.3 ± 2.7	34.4 ± 2.8	14.3 ± 0.7	12.6 ± 1.9
12	22.1 ± 4.1	91.2 ± 5.0	35.1 ± 3.0	37.9 ± 3.8	18.7 ± 2.2	17.9 ± 2.6

All measurements were carried out in a conventional flow cytometry. Untreated cells were used as control. Each value corresponds to the mean of three independent experiments ± SD.

Table S2. Percentage of YOYO®-1 ND7/23 positive cells after a 2 h incubation of neuron-targeted NPs functionalized with hetero PEG brushes

Formulation	% of positive cells
Tg NPs	97.6 ± 3.5
Tg2:1 NPs	94.5 ± 6.3
Tg1:1 NPs	96.4 ± 4.8
Tg1:2 NPS	92.1 ± 7.1

All NPs were prepared at N/P ratio of 8 with a final grafting density of 2 mol% per primary amine group in TMC. The percentage of YOYO®-1 positive cells was evaluated by conventional flow cytometry. Each value corresponds to the mean of two independent experiments performed with three replicates each ± SD.

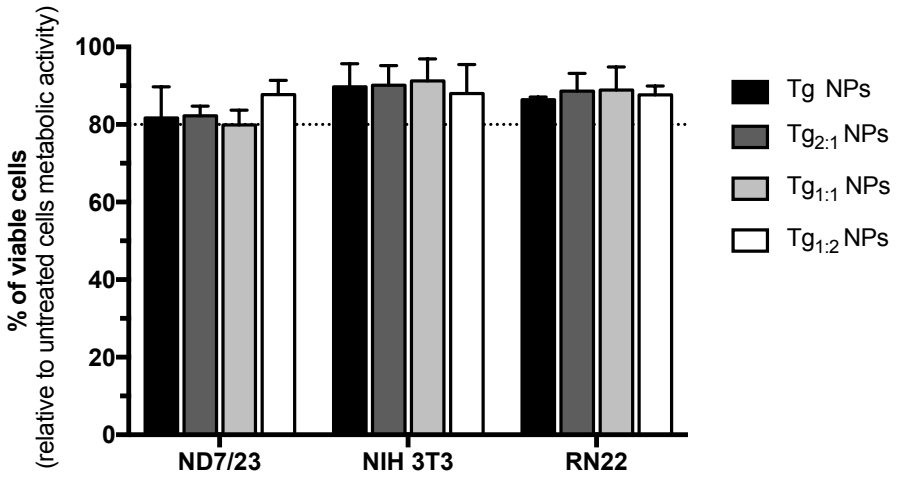

Figure S1. Cytotoxicity profile of neuron-targeted NPs bearing hetero PEG brushes upon incubation in different cell lines. Cellular viability was assessed 72 h after cells incubation with the different neuron-targeted NPs by the resazurin reduction method. Results are expressed as percentage of cellular metabolic activity relative to untreated cells. Each bar represents the mean of three independent experiments ± SD.

References

1. Cheng, C.J., et al., "A holistic approach to targeting disease with polymeric nanoparticles." Nat Rev Drug Discov, 2015. 14(4): p. 239-47.
2. Parveen, S., R. Misra, and S.K. Sahoo, "Nanoparticles: a boon to drug delivery, therapeutics, diagnostics and imaging." Nanomedicine, 2012. 8(2): p. 147-66.
3. Arachchige, M., Y. Reshetnyak, and O. Andreev, "Advanced targeted nanomedicine." J Biotechnol, 2015. 202: p. 88-97.
4. Kamaly, N., et al., "Targeted polymeric therapeutic nanoparticles: design, development and clinical translation." Chem Soc Rev, 2012. 41(7): p. 2971-3010.
5. Peer, D., et al., "Nanocarriers as an emerging platform for cancer therapy." Nature nanotechnology, 2007. 2(12): p. 751-60.
6. Byrne, J.D., T. Betancourt, and L. Brannon-Peppas, "Active targeting schemes for nanoparticle systems in cancer therapeutics." Adv Drug Deliv Rev, 2008. 60(15): p. 1615-26.
7. Jokerst, J.V., et al., "Nanoparticle PEGylation for imaging and therapy." Nanomedicine (Lond), 2011. 6(4): p. 715-28.
8. Mishra, S., P. Webster, and M.E. Davis, "PEGylation significantly affects cellular uptake and intracellular trafficking of non-viral gene delivery particles." European Journal of Cell Biology, 2004. 83(3): p. 97-111.
9. Hatakeyama, H., H. Akita, and H. Harashima, "A multifunctional envelope type nano device (MEND) for gene delivery to tumours based on the EPR effect: a strategy for overcoming the PEG dilemma." Adv Drug Deliv Rev, 2011. 63(3): p. 152-60.
10. Hama, S., et al., "Overcoming the polyethylene glycol dilemma via pathological environment-sensitive change of the surface property of nanoparticles for cellular entry." J Control Release, 2015. 206: p. 67-74.
11. Gomes, C.P., et al., "Translating chitosan to clinical delivery of nucleic acid-based drugs." MRS Bulletin, 2014. 39(01): p. 60-70.
12. Gomes, C.P., et al., "A high-throughput bioimaging study to assess the impact of chitosan-based nanoparticle degradation on DNA delivery performance." Acta Biomater, 2016. 46: p. 129-140.
13. Gomes, C.P., et al., "Atomic Force Microscopy as a Tool to Assess the Specificity of Targeted Nanoparticles in Biological Models of High Complexity." Advanced Healthcare Materials, 2017. 6(21): p. 1700597-n/a.
14. Lopes, C.D., et al., "Microfluidic-based platform to mimic the in vivo peripheral administration of neurotropic nanoparticles." Nanomedicine (Lond), 2016. 11(24): p. 3205-3221.
15. Lopes, C.D., et al., "BDNF gene delivery mediated by neuron-targeted nanoparticles is neuroprotective in peripheral nerve injury." Biomaterials, 2017. 121: p. 83-96.
16. Ishii, T., et al., "Enhanced target recognition of nanoparticles by cocktail PEGylation with chains of varying lengths." Chem Commun (Camb), 2016. 52(7): p. 1517-9.

17. Administration, U.F.a.D., "Guidance for Industry - Pyrogen and Endotoxins Testing." 2012.

18. Oliveira, H., et al., "Targeted gene delivery into peripheral sensorial neurons mediated by self-assembled vectors composed of poly(ethylene imine) and tetanus toxin fragment c." Journal of Controlled Release, 2010. 143(3): p. 350-358.

19. Sinha, K., et al., "Analysis of mutants of tetanus toxin HC fragment: ganglioside binding, cell binding and retrograde axonal transport properties." Molecular Microbiology, 2000. 37(5): p. 1041-1051.

20. Oliveira, H., et al., "Chitosan-based gene delivery vectors targeted to the peripheral nervous system." Journal of Biomedical Materials Research Part A, 2010. 95A(3): p. 801-810.

21. Ortyn, W.E., et al., "Extended depth of field imaging for high speed cell analysis." Cytometry A, 2007. 71(4): p. 215-31.

22. O'Brien, J., et al., "Investigation of the Alamar Blue (resazurin) fluorescent dye for the assessment of mammalian cell cytotoxicity." Eur J Biochem, 2000. 267(17): p. 5421-6.

23. Csaba, N., M. Koping-Hoggard, and M.J. Alonso, "Ionically crosslinked chitosan/tripolyphosphate nanoparticles for oligonucleotide and plasmid DNA delivery." Int J Pharm, 2009. 382(1-2): p. 205-14.

24. Silva, A.M., et al., "Integrated Analysis of Biological Samples by Imaging Flow Cytometry." Microsc Microanal, 2015. 21 Suppl 5: p. 95-6.

25. Rabanel, J.M., P. Hildgen, and X. Banquy, "Assessment of PEG on polymeric particles surface, a key step in drug carrier translation." J Control Release, 2014. 185: p. 71-87.

26. Nel, A.E., et al., "Understanding biophysicochemical interactions at the nano-bio interface." Nature Materials, 2009. 8(7): p. 543-557.

27. Salvati, A., et al., "Transferrin-functionalized nanoparticles lose their targeting capabilities when a biomolecule corona adsorbs on the surface." Nature Nanotechnology, 2013. 8(2): p. 137-143.

28. Mirshafiee, V., et al., "Protein corona significantly reduces active targeting yield." Chemical Communications, 2013. 49(25): p. 2557-2559.

29. Fontana, G., et al., "Amoxicillin-loaded polyethylcyanoacrylate nanoparticles: Influence of PEG coating on the particle size, drug release rate and phagocytic uptake." Biomaterials, 2001. 22(21): p. 2857-2865.

30. Mao, S., et al., "Synthesis, characterization and cytotoxicity of poly(ethylene glycol)-graft-trimethyl chitosan block copolymers." Biomaterials, 2005. 26(32): p. 6343-6356.

31. Kunath, K., et al., "The Structure of PEG-Modified Poly(Ethylene Imines) Influences Biodistribution and Pharmacokinetics of Their Complexes with NF-κB Decoy in Mice." Pharmaceutical Research, 2002. 19(6): p. 810-817.

32. Petersen, H., et al., "Polyethylenimine-graft-poly(ethylene glycol) copolymers: influence of copolymer block structure on DNA complexation and biological activities as gene delivery system." Bioconjug Chem, 2002. 13(4): p. 845-54.

33. Lee, H., J.H. Jeong, and T.G. Park, "PEG grafted polylysine with fusogenic peptide for gene delivery: high transfection efficiency with low cytotoxicity." J Control Release, 2002. 79(1-3): p. 283-91.

34. Gutoaia, A., et al., "Fine-tuned PEGylation of chitosan to maintain optimal siRNA-nanoplex bioactivity." Carbohydr Polym, 2016. 143: p. 25-34.

35. Pozzi, D., et al., "Effect of polyethyleneglycol (PEG) chain length on the bio-nano-interactions between PEGylated lipid nanoparticles and biological fluids: from nanostructure to uptake in cancer cells." Nanoscale, 2014. 6(5): p. 2782-92.

36. deGennes, P.G., "Conformations of Polymers Attached to an Interface." Macromolecules, 1980. 13(5): p. 1069-1075.

37. Allen, C., et al., "Controlling the Physical Behavior and Biological Performance of Liposome Formulations through Use of Surface Grafted Poly(ethylene Glycol)." Bioscience Reports, 2002. 22(2): p. 225-250.

38. Pack, D.W., et al., "Design and development of polymers for gene delivery." Nat Rev Drug Discov, 2005. 4(7): p. 581-93.

39. Sonawane, N.D., F.C. Szoka, Jr., and A.S. Verkman, "Chloride accumulation and swelling in endosomes enhances DNA transfer by polyamine-DNA polyplexes." The Journal of biological chemistry, 2003. 278(45): p. 44826-31.

40. Ragelle, H., G. Vandermeulen, and V. Preat, "Chitosan-based siRNA delivery systems." Journal of controlled release : official journal of the Controlled Release Society, 2013. 172(1): p. 207-18.

41. Miyata, K., "Smart polymeric nanocarriers for small nucleic acid delivery." Drug Discov Ther, 2016. 10(5): p. 236-247.

CHAPTER VIII

CONCLUDING REMARKS AND FUTURE PERSPECTIVES

Aiming at developing new therapeutic strategies to promote neuroregeneration in the peripheral nervous system (PNS), in this work we have chosen trimethyl chitosan (TMC) as the starting material for the development of neuron-targeted gene-carrying nanoparticles (NPs) to mediate the delivery of therapeutic molecules to specific neuronal cell populations.

TMC is a quaternized (methylation) derivative of chitosan with proven solubility at a wider pH range (pH 1-9) [1]. Due to its fixed positive charges, it condenses plasmid DNA (pDNA) at physiological pH more effectively, and therefore it presents a higher application potential in a clinical scenario.

The formation of stable and small-sized NPs is imperative to assure pDNA protection and colloidal stability in the extracellular environment, which ultimately will result in efficient cellular binding and uptake [2]. Moreover, an ideal vector must provide high protection of the complexed pDNA from degradation prior to its efficient release near or within the nucleus of a target cell. However, many of the polymeric features that contribute to pDNA protection also hamper its release once NPs are inside the cell. Various strategies have been tried to design vectors able to trigger pDNA release at the right time and space but little attention has been paid to the contribution of vector degradation to this process.

As we believe that pDNA bioavailability is highly dependent on NP disassemble and, consequently, polymer degradation, one of the goals for this thesis was to optimize the biodegradation rate of TMC-based NPs. In the work described in **Chapter V**, we altered the biodegradation rate of the TMC NPs by varying the degree of acetylation (DA) of the polymer (DA from 4 to 21%), giving rise to NPs with different enzymatic degradation profiles [3]. Our data showed that while the biodegradation rate of the developed NPs did not affect NP size, charge or ability to condense and protect pDNA, it had a significant impact on cell transfection efficiency, having the NPs based on TMC with an intermediate DA (16%) revealed to be most effective in transfecting neuronal-like cells among the ones tested. Subsequently, by means of a single quantitative technique – imaging flow cytometry, we were able to follow, for each tested formulation, major steps of the NP-mediated gene delivery process – NP cell membrane association, internalization and intracellular trafficking, including pDNA transport towards the nucleus. It has also been possible to assess NP cytotoxicity by quantification of cell apoptosis. Overall, the obtained data revealed that the biodegradation rate of these NPs affected their intracellular trafficking and,

consequently, their efficiency to transfect cells. In sum, in this work we provide novel information about the importance of vector degradation rate for gene delivery into cells as a way to tune gene expression in function of the desired application, and advances novel approaches to optimize NP formulation. Taking advantage of imaging flow cytometry, we were able to unravel some critical aspects for NP formulation and contribute to the design of more efficient nucleic acid delivery vectors.

In the future, it would be interesting to scrutinize the intracellular pathway even further and to understand the kinetics and compartment of pDNA release inside the cells.

After optimization of the NP core, the polymer with the best performance in terms of transfection efficiency (TMC with a DA of 16%) was further modified with thiol groups to allow for the preparation of neuron-targeted NPs. To attain NP neurotropism, our group has been exploring the tethering of the non-toxic 50 kDa carboxylic fragment from the tetanus toxin (HC), through the use of an intermediate poly(ethylene glycol) (PEG) spacer [4-9], since the former has been described to be neurotropic and capable of being retrogradely transported along the axonal terminals [8, 10, 11].

The ability to design NP delivery systems able to effectively and selectively target their payloads to specific cell populations is still a major caveat in the nanomedicine field. More importantly, there is an urgent need to develop biotechnological techniques able to correctly evaluate NPs vectoring capacity in a reliable manner, with reproducible and comparable results independently of the biological model being tested. In **Chapter VI,** molecular recognition force spectroscopy (MRFS) is presented as a tool to evaluate the specificity of HC-functionalized TMC-based NPs towards neuronal cell populations in biological samples of different complexity [12].

The use of atomic force microscopy tips functionalized with targeted *versus* non-targeted NPs made it possible to assess the specific interaction of each formulation with determined cell surface receptors in a precise fashion from biological models with different complexity. Our results show the selective binding and internalization of the targeted NPs toward the neuronal cell line, in opposition to fibroblasts or Schwann cells. More importantly, this selectivity towards neuronal cells was reinforced when these tips were probed in a more complex culture system as the dissociated dorsal root ganglia (DRG) primary cultures. Furthermore, in this model, a higher frequency of multiple unbinding events was observed

on the primary DRG neurons, pointing to a higher abundance of HC receptors expression than on the *in vitro* cell line. In contrast, the non-targeted NPs presented a statistically significant lower binding probability, independently of being probed against neuronal or non-neuronal cells. As the ultimate goal of the development of this NP system is to obtain a vector to be administered *in vivo* via a minimal invasive route, we further evaluated the vectoring capacity of the neuron-targeted TMC NPs in histological tissue sections of clinically relevant sites of administration. Our results show similar results of binding probability and forces for force-distance curves acquired in the sciatic nerve, when compared to the results obtained in neuronal cells from the primary dissociated DRG cultures. Remarkably, in the innervated neuromuscular junction (NMJ) from gastrocnemius muscle samples, a statistically significant high percentage of unbinding events per tip was observed, confirming this as a suitable tissue for the peripheral administration of the NPs. Also, our data show that the HC receptors density is higher at the NMJ location than in sciatic nerve. Altogether, this biotechnological study disclosed the feasibility of MRFS for the development and characterization of targeted nanomedicines in different biological models, proving to be a reliable and reproducible method, independently of the biological model being tested. We believe that MRFS has the potential to fasten comparative investigations of different drug-delivery systems and targeting agents. Moreover, by combining fluorescent microscopy with AFM force spectroscopy one was able to correlate the specific interactions of the ligand–receptor pair in specific cells of heterogeneous primary cultures or cellular regions of histological sections.

Having established the technology, in the future it would be interesting to test other neuronal-targeting moieties, such as small peptides like Tet1, a 12-aminoacid neuropeptide that competes effectively with the tetanus toxin for receptor binding and was identified by phage display [13]. The use of a smaller peptide for NP functionalization would offer some advantages as the easiness of purification, more controlled assembly with the right orientation at the NP surface and, considering an *in vivo* application, the lower production of immunogenic effects.

In fact, the amount and exposure of the targeting moieties at the NP surface are critical parameters regarding the targeting potential of a nanosized delivery system [14]. Following that idea, in **Chapter VII** we established the formulation that maximizes cell-nanoparticle specific interaction by varying the PEG spacer length and the HC density at the NPs

surface. For this, we performed NP internalization and transfection studies on neuronal *versus* non-neuronal cell lines that allowed us to determine the grafting density of 2 mol% of PEG chains per mol of primary amine groups in the polymer as the one with superior biological performance. To enhance HC exposure and maximize cell-NP specific interaction, NPs containing hetero PEG brushes composed by HC-PEG_{5k} and a shorter methoxy-PEG at a final grafting density of 2 mol%. By intercalating HC-PEG_{5k} with methoxy-PEG_{2k} we attained the best performance in terms of internalization (higher payload delivery into cells) and transfection efficiency, using two times lower amount of HC. This outcome highlights the need for fine-tuning of PEG-modified nanoparticles for optimal targeting.

Future work should be performed to evaluate the binding probability and forces of these formulations containing hetero PEG brushes towards neuronal cell populations in more complex biological models by MRFS, before their application in an *in vivo* setting.

The fact that the developed TMC-based vectors are biodegradable, non-toxic, mediate efficient gene transfer into mammalian neurons and exhibit adequate properties for *in vivo* administration render these type of complexes as very promising tools for gene therapy based strategies to promote neuroregeneration. Moreover, the proposed system, based on the design of modular structures and therefore more versatile ones, can be easily adapted to be targeted to different cell types and demands by exploring other targeting moieties, broadening the scope of their possible application in regenerative medicine.

References

1. Mourya, V.K. and N.N. Inamdar, "Trimethyl chitosan and its applications in drug delivery." J Mater Sci Mater Med, 2009. 20(5): p. 1057-79.
2. Wiethoff, C.M. and C.R. Middaugh, "Barriers to nonviral gene delivery." J Pharm Sci, 2003. 92(2): p. 203-17.
3. Gomes, C.P., et al., "A high-throughput bioimaging study to assess the impact of chitosan-based nanoparticle degradation on DNA delivery performance." Acta Biomater, 2016. 46: p. 129-140.
4. Oliveira, H., et al., "Targeted gene delivery into peripheral sensorial neurons mediated by self-assembled vectors composed of poly(ethylene imine) and tetanus toxin fragment c." Journal of Controlled Release, 2010. 143(3): p. 350-358.
5. Oliveira, H., et al., "Chitosan-based gene delivery vectors targeted to the peripheral nervous system." Journal of Biomedical Materials Research Part A, 2010. 95A(3): p. 801-810.
6. Oliveira, H., et al., "Molecular Recognition Force Spectroscopy: A New Tool to Tailor Targeted Nanoparticles." Small, 2011. 7(9): p. 1236-1241.
7. Lopes, C.D., et al., "In vivo targeted gene delivery to peripheral neurons mediated by neurotropic poly(ethylene imine)-based nanoparticles." Int J Nanomedicine, 2016. 11: p. 2675-83.
8. Lopes, C.D., et al., "Microfluidic-based platform to mimic the in vivo peripheral administration of neurotropic nanoparticles." Nanomedicine (Lond), 2016. 11(24): p. 3205-3221.
9. Lopes, C.D., et al., "BDNF gene delivery mediated by neuron-targeted nanoparticles is neuroprotective in peripheral nerve injury." Biomaterials, 2017. 121: p. 83-96.
10. Fishman, P.S. and D.R. Carrigan, "Retrograde transneuronal transfer of the C-fragment of tetanus toxin." Brain research, 1987. 406(1-2): p. 275-9.
11. Herreros, J., G. Lalli, and G. Schiavo, "C-terminal half of tetanus toxin fragment C is sufficient for neuronal binding and interaction with a putative protein receptor." The Biochemical journal, 2000. 347 Pt 1: p. 199-204.
12. Gomes, C.P., et al., "Atomic Force Microscopy as a Tool to Assess the Specificity of Targeted Nanoparticles in Biological Models of High Complexity." Adv Healthc Mater, 2017.
13. Liu, J.K., et al., "A novel peptide defined through phage display for therapeutic protein and vector neuronal targeting." Neurobiology of disease, 2005. 19(3): p. 407-18.
14. Gu, F., et al., "Precise engineering of targeted nanoparticles by using self-assembled biointegrated block copolymers." Proc Natl Acad Sci U S A, 2008. 105(7): p. 2586-91

APPENDICES

APPENDIX I

MOLECULAR RECOGNITION FORCE SPECTROSCOPY FOR PROBING CELL TARGETED NANOPARTICLES IN VITRO

Molecular Recognition Force Spectroscopy for Probing Cell Targeted Nanoparticles in vitro

Carla Pereira Gomes[1,2,3,#], Hugo Oliveira[4], Andreas Ebner[5], Peter Hinterdorfer[5] and Ana Paula Pêgo[1,2,3,6]

1 – Instituto de Engenharia Biomédica (INEB), Universidade do Porto, Porto Portugal
2 – Instituto de Investigação e Inovação em Saúde (i3S), Universidade do Porto, Porto, Portugal
3 – Faculdade de Engenharia, Universidade do Porto, Porto, Portugal
4 – University of Bordeaux, Tissue Bioengineering, U1026, F-33076 Bordeaux, France; Inserm, Tissue Bioengineering, U1026, F-33076 Bordeaux, France
5 – Institute of Biophysics, Johannes Kepler University, Linz, Austria
6 – Instituto de Ciências Biomédicas Abel Salazar (ICBAS), Universidade do Porto, Porto, Portugal

#Current adress: Instituto de Medicina Molecular, Faculdade de Medicina, Universidade de Lisboa. Avenida Professor Egas Moniz, 1649-028, Lisboa, Portugal

In press **in Methods in Molecular Biology, 2017**

Abstract

In the development and design of cell targeted nanoparticle-based systems the targeting moieties density plays a fundamental role in allowing maximal cell-specific interaction. Here, we describe the use of molecular recognition force spectroscopy as a valuable tool for the characterization and optimization of targeted nanoparticles towards attaining cell specific interaction. By tailoring the density of targeting moieties at the nanoparticle surface, one can correlate the unbinding event probability between nanoparticles tethered to an atomic force microscopy tip and cells to the nanoparticle vectoring capacity. This novel approach allows for a rapid and cost-effective design of targeted nanomedicines reducing the need of long and tedious *in vitro* tests.

1. Introduction

Tailored drug-delivery systems have become increasingly important in the development of novel medical therapies and pharmaceutical products [1]. The use of targeted nanoparticles, which have the capability of encapsulating different therapeutic agents and preferentially delivering them to specific tissues and cells, hold the promise of revolutionizing the treatment of many diseases including cancer, cardiovascular, neurological and immunological disorders [2]. In this context, the optimal ligand density of targeting moieties in a nanoparticle-based system, allowing maximal cell-specific interaction, plays a fundamental role in the development and design of efficient targeted systems. However, the optimization of the density of targeting moieties implies tedious and time-consuming *in vitro* studies.

In recent years, atomic force microscopy (AFM) has emerged as a powerful characterization platform in the field of biosciences, providing valuable insight into many biological processes that may have major implications for drug design and development [1]. Because of its piconewton force sensitivity and nanometer positional accuracy, the AFM allows to explore the forces and the dynamics of the interaction between individual ligands and receptors, either on isolated molecules or on cellular surfaces [3, 4].

Our group has previously proposed molecular recognition force spectroscopy (MRFS) as a valuable tool for the characterization and optimization of poly(ethylene imine) based nanoparticles complexed with plasmid DNA towards improving receptor-specific binding of the nanoparticle-based gene-delivery system to the ND7/23 neuronal cell line [5]. In more detail, the 50 kDa non-toxic carboxylic fragment of the tetanus toxin (HC fragment), known to specifically bind to the trisialoganglioside GT1b receptor in the membrane of neuronal cells, was used as the targeting moiety for the development of ternary nanoparticles [6]. Both the HC fragment alone and the ternary nanoparticles were tethered to an AFM tip via hetero-bifunctional PEG-linkers as previously described [7-9], and probed against neuronal (sample) and fibroblasts (control) cells. Specific interactions with the ND7/23 cells had a similar binding probability of around 16% for both the HC fragment and the ternary nanoparticles, with a dramatic drop after blocking cell receptors with soluble HC fragment.

More recently, we took advantage of MRFS to evaluate the specificity of neuron-targeted trimethyl chitosan nanoparticles towards neuronal cell populations in biological models of high complexity, such as primary mixed cultures as well as specific subcellular regions in histological tissue sections [10].

In conclusion, the use of MRFS allowed us to determine the optimal targeted nanoparticle formulation regarding neuronal cell internalization and transfection, as well as to obtain new insights into the ligand–receptor mechanism. The obtained results illustrate the potential of this novel approach for the rapid and cost-effective design of targeted nanoparticle systems, as MRFS has proved to be a reliable method that allows reproducible and comparable results independently of the biological model being tested (isolated cell lines, heterogeneous cultures or tissue samples).

Although MRFS experiments are relatively straightforward to set up, there are critical steps such as sample preparation, AFM tips functionalization and data evaluation that are critical and of paramount importance to obtain suitable data. Taking this into consideration, in this chapter we present the protocol established by us for the evaluation of nanoparticles targeting potential towards isolated cell lines, as well as valuable tips for the experimental design and data interpretation.

2. Materials

Prepare all solutions using ultrapure water (prepared by purifying deionized water, to attain a resistivity of 18.18 MΩ.cm at 25°C) and analytical grade reagents. Prepare and store all reagents at room temperature (RT), unless indicated otherwise. Diligently follow all waste disposal regulations when disposing waste materials.

2.1. Cell culture

a) 0.1% (w/v) poly-*D*-lysine (PDL)
b) ND7/23 cells (mouse neuroblastoma (N18 tg 2) x rat dorsal root ganglion neuron hybrid cell line) (this neural cell line was selected as these cells express HC receptors) (*see* Reference [6])
c) NIH 3T3 cells (mouse embryonic fibroblasts) (control cell line; these cells do not express HC receptors - *see* Reference [6])
d) Dulbecco's Modified Eagle's Medium (DMEM)
e) Fetal bovine serum (FBS) (heat inactivated at 57°C for 30 min)
f) Antibiotic solution (P/S; 10,000 $U.mL^{-1}$ penicillin and 10,000 $\mu g.mL^{-1}$ streptomycin)
g) Tissue culture polystyrene flasks
h) Polystyrene petri dishes (35 mm x 10 mm)
i) 4% (w/v) paraformaldehyde
j) Phosphate-buffered saline (PBS) solution
k) Glass coverslips (diameter 22 mm)
l) Tweezers
m) Sterilization filters (0.22 µm pore) and syringes

2.2. Nanoparticle preparation

a) Thiolated poly(ethylene imine) – PEISH (for further details on the synthesis of the modified polymer see Reference [6])
b) Plasmid DNA (in this report we considered a 7.4 kb plasmid encoding for the green fluorescent protein (GFP) under a CMV promoter)
c) 5% (w/v) glucose solution (pH 7.4)
d) HC fragment (*see* **Note 1**)
e) Phosphate buffer (pH 8)

f) Hetero-bifunctional 5 kDa PEG bearing an *N*-hydroxysuccinimide (NHS) and a maleimide end group (Maleimide-PEG_{5000}-NHS)

2.3. Tip funcitionaliztion

a) Aminopropyltriethoxysilane (APTES)
b) Chloroform
c) Triethylamine (TEA)
d) Sodium cyanoborohydride, $NaCNBH_3$
e) Ethanolamine
f) 1% (v/v) citric acid prepared in ultrapure water
g) Sodium hydroxide, NaOH
h) EDTA disodium salt (EDTA-$Na_2.H_2O$)
i) 4-(2-hydroxyethyl)-1-piperazineethanesulfonic acid, HEPES
j) Tris(carboxyethyl)phosphine (TCEP) hydrochloride
k) PBS
l) Hetero-bifunctional PEG bearing an NHS and an acetal end group (Acetal-PEG_{18}-NHS)
m) Hetero-bifunctional PEG bearing an NHS and a maleimide end group (Maleimide-PEG_{18}-NHS)
n) Polystyrene Petri dishes
o) Parafilm “M”®
p) Silicon nitride AFM cantilevers with nominal spring constants ranging from 0.01 to 0.05 $N.m^{-1}$ (MSCT, Bruker)

2.4. Others

a) Gold-coated mica surface (Agilent Technologies or commercially available gold spin-coated mica)
b) Nitrogen gas source (purity 99.9992%)
c) Argon gas source (purity 99.9997%)
d) Tweezers
e) Glass pipettes
f) Micropipettes and pipette tips
g) Glass desiccator (5 L)

2.5. Equipment

a) PicoPlus 5500 AFM setup and fluid cell equipped with flow cell (Agilent Technologies)

b) CCD camera

c) Laminar flow hood (Type II)

d) Cell incubator

3. Methods

3.1. Cell sample preparation

Cell handling and media preparation should be performed in a laminar flow hood under aseptic conditions.

3.1.1. ND7/23 and NIH 3T3 cells should be grown in complete DMEM medium (with 10 % (v/v) heat inactivated FBS and 1% (v/v) P/S) under 5% CO_2 at 37 °C. Renew culture medium every other day and subculture cells at 80% confluence.

3.1.2. Seed cells on PDL–coated glass coverslips placed inside a petri dish (*see* **Note 2**) in order to achieve a confluence state of around 50%.

3.1.3. One or two days after cell seeding remove media, wash cells with warm PBS (37 °C) and fix cells with 4 % (w/v) paraformaldehyde for 20 min at RT (*see* **Note 3**).

3.1.4. Wash cells twice with PBS, close the petri dish with Parafilm "M"® and store them at 4 ºC until further use (when no sodium azide is used cells can be stored up to 2 weeks).

3.2. Nanoparticle preparation

3.2.1. After production and purification of the HC fragment (*see* **Note 1**), incubate the protein solution with the hetero-bifunctional Maleimide-PEG_{5000}-NHS, at a 2.5 PEG/HC protein molar ratio (for further details *see* reference [6]).

3.2.2. Prepare the nanoparticle core by mixing, while vortexing, equal volumes of plasmid DNA and PEISH solutions (both at 1 $mg.mL^{-1}$ in 5% (w/v) glucose aqueous solution, pH 7.4) at an N/P molar ratio of 3 (*see* **Note 4**).

3.2.3. Incubate the complex mixture for 15 min at RT to allow for nanoparticle formation and stabilization.

3.2.4. Subsequently, add the HC previously coupled with PEG at a final concentration ranging from 1.25 to 7.5 µg per 2 µg of plasmid DNA to the complex mixture and immediately use for AFM tip functionalization with the maleimide linkers (*see* **Section 3.5**).

3.3. AFM tips amino-functionalization with APTES

Perform the whole procedure in a well-ventilated hood (*see* **Note 5**).

3.3.1. Wash the AFM cantilevers in chloroform 3 x 5 min. Every washing step should be performed using a clean beaker with fresh chloroform. Finally, dry the AFM cantilevers in a stream of nitrogen gas.

3.3.2. Flush desiccator chamber with argon gas.

3.3.3. Place one tray with 30 µL APTES and another tray with 10 µL TEA in the desiccator (*see* **Note 6**).

3.3.4. Place the cantilevers in the desiccator close to the two trays, close the desiccator lid and incubate for 2 h.

3.3.5. Remove the trays containing APTES and TEA and flush the desiccator with argon. Subsequently place the tips under argon atmosphere for at least 2 days ("curing").

3.3.6. Store the tips under argon in a dust free box for up to 3 weeks.

3.4. AFM tips functionalization with acetal linkers

Perform the whole procedure in a well-ventilated hood.

3.4.1. Dissolve 1 mg of the acetal-PEG_{18}-NHS linker in 0.5 mL chloroform, transfer the solution into a small container (the tips must fit and be fully covered with the liquid), add TEA (30 µL) and mix (*see* **Note 7**).

3.4.2. Immediately place the APTES functionalized cantilever(s) in the same container, cover with lid to prevent chloroform evaporation and incubate for 2 h.

3.4.3. Wash with chloroform (3 × 10 min) and dry with nitrogen gas.

3.4.4. Store cantilever(s) for up to several weeks under argon, or continue with next step.

3.4.5. Immerse cantilever(s) for 10 min in 1% (v/v) citric acid.

3.4.6. Wash cantilever(s) in ultrapure water (3 × 5 min), dry with nitrogen gas and immediately continue to the next step.

3.4.7. Place the cantilever(s) on a piece of Parafilm “M”® in a polystyrene Petri dish: to do so, a piece of Parafilm “M”® is pressed onto the inner surface of a polystyrene Petri dish and several cantilevers are placed onto the Parafilm “M”® in a radial arrangement, with the tips in the center and facing upwards. The tipped ends should be so close together so that one droplet of the protein solution covers all tips at the same time.

3.4.8. Pipette 100 µL protein solution (1 µM) onto the cantilever(s).

3.4.9. Add 2 µL of a freshly prepared 1 M of sodium cyanoborohydride solution (with 20 mM NaOH), mix carefully into the protein solution droplet with the pipette, cover with lid and incubate for 1 h (*see* **Note 8**)

3.4.10. Add 5 µL of ethanolamine (1 M, pH 8.0) to the drop on the cantilever(s), mix cautiously, cover with lid and incubate for another 10 min.

3.4.11. Wash in PBS (3 × 5 min).

3.4.12. Mount cantilever in AFM setup (or store immersed in PBS containing 0.02% (v/v) sodium azide at 4°C, up to 1-2 weeks) (*see* **Figure 1a**).

3.5. AFM tips functionalization with maleimide linkers

Perform the whole procedure in a well-ventilated hood.

3.5.1. Dissolve 1 mg of the maleimide-PEG_{18}-NHS in 0.5 mL chloroform, transfer the solution into a small container, add TEA (30 µL) and mix.

3.5.2. Immediately place cantilever(s) into the container, cover with lid and incubate for 2 h.

3.5.3. Wash with chloroform (3 × 10 min) and dry with nitrogen gas. Continue with next step.

3.5.4. Place cantilever(s) on a piece of Parafilm “M”® in a polystyrene Petri dish.

3.5.5. Pre-mix the following components (*see* **Note 9**):

- 100 µ L nanoparticle dispersion in 5% (w/v) glucose (pH 7.4) (*see* **Note 10**)
- 2 µL EDTA (100 mM, pH 7.5)
- 5µL HEPES (1 M, pH 7.5)
- 2 µL TCEP hydrochloride (100 mM)
- 2 µL HEPES (1 M, pH 9.6) – or more if the thiol component is in a strongly acidic solution

3.5.6. Pipet the mixture onto the cantilever(s), cover with lid and incubate for 2-4 h.

3.5.7. Wash in PBS or any other buffer of choice (3 x 5 min).

3.5.8. Mount cantilever in AFM setup (or store immersed in PBS at 4ºC for 1-2 weeks) (*see* **Figure 1b**).

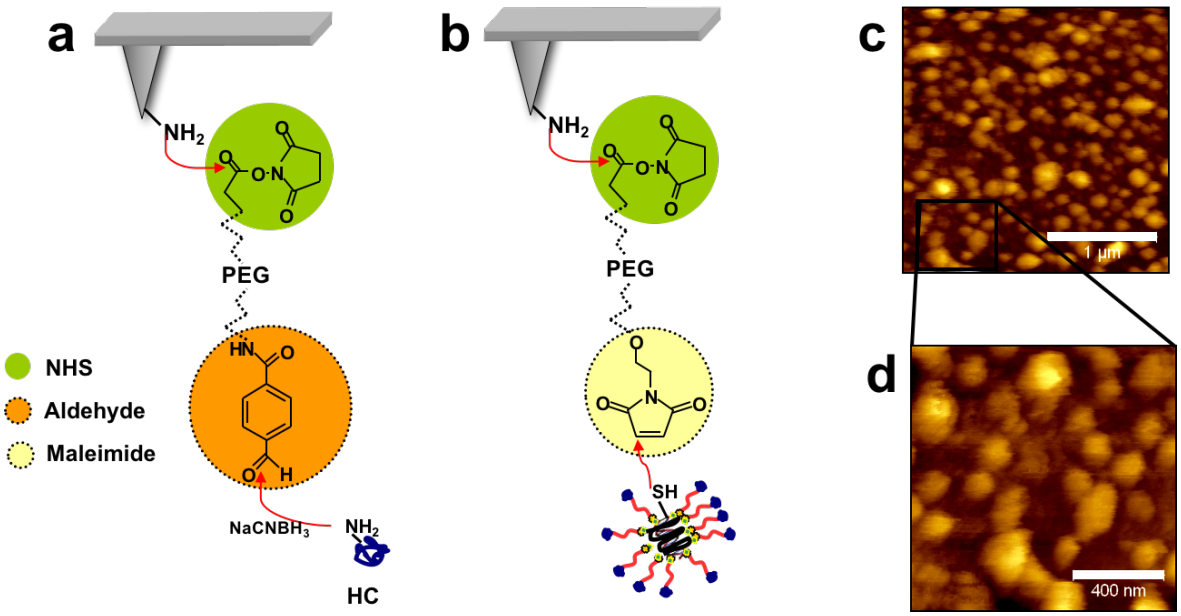

Figure 1. Schematic representation of the chemical tethering strategies used to bind the non-toxic carboxylic fragment from the tetanus toxin (HC fragment) (a) and the functionalized nanoparticles (b) to the AFM tip via a hetero-bifunctional PEG_{18}. Both tips were amino-functionalized using 3-aminopropyltriethoxysilane (APTES). The tethering of the nanoparticles was confirmed by imaging the surface of the cantilever using magnetic AC mode (c) and therefore single nanoparticles could be resolved by AFM imaging (d) (adapted from Ref. [5] with permission from John Wiley and Sons).

3.6. Force measurements

3.6.1. Clean tweezers and AFM fluid cell with a mild detergent solution (1% (w/v) SDS in water) and rinse extensively with ultrapure water and, finally, with ethanol. Air-dry.

3.6.2. Place the glass coverslip containing cell samples onto the gold-coated mica (*see* **Note 11**) and place them on the AFM sample plate (*see* **Note 12**).

3.6.3. Gently wash the cell sample with PBS at RT 3-5 times to remove any loose cells. Fill the fluid cell with PBS until it is fully covered. Ensure that the liquid is not leaking (*see* **Note 13**).

3.6.4. Allow the AFM setup to thermo stabilize for about 30 min before use. Meanwhile, set the program to conventional contact mode. Place the AFM scanner into the AFM station and adjust the position with the sample stage to allow enough space between them (*see* **Note 14**).

3.6.5. Insert the functionalized cantilever into the AFM scanner. Assemble the AFM fluid cell with care and let the system to equilibrate for 10 min to minimize thermal drift. During this time, adjust the CCD camera to clearly see the cells underneath the AFM tip. Localize the tip above an isolated cell. Thereafter, align and focus the laser beam onto the cantilever end and adjust the photodiode signal to zero (*see* **Note 15** and **Figure 2a**).

3.6.6. Approach the functionalized AFM tip towards cells using the contact mode. Select cells that are firmly attached and have a flat-shaped morphology. Avoid round-shaped cells that are loosely attached to the surface as this may indicate that at the time of fixation they were detaching, undergoing apoptosis or already dead. These cells can adsorb to the AFM tip and damage it.

3.6.7. Open the conventional contact force calibration plot mode. Set the sweep amplitude of the force-distance cycle to 1 Hz vertical sweeping frequency and 500 nm z-range (*see* **Note 16**).

3.6.8. Start the force-distance cycles acquisition (*see* **Figure 2b**) and slightly lower the cantilever closer to the cell surface until you achieve optimal contact (*see* **Note 17**).

3.6.9. Observe the unbinding events in the force-distance curves. For each cell, record at least 1,000 force-distance curves, changing the tip position (to an area nearby within the same cell, without withdrawing) every 200 curves to ensure statistical significance.

3.6.10. Withdraw the tip and re-approach again on a different cell. Ensure that the laser spot has not moved (*see* **Note 18**). Repeat the recording of force-distance curves on at least 5 different cells (*see* **Note 19**).

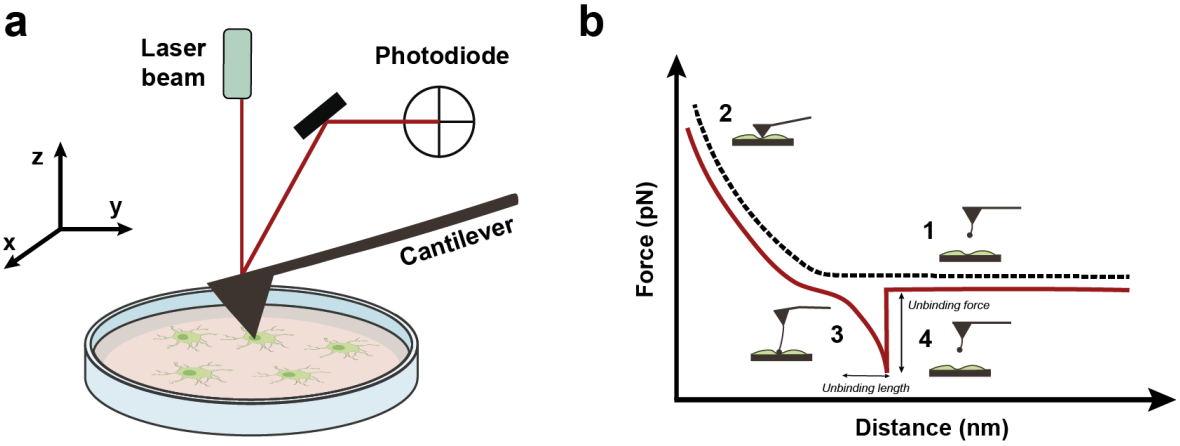

Figure 2. Typical setup of an AFM instrument (a). The tip-sample interactions can arise from a variety of forces (electrostatic, van der Waals, capillary, chemical, etc.) and yields the cantilever deflection, which is detected by using a laser beam reflecting off the back of the cantilever onto a position-sensitive photodiode. **Schematic representation of a force-distance cycle representative of a specific unbinding event for a single biomolecular complex (b).** The force is plotted against the piezo traveling distance. As the functionalized AFM tip approaches the cell sample surface (black dotted line, 1), the ligand encounters its paired receptor, resulting in the cantilever deflection (2). Subsequently, the tip is pulled away from the surface (red solid line), which leads to the linker stretching and originates a nonlinear curve (3) and the force continues to increase until the break of the ligand-receptor bond (4).

3.7. Specificity proof of the functionalized AFM tip

3.7.1. Withdraw the tip from the sample by 100 µm (see Note **20**).

3.7.2. Remove the sample and add soluble protein solution (HC protein) to the cell medium in order to achieve a final concentration of 1 mg.mL^{-1} (*see* **Note 21**).

3.7.3. Mount the liquid cell on the AFM setup and incubate the system for 1 hour to allow the blocking molecules to distribute homogenously in the system.

3.7.4. Re-approach the tip towards the sample and record force-distance curves as previously mentioned (*see* **Note 22**).

3.7.5. Withdraw the tip by 200 µm from the surface, remove the liquid cell from the AFM setup and gently wash the surface several times with PBS.

3.7.6. Mount the liquid cell into the system, approach the tip as previously mentioned and repeat the force-distance curves as described. If the blocking ligands are completely removed, unbinding events similar to the initial conditions should be observed (*see* **Note 23** and **Figure 3**). If this is the case, the block-washout experiment is now completed and will confirm the specificity of the functionalized AFM tip (*see* **Note 18**).

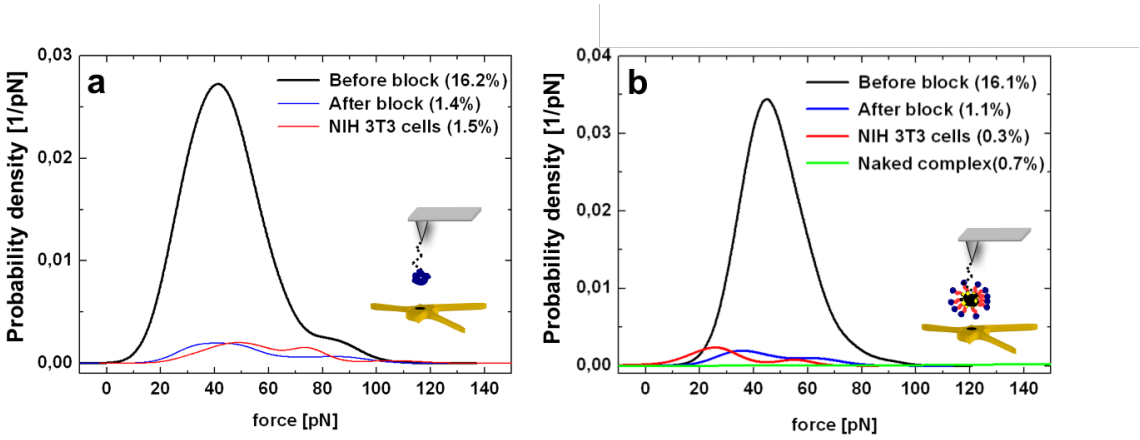

Figure 3. Probability density function of rupture forces considering the interaction between the isolated HC fragment (a) or the ternary nanoparticles (b) and neuronal cells. To determine the specificity of each functionalized tip, controls were performed by surface blocking with free HC fragment (0.1 mg.mL^{-1} for 1 hour; after block), in the control cell line (NIH 3T3 cells) or using nanoparticles lacking the HC moieties (naked complex). The unbinding probability of each condition is presented inside parentheses (adapted from Ref. [5] with permission from John Wiley and Sons).

3.8. Data analysis

All numerical calculations were performed using the matrix oriented computer environment MatLab^{TM} Version R2009b (MATH WORKS Inc.) and the previous algorithms described to find the position of unbinding events and calculate the respective unbinding forces (*see* Reference [11]).

3.8.1. For each data set with a given tip, determine the cantilever deflection sensitivity. This value depends on the type of the cantilever, but also on the optical path of the AFM detection laser, and will be slightly different each time the cantilever is mounted in the instrument. To do so, record a few force-distance curves on a cell-free zone of the glass coverslip (bare hard substrate). (*see* **Note 24**).

3.8.2. Separately analyze the results acquired for each condition, i.e., initial condition, block experiment and washout for each cantilever used. Detect the unbinding events that present the unique characteristic shape of specific interaction between ligand-receptor in the retrace curves (*see* **Note 25**).

3.8.3. For quantitative analysis of the unbinding forces determine the spring constants of the cantilevers, so that the deflection of the cantilever can be converted into actual force values (F), using the well-known Hooke's law:

$F = kx$,

Where k represents the cantilever spring constant and x the known distance of the cantilever deflection. For this calibration we used the thermal noise method [12, 13]. This is the most widely and commonly accepted method for cantilever spring constant determination.

4. Notes

1. The HC fragment was produced recombinantly using the BL21 *E. coli* strain. The plasmid encoding for the HC fragment, together with a coding sequence for six histidines in the N terminal, was a kind offer from Prof. Neil Fairweather (King's College, UK). For further details on the protocol for HC production and purification refer to reference [14].

2. Immobilization of cells depends mainly on the cell type and on the substrate where the cells grow on. Here cells are to be seeded on glass coverslips, so prior cell seeding the glass slides have to be coated with an adhesive coating. Briefly, before cell seeding glass coverslips were cleaned with 70% (v/v) ethanol overnight. Afterwards, they were rinsed in absolute ethanol and air-dried under sterile conditions. The coverslips were placed in small petri dishes (35 mm x 10 mm) and 2 mL of 0.1% (w/v) of PDL (prepared in ultrapure water; after preparation, the solution was sterilized by passing through a 0.22 µm filter, aliquoted and stored at -20 ºC for up to 1 year) was added onto the glass. After an incubation period of 1 hour at 37 ºC, the solution was removed and coverslips were washed twice with sterile ultrapure water and air-dried. After this procedure, the glass coverslips can be used directly or stored (seal the containers) in the refrigerator at 4 ºC for up to one day.

3. Depending on the cells growth rate, the required cell culture time to achieve optimal cell density may vary. As soon as cells are adhered to the coverslips, they can be fixed. The duration and reagent used for fixation can vary depending on the cell type used and on the ligand-receptor pair. Ideally, cells should be used live if you have a setup that allows temperature and CO_2 control. Otherwise, select fixation conditions that do not alter the ligand-receptor bond properties.

4. The N/P ratio stands for the ratio of free amino groups from the polymer (N) and the phosphate groups from the plasmid DNA (P).

5. Factors to be considered during tip functionalization include:

- the selection of a suitable AFM probe is critical, the key factors being sharpness of the tip and the cantilever's spring constant;
- the selection of tip functionalization chemistry – the ligand molecule must be connected to the tip so that the binding strength between the tip and the molecule is higher than the interaction between the molecule and the surface receptor;

- the temperature, buffer composition and pH must be carefully chosen during tip functionalization and force measurements, so the binding activity of the molecule is not altered;
- the correct orientation and function of the attached molecule are crucial for proper binding experiments.

6. The reagent APTES must not contain any aggregates; therefore, it must be used immediately after purchase. Any contact with humidity has to be avoided. Thus, it has to be transferred into the desiccator as fast as possible. Alternatively, it can be re-distilled under vacuum. New (or re-distilled) APTES can be kept "fresh" if small aliquots are sealed in crimp vials under argon gas and stored at -20°C for no longer than 12 months.

7. You can functionalize as many cantilevers as you can fit into the small container. We never functionalized less than 5 or more than 10. Do not move the container after putting the cantilever inside, otherwise you can break the cantilever tips. The acetal linking method is not applicable if the protein sample contains buffer components with primary amines, ammonium bicarbonate or ammonium acetate. It also does not work for proteins stored in the presence of detergent. Pipetting of chloroform and TEA should be performed with glass pipettes and a pipette bulb (or with a graduated glass capillary in case of TEA) and not with the plastic tips of pipettes because the contact of the solvent with the plastic tips may lead to the presence of extractable in chloroform and/or TEA that in turn can interfere with the process. Similarly, you should pay attention to the material of the small container used for tips functionalization (do not use a plastic container).

8. Extreme caution is necessary when weighing the aliquots of $NaCNBH_3$. Use a gas mask, a lab coat, and gloves for weighing. All material transfers must be performed in a well-ventilated hood. For proper waste, dissolve 3 pellets of NaOH in 500 mL tap water, add the unused $NaCNBH_3$ solution, mix, pour into the drain and flush with tap water.

9. The order of the pipetting steps is critical and must not be changed. The sequence of pipetting steps has been optimized to minimize the adverse effect of air on TCEP and on the thiol component. The amount of EDTA is necessary (and sufficient) to prevent re-oxidation during the coupling procedure on a time scale of few hours. For longer reaction times, it is advantageous to conduct the reaction under argon. Optimal pH conditions should be tested for different nanoparticle dispersion formulations.

10. The buffer of the thiol molecule to couple to the maleimide linker should not contain amino groups, 2-mercaptoethanol, dithiothreitol, dithioerythrol or glutathione reagents.

11. The use of a gold-coated mica helps to achieve a better contrast on a transmission image recorded with a CCD camera when observing cells and AFM tips.

12. When mounting the AFM fluid cell on the sample plate it is important to ensure that no air bubbles are trapped within the fluid cell assembly, as they will interfere with the AFM measurements.

13. The PBS solution should be filtered before its usage in the AFM fluid cell to avoid the presence of particles that could contaminate the sample. These can obstruct the cantilever and affect the purity of the sample.

14. The space between the AFM scanner and the AFM sample stage should be adequate for the thickness of the sample, glass and gold-coated mica to avoid damage to the coated tip.

15. It is important to maintain the functionalized tips permanently in liquid; otherwise the ligands may denature (this is particularly relevant for proteins or antibodies). This can be achieved by placing one drop of buffer on the tip of the AFM cantilever after mounting it on the AFM scanner.

16. You can reduce or increase the sweep amplitude and distance range depending on the cell type and the ligand-receptor pair. After you have found an appropriate sweep amplitude, hold the value constant throughout the experiment. Sweep amplitude or the speed of the retraction rate must be indicated in the results of the unbinding forces. Varying the speed of the tip movement can give further information about the ligand-receptor pair. The approach and retraction rates can be varied independently, and waiting times can be added at the surface or at the retraction position. Moreover, as the rupture force distributions depend on the speed of the retraction rate (more precisely, the loading rate), varying the pulling rate can be useful for studying the dynamics of unbinding [15, 16].

17. When performing force spectroscopy in cells be carefully to not use high forces in contact mode, as it can cause damage to the cells membrane. We do not recommend to use forces above 200 pN.

18. If, after trying all functionalized tips from the same batch of cantilevers, you could not observe any unbinding events, you should try one of the following procedures: a) functionalize a new batch of cantilevers and perform longer incubation times at each step and b) use a new

batch of cells. If there is still no success, it is probable a result of a problem with the cell system (low density of receptors at the cell surface for the ligand being tested or inaccessibility of the binding site to the specific ligand), wrong buffer or pH composition (for instance, lack of specific ions required for binding).

19. The number of cells necessary to achieve good statistic strength will depend on the ligand-receptor pair and on the number of unbinding events in your sample *versus* your controls. The higher the number of cells tested, the higher the confidence level you can attain on your results.

20. You should continue with the same tip, in order to prove specificity for the unbinding events obtained in the force measurements.

21. Unequivocal demonstration of binding specificity through competitive binding, which eliminates measurable binding events using a soluble agonist, ion-dependent disruption of receptor binding or blocking/cleaving of the tip bound ligand is absolutely necessary.

22. Move the tip carefully when you change to a new location to avoid crashing the tip. The position of the cantilever in the scanner and the laser spot must not be moved; otherwise, both deflection sensitivity and spring constant need to be reassessed (*see* **Section 3.8**).

23. In block experiments, the unbinding events should be rare or disappear completely (or at least be statistically significantly lower). The incubation time also depends on each biological system. For some systems, buffer conditions can be changed to observe specificity of binding.

24. This method will allow for the determination of the tip deflection in nanometers for a given movement of the detection laser on the photodetector. Since the hard repulsive interaction regime is used for the sensitivity measurement, it should be performed at the end of an experiment, to avoid damaging the tip.

25. To determine whether the unbinding events observed are specific for the proteins under investigation, compare cells that express the receptor with those that do not express it. For our experiments, we use a sensorial neuronal-like cell line that express receptors for the HC protein and a mouse fibroblasts cell line that do not express HC receptors as control (*see* Reference [6]). If you observe the rare occurrence of multiple binding events and adhesion curves, exclude them from further analysis. The use of a flexible PEG cross-linker allow for the distinction between specific binding and non-specific adhesion by observing the polymer stretching in the retrace curve.

References

1. Lamprecht, C., P. Hinterdorfer, and A. Ebner, "Applications of biosensing atomic force microscopy in monitoring drug and nanoparticle delivery." Expert Opin Drug Deliv, 2014. 11(8): p. 1237-53.
2. Riehemann, K., et al., "Nanomedicine--challenge and perspectives." Angew Chem Int Ed Engl, 2009. 48(5): p. 872-97.
3. Hinterdorfer, P. and Y.F. Dufrêne, "Detection and localization of single molecular recognition events using atomic force microscopy." Nature Methods, 2006. 3(5): p. 347-355.
4. Hinterdorfer, P., et al., "Detection and localization of individual antibody-antigen recognition events by atomic force microscopy." Proceedings of the National Academy of Sciences, 1996. 93(8): p. 3477-3481.
5. Oliveira, H., et al., "Molecular Recognition Force Spectroscopy: A New Tool to Tailor Targeted Nanoparticles." Small, 2011. 7(9): p. 1236-1241.
6. Oliveira, H., et al., "Targeted gene delivery into peripheral sensorial neurons mediated by self-assembled vectors composed of poly(ethylene imine) and tetanus toxin fragment c." Journal of Controlled Release, 2010. 143(3): p. 350-358.
7. Ebner, A., P. Hinterdorfer, and H. Gruber, "Comparison of different aminofunctionalization strategies for attachment of single antibodies to AFM cantilevers." Ultramicroscopy, 2007. 107(10-11): p. 922-7.
8. Ebner, A., et al., "A new, simple method for linking of antibodies to atomic force microscopy tips." Bioconjug Chem, 2007. 18(4): p. 1176-84.
9. Wildling, L., et al., "Linking of sensor molecules with amino groups to amino-functionalized AFM tips." Bioconjug Chem, 2011. 22(6): p. 1239-48.
10. Gomes, C.P., et al., "Atomic Force Microscopy as a Tool to Assess the Specificity of Targeted Nanoparticles in Biological Models of High Complexity." Advanced Healthcare Materials, 2017. 6(21): p. 1700597-n/a.
11. Baumgartner, W., P. Hinterdorfer, and H. Schindler, "Data analysis of interaction forces measured with the atomic force microscope." Ultramicroscopy, 2000. 82(1): p. 85-95.
12. Butt, H.-J. and M. Jaschke, "Calculation of thermal noise in atomic force microscopy." Nanotechnology, 1995. 6(1): p. 1.
13. Hutter, J. and J. Bechhoefer, "Calibration of atomic force microscopy cantilevers." Rev. Sci. Instrum, 1993. 66: p. 1868-1873.
14. Sinha, K., et al., "Analysis of mutants of tetanus toxin HC fragment: ganglioside binding, cell binding and retrograde axonal transport properties." Molecular Microbiology, 2000. 37(5): p. 1041-1051.
15. Evans, E. and K. Ritchie, "Dynamic strength of molecular adhesion bonds." Biophys J, 1997. 72(4): p. 1541-55.
16. Evans, E. and K. Ritchie, "Strength of a weak bond connecting flexible polymer chains." Biophys J, 1999. 76(5): p. 2439-47.

APPENDIX II

BDNF GENE DELIVERY MEDIATED BY NEURON-TARGETED NANOPARTICLES IS NEUROPROTECTIVE IN PERIPHERAL NERVE INJURY

BDNF Gene Delivery Mediated by Neuron-Targeted Nanoparticles is Neuroprotective in Peripheral Nerve Injury

Cátia Daniela Ferreira Lopes[1,2,3], Nádia Pereira Gonçalves[1,4,#], Carla Pereira Gomes[1,2,5], Maria João Saraiva[1,4], Ana Paula Pêgo[1,2,5,6*]

1 – i3S – Instituto de Investigação e Inovação em Saúde, Universidade do Porto, Rua Alfredo Allen, 208, 4200-135 Porto, Portugal
2 – INEB – Instituto de Engenharia Biomédica, Universidade do Porto, Rua Alfredo Allen, 208, 4200-135 Porto, Portugal
3 – FMUP – Faculdade de Medicina da Universidade do Porto, Alameda Prof. Hernâni Monteiro, 4200-319 Porto, Portugal
4 – IBMC – Instituto de Biologia Molecular e Celular, Universidade do Porto, Rua Alfredo Allen, 208, 4200-135 Porto, Portugal
5 – FEUP – Faculdade de Engenharia, Universidade do Porto, Porto, R. Dr. Roberto Frias s/n, 4200-465 Porto, Portugal
6 – ICBAS – Instituto de Ciências Biomédicas Abel Salazar, Universidade do Porto, R. Jorge de Viterbo Ferreira 228 Porto, Portugal

#Current address: Danish Research Institute of Translational Neuroscience DANDRITE, Nordic EMBL Partnership, Department of Biomedicine, Aarhus University, Denmark

Published in Biomaterials, Volume 121, 2017

Abstract

Neuron-targeted gene delivery is a promising strategy to treat peripheral neuropathies. Here we propose the use of polymeric nanoparticles based on thiolated trimethyl chitosan (TMCSH) to mediate targeted gene delivery to peripheral neurons upon a peripheral and minimally invasive intramuscular administration. Nanoparticles were grafted with the non-toxic carboxylic fragment of the tetanus neurotoxin (HC) to allow neuron targeting and were explored to deliver a plasmid DNA encoding for the brain-derived neurotrophic factor (BDNF) in a peripheral nerve injury model. The TMCSH-HC/BDNF nanoparticle treatment promoted the release and significant expression of BDNF in neural tissues, which resulted in an enhanced functional recovery after injury as compared to control treatments (vehicle and non-targeted nanoparticles), associated with an improvement in key pro-regenerative events, namely, the increased expression of neurofilament and growth-associated protein GAP-43 in the injured nerves. Moreover, the targeted nanoparticle treatment was correlated with a significantly higher density of myelinated axons in the distal stump of injured nerves, as well as with preservation of unmyelinated axon density as compared with controls and a protective role in injury-denervated muscles, preventing them from denervation. These results highlight the potential of TMCSH-HC nanoparticles as non-viral gene carriers to deliver therapeutic genes into the peripheral neurons and thus, pave the way for their use as an effective therapeutic intervention for peripheral neuropathies.

1. Introduction

Treatment of peripheral neuropathies has always been a clinical challenge. Peripheral neuropathies may take weeks to months to develop after the exposure of the neural tissue to the insulting agents and often these cause irreversible damage to the affected nerves. Presently, there is a single clinical therapeutic strategy available, consisting into the identification of the peripheral neuropathy etiology and, if possible, treatment of the underlying cause and/ or management of the associated symptoms [1]. There is no treatment addressing the damaged nerves, which makes vital the development of effective regenerative strategies.

Neurotrophic factors have been extensively studied as a restorative treatment option for peripheral neuropathies due to their role in neuronal survival, growth and synaptic plasticity [2]. The promising results of several neurotrophic factors in pre-clinical tests are consensual and have prompted their evaluation in clinical trials (in which the recombinant proteins have been directly administered to patients) but the outcomes have failed to demonstrate a significant beneficial effect of these agents [3, 4]. One justification for this failure can be attributed to the employed administration strategy that was either systemic or subcutaneous. The blood-nerve barrier (BNB), the interface that isolates the endoneurium from the intravascular component, is relatively impermeable to molecules of larger sizes (such as neurotrophic factors) and, thus, prevents the exit of such factors from circulation to reach the targeted cells [5, 6]. Moreover, due to their short systemic half-life and pleiotropic actions, the direct administration of neurotrophic factors can cause systemic, as well as peripheral adverse effects that overrule the desired protective action [7]. Thus, novel delivery tools and application forms are being explored to attain the efficient local delivery of neurotrophic factors while limiting their action to the target area to prevent unwanted adverse side-effects [8].

Gene therapy has been considered as one of the promising strategies to treat both inherited and acquired diseases. The principle of gene therapy relies on the use of nucleic acids as a pro-drug that can lead to the modulation of the expression of therapeutic proteins within cells. In this sense, it has been proposed as a strategy to promote the local expression of neurotrophic factors and restore the functional properties of the damaged nerves in numerous neuropathic conditions [9].

Recently, extensive research is being conducted towards the design of safe and effective non-viral vectors that could achieve comparable levels of gene expression and specificity attained by viral vectors, while providing greater flexibility in terms of cargo size, immunological

compatibility and reduced safety concerns [9]. Among these, chitosan-based carriers have gained special attention due to chitosan ability to condense nucleic acids and protect them from endonuclease degradation, its biocompatibility and biodegradability [10]. In particular, the use of quaternized chitosan derivatives overcomes one of the major caveats of this polycation, the low pKa that leads to its low solubility at physiologic pH. The presence of a permanent positively charged group in the chitosan backbone enables the electrostatic interactions between the polymer and the negatively charged nucleic acids to occur even under physiological conditions, improving the stability of the resulting polyplexes, an important feature for their applicability *in vivo* [11]. Here we propose the use of a polymeric nanoparticle based on trimethyl chitosan (TMC) to vectorize therapeutic genes to peripheral neurons *in vivo* and in a targeted fashion, after a peripheral and minimally invasive intramuscular administration. The explored nanoparticle-targeting moiety was the non-toxic carboxylic terminal fragment from the tetanus neurotoxin (HC), which we have previously shown to mediate nanoparticle retrograde transport after a peripheral administration in the proximity of neuron terminals [12, 13]. The performance of this neuron-targeted TMC-based nanoformulation to deliver therapeutic genes to peripheral neurons and rescue them from degeneration was assessed *in vivo*, in a peripheral nerve crush injury animal model, using as therapeutic transgene a plasmid DNA encoding for the brain-derived neurotrophic factor (BDNF). The rationale for using BDNF is based on its reported protective role in neuronal survival after injury. BDNF has been advocated as a potential candidate to promote nerve protection and/or regeneration for the following well-established reasons. After peripheral nerve injury BDNF mRNA is up-regulated in dorsal root ganglia (DRG), Schwann cells and target muscles fibers [14-16]. At protein level, BDNF expression is also increased in the DRG and in the spinal dorsal horn after an injury [15, 17, 18]. It has also been found that the high affinity tyrosine kinase receptor B (trkB), one of the major BDNF cell receptors, is overexpressed in regenerating sensory and motor neurons [19, 20]. Moreover, the deprivation of endogenous BDNF results in an impairment of regeneration and remyelination of peripheral nerves [14]. These observations have pointed to the key role of BDNF in nerve regeneration mediated by the trkB receptors present in motor and a subset of sensory neurons, making this neurotrophic factor of critical relevance to be applied in the treatment of motor and sensory dysfunctions present in peripheral neuropathies [14]. Previous studies showed that BDNF gene therapy mediated by viral vectors corroborate the crucial role of BDNF in conditions such as blindness [21-23], deafness [24, 25], sciatic nerve [26] and adult motor neuron injuries [27]. Despite the promising results obtained so far, the *in vivo* application of viral vectors has

demonstrated problems of toxicity, immunogenicity and inflammatory potential. In this study, using a peripheral nerve crush injury model, in which nerve degeneration and regeneration occurs in a well-established cascade of events, we were able to establish the effect of the proposed TMCSH-HC/BDNF nanoparticles in protecting peripheral nerves from degeneration and enhancing the speed of nerve regeneration.

2. Materials and Methods

2.1. TMC purification and modification

TMC derived from ultrapure chitosan produced from Agaricus bisporus mushrooms, under cGMP standards, (40 kDa, KitoZyme, Belgium) was purified by filtration and dialysis prior to use, as previously described [28]. In brief, TMC was diluted in 5 mM HCl solution at a final concentration of 0.5% (w/v), filtered through a Buchner funnel and purified by dialysis using a 3.5 kDa molecular weight cut-off membrane (Spectrum Labs, CA, USA) for 3 days against deionized water and collected after freeze-drying. The degree of acetylation (DA) and quaternization (DQ) of the purified TMC were determined by ^{1}H-nuclear magnetic resonance spectroscopy (^{1}H-NMR; see **Figure S1** in Supplementary Information for a characteristic TMC ^{1}H-NMR spectrum) and found to be 15.7 ± 0.9% and 30.1 ± 4.6%, respectively. Endotoxin levels of the purified polymer extracts were assessed using the Limulus Amebocyte Lysate Assay (QCL-1000, Cambrex, NJ, USA), following the manufacturer instructions. Endotoxin levels were found to be < 0.1 EU/ml (an EU corresponding to a unit of measurement for endotoxin activity), respecting the US Department of Health and Human Services guidelines for implantable devices [29]. After freeze-dried, TMC was dissolved in 20 mM HEPES (Sigma-Aldrich Co, MO, USA) buffered saline solution containing 5% (w/v) glucose (pH 7.4) at a 0.25% (w/v) final concentration. Purified TMC was then thiolated (for reaction scheme - see **Figure S2** in Supplementary Information) by the tethering of thiol groups from 2-iminothiolane on the primary amino groups of the polymer, as described elsewhere [12]. Briefly, TMC was dissolved in 20 mM HEPES buffer at 5 mg/ml and 2- iminothiolane HCl (Sigma-Aldrich Co) was added to the polymer solution, in order to attain a theoretical modification of 10% of the polymer primary amine groups. Afterwards, the pH of the solution was adjusted to 8 with NaOH. After 6 h of incubation at room temperature (RT), under an inert atmosphere saturated with argon and with continuous stirring, the resulting thiolated TMC (TMCSH) was dialyzed for 3 days against 5 mM HCl at 4°C. Thereafter samples were frozen at -80°C and lyophilized for 3 days. The resulting powders were stored at -20°C until further use.

The degree of polymer thiolation was quantified with 5,5-dithio-bis-(2-nitrobenzoic acid) (DTNB, Ellman's reagent). The amount of free thiol groups grafted to the polymer was determined based on a previously described protocol with some modifications [30] and found to be 149.1 ± 15.8 µmol/g, corresponding to 4.7 ± 0.5 % substitution of TMC primary amines by thiol groups. Briefly, DTNB was dissolved in 0.1 M sodium phosphate buffer, pH 8 at a final concentration of 100 µg/ml. The polymer samples were dissolved in the same solution at a

final concentration of 2.5 mg/ml. Then, 20 µL of the polymer solution was mixed with 180 µL of DTNB reagent solution in a microplate and after incubation of 15 min at RT the absorbance was measured at a wavelength of 405 nm (Spectra Max GeminiXS, Molecular Devices, CA, USA). Cysteine standard solutions were used to calculate the amount of free thiol moieties in the polymer.

2.2. BDNF encoding plasmid DNA (pDNA) production and purification

The pDNA used encoded for the BDNF protein under the cytomegalovirus promoter (pCMV-BDNF, 7.7 kb, a kind offer from Prof. Joost Verhaagen, Netherlands Institute for Neuroscience) was produced in DH5α competent *E. coli* strain and purified using an EndoFree plasmid Giga kit (Qiagen, Germany) following the manufacturer's instructions. Plasmid concentration and purity were assessed by UV spectroscopy (Nanodrop ND-1000, Thermo Fisher Scientific Inc., MA, USA) and the absorbance ratio achieved (260 nm/280 nm) was between 1.8 and 2.0.

2.3. HC fragment production, purification and modification

The plasmid encoding for HC fragment was a kind offer from Prof. Neil Fairweather (King´s College, UK) and was produced and purified as previously described [31]. The purified fragment was modified with a bifunctional 5 kDa poly(ethylene glycol) (PEG) spacer (Jenkem Technology, China) bearing an N-hydroxysuccinimide (NHS) and a maleimide (MAL) end group, at a 2.5 PEG/ HC protein molar ratio. The amount of reactive MAL groups in the HC fragment was determined using the Ellman´s assay [30] and found to be 1.5 mol PEG/HC.

2.4. Preparation and characterization of TMC-based nanoparticles

TMCSH-based nanoparticles were prepared using a molar ratio of quaternized amine groups (N) to DNA phosphate groups (P) (N/P) of 2. As illustrated in **Scheme 1**, the nanoparticle core was formed by mixing, while vortexing, equal volumes of pDNA solution with TMCSH solution in 20 mM HEPES buffered saline solution containing 5% (w/v) glucose, pH 7.4. Complexes were let to stabilize for 15 min at RT and immediately frozen. After freeze-dried, nanoparticles were suspended in sterile distilled water (naked TMCSH nanoparticles) or in sterile distilled water containing the HC-PEG fragment in a w/w ratio of HC-PEG per pDNA of 4 (TMCSH-HC nanoparticles) and let to react for 24 h under agitation (RT). Both nanoparticles were characterized in terms of size, polydispersity index (Pdi) and zeta potential using a Zetasizer Nano Zs (Malvern, UK). The Smoluchowski model was applied for zeta potential determination and cumulant analysis was used for Z-average particle size determination. Ten µg of pDNA

was used to prepare the tested formulations. All measurements were performed in triplicate at 25°C.

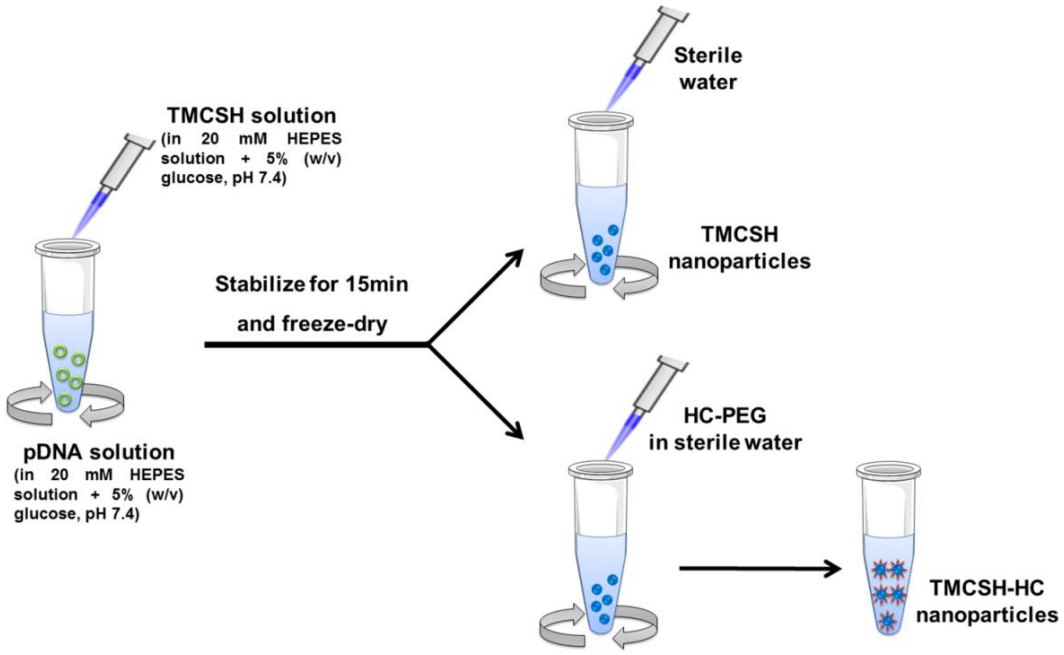

Scheme 1. Schematic illustration of TMCSH-based nanoparticle preparation for *in vivo* administration.

2.5. In vitro transfection of dissociated DRG primary cultures

All animal experiments described in this report were carried out with the permission of the local animal ethical committee in accordance with the EU Directive (2010/63/EU) and Portuguese law (DL 113/2013). The experimental protocol (reference 421/000/000/2013) was approved by the ethics committee of the Portuguese official authority on animal welfare and experimentation (Direção-Geral de Alimentação e Veterinária). Primary embryonic rat DRG neurons were isolated from Wistar embryo rats (E18) as described elsewhere [12]. From the final cell suspension, $5x10^4$ cells/cm^2 of viable cells were seeded in a 24-well plate on glass coverslips (12 mm, MGF-Slides) pre-treated with 0.01 mg/ml of poly(*D*-lysine) (PDL, molecular weight 30 – 70 kDa, Sigma-Aldrich Co) and, subsequently, with 5 µg/ml laminin-1 isolated from mouse Engelbreth-Holm-Swarm sarcoma (Sigma-Aldrich Co), in DMEM/Ham´s F12 with GlutaMAX™, 50 µg/ml of penicillin and streptomycin, 25 ug/ml fungizone, 2% (v/v) B27 supplement (all from Gibco®, Thermo Fisher Scientific Inc.) and 50 ng/ml of nerve growth factor (NGF) 7S (Calbiochem®, Millipore, France). This protocol allowed a neuron purity >70% at 48 hours post-seeding [12]. At 3 days post-seeding dissociated DRG primary cultures were incubated for 6 hours with naked BDNF encoding plasmid DNA (pBDNF), TMCSH/pBDNF nanoparticles or TMCSH-HC/pBDNF nanoparticles. Untreated cultured cells were used as

control. Seventy-two hours after transfection the relative expression of BDNF mRNA in DRG dissociated primary cultures was determined by reverse transcription and quantitative real-time PCR (RT-qPCR) (see section 2.12 for experimental details).

2.6. Nanoparticle administration and sciatic nerve crush injury

A total of 48 young adult female BALB/c mice (10 weeks old) were used in this study. Animals were randomly divided into four groups as follows: (A) Vehicle group (received 20 mM HEPES buffer containing 5% (w/v) glucose, pH 7.4, n=15), (B) TMCSH group (received TMCSH nanoparticles in 20 mM HEPES buffer containing 5% (w/v) glucose, pH 7.4, n=15), (C) TMCSH-HC group (received HC-functionalized TMCSH nanoparticles in 20 mM HEPES buffer containing 5% (w/v) glucose, pH 7.4, n=15) and (D) Wild-type group (uninjured animals used for mRNA quantification, n=3).

Eight days before nerve crush, animals were injected with either 50 µl of the vehicle solution or nanoparticle suspension (containing 50 µg of BDNF pDNA) in the left medial gastrocnemius muscle under volatile anesthesia with isoflurane (5% (v/v) isoflurane + 0.8 l/min oxygen for induction; 2% - 2.5% (v/v) isoflurane + 0.2 l/min oxygen for maintenance). After injection, the needle was left in place for 1 min to avoid leakage.

Eight days later, animals were subjected to a unilateral crush injury in the left sciatic nerve, as we previously reported [32]. Animals were anesthetized with isoflurane, as described above, and shaved in the left hind limb. After skin incision, the left sciatic nerve was exposed and crushed twice within a 15 s period, using a Micro-Mosquito hemostat (Fine Science Tools GmbH, Germany). To standardize the procedure and yield reproducible sensorimotor deficits, the crush site was maintained constant for each animal. The skin incision was then closed with absorbable 6/0 poly(glycolic acid) suture (Surgicryl PGA, SMI, Belgium). After surgery and twice a day (for 48 h) animals received 0.05 mg/kg buprenorphine as analgesic. Animals were maintained in study during the following 21 days.

2.7. Sensorimotor recovery analysis

The sensorimotor recovery of animals from each treatment group was evaluated once a week throughout the study, namely before nanoparticle treatment (pre-treatment) and at 1, 7, 14 and 21 days after sciatic nerve injury.

The locomotor function recovery was evaluated by the walking tract analysis. In brief, mice footprints were recorded by dipping the mice paws in ink and having the animals walking unassisted along a 60 x 11 x 6 cm corridor lined on the bottom with a sheet of white paper. The obtained tracts were then used to calculate the sciatic functional index (SFI) using the empirical equation adapted for mice by Inserra *et al* [33]: SFI = 118.9 x ((ETS-CTS)/CTS) – 51.2 x ((EPL-CPL)/CPL)-7.5, where ETS stands for operated experimental toe spread (distance between the first and fifth toes), CTS for control toe spread, EPL for operated experimental print length and CPL for control print length. The SFI scores vary among -100 (representing a non-functional nerve) and 0 (representing normal nerve function or completely nerve recovery). The pre-treatment SFI values were used as control for comparison.

The sensory nociceptive function recovery of sciatic nerve was evaluated by the hot plate test through which the response to a noxious thermal stimulus is measured. This test is based on the measurement of the latency time before a withdrawal reflex when the mice feet are placed on a standard temperature-controlled plate. Mice were placed within a transparent Plexiglas box (12 x 22.5 cm) on a standard temperature-controlled metal plate (hot plate analgesia meter, IITC Life Science, CA, USA) at 52°C, and a 30 s cut-off time was used for nonresponsive mice. The latency time to respond with a hind paw lick or shake/jump was measured and used as an index of nociception. To prevent sensitization, animals were subject to test only once per time point. The pretreatment latency time was used as control for comparison.

The mechanical allodynia was measured using a series of calibrated Von Frey filaments (Ugo Basile, Italy), through the up–down method as described elsewhere [34] with minor modifications. Animals were placed in an opaque cage over a wire mesh floor and let to adapt to the testing environment for at least 20 min. A set of ten calibrated von Frey filaments (ranging from 0.008 to 2 g of target force) were applied to the mid-plantar surface of the hind paw until they bent. This procedure was repeated 5 times with each filament and the threshold force (filament) that resulted in paw withdrawal was recorded. The contralateral paws were used to assess the uninjured paw withdrawal threshold.

2.8. Motor nerve conduction velocity (MNCV)

MNCV was determined at 21 days after sciatic nerve injury as previously described by Ferdinandusse *et al.* [35] with a Powerlab 4/25 (ADInstruments, UK) using the Chart5 software. The left sciatic nerve was stimulated by placing the stimulator electrode (monopolar needle,

29G, surgical steel) first at the sciatic notch (proximal stimulation) and then at the ankle (distal stimulation). The recording electrode was placed in the footpad. MNCV was calculated as the ratio of the distance between both sites of stimulation divided by the difference between proximal and distal latencies. The MNCV is expressed in meters per second (m/s). The MNCV of the contralateral uninjured sciatic nerves were used as control.

2.9. Tissue processing and histological analysis

Twenty nine days after nanoparticle administration, animals were anesthetized by intraperitoneal administration of sodium pentobarbital (50 mg/kg) and intracardially perfused with phosphate buffered saline (PBS; 1 mM KH_2PO_4; 5.6 mM Na_2HPO_4; 154 mM NaCl) followed by freshly prepared 4% (w/v) paraformaldehyde in 0.1 M phosphate buffer, pH 7.4. The ipsi- and contralateral sciatic nerves, lumbar DRG and the L3-L5 lumbar segments of spinal cord were collected and post-fixed in the same fixative overnight at 4°C. Gastrocnemius muscles were collected after PBS perfusion, weighted and fixed in 4% (w/v) paraformaldehyde in 0.1 M phosphate buffer, pH 7.4. Muscles used for muscle fiber morphological analysis were embedded in paraffin and the ones used for BDNF immunohistochemistry and neuromuscular junctions (NMJs) reinnervation analysis, as well as the remaining tissues, were cryopreserved in a 30% (w/v) sucrose solution and sectioned in a cryostat (HM550, Microm).

Immunofluorescence (IF) analysis. Frozen sections of gastrocnemius muscles (50 µm thick), sciatic nerves (10 µm-thick), DRGs (10 µm-thick) and spinal cord (16 µm-thick) were immunostained for the detection of BDNF protein expression. Sciatic nerves were also immunostained for the detection of neurofilament-H (NF-H), growth-associated protein GAP-43 (both neuronal cell markers) and S100 protein (Schwann cell marker) expression. Briefly, tissue sections were blocked and permeabilized for 1 h at RT with 5% (v/v) normal goat serum in PBS containing 0.3% (v/v) Triton X-100. Afterwards, tissue sections were incubated with primary antibody solution overnight at 4°C. After washing in PBS, tissue sections were incubated with fluorescently-labeled secondary antibody solution for 1 h at RT. Nuclei were stained with 0.1 µg/ml 4',6-diamidino-2- phenylindole (DAPI, Sigma-Aldrich Co). The primary antibodies used were: polyclonal rabbit anti-BDNF antibody (Santa Cruz, CA, USA; 1:50), monoclonal mouse anti-NF-H antibody (Santa Cruz Biotechnology; 1:100), polyclonal rabbit anti-GAP-43 Alexa Fluor® 488 conjugate (Novus Biologicals, Abingdon, UK; 1:100) and polyclonal rabbit anti-S100 antibody (Dako, Denmark; 1:200). As secondary antibodies were used a goat anti-mouse Alexa Fluor® 568 conjugate and goat anti-rabbit Alexa Fluor® 488

conjugate diluted in blocking buffer (all from Molecular Probes®, Thermo Fisher Scientific Inc; 1:1000).

The semi-quantitative expression of BDNF, NF-H, GAP-43 and S100 protein in the sciatic nerves was assessed in the proximal, injury and distal segments of 3 sciatic nerve sections/animal, using the ImageJ 1.49t software (NIH, USA, http://imagej.nih.gov/ij/). The contralateral sciatic nerves were used as uninjured control. Results shown represent the area occupied by pixels corresponding to the fluorescent signal, normalized in relation to the total area.

The semi-quantitative expression of BDNF in lumbar DRGs (L4 and L5) and in the L3- L5 lumbar segments of spinal cord was assessed in 3 tissue sections/animal using a custom made program written in MATLAB (The MathWorks, version 2015a, Natick MA, USA). The contralateral L4 and L5 DRGs and the contralateral (right) spinal cord hemisection were used as uninjured controls, respectively. Results were expressed as mean pixel intensity levels (fluorescence).

The analysis of NMJ reinnervation was performed in 50 µm-thick frozen sections of gastrocnemius muscle through a double staining for the postsynaptic marker α-bungarotoxin and the neurofilament 200 (NF200) marker. In brief, tissue sections were blocked and permeabilized for 1 h at RT with 5% (v/v) normal goat serum in PBS containing 0.3% (v/v) Triton X-100 and incubated with the primary polyclonal rabbit anti-NF200 antibody (Abcam, Cambridge, UK; 1:500) overnight at 4°C. After washing in PBS, tissue sections were incubated with a secondary antibody goat anti-rabbit Alexa Fluor® 488 conjugate and α-bungarotoxin – tetramethylrhodamine conjugate diluted in blocking buffer for 90 min at RT (both from Molecular Probes®, Thermo Fisher Scientific Inc.; 1:1000 and 1:200, respectively). The fraction of denervated, partial and complete reinnervated NMJ was counted in Z-stack confocal microscopy images using the maximum intensity projection. The innervation status of individual NMJ was classified according to the extent to which the neurofilament labeling overlaid with α-bungarotoxin staining and was presented as relative to 100% (referent to a tissue where all NMJ are completely innervated (uninjured)). Denervated NMJs were devoid of any NF200 labeling. Partial innervated NMJs were identified as only part of the α-bungarotoxin positive endplates being covered by NF200 marker labeling. Complete innervated NMJs were defined by the complete overlap of NF200 and α-bungarotoxin labeling. For each muscle sample at least 50 NMJ were evaluated from randomly selected visual fields.

For morphological analysis and quantification of cross sectional muscle fibers area, transversal paraffin sections of ipsi- and contralateral gastrocnemius muscles (3 µm-thick) were stained with hematoxylin and eosin (H&E). A total of 40 muscle fibers per animal was randomly selected and used to quantify the cross sectional area (20 fibers from lateral and 20 fibers from medial gastrocnemius muscle). The quantification was performed using the ImageJ 1.49t software (NIH, USA, http://imagej.nih.gov/ij/). The contralateral gastrocnemius muscles were used as uninjured control.

2.10. Gastrocnemius muscle wet weight

The ratio between the wet weight of the gastrocnemius muscle from the experimental side and the contralateral side (uninjured) was used to indirectly assess the target muscle innervation recovery. Twenty-one days post-injury, after PBS perfusion, the ipsi- and contralateral gastrocnemius muscles were dissected and weighed.

2.11. Myelinated vs. unmyelinated axon quantification by transmission electron microscopy (TEM)

After perfusion, distal sciatic nerve segments of 5 animals/ group were harvested and post-fixed in 2.5% (w/v) glutaraldehyde and 2% (w/v) paraformaldehyde diluted in 0.1 M sodium cacodylate for 4 h. The nerve segments were subsequently post-fixed in 1% (v/v) osmium tetroxide for 2 h and dehydrated in series of graded ethanol. Tissues were embedded in Spurr resin (EMS- Electron Microscopy Sciences, Hatfield, PA, USA) in a 60°C oven for 48 h. Semi-thin sections (1-2 µm) were stained with 0.01% (w/v) toluidine blue, 0.05% (w/v) methylene blue and 0.05% (w/v) borax in aqueous solution. Afterwards, the density of myelinated axons was counted in the whole nerve area. Regarding unmyelinated axons, ultra-thin transverse sciatic nerve sections (60–90 nm) were cut and stained with 2% (w/v) uranyl acetate in aqueous solution. The stained samples were mounted on mesh grids and observed under a transmission electron microscope (JEM-1400EX; JEOL Ltd., Tokyo, Japan). For each animal, the density of unmyelinated axons was counted in 50 random and non-overlapping photographs (magnification 12000X).

2.12. One-step RT-qPCR

At 72h after transfection, the dissociated DRG primary cultures were gently trypsinized, collected, washed with cold PBS and placed on ice to be freshly processed (not frozen). Total

RNA was extracted and purified from cultured cells using the mirVana™ miRNA Isolation Kit (LifeTechnologies, CA, USA) with DNase digestion.

For the *in vivo* studies, 3 animals/ group were sacrificed by a lethal intraperitoneal injection of 20% (v/v) sodium pentobarbital and tissues were collected and snap frozen. Total RNA was extracted and purified from frozen tissues using the Quick-RNA™ Miniprep kit (Zymo Research Corp., CA, USA) with DNase I treatment.

For detection of BDNF mRNA levels, 10 ng of purified RNA was used per sample and amplified in duplicate in an iCycler iQ5 (Bio-Rad, CA, USA) using the SYBR Green One-step qPCR Kit (Biotool.com, Germany), according to the manufacturer´s instructions. The glyceraldehyde-3´ phosphate dehydrogenase (GAPDH) mRNA levels were used as an internal control to normalize the variability in expression levels. The sequences of the primers used for BDNF gene were 5´-TGGCTGACACTTTTGAGCAC-3´ and 5´-GTTTGCGGCATCCAGGTAAT-3´ and for GAPDH gene were 5´-GCCTTCCGTGTTCCTACC-3´ and 5´-AGAGTGGGAGTTGCTGTTG-3´. At the end of the PCR cycling, correspondent melting curves were performed in order to ascertain the amplification of a single product and the absence of primer dimmer formation. The normalized BDNF expression levels in treatment groups were calculated relative to untreated cultured cells (*in vitro* transfection studies) or to the uninjured wild-type group (*in vivo* studies) using the $2^{-\Delta\Delta CT}$ relative quantification method described by Livak and Schmittgen [36].

2.13. Statistical analysis

Statistical analysis was performed using GraphPad Prism version 6.0 for Windows (San Diego California, USA). Results are presented as mean ± standard deviation (SD). Significant differences between treatment groups were determined by using the ordinary one-way ANOVA test followed by the Newman-Keuls post-test for multiple comparisons. The one sample t-test was used to compare the mean BDNF mRNA expression levels (RT-qPCR analysis) between treatments groups and wild-type animals. Results with $p < 0.05$ were considered statistically significant.

3. Results

3.1. Characterization of TMCSH-based nanoparticles

The prepared TMCSH-based nanoparticles were characterized in terms of size, Pdi and zeta potential in 20 mM HEPES buffer containing 5% (w/v) glucose, pH 7.4 As shown in **Table 1**, the mean size diameter and Pdi values obtained for TMCSH-HC nanoparticles were not significantly different from the TMCSH ones, showing that HC-functionalization does not influence the average size and polydispersity of the nanoparticles.

Although significantly lower for the TMCSH-HC, zeta potential values obtained for both nanoparticles were positive, indicating a cationic surface charge of both nanoparticles with a good colloidal stability.

Table 1. Physicochemical characterization of TMCSH-based nanoparticles at an N/P ratio (moles of quaternized amine groups (N) to moles of DNA phosphate groups (P)) of 2.

Formulations	Size (nm)	Pdi	Zeta Potential (mV)
TMCSH	270.8 ± 5.7	0.16 ± 0.02	19.1 ± 0.5
TMCSH-HC	262.8 ± 1.6	0.17 ± 0.01	17.2 ± 0.9

Nanoparticles were characterized in terms of size, polydispersity index (Pdi) and zeta potential in 20 mM HEPES buffered saline solution containing 5% (w/v) glucose, pH 7.4. All values are representative of 3 independent experiments and are expressed as mean ± SD. * $p<0.05$.

3.2. Sensorimotor functional recovery

All animals under study were frequently checked for weight variation and autotomy. After sciatic nerve injury, rodents frequently scratch and bite theirs anesthetized foot which ultimately can result in autotomy of one or more toes, usually observed in the beginning of the third post-injury week [37]. No weight variation and autotomy were observed in all groups in study, but 3 out of 15 total animals of vehicle group showed nibbling of one or two toenails. Additionally, 2 and 1 out of 15 total animals of TMCSH and TMCSH-HC treatment groups, respectively, showed some swelling of one or two toes, with no apparent lesion. Even so, these animals did not reveal a painful behavior and their locomotor activity was not altered.

The locomotor functional recovery of animals in each treatment group was monitored once a week by determining the sciatic functional index (SFI). Based on SFI values, one can infer crucial aspects of locomotor activity involving the recovery of hind limb sensory and motor

function after an injury. **Figure 1A** displays the changes in the SFI values as a function of time for the three treatment groups. The preoperative SFI scores are indicative of normal nerve function. Postoperative SFI scores sharply decreased, oscillating between -90 to -80 during the first week, due to injury-induced loss of function, and start to gradually increase during the following weeks, reflecting a functional recovery in all groups under investigation. At the end of the study all groups showed a marked recovery, reaching SFI values around -20. No significant differences were observed between groups.

The thermal nociceptive sensory function in response to a noxious thermal stimulus was measured by the hot plate assay. Seven days after nerve injury, all treatment groups showed a delay in response to the thermal stimulus that was progressively recovered in the subsequent time points of the study (**Figure 1B**). At 21 days after crush injury, the latency time to respond to the thermal stimulus was significantly lower in the TMCSH and TMCSH-HC groups when compared to the control vehicle group, reaching similar values to the pre-treatment time-point. In contrast, the latency time response of animals in the control vehicle was significantly different between 21 days after injury and the pre-treatment time-point. Moreover, animals belonging to the TMCSH-HC group showed a significantly quicker response than the ones in the TMCSH group.

The mechanical nociceptive sensory function was assessed with the Von Frey filaments stimulation (**Figure 1C**). Mechanical allodynia was observed in the period span of the study in all treatment groups, starting as soon as 7 days after nerve injury for the TMCSH treated animals. At this time point, animals from the vehicle and TMCSH-HC treatment groups showed no indication of mechanical allodynia. In the TMCSH-HC group, mechanical threshold values were unchanged in comparison to the contralateral values while in the vehicle group an increase in the mechanical threshold values were observed although not significantly different from the contralateral values.

The electrophysiological assessments of the motor nerve conduction velocity (MNCV) performed at 21 days after nerve injury provided further evidence for the functional recovery of the crushed sciatic nerves. Although the MNCV values in each treatment group were significantly lower than those recorded in the contralateral uninjured nerves (**Figure 1D**), animals treated with TMCSH-HC nanoparticles showed a significant elevation in their MNCV values when compared to the control vehicle group.

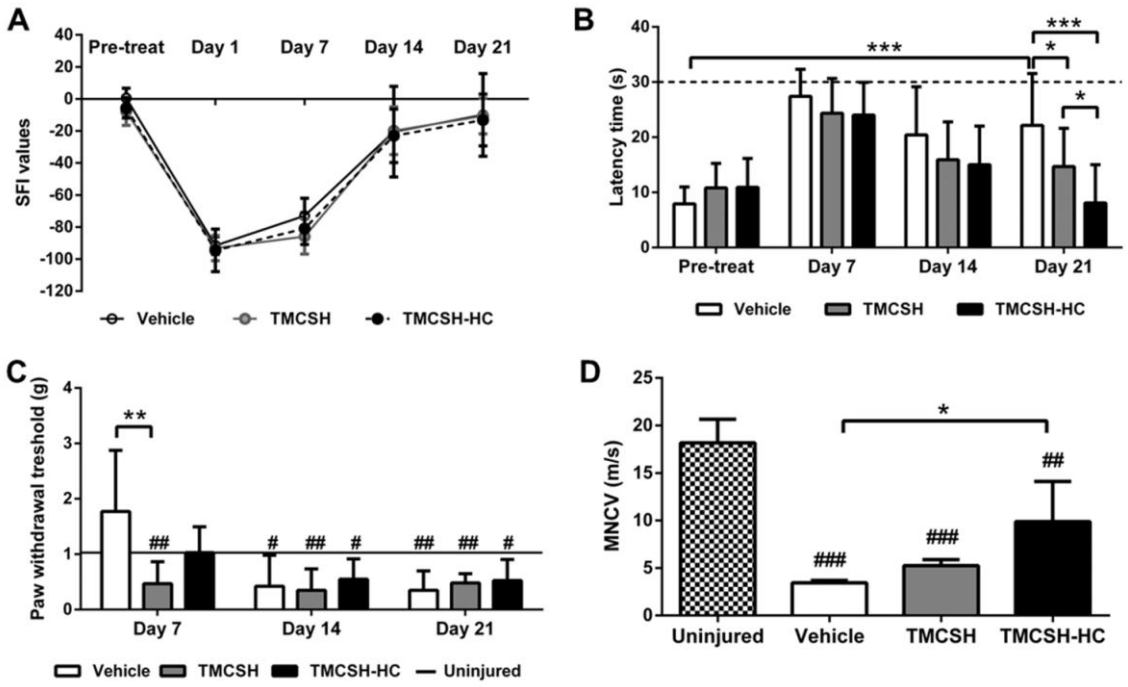

Figure 1. Sensorimotor functional recovery analyses after sciatic nerve crush injury. (A) Locomotor function recovery assessed by sciatic functional index (SFI) at pretreatment (Pre-treat), 1, 7, 14 and 21 days after nerve crush injury; n=12 per group. (B) Thermal nociceptive function recovery measured through the hot plate at pre-treatment (Pre-treat), 7, 14 and 21 days after nerve crush injury; n=12 per group. The dashed line represents the 30 s cut-off time. (C) Mechanical nociceptive function recovery evaluated using the Von Frey filaments at 7, 14 and 21 days after nerve crush injury. Line represents the paw withdrawal threshold in the uninjured paws; n=7 per group. (D) Motor nerve conduction velocities (MNCV) analysis at 21 days after nerve crush injury; n=3 per group. Values represent mean ± SD. $^{###}$ p<0.001 $^{##}$ p<0.01, $^{#}$ p<0.05 vs uninjured (contralateral). *** p<0.001, ** p<0.01, * p<0.05 in multiple comparisons between treatment groups or time-points of analysis.

3.3. BDNF biodistribution

At the end of the study, the expression levels of BDNF mRNA were determined in the left gastrocnemius muscle, injured sciatic nerve, ipsilateral lumbar DRGs and lumbar spinal cord and expressed as relative to levels in the respective tissue in wild-type animals (uninjured and untreated) (**Figure 2**). In the gastrocnemius muscle, one observed a significant decrease of BDNF mRNA levels in the vehicle group as compared to wild-type animals while in the TMCSH group those were maintained unchanged (**Figure 2A**). Additionally, the TMCSH-HC group showed a significantly higher expression of BDNF mRNA than those presented in vehicle and TMCSH treatment groups, although not significantly different from the one of wild-type animals (**Figure 2A**). In the ipsilateral lumbar DRGs, the BDNF mRNA expression levels were similar between the TMCSH group and wild-type animals (**Figure 2B**). In contrast, the BDNF mRNA expression was significantly decreased in the vehicle group and increased in the TMCSH-HC treatment group as compared to wild-type animals (**Figure 2B**). Moreover, the mRNA expression levels in the TMCSH-HC group were significantly higher than the BDNF mRNA levels expressed in the animals treated with the vehicle solution (**Figure 2B**). These results are in line with our in vitro dissociated DRG primary culture transfection data that show a significant increase in the BDNF mRNA expression levels in DRG cultures treated with the TMCSH-HC nanoparticles as compared to the TMCSH nanoparticles or naked plasmid (see **Figure S3** in Supplementary Information). In the ipsilateral sciatic nerves and lumbar spinal cords the BDNF mRNA levels were similar between all treatment groups and wild-type animals, with no significant differences being observed between treatment groups (**Figures 2C and D**, respectively).

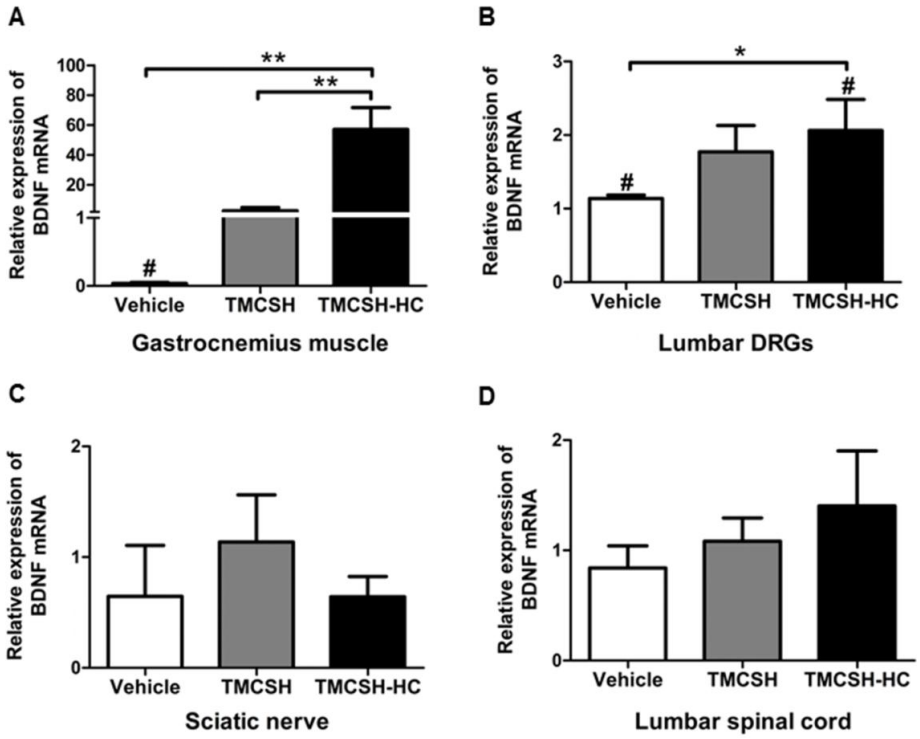

Figure 2. Relative expression of BDNF mRNA in selected tissues at 21 days after nerve crush injury. BDNF mRNA expression was normalized to GAPDH expression levels and expressed as relative to wild-type animals (uninjured and untreated) in (A) gastrocnemius muscle, (B) lumbar DRGs, (C) sciatic nerve and (D) lumbar spinal cord segments. Values represent mean ± SD; n=3 per group. $^{\#}$ $p<0.05$ vs wild-type animals.
** $p<0.01$, * $p<0.05$ in multiple comparisons between treatment groups.

The BDNF protein expression levels were also evaluated in the same tissues at 21 days after injury (**Figure 3**). In the gastrocnemius muscle, the BDNF protein was not immuno detected in any of the treatment groups (data not shown). Contrarily, BDNF was detected in sciatic nerves of animals from all treatment groups (**Figures 3A-D**). However, solely animals treated with TMCSH-HC nanoparticles revealed a significant increase in the BDNF protein expression when compared to the basal contralateral (uninjured nerve) BDNF expression levels (**Figure 3E**). Similarly, animals treated with TMCSH-HC were the ones displaying higher levels of BDNF protein in the lumbar DRGs and spinal cord (**Figure 3F-J and K-N**, respectively), being these significantly different from the basal contralateral (uninjured) BDNF expression levels in the case of the DRGs.

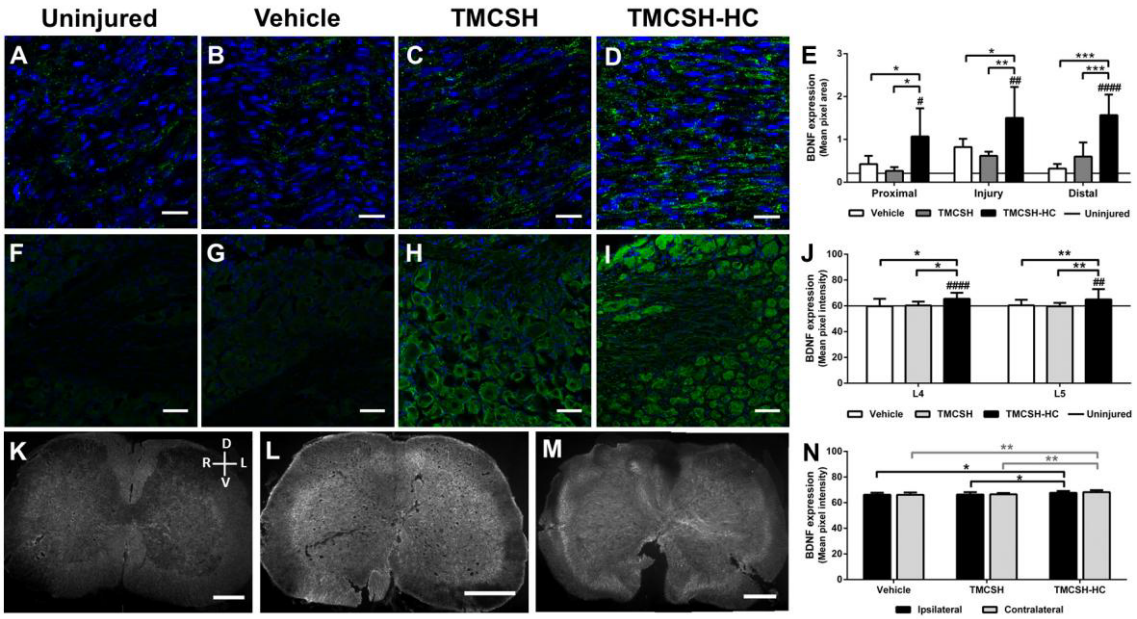

Figure 3. BDNF protein expression profile. BDNF protein was detected by immunohistochemistry in the sciatic nerve, lumbar DRGs and lumbar spinal cord, at 21 days after nerve crush injury. (A-D) Representative images of sciatic nerve distal segments immunostained for BDNF (green) from animals in the (A) uninjured (contralateral), (B) vehicle, (C) TMCSH and (D) TMCSH-HC groups; Nuclei stained with DAPI (blue). Scale bars represent 25 µm. (E) Semi-quantification of BDNF protein expression in the proximal, injury and distal portions of sciatic nerves. Line represents the BDNF expression levels in uninjured nerves (contralateral). Values represent the mean area occupied by pixels corresponding to the fluorescent signal normalized in relation to the total area (mean ± SD); n=5 per group. $^{\#\#\#\#}$ p<0.0001, $^{\#\#}$ p<0.01, $^{\#}$ p<0.05 vs uninjured. *** p<0.001, ** p<0.01, * p<0.05 in multiple comparisons between treatment groups. (F-I) Representative images of lumbar DRG immunostained for BDNF (green) from animals in the (F) uninjured (contralateral) (G) vehicle, (H) TMCSH and (I) TMCSH-HC group; Nuclei stained with DAPI (blue). Scale bars represent 50 µm. (J) Semi-quantification of BDNF protein expression in the L4 and L5 DRGs. Line represents the BDNF expression levels in contralateral DRGs. Values represent the mean pixel intensity levels ± SD; n=5 per group. $^{\#\#\#\#}$ p<0.0001, $^{\#\#}$ p<0.01 vs contralateral DRGs ** p<0.01, * p<0.05 in multiple comparisons between treatment groups. (K-M) Representative grayscale images of lumbar spinal cord hemisection immunostained for BDNF from the (K) vehicle, (L) TMCSH and (M) TMCSH-HC group; D: dorsal, V: ventral, R: right, L: left; Scale bars represent 500 µm. (N) Semi-quantification of BDNF protein expression in the lumbar spinal cord. Values represent the mean pixel intensity levels ± SD; n=5 per group. ** p<0.01, * p<0.05 in multiple comparisons between treatment groups.

3.4. Histological analysis of crushed sciatic nerves

At 21 days after sciatic nerve crush injury, nerves from the different treatment groups were immunostained for the detection of NF-H, GAP-43 protein and the S100 Schwann cell marker.

Axonal protection and regeneration was investigated through the staining of neurofilament NF-H and the growth-associated protein GAP-43 positive axons. Results showed that the amount of NF-H positive nerve axons were progressively lower along the crushed sciatic nerves - from the proximal to the distal stump - in the vehicle and TMCSH treated groups (**Figures 4A-D and M**). Contrarily, 21 days after injury the levels of NF-H positive axons in the TMCSH-HC group were similar in all analyzed nerve segments, being these significantly higher than those expressed in both the vehicle and TMCSH groups at the distal nerve segment (**Figures 4A-D and M**). The levels of GAP-43 protein were generally increased in all nerve segments of all treatment groups as compared to the GAP-43 levels of the contralateral uncrushed nerves. In the control vehicle group, the expression of GAP-43 protein was progressively reduced in nerve segments reaching similar levels to the contralateral nerves in the distal nerve stump (**Figures 4E-H and N**). This expression levels were significantly lower than those present in the distal nerve segments of animals treated with TMCSH and TMCSH-HC nanoparticles.

Schwann cells response to injury was evaluated by the immunostaining of sciatic nerves with the S100 protein marker. **Figure 4O** points to a significant increase in the S100 protein expression levels, as compared to those in the contralateral uninjured tissue, in the nerve proximal stump for all treatment groups and in the nerve injury region for the TMCSH-HC treatment. Although not statistically significant, the levels of S100 protein expression in the distal portion of sciatic nerve were higher for animals treated with both nanoparticle formulations (**Figures 4I-L and O**), evidencing a slight improvement in Schwann cell proliferation.

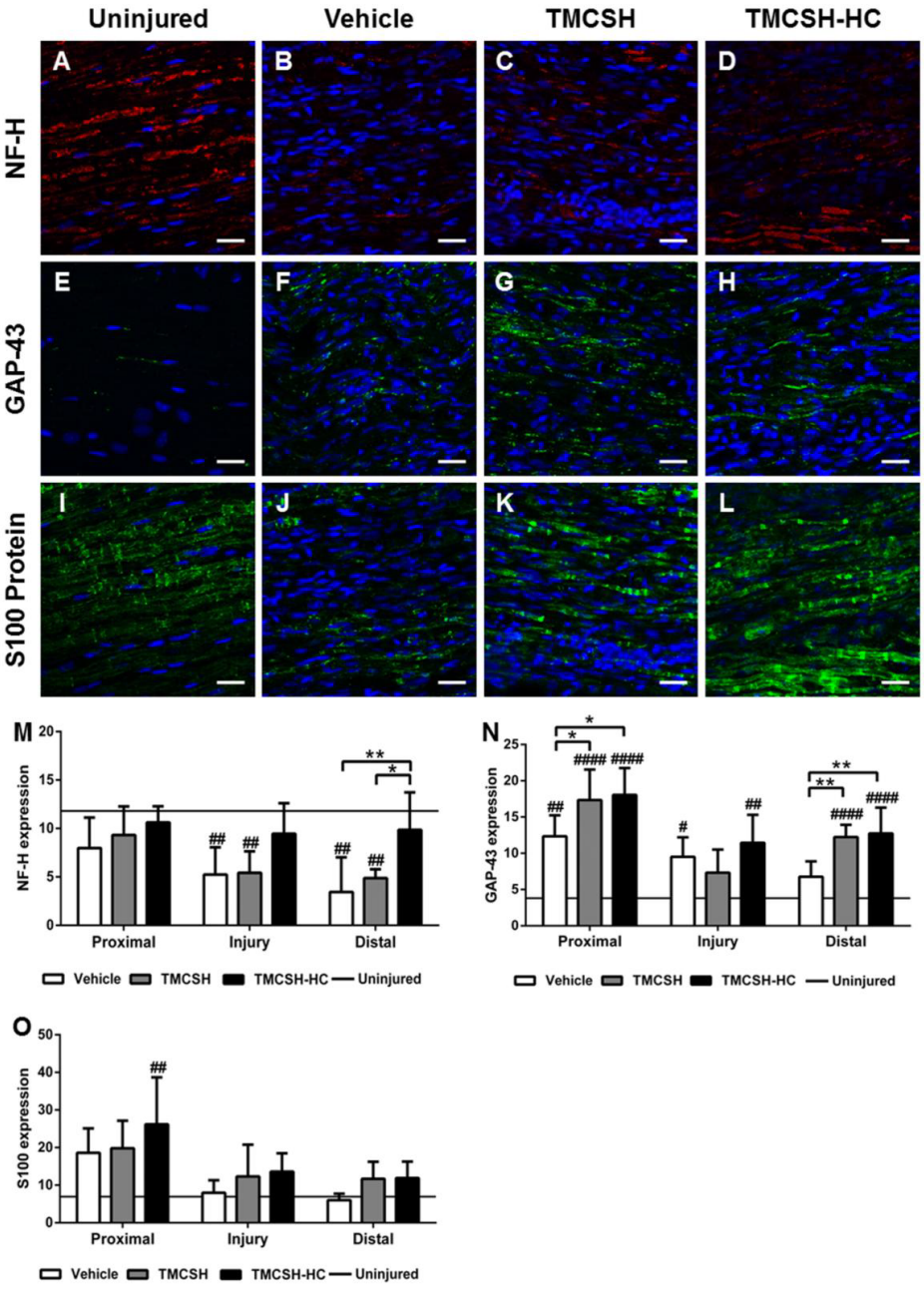

Figure 4. Histological analysis of injured sciatic nerves at 21 days after nerve crush injury. (A-D) Immunohistochemistry representative images of sciatic nerve sections for the detection of NF-H (red) from (A) uninjured nerves, (B) vehicle group, (C) TMCSH group and (D) TMCSH-HC group. (E-H) Immunohistochemistry representative images of sciatic nerve sections for the detection of growth associated protein GAP-43 (green) from (E) uninjured nerves (contralateral), (F) vehicle group, (G) TMCSH group and (H) TMCSH-HC group. (I-L) Immunohistochemistry representative images of sciatic nerve sections for the detection of S100 protein (green) from (I) uninjured nerves, (J) vehicle group, (K) TMCSH group and (L) TMCSH-HC group. Nuclei stained with DAPI (blue). Scale bars represent 25μm. (M-O) Semi-quantification of NF-H (M), GAP-43 (N) and S100 protein expression (O) in the sciatic nerve sections. Line represents the respective marker expression levels in the uninjured nerves (contralateral). Values represent mean ± SD; n=5 per group. $^{\#\#\#\#}$ p<0.0001, $^{\#\#}$ p<0.01, $^{\#}$ p<0.05 vs uninjured nerves. ** p<0.01, * p<0.05 in multiple comparisons between treatment groups.

Following a nerve crush injury, axonal damage, demyelination and subsequent remyelination of the regenerating axons occur sequentially in time. Consequently, the degree of axonal re-myelination observed after an injury can be used as an indicator of nerve recovery. To assess the re-myelination extent after injury, transverse semi-thin sections of the distal nerve segment were analyzed by toluidine blue staining (**Figure 5A to D**). Results showed a large number of well myelinated axons, with thick myelin sheaths, in the TMCSH and TMCSH-HC groups (**Figures 5C-D**). In contrast, sciatic nerve axons treated with vehicle solution exhibited thinner myelin sheaths and several degenerating axons (**Figure 5B**). The quantification of myelinated axons per surface area showed a significantly higher density of myelinated axons in animals treated with TMCSH-HC nanoparticles, being these values similar to the ones found for the uninjured contralateral nerves (**Figure 5I**). We also evaluated the extent of the regeneration of unmyelinated axons in transverse ultra-thin sections of the distal nerve segment by TEM (**Figure 5E to H**). Sciatic nerves from vehicle group showed many Remak bundles (group of unmyelinated axons) containing a number of very tightly grouped unmyelinated axons of different sizes surrounded by a single Schwann cell. In contrast, sciatic nerves from TMCSH and TMCSH-HC groups presented less compact Remak bundles being the unmyelinated axons relatively homogenous in size, similar to the contralateral uninjured nerves (**Figure 5E**). The density of unmyelinated axons in the nanoparticle treated animals was found to be similar to the one observed in uninjured animals, independently of the formulation (targeted vs. non-targeted) (**Figure 5J**). In opposition, animals in the vehicle treatment group showed a significant increase, of approximately 59%, in the density of unmyelinated axons (**Figure 5J**).

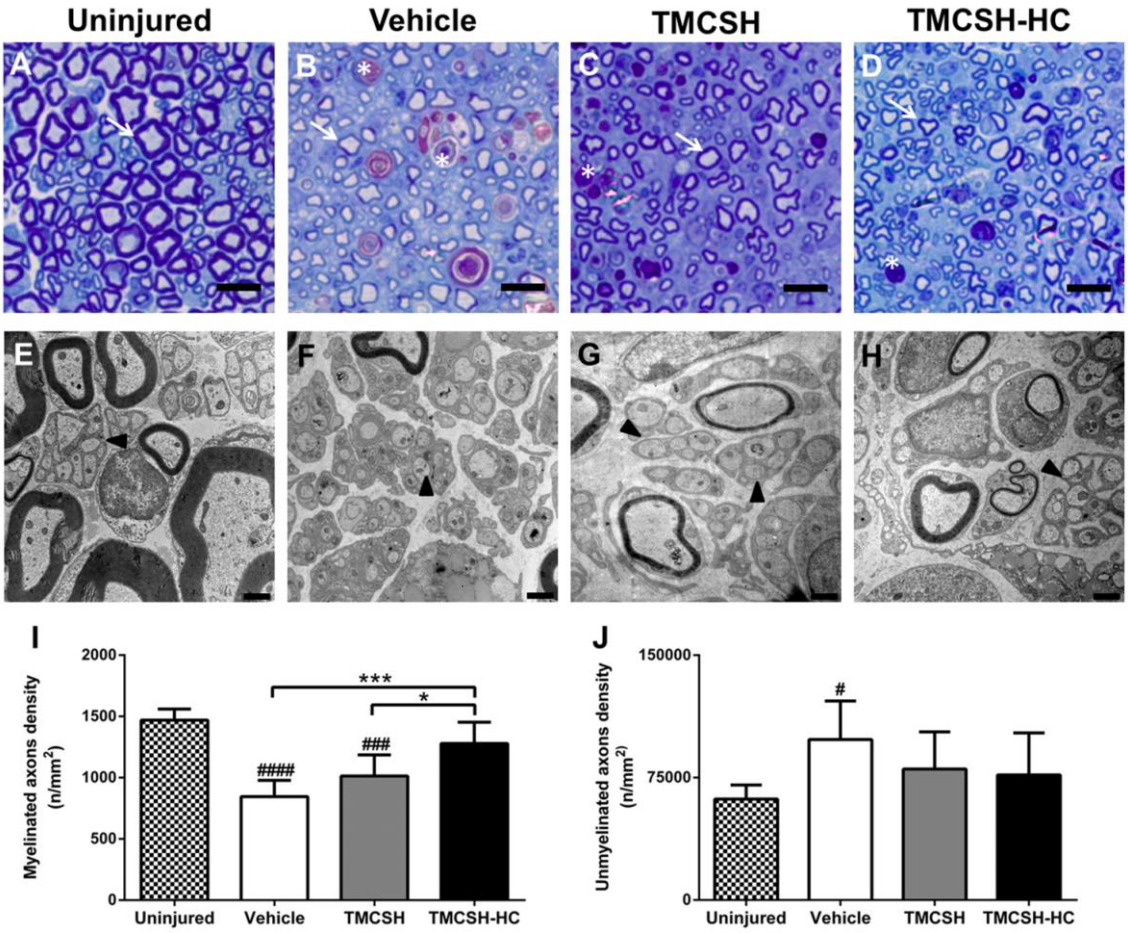

Figure 5. Morphometric analysis of distal portions of sciatic nerves at 21 days after nerve crush injury. (A-D) Representative images of semi-thin transverse sciatic nerve sections from (A) uninjured nerves (contralateral), (B) vehicle group, (C) TMCSH group and (D) TMCSH-HC group. Arrows indicate myelinated axons; * depicts degenerating axons. Scale bar represents 25 µm. (E-H) Representative images of ultra-thin transverse sciatic nerve sections from (E) uninjured nerves (contralateral), (F) vehicle group, (G) TMCSH group and (H) TMCSH-HC group. Arrowheads show Remak bundles. Scale bar represents 1 µm. (I) Density of myelinated axons expressed as number of myelinated axons per square millimeter (n/mm^2). (J) Density of unmyelinated axons expressed as number of unmyelinated axons per square millimeter (n/mm^2). Values represent mean ± SD; n=5 per group. $^{####}$ p<0.0001, $^{###}$ p<0.001 vs uninjured nerves. *** p<0.001, * p<0.05 in multiple comparisons between treatment groups.

3.5. Reinnervation of target gastrocnemius muscle

Hematoxylin and eosin stained sections of gastrocnemius muscles after 21 days postinjury were used to assess the reinnervation of the denervated gastrocnemius muscle on the injured side (**Figure 6A to D**). The gastrocnemius muscle in all treatment groups displayed signs of muscle denervation, with a maximal muscle mass loss of 35% being observed in the vehicle group, as compared to the contralateral normal muscle (**Figure 6E**). In the vehicle group muscle fibers revealed a considerable atrophy as compared to that in the other treatment groups. The myofibers lost their scattered distribution and were rearranged in groups of small

rounded fibers separated from each other by a number of adipocytes (**Figure 6B**). In both nanoparticle treatment groups, muscle fibers also presented a round-shape but were less shrunk then the ones observed in the vehicle treatment group. Few or none adipocytes were seen between myofibers. The morphometric analysis further indicated that the cross sectional area of muscle fibers in the three treatment groups showed significant differences compared to the contralateral normal gastrocnemius muscle. As shown in **Figure 6F**, animals treated with nanoparticles showed a significant higher muscle fiber cross sectional area than the ones in vehicle group. The greater effect on the recovery of gastrocnemius muscle cross sectional area was observed in the TMCSH nanoparticle treatment group. These findings were further corroborated by the analysis of the degree of reinnervation of the denervated gastrocnemius muscle. At 21 days after sciatic nerve crush, double staining for the postsynaptic marker α-bungarotoxin and the NF200 marker revealed a difference in the fraction of denervated and re-innervated NMJ between treatment groups. As shown in **Figure 6G**, animals from the vehicle group showed a significantly higher percentage of denervated NMJ (40.2 ± 4.4%) as compared to the TMCSH and TMCSH-HC treated animals (13.2 ± 12.0% and 10.0 ± 6.1%, respectively). On the other hand, although not statistically significant, the percentage of completely innervated NMJ was higher in the TMCSH-HC group when compared to the TMCSH and vehicle groups.

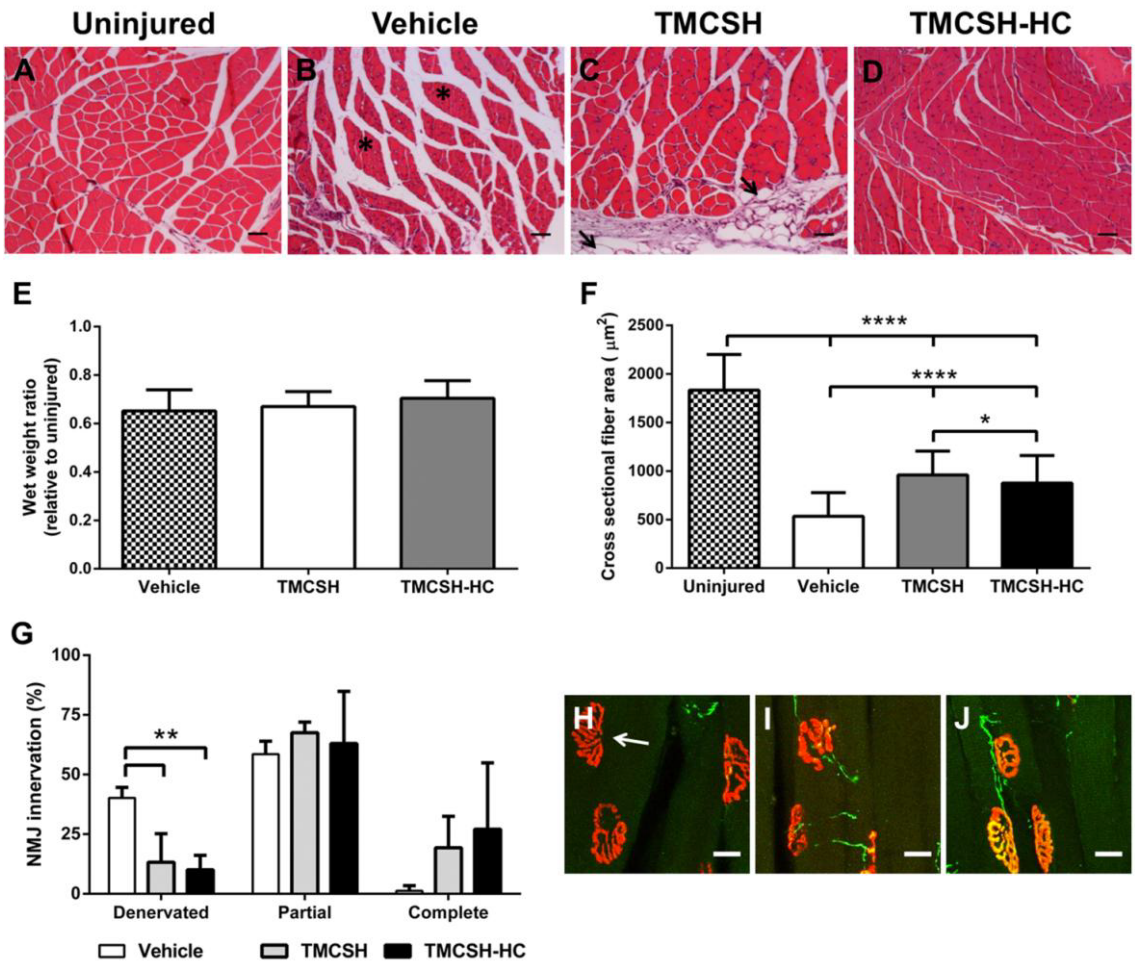

Figure 6. Morphometric analysis of gastrocnemius muscles at 21 days after nerve crush injury. Representative images of gastrocnemius muscles from (A) uninjured (contralateral), (B) vehicle group, (C) TMCSH group and (D) TMCSH-HC group. * Depicts groups of atrophic muscle fibers; Arrows indicate the presence of adipocytes. Scale bar 50 µm. (contralateral) (E) Gastrocnemius muscle wet weight represented as the ratio between muscle wet weight in the injured limb relative to the uninjured muscle wet weight (uninjured limb); n=12 per group. (F) Cross sectional area (µm2) of gastrocnemius muscle fibers; n=3 per group. (G) Quantification of fraction of NMJ innervation from at least 50 NMJs; n=3 per group. 100% represents a tissue where all NMJ are completely innervated (uninjured). (H-J) Representative images of denervated (H, arrow), partially innervated (I) and completely innervated NMJs (J) from gastrocnemius muscle using the NF200 marker (green) and the postsynaptic marker α-bungarotoxin (red) at 21 days after injury. Scale bar represents 20 µm. Values represent mean ± SD. **** p<0.0001, ** p<0.01, * p<0.05.

4. Discussion

The management of nerve lesions resulting from peripheral neuropathies remains a major clinical challenge. The pathological features of axonal degeneration occurring in the majority of human peripheral neuropathies are quite similar to Wallerian degeneration, being neuropathies commonly described as “Wallerian-like” degenerative conditions [38, 39]. This similarity makes the experimental Wallerian degeneration models useful tools for studying the pathogenesis and the efficacy of potential treatments for peripheral neuropathies. In a scenario of Wallerian degeneration, Schwann cells, together with macrophages, respond by clearing the degenerated axons and myelin debris. Further, Schwann cells enter in a dedifferentiation process, starting to proliferate to form bands of Büngner, important for guiding the regrowing axons. Schwann cells also secrete neurotrophic factors and proteins of the extracellular matrix that promote the regeneration of the injured nerve. However, in severe and/or prolonged denervation conditions, Schwann cells are not capable of sustaining this process in time, limiting the ability of peripheral nerves to fully regenerate [40, 41].

Several studies have demonstrated that the administration of neurotrophic factors could aid preventing nerve degeneration and denervation of target tissues in the context of neuropathy, as well as promote nerve regeneration and consequent functional recovery of regenerating nerves [42]. But neurotrophic factors have a very short half-life being quickly cleared in vivo and, due to their pleiotropic actions, they can cause negative off-target effects. Motivated to contribute to the development of safe and targeted therapeutic strategies to promote peripheral nerve repair here we describe a non-viral, non-toxic and biodegradable nanocarrier based on TMC [28], designed to allow the targeted and efficient delivery and expression of a BDNF gene in peripheral neurons. The aim of the current study was to evaluate if the intramuscular administration of the developed neuron-targeted TMCSH-HC/BDNF nanoparticles in a nerve injury scenario would protect peripheral neurons from prolonged degeneration and/ or enhance their regeneration ability.

Nanoparticles were intramuscularly administrated in the gastrocnemius muscle, a clinically relevant route of administration, 8 days before sciatic nerve crush injury. This nerve injury model is particularly helpful to study the effect of therapeutic agents for neuroprotection and regeneration, for the reason that it causes the rupture of nerve axons without destroying most of the nerve's supporting structures, i.e. endoneurial tubes, thereby providing a guide for axons to regenerate spontaneously and even partially reinnervate their targets, mimicking the observed series of events that can occur in an axonal neuropathy. Therefore, using this injury

model, the success of a particular therapeutic agent is directly correlated with the evidence of axonal degeneration prevention and/or acceleration of nerve regeneration. The pre-injury administration would allow the nanoparticles to reach the neuron cell bodies before the injury [13], and in this way one could evaluate their potential to create a cellular milieu that would protect neurons from prolonged degeneration and/ or enhance the regeneration process.

The treatment with TMCSH-HC nanoparticles significantly elevated the BDNF expression in neural tissues, as observed 21 days after injury. The BDNF mRNA levels were significantly increased in the lumbar DRGs, as compared to wild-type animals (uninjured) and vehicle group, being the respective protein expression levels also augmented in the lumbar DRGs, lumbar spinal cord segments and sciatic nerves. Taking into account these observations, we consider that the BDNF levels elevation observed in TMCSH-HC treated animals is a result of nanoparticle-mediated BDNF gene delivery in these tissues and not a response to the nerve injury itself.

Further we confirmed that BDNF delivery and expression within the neural tissues promoted a general recovery of injured peripheral nerves. Vehicle treated animals showed a progressive recovery of their locomotor activity, significant alterations in their thermal response latency throughout the study (thermal hypoalgesia), mechanical hypoalgesia in the first week post-injury and mechanical allodynia, which was evident within 2 weeks after nerve injury. In addition, vehicle treated animals showed a marked reduction of their motor nerve conduction velocities (MNCVs), which was correlated to the lower density of myelinated axons evidenced in this treatment group. In contrast, animals treated with targeted and non-targeted nanoparticles demonstrated a gradual recovery of their thermal nociceptive function, more evident for the TMCSH-HC group, reaching the preoperative response latency values at the end of the study. In the timeframe of the study, nanoparticle treatment did not prevented mechanical allodynia, but animals from the TMCSH-HC group showed a delay in the allodynia onset, with treated animals presenting similar paw withdrawal thresholds to the contralateral side at 7 days post-injury. No significant differences were observed in the locomotion activity recovery between all treatment groups. However, treatment with TMCSH-HC nanoparticles resulted in a significant increase in the MNCV in comparison with the vehicle group animals, although these values were still reduced as compared to the contralateral normal MNCV values. It is considered that noxious heat nociception is predominantly mediated by unmyelinated axons (C-fibers), organized as Remak bundles, whereas mechanical nociception and MNCV are mainly transmitted through the myelinated axons (A-fibers) [43].

Therefore, these sensorimotor functional results demonstrate that the BDNF delivery mediated by the targeted TMCSH-HC nanoparticles might have an effect in both myelinated and unmyelinated axons.

To determine the structural changes in both myelinated and unmyelinated axons of the sciatic nerve that may underlie the functional differences observed between treatment groups, a detailed morphometric study of the injured nerves was conducted 21 days post-injury (29 days post-nanoparticle treatment). A significant decrease in the myelinated axon density in the vehicle and TMCSH groups was observed, as compared to the contralateral uninjured nerves. In contrast, animals treated with TMCSH-HC nanoparticles presented similar density of myelinated axons to the contralateral uninjured nerves, being these values significantly higher than the ones presented by vehicle and TMCSH treated animals. Despite that the density of myelinated axons was close to the normal levels, TMCSH-HC treated nerves were not yet fully functional suggesting that the remyelination process was not completed at this time point of analysis. On the other hand, the density of unmyelinated axons appeared to be significantly unaffected in the animals treated with both nanoparticle formulations (targeted and non-targeted), justifying the great thermal nociceptive recovery observed in the nanoparticle-treated animals. In opposition, animals in the vehicle treatment group showed a significant increase, of approximately 59%, in the density of unmyelinated axons. These results are in line with previous reports showing that following a nerve crush injury unmyelinated axons branch in a tentative to search for a target [44]. Without a therapeutic intervention this branching can persist for a prolonged period of time until the axons reach the target tissues, an event that stops additional branching and triggers pruning to eliminate redundant branches. In accordance, we consider that, at the time point of analysis, unmyelinated axons of the vehicle treated animals might have not yet fully reached the target tissues and are still responsive to the injury stimulus. In these conditions, unmyelinated axons are not totally functional, which is supported by the thermal hypoalgesia observed. These findings are corroborated by the analysis of the expression of the NF-H and GAP-43 markers. In contrast with animals from vehicle group, TMCSH-HC treated animals exhibited similar levels of NF-H expression to the contralateral uninjured nerves and a significant rise of GAP-43 protein, indicating that, in this treatment group, the original nerve structure was recovered and injured axons were actively regenerating.

Upon a sciatic nerve crush injury the target limb muscles become denervated. Previous studies have shown that, after denervation, muscle wet weight was found to dramatically decrease in

the first days after injury, reaching a minimum level at about day 14, and then progressively recovering its mass to approximately 80% the weight of normal contralateral muscle by 28 days after nerve injury [45, 46]. Our results are in concordance with the ones previously reported. Additionally, our data shows that animals treated with TMCSH and TMCSH-HC nanoparticles displayed a decrease in the muscle fiber atrophy, as well as a higher and earlier reinnervation of the NMJ in the gastrocnemius muscles, which seems to correlate with the nerve protection observed in these groups. This can also explain the normal levels of BDNF mRNA expression observed in both treatment groups 21 days after injury, which contrast with the reduced levels observed in the vehicle group.

Similarly to targeted nanoparticles, our study showed that non-targeted nanoparticles were also able to exert a beneficial effect in the injury recovery, mainly in what regards to target muscle recovery. We believe these nanoparticles, without targeting moieties, were preferentially retained at the injection site where they probably lead to the transient muscle cell transfection. Previous studies have shown that BDNF can potentiate *in vivo* muscle regeneration, through its stimulatory effect on muscle stem cells function [47], as well as nerve regeneration, acting as a retrograde signal for survival of innervating neurons via the TrkB receptor [48, 49]. Thus, the local expression of BDNF may then have exerted its action locally, by autocrine signaling, or remotely, via paracrine signaling, in Schwann cells and/or in the distal portion of injured sciatic nerves, which resulted in the reversion of the target muscle amyotrophic status and in the improvement of sciatic nerve recovery as well. Despite that, the HC-functionalization of the nanoparticles increases the chance of nanoparticle binding and internalization in neural populations, leading to an improvement in the BDNF expression in neural tissues and consequent better sciatic nerve recovery. This highlights the superior efficacy of the targeted nanoparticles to be applied in the context of peripheral nerve injury.

Altogether, our findings indicate that the developed neuron-targeted TMCSH-HC nanoparticles are capable of mediating the delivery and subsequent expression of BDNF transgene in peripheral neurons after a peripheral intramuscular administration, providing the trophic support needed to allow injured neurons to more quickly respond to the injury and accelerate their regeneration and target muscle reinnervation. This neuroprotection and enhanced regeneration resulted in satisfactory sensorimotor functional recovery.

To the best of our knowledge this is the first study that reports the improvement of nerve regeneration as a result of a gene therapy treatment mediated by a non-viral vector. On the basis of our results, we believe that the intramuscular injection of the non-viral TMCSH-HC

nanoparticles carrying therapeutic transgenes that encode for neurotrophic factors is an efficient and safe way of preventing prolonged nerve degeneration and, consequently, accelerate nerve regeneration. It should be highlighted that due to its safety profile these nanoparticles can also be foreseen for multiple administrations, to extend the envisaged therapeutic effect.

5. Conclusions

Aiming at developing alternative therapeutic strategies to treat peripheral neuropathies, in this study we introduced a versatile, safe and efficient neuron-targeted non-viral vector based on thiolated TMC to be used as gene delivery carrier. The ability of these nanoparticles to specifically mediate a therapeutic transgene delivery to peripheral neurons after a minimally invasive clinically relevant peripheral administration and promote the recovery of a crushed nerve by preventing nerve degeneration and enhancing nerve regeneration was demonstrated. This opens new avenues for the treatment of nerve injury deriving from peripheral neuropathies based on safe nanoparticle-mediated gene delivery strategies.

Acknowledgements

The work was financed by Portuguese funds through FCT – *Fundação para a Ciência e a Tecnologia* in the framework of theprojects PTDC/CTM-NAN/115124/2009 and PTDC/CTM-NAN/3547/2014. Catia D. F. Lopes, Nadia P. Gonçalves and Carla P. Gomes acknowledge FCT for their Ph.D. scholarships (SFRH/BD/77933/2011, SFRH/BD/74304/2010 and SFRH/BD/77930/2011, respectively). Authors further acknowledge the Biointerfaces and Nanotechnology Service of i3S for the nanoparticle characterization studies, Centro de Materiais da Universidade do Porto (CEMUP) for NMR analysis and Bioimaging Center for Biomaterials and Regenerative Therapies (b.IMAGE) for the confocal microscopy. The contribution of Dr. Paulo Aguiar (INEBji3S) to MATLAB programing is also acknowledged.

Supplementary Information

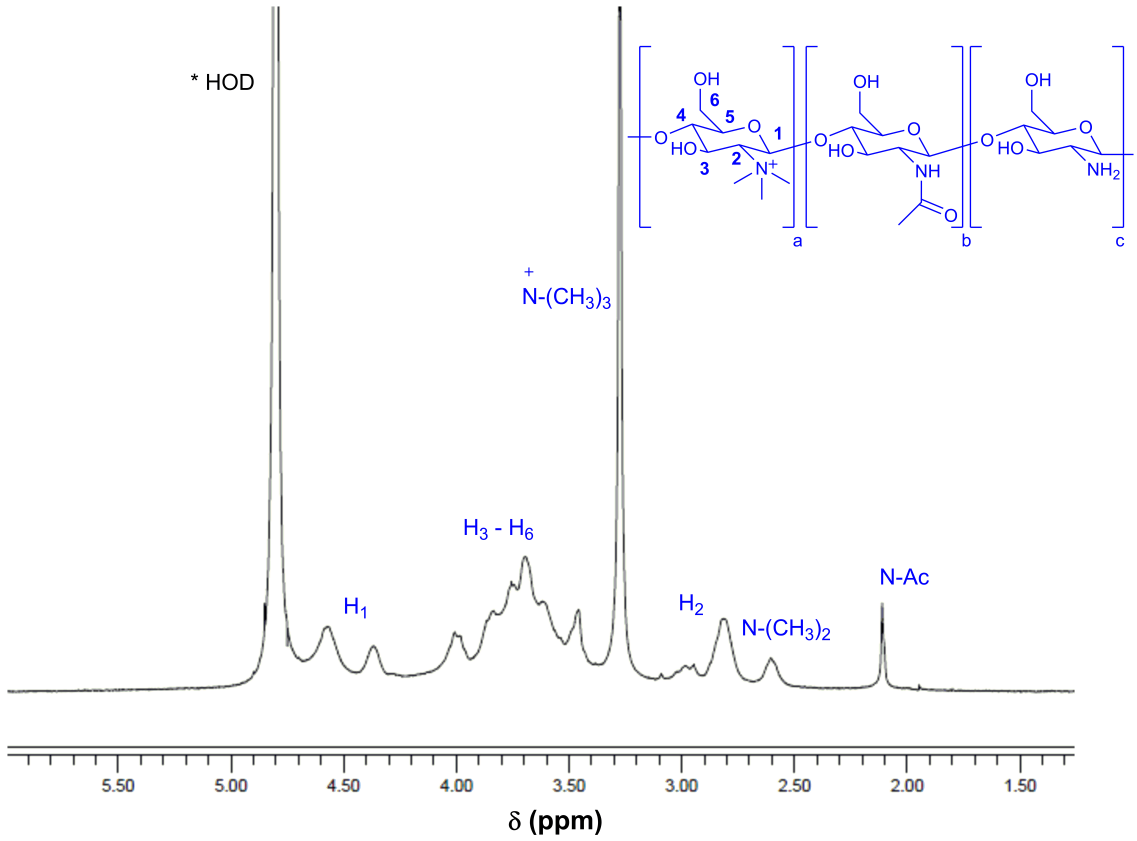

Figure S1. ^{1}H-NMR spectrum of TMC (400 MHz, in D_2O).

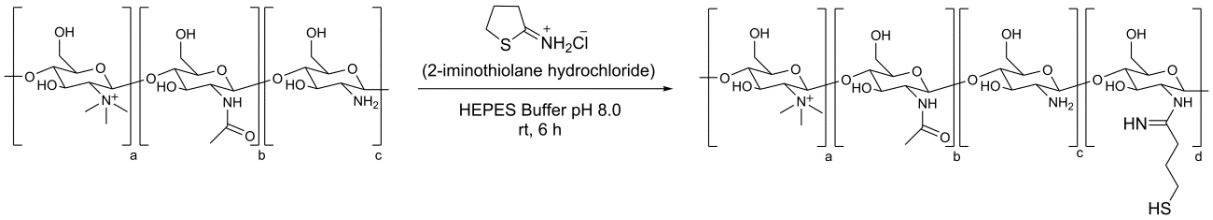

Figure S2. Schematic representation of the synthetic chemical route followed for the preparation of the thiolated trimethyl chitosan (TMCSH).

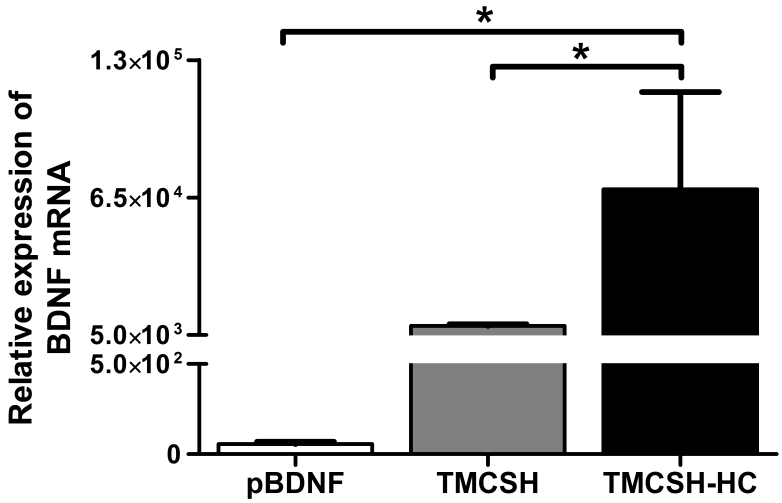

Figure S3. Relative expression of BDNF mRNA in dissociated DRG primary cultures at 72 hours after transfection with naked plasmid DNA encoding for BDNF (pBDNF), TMCSH/pBDNF or TMCSH-HC/pBDNF nanoparticles. BDNF mRNA expression was normalized to GAPDH expression levels and expressed as relative to untreated DRG primary cultures. * $p<0.05$ in multiple comparisons between treatment groups.

References

1. Watson, J.C. and P.J. Dyck, "Peripheral Neuropathy: A Practical Approach to Diagnosis and Symptom Management." Mayo Clin Proc, 2015. 90(7): p. 940-51.
2. Goss, J.R., "The therapeutic potential of gene transfer for the treatment of peripheral neuropathies." Expert Rev Mol Med, 2007. 9(8): p. 1-20.
3. Apfel, S.C., et al., "Efficacy and safety of recombinant human nerve growth factor in patients with diabetic polyneuropathy: A randomized controlled trial. rhNGF Clinical Investigator Group." Jama, 2000. 284(17): p. 2215-21.
4. Wellmer, A., et al., "A double-blind placebo-controlled clinical trial of recombinant human brain-derived neurotrophic factor (rhBDNF) in diabetic polyneuropathy." Journal of the peripheral nervous system : JPNS, 2001. 6(4): p. 204-10.
5. Poduslo, J.F. and G.L. Curran, "Permeability at the blood-brain and blood-nerve barriers of the neurotrophic factors: NGF, CNTF, NT-3, BDNF." Brain research Molecular brain research, 1996. 36(2): p. 280-6.
6. Poduslo, J.F., G.L. Curran, and J.S. Gill, "Putrescine-modified nerve growth factor: bioactivity, plasma pharmacokinetics, blood-brain/nerve barrier permeability, and nervous system biodistribution." Journal of neurochemistry, 1998. 71(4): p. 1651-60.
7. Saragovi, H.U. and K. Gehring, "Development of pharmacological agents for targeting neurotrophins and their receptors." Trends in pharmacological sciences, 2000. 21(3): p. 93-8.
8. Glorioso, J., M. Mata, and D. Fink, "Therapeutic gene transfer to the nervous system using viral vectors." J Neurovirol, 2003. 9(2): p. 165-72.
9. Pêgo, A.P., H. Oliveira, and P.M. Moreno, *Biomaterial-Based Vectors for Targeted Delivery of Nucleic Acids to the Nervous System*, in *Drug Delivery Systems: Advanced Technologies Potentially Applicable in Personalised Treatment*, J. Coelho, Editor. 2013, Springer Netherlands: Dordrecht. p. 185-224.
10. Gomes, C.P., et al., "Translating chitosan to clinical delivery of nucleic acid-based drugs." MRS Bulletin, 2014. 39(01): p. 60-70.
11. Thanou, M., et al., "Quaternized chitosan oligomers as novel gene delivery vectors in epithelial cell lines." Biomaterials, 2002. 23(1): p. 153-9.
12. Lopes, C.D., et al., "Microfluidic-based platform to mimic the in vivo peripheral administration of neurotropic nanoparticles." Nanomedicine (Lond), 2016. 11(24): p. 3205-3221.
13. Lopes, C.D., et al., "In vivo targeted gene delivery to peripheral neurons mediated by neurotropic poly(ethylene imine)-based nanoparticles." Int J Nanomedicine, 2016. 11: p. 2675-83.
14. Zhang, J.Y., et al., "Endogenous BDNF is required for myelination and regeneration of injured sciatic nerve in rodents." The European journal of neuroscience, 2000. 12(12): p. 4171-80.
15. Fukuoka, T., et al., "Brain-derived neurotrophic factor increases in the uninjured dorsal root ganglion neurons in selective spinal nerve ligation model." The Journal of neuroscience : the official journal of the Society for Neuroscience, 2001. 21(13): p. 4891-900.
16. Kobayashi, H., et al., "Expression changes of multiple brain-derived neurotrophic factor transcripts in selective spinal nerve ligation model and complete Freund's adjuvant model." Brain research, 2008. 1206: p. 13-9.
17. Miletic, G. and V. Miletic, "Increases in the concentration of brain derived neurotrophic factor in the lumbar spinal dorsal horn are associated with pain behavior following chronic constriction injury in rats." Neuroscience letters, 2002. 319(3): p. 137-40.
18. Geng, S.-J., et al., "Contribution of the spinal cord BDNF to the development of neuropathic pain by activation of the NR2B-containing NMDA receptors in rats with spinal nerve ligation." Experimental neurology, 2010. 222(2): p. 256-66.

19. Foster, E., B. Robertson, and K. Fried, "trkB-like immunoreactivity in rat dorsal root ganglia following sciatic nerve injury." Brain research, 1994. 659(1-2): p. 267-71.

20. Hammarberg, H., et al., "Differential regulation of trophic factor receptor mRNAs in spinal motoneurons after sciatic nerve transection and ventral root avulsion in the rat." The Journal of comparative neurology, 2000. 426(4): p. 587-601.

21. Gauthier, R., et al., "Brain-derived neurotrophic factor gene delivery to muller glia preserves structure and function of light-damaged photoreceptors." Investigative ophthalmology & visual science, 2005. 46(9): p. 3383-92.

22. Ren, R., et al., "Long-term rescue of rat retinal ganglion cells and visual function by AAV-mediated BDNF expression after acute elevation of intraocular pressure." Investigative ophthalmology & visual science, 2012. 53(2): p. 1003-11.

23. Wan, C., et al., "Effect of adenovirus-mediated brain derived neurotrophic factor in early retinal neuropathy of diabetes in rats." International journal of ophthalmology, 2010. 3(2): p. 145-8.

24. Fukui, H., et al., "BDNF gene therapy induces auditory nerve survival and fiber sprouting in deaf Pou4f3 mutant mice." Scientific reports, 2012. 2: p. 838.

25. Nakaizumi, T., et al., "Adenovirus-mediated expression of brain-derived neurotrophic factor protects spiral ganglion neurons from ototoxic damage." Audiology & neuro-otology, 2004. 9(3): p. 135-43.

26. Alrashdan, M.S., et al., "Effects of combining electrical stimulation with BDNF gene transfer on the regeneration of crushed rat sciatic nerve." Acta neurochirurgica, 2011. 153(10): p. 2021-9.

27. Sakamoto, T., et al., "Adenoviral gene transfer of GDNF, BDNF and TGF beta 2, but not CNTF, cardiotrophin-1 or IGF1, protects injured adult motoneurons after facial nerve avulsion." Journal of neuroscience research, 2003. 72(1): p. 54-64.

28. Gomes, C.P., et al., "A high-throughput bioimaging study to assess the impact of chitosan-based nanoparticle degradation on DNA delivery performance." Acta Biomater, 2016. 46: p. 129-140.

29. Administration, U.F.a.D., "Guidance for Industry - Pyrogen and Endotoxins Testing." 2012.

30. Ellman, G.L., "Tissue sulfhydryl groups." Arch Biochem Biophys, 1959. 82(1): p. 70-7.

31. Oliveira, H., et al., "Targeted gene delivery into peripheral sensorial neurons mediated by self-assembled vectors composed of poly(ethylene imine) and tetanus toxin fragment c." Journal of Controlled Release, 2010. 143(3): p. 350-358.

32. Goncalves, N.P., et al., "A novel nanoparticle delivery system for in vivo targeting of the sciatic nerve: impact on regeneration." Nanomedicine (London, England), 2012. 7(8): p. 1167-80.

33. Inserra, M.M., D.A. Bloch, and D.J. Terris, "Functional indices for sciatic, peroneal, and posterior tibial nerve lesions in the mouse." Microsurgery, 1998. 18(2): p. 119-24.

34. Goncalves, N.P., M. Teixeira-Coelho, and M.J. Saraiva, "The inflammatory response to sciatic nerve injury in a familial amyloidotic polyneuropathy mouse model." Experimental neurology, 2014. 257: p. 76-87.

35. Ferdinandusse, S., et al., "Ataxia with loss of Purkinje cells in a mouse model for Refsum disease." Proceedings of the National Academy of Sciences of the United States of America, 2008. 105(46): p. 17712-7.

36. Livak, K.J. and T.D. Schmittgen, "Analysis of relative gene expression data using real-time quantitative PCR and the 2(-Delta Delta C(T)) Method." Methods (San Diego, Calif), 2001. 25(4): p. 402-8.

37. Sarikcioglu, L., B.M. Demirel, and A. Utuk, "Walking track analysis: an assessment method for functional recovery after sciatic nerve injury in the rat." Folia morphologica, 2009. 68(1): p. 1-7.

38. Wang, M.S., et al., "Pathogenesis of axonal degeneration: parallels between Wallerian degeneration and vincristine neuropathy." Journal of neuropathology and experimental neurology, 2000. 59(7): p. 599-606.

39. Glass, J.D., "Wallerian degeneration as a window to peripheral neuropathy." Journal of the neurological sciences, 2004. 220(1-2): p. 123-4.

40. Gordon, T., O.A.R. Sulaiman, and A. Ladak, "Electrical Stimulation for Improving Nerve Regeneration: Where Do We Stand?" Essays on Peripheral Nerve Repair and Regeneration, 2009. 87: p. 433-444.

41. Gordon, T., N. Tyreman, and M.A. Raji, "The basis for diminished functional recovery after delayed peripheral nerve repair." The Journal of neuroscience : the official journal of the Society for Neuroscience, 2011. 31(14): p. 5325-34.

42. Faroni, A., et al., "Peripheral nerve regeneration: experimental strategies and future perspectives." Advanced drug delivery reviews, 2015. 82-83: p. 160-7.

43. Dubin, A.E. and A. Patapoutian, "Nociceptors: the sensors of the pain pathway." The Journal of clinical investigation, 2010. 120(11): p. 3760-72.

44. Toft, P.B., K. Fugleholm, and H. Schmalbruch, "Axonal branching following crush lesions of peripheral nerves of rat." Muscle & nerve, 1988. 11(8): p. 880-9.

45. Liu, M., et al., "Expression pattern of myostatin in gastrocnemius muscle of rats after sciatic nerve crush injury." Muscle & nerve, 2007. 35(5): p. 649-56.

46. Wu, R.H., et al., "A potential indicator of denervated muscle atrophy: the ratio of myostatin to follistatin in peripheral blood." Genetics and molecular research : GMR, 2011. 10(4): p. 3914-23.

47. Clow, C. and B.J. Jasmin, "Brain-derived Neurotrophic Factor Regulates Satellite Cell Differentiation and Skeltal Muscle Regeneration." Molecular Biology of the Cell, 2010. 21(13): p. 2182-2190.

48. Mousavi, K., D.J. Parry, and B.J. Jasmin, "BDNF rescues myosin heavy chain IIB muscle fibers after neonatal nerve injury." American Journal of Physiology-Cell Physiology, 2004. 287(1): p. C22-C29.

49. Mousavi, K. and B.J. Jasmin, "BDNF is expressed in skeletal muscle satellite cells and inhibits myogenic differentiation." Journal of Neuroscience, 2006. 26(21): p. 5739-5749.

APPENDIX III

SHORT BIOGRAPHY

Carla Pereira Gomes was born in Esmoriz, Portugal, in 1988. She obtained her Degree on Biomedical Sciences with a minor in Molecular Biomedicine, at the University of Aveiro, in 2009 and her Master degree in Cell and Molecular Biology, at the University of Coimbra, in 2011. Her MSc project was developed at the Center for Neurosciences and Cell Biology (CNC) from the University of Coimbra, under the supervision of Prof. João Nuno Moreira and co-supervision of Prof. Maria Conceição Pedroso Lima, both researchers from the Vectors and Gene Therapy Group at CNC.

Still in 2011, Carla P. Gomes integrated INEB (Instituto Engenharia Biomédica) and started her PhD work as a participant of the TARGETS (TARgeted GEne Therapy Strategies to treat nerve injury) research project, financed by the Portuguese Foundation for Science and Technology (FCT) (FCT - PTDC/CTM-NAN/115124/2009). She got funded by an individual grant from FCT that started in January 2012 (SFRH/BD/79930/2011), under the supervision of Doctor Ana Paula Pêgo. From January to April 2014, Carla was a visiting researcher at the Institute of Biophysics at the Johannes Kepler University, in Linz, in a collaboration work with the research group of Peter Hinterdorfer. In the same year, she also co-supervised the Master thesis of Aida Varela-Moreira, entitled “Gene Delivery Mediated by *N*-Trimethyl Chitosan Nanoparticles: the Impact of the Polymer Degree of Acetylation on Transfection”, who had Ana Paula Pêgo as principal supervisor.

During her PhD training, Carla finished a post-graduate course entitled “Seeding of nerve cells – Implementation and characterization” – 2nd Edition, from the Faculty of Pharmacy of the University of Lisbon. She additionally took a course in Laboratory Animal Science at IBMC (University of Porto), with accreditation as category C personnel by the Federation of European Laboratory Animal Science Associations – FELASA.

Along this period, Carla has also participated in many outreach scientific activities, namely “Mostra de Ciência” or “Noite Europeia dos Investigadores”, and was part of the organizing team of “Science Club” at INEB.

LIST OF PUBLICATIONS

Thesis

Master Thesis: 'Impact of therapeutic gene silencing on cancer cell lines of different histological origins' (2011) University of Coimbra, Coimbra, Portugal

Papers in peer-reviewed scientific journals:

Gomes CP, Gomes-da-Silva LC, Ramalho JS, de Lima MC, Simões S, Moreira JN. 'Impact of PLK-1 Silencing on Endothelial Cells and Cancer Cells of Diverse Histological Origin'. (2013) *Curr Gene Ther*, 13(3), 189-201

Gomes CP, Lopes CDF, Moreno PMD, Varela-Moreira A, Alonso MJ, Pêgo AP. 'Translating chitosan to clinical delivery of nucleic acid-based drugs'. (2014) *MRS Bulletin*, 39, 60-70

Sadio A, Gustafsson JK, Pereira B, **Gomes CP**, Hansson GC, David L, Pêgo AP, Almeida R. 'Modified-Chitosan/siRNA Nanoparticles Downregulate Cellular CDX2 Expression and Cross the Gastric Mucus Barrier'. (2014) *PLoS ONE*, 9(6), e99449

Silva AM, Varela-Moreira A, **Gomes CP**, Molinos M, Leite M, Almeida M, Ribeiro D, Schrader M, Figueiredo C, Barbosa M, Gonçalves R, Almeida C, Pêgo A, Santos SG, Gomez-Lazaro M. 'Integrated Analysis of Biological Samples by Imaging Flow Cytometry'. (2015) *Microscopy and Microanalysis*, 21, 95-96

Moreno PMD, Santos JCC, **Gomes CP**, Varela-Moreira A, Costa A, Leiro V, Mansur HS, Pêgo AP. 'Delivery of splice switching oligonucleotides by amphiphilic chitosan-based nanoparticles'. (2016) *Molecular Pharmaceutics,*13, 344-356

Lopes CD, **Gomes CP**, Neto, E, Sampaio P, Aguiar P, and Pêgo AP. 'Microfluidic-based platform to mimic the in vivo peripheral administration of neurotropic nanoparticles'. (2016) *Nanomedicine (Lond)*, 11, 3205-3221.

Gomes CP*, Varela-Moreira A*, Leiro V, Lopes CD, Moreno PMD, Gomez-Lazaro M, and Pêgo AP. 'A high-throughput bioimaging study to assess the impact of chitosan-based nanoparticle degradation on DNA delivery performance'. (2016) *Acta Biomater*, 46, 129-140.

Lopes CD, Goncalves NP, **Gomes CP**, Saraiva MJ, and Pêgo AP. 'BDNF gene delivery mediated by neuron-targeted nanoparticles is neuroprotective in peripheral nerve injury'. (2017) *Biomaterials*, 121, 83-96.

Gomes CP, Lopes CDF, Leitner M, Ebner A, Hinterdorfer P, and Pêgo AP. 'Atomic Force Microscopy as a Tool to Assess the Specificity of Targeted Nanoparticles in Biological Models of High Complexity'. (2017) *Adv Healthc Mater,* 6, 1700597.

Gomes CP, Oliveira H, Ebner A, Hinterdorfer P, and Pêgo AP. 'Molecular recognition force spectroscopy for probing cell targeted nanoparticles in vitro'. (2017) *in* Methods of Molecular Biology, Springer. (*In press*)

ORAL COMMUNICATIONS

Gomes C, Silva LG, Fonseca NA, Ramalho JS, Moreira JN. 'Activity of anti-Plk-1 siRNA on cancer cell lines of different histological origin'. III Congress of the Portuguese Society of Pharmaceutical Sciences and IX Spanish-Portuguese Conference on Controlled Drug Delivery, 13-15 October, 2011. Porto, Portugal

Gomes CP, Moreira A, Moreno P, Pêgo AP. 'Trimethyl Chitosan-Based Nanoparticles for Targeted Gene Delivery to the Peripheral Nervous System'. 11th International Conference of the European Chitin Society, 5-8 May, 2013. Porto, Portugal

Sadio A, **Gomes C**, Moreno P, Gustafsson JK, Hansson GC, David L, Pêgo AP, Almeida R. 'Regulação da expressão de CDX2 e penetrabilidade no muco gastrointestinal usando nanopartículas de siRNA e quitosano'. Semana digestiva, 12-15 June 2013. Vilamoura, Portugal.

Gomes CP, Moreira A, Moreno P, Pêgo AP. 'Trimethyl chitosan as a gene carrier to the peripheral nervous system'. 25th European Conference on Biomaterials and 10th Young Scientific Forum, 8-12 September, 2013. Madrid, Spain

Gomes CP, Moreira A, Gomez-Lazaro M, Moreno P, Pêgo AP. 'Uptake and intracellular localization of TMC-based nanoparticles assessed by imaging flow cytometry'. International Symposium in Applied Bioimaging – From Molecule to Man, 3-4 October, 2013. Porto, Portugal

Gomes CP, Varela-Moreira A, Gomez-Lazaro M, Leitner M, Ebner A, Hinterdorfer P, Pêgo AP. 'Targeted Gene Delivery into Peripheral Nervous System Mediated by Trimethyl Chitosan Nanoparticles'. 26th European Conference on Biomaterials and 11th Youth Scientific Forum, 31 August – 3 September, 2014. Liverpool, UK

Gomes CP, Varela-Moreira A, Gomez---Lazaro M, Leitner M, Ebner A, Hinterdorfer P, Pêgo AP. 'ImageStream® and Atomic Force Microscopy as Valuable Tools for the Characterization and Design of Targeted Nanoparticles'. International Symposium in Applied Bioimaging – Capturing life in a pixel, 16-17 October, 2014. Porto, Portugal

Lopes CDF, **Gomes CP**, Sampaio P, Pêgo AP. 'Neuronal targeting and retrograde axonal transport of TMC-based nanoparticles in primary neurons'. International Symposium in Applied Bioimaging – Capturing life in a pixel, 16-17 October, 2014. Porto, Portugal.

Varela-Moreira A, **Gomes CP**, Gomez-Lazaro M, Moreno PMD, Pêgo AP. 'Trimethyl Chitosan-Based Nanoparticles Intracellular Trafficking and Transfection: a Bioimaging Study'. International Symposium in Applied Bioimaging – Capturing life in a pixel, 16-17 October, 2014. Porto, Portugal.

Gomes CP, Varela-Moreira A, Gomez-Lazaro M, Moreno PMD, Pêgo, AP. 'Tuning Transfection Efficiency by Modulating the Biodegradation Rate of Trimethyl Chitosan Nanoparticles'. 27th European Conference on Biomaterials and 12th Youth Scientific Forum, 30 August – 3 September, 2015. Kraków, Poland.

Lopes CDF, **Gomes CP**, Pêgo AP. 'Targeted BDNF Gene Delivery Mediated by TMC-based Non-viral Vectors is Neuroprotective in Nerve Injury '. 4th TERMIS World Congress. 2015, Setembro 8-11, Boston, EUA

POSTERS IN CONFERENCES

Sadio A, Camilo V, **Gomes C**, Pires L, David L, Pêgo AP, Almeida R. 'Downregulation of CDX2 expression in gastric cells using chitosan/siRNA nanoparticles – A strategy to revert gastric intestinal metaplasia'. XXVth International Workshop on Helicobacter and related bacteria in chronic digestive inflammation and gastric cancer, 13 – 15 September, 2012. Ljubljana, Slovenia

Sadio A, Camilo V, **Gomes C**, Pires L, David L, Pêgo AP, Almeida R. 'Downregulation of CDX2 expression in gastric cells using chitosan/siRNA nanoparticles – A strategy to revert gastric intestinal metaplasia'. A One Day Symposium with Carlos Caldas sponsored by EACR, 29 October, 2012. Porto, Portugal

Sadio A, **Gomes C**, Moreno P, David L, Pêgo AP, Almeida R. 'Downregulation of CDX2 expression in gastric cells using chitosan modified with imidazole and trimethylchitosan/siRNA nanoparticles'. 11th International Conference of the European Chitin Society, 5-8 May, 2013. Porto, Portugal

Moreira A, **Gomes CP**, Moreno P, Pêgo AP. 'Biodegradation of Trimethyl chitosan-based nanoparticles for gene delivery'. International Symposium in Applied Bioimaging – From Molecule to Man, 3-4 October, 2013. Porto, Portugal

Varela-Moreira A, **Gomes CP**, Gomez-Lazaro M, Moreno PMD, Pêgo AP. 'Trimethyl chitosan-based Nanoparticles intracellular trafficking and transfection: a bioimaging study'. 26th European Conference on Biomaterials and 11th Youth Scientific Forum, 31 August – 3 September, 2014. Liverpool, UK

Moreno PMD, Santos JC, **Gomes CP**, Varela-Moreira A, Costa A, Mendonça F, Pêgo AP. 'Hydrophobic quaternized chitosan for efficient nanoparticle formation and transfection of therapeutic oligonucleotides'. 26th European Conference on Biomaterials and 11th Youth Scientific Forum, 31 August – 3 September, 2014. Liverpool, UK

Lopes CDF, **Gomes CP**, Sampaio P, Pêgo AP. "Neuronal targeting and retrograde axonal transport of TMC-based nanoparticles in primary neurons 4th Annual I3S Meeting. 2014, October 30-31, Porto, Portugal.

Lopes CDF, **Gomes CP**, Sampaio P, Aguiar P, Pêgo, AP. "Chitosan-based platform for targeted gene delivery to peripheral nervous system" 4th FMUP PhD Students Meeting. 2014, December 9, Porto, Portugal

Lopes CDF, **Gomes CP**, Pêgo, AP. "Beneficial effects of neuron-targeted BDNF gene delivery mediated by non-viral TMC-based vectors" XIV Meeting of the Portuguese Society for Neurosciences. 2015, Junho 4-5, Póvoa de Varzim, Portugal

Gomes CP, Varela-Moreira A, Gomez-Lazaro M, Leitner M, Ebner A, Hinterdorfer P, Pêgo AP. 'Targeted Gene Delivery into Peripheral Nervous System Mediated by Trimethyl Chitosan Nanoparticles'. 42nd Controlled Release Society Annual Meeting and Exposition – Creating Value through Customised Delivery, 26-29 July, 2015. Edinburgh, Scotland.

Gomes CP, Varela-Moreira A, Gomez-Lazaro M, Lopes CDF, Leiro V, Moreno PMD, Pêgo AP. 'Tailored Trimethyl Chitosan Nanoparticles for Specific Gene Delivery to the Nervous System'. European Society for Gene and Cell Therapy (ESGCT) and Finish Society of Gene Therapy (FSGT) Collaborative Congress, 17-20 September, 2015. Helsinki, Finland.

Lopes CDF, Aguiar P, **Gomes CP**, Sampaio P, Pêgo AP. "Targeted and active retrograde axonal transport of TMC-based nanoparticles in primary neurons: a bioimaging challenge". 4th International Symposium in Applied Bioimaging – The pre-clinical challenge in 3D. 2015, November 5-6, Porto, Portugal